



**Numerical methods for parametric PDE
models in time-harmonic acoustics**

Von der Fakultät für Mathematik und Naturwissenschaften der Carl von
Ossietzky Universität Oldenburg zur Erlangung des Grades und Titels
eines

Doctor rerum naturalium (Dr. rer. nat.)

angenommene Dissertation

von Herrn Nick Wulbusch
geboren am 20.04.1993 in Oldenburg

Gutachter: Prof. Dr. Alexey Chernov

Weitere Gutachter:

Prof. Dr. Fabio Nobile

Prof. Dr. Volker Hohmann

Tag der Disputation: 14.03.2025

Eidesstattliche Erklärung

Ich versichere, dass ich die vorliegende Arbeit selbstständig verfasst und keine anderen als die angegebenen Quellen und Hilfsmittel benutzt und die allgemeinen Prinzipien wissenschaftlicher Arbeit und Veröffentlichungen, wie sie in den Leitlinien guter wissenschaftlicher Praxis der Carl von Ossietzky Universität Oldenburg festgelegt sind, befolgt habe.

Oldenburg,

Abstract

Wave propagation phenomena play a fundamental role in current technologies, industrial application and scientific research. It can be found in acoustics, electromagnetism, seismology and other fields. The underlying mathematical models are typically more involved to solve than for stationary problems like diffusion and linear elasticity due to the oscillatory behavior of the solutions. This thesis explores different numerical methods in order to enhance the accuracy of solutions for acoustic wave propagation.

The main focus of the first part of this work is the estimation of sound pressure transfer to the eardrum. The transfer is highly influenced by the shape of the ear canal and its acoustic properties, such as the acoustic impedance at the eardrum. Invasive procedures to measure the sound pressure at the eardrum are usually elaborate or costly. We propose a numerical method to estimate the transfer impedance of the ear canal given only input impedance measurements at the ear canal entrance, by using one-dimensional first-order finite elements and Nelder-Mead optimization algorithm. Estimations on the area function of the ear canal and the acoustic impedance at the eardrum are obtained. Results are validated through numerical simulations on ten different ear canal geometries and three different acoustic impedances at the eardrum, using synthetically generated data from three-dimensional finite element simulations.

Further, we consider the problem of identifying the acoustic impedance of a wall surface from noisy pressure measurements in a closed room using a Bayesian approach. The room acoustics are modeled by the interior Helmholtz equation with impedance boundary conditions. The aim is to compute moments of the acoustic impedance to estimate a suitable density function of the impedance coefficient. For the computation of moments we use ratio estimators and Monte Carlo sampling. We consider two different experimental scenarios. In the first scenario, the noisy measurements correspond to a wall modeled by impedance boundary conditions. In this case, the Bayesian algorithm uses a model that is (up to the noise) consistent with the measurements and our algorithm is able to identify acoustic impedance with high accuracy. In the second scenario, the noisy measurements come from a coupled acoustic-structural problem, modeling a wall made of glass, whereas the Bayesian algorithm still uses a model with impedance boundary conditions. In this case, the parameter identification model is inconsistent with the measurements and therefore is not capable to represent them well. Nonetheless, for particular frequency bands the Bayesian algorithm identifies estimates with high likelihood. Outside these frequency bands the algorithm fails. We discuss the results of both examples and possible reasons for the failure of the latter case for particular frequency values. We also compare the approach of using ratio estimators for computing

moments with a Markov-Chain Monte Carlo method.

The thesis also addresses stochastic partial differential equation constrained shape optimization. The constraint is represented by a time-harmonic wave problem having a source term with an uncertain location. A typical goal functional represents the misfit between the computed solution and a prescribed function within the computational domain. The aim is to determine the optimal shape of the domain boundary minimizing the goal functional. We investigate theoretically and numerically convergence of gradient-based optimization algorithms and for time-harmonic acoustic problems.

Finally, we examine numerical methods for solving exterior acoustic problems using the finite element method. In such cases, the radiation condition is approximated by truncating the domain with an artificial absorbing boundary. Popular choices include absorbing boundary conditions (ABC) or absorbing layers, where the implementation of the latter is usually more involved. This thesis proposes an alternative method: Since reflection error is typically small for waves with normal (0 degrees) incidence, we propose positioning the artificial boundary such that the incident angles become small. We consider several two-dimensional problems and study our approach numerically using different ABCs.

Zusammenfassung

Wellenausbreitungsphänomene spielen eine fundamentale Rolle in modernen Technologien, industriellen Anwendungen und der wissenschaftlichen Forschung. Sie treten in der Akustik, dem Elektromagnetismus, der Seismologie und anderen Gebieten auf. Aufgrund des oszillierenden Verhaltens der Lösung ist der Aufwand zur Lösung der zugrunde liegenden Modelle im Allgemeinen größer als beispielsweise bei stationären Problemen der Diffusion oder linearen Elastizität. Diese Dissertation untersucht verschiedene numerische Methoden um, die Genauigkeit von Lösungen für akustische Wellenausbreitung zu verbessern.

Der wesentliche Inhalt des ersten Teils dieser Arbeit ist die Schätzung des Schalldrucktransfers am Trommelfell. Der Transfer hängt stark von der Form des Gehörgangs und akustischen Eigenschaften wie der akustischen Impedanz am Trommelfell ab. Invasive Methoden, um den Schalldruck am Trommelfell zu messen, sind üblicherweise aufwendig oder teuer. Wir schlagen eine numerische Methode zur Schätzung der Transferimpedanz des Gehörgangs vor, wobei nur Eingangsimpedanzmessungen am Gehörgangseingang gegeben sind. Dies bewerkstelligen wir mit eindimensionalen finiten Elementen und dem Nelder-Mead-Optimierungsalgorithmus. Zusätzlich erhalten wir Schätzungen der Flächenfunktion des Gehörgangs und der akustischen Impedanz des Trommelfells. Die Ergebnisse werden mit synthetisch generierten Daten aus dreidimensionalen Finite-Elemente-Simulationen für zehn verschiedene Gehörgangsformen und drei verschiedene akustische Impedanzen validiert.

Ferner wird das Problem der Identifikation der akustischen Impedanz an einer Wandoberfläche anhand von verrauschten Messdaten in einem geschlossenen Raum mit Hilfe eines Bayes'schen Ansatzes behandelt. Die Raumakustik wird durch die innere Helmholtzgleichung mit Impedanzrandbedingungen modelliert. Das Ziel ist die Schätzung statistischer Momente der akustischen Impedanz und die Schätzung einer nützlichen Dichtefunktion des Impedanzkoeffizienten. Für die Berechnung der Momente verwenden wir Quotientenschätzer und Monte-Carlo-Stichproben. Wir betrachten zwei unterschiedliche Szenarien. Im ersten Szenario entsprechen die verrauschten Messungen denen einer durch Impedanzrandbedingungen modellierten Wand. In diesem Fall nutzt der Bayes'sche Algorithmus ein Modell, das (bis auf das Rauschen) konsistent mit den Messungen ist. In diesem Fall ist unser Algorithmus in der Lage die akustische Impedanz mit hoher Genauigkeit zu identifizieren. Im zweiten Szenario stammen die verrauschten Messdaten von einem gekoppelten Akustik-Struktur-Problem, bei dem eine Wand aus Glas modelliert wird. Der Bayes'sche Algorithmus verwendet weiterhin die Impedanzrandbedingungen. In diesem Fall ist die Parameteridentifikation inkonsistent

mit den Messungen und daher nicht fähig diese darzustellen. Dennoch identifiziert der Bayes'sche Algorithmus für bestimmte Frequenzbänder Schätzungen mit hoher Plausibilität. Außerhalb dieser Frequenzbänder versagt der Algorithmus. Wir diskutieren die Ergebnisse für beide Beispiele und mögliche Gründe für das Versagen im letzten Fall für spezielle Frequenzbänder. Wir vergleichen ferner den Ansatz mit Quotientenschätzern zur Berechnung statistischer Momente mit einem Markov Chain Monte Carlo Verfahren.

Diese Arbeit befasst sich außerdem mit Formoptimierung mit stochastischen partiellen Differentialgleichungen als Nebenbedingung. Die Nebenbedingung ist ein zeitharmonisches Wellenproblem mit einer Quelle, deren Position unsicher ist. Ein typisches Zielfunktional repräsentiert die Diskrepanz zwischen der berechneten und einer vorgegeben Funktion innerhalb des Rechengebiets. Das Ziel ist die Bestimmung der optimalen Form der Berandung des Gebietes, die das Zielfunktional minimiert. Wir untersuchen theoretisch, und die Konvergenz numerisch, gradientenbasierte Optimierungsalgorithmen für zeitharmonische akustische Probleme.

Schließlich untersuchen wir numerische Methoden für akustische Außenraumprobleme mittels der finiten Elemente Methode. In diesem Fall muss die Abstrahlungsbedingung durch Begrenzung des Gebietes mit einem künstlich absorbierenden Rand geschehen. Gängige Möglichkeiten der Modellierung sind absorbierende Randbedingungen oder absorbierende Schichten. Diese Dissertation schlägt eine alternative Methode vor: Da Reflektionsfehler für senkrecht eintreffende Wellen typischerweise klein sind, schlagen wir vor die künstliche Begrenzung des Gebiets so vorzunehmen, dass der Einfallswinkel am gesamten Rand klein wird. Dazu betrachten wir mehrere zwei-dimensionale Probleme und untersuchen unseren Ansatz numerisch mit verschiedenen absorbierenden Randbedingungen.

Acknowledgements

I want to thank my supervisor Prof. Dr. Alexey Chernov for his guidance, expertise and encouragement.

I am also grateful to Prof. Dr. Matthias Blau, Prof. Dr. Andrea Moiola, Dr. Frank Schöpfer and Reinhild Roden for the collaboration and many interesting discussions. I further want to thank Erik and Tùng with whom I luckily was able to share an office for many years. I am grateful for all your support and discussions.

I want to thank Marvin and Tim and all the other friends and family who emotionally supported and encouraged me. I want to thank my children Thilo, Jaron and Thekla for their patience and understanding during the demanding phases of this work. Finally, I want to express my deepest thanks to my partner, Astrid, for the unconditional and unwavering support and encouragement.

This work would not have been possible without all of you - thank you.

Contents

List of Figures	xi
List of Tables	xvii
1 Introduction	1
2 Preliminaries	5
2.1 Introduction	5
2.2 Uniqueness and existence of solutions to elliptic second order BVPs	7
2.2.1 Time-harmonic horn equation	10
2.2.2 Helmholtz equation in 2D/3D	13
2.3 Discretization using finite elements	17
2.3.1 Finite element space	17
2.3.2 Approximation in V_h	17
3 Estimating individual ear canal acoustic transfer	21
3.1 Introduction	21
3.2 Modeling approach and parameter estimation	23
3.3 Synthetic and validation data preparation	26
3.4 Original parameter fitting and refinement of the method	28
3.4.1 Avoiding negative areas	30
3.4.2 Accommodating long and short ear canals	32
3.4.3 Influence of the bandwidth and frequency spacing used in the parameter fitting	33
3.4.4 Influence of the number of parameters in the area function expansion	35
3.5 Validation	36
3.5.1 Transfer impedance	36
3.5.2 Ear canal area function	38
3.5.3 Impedance at eardrum	39
3.6 Conclusion	39
4 Bayesian Parameter Identification	41
4.1 Introduction	41
4.2 Preliminaries	43
4.2.1 Weak formulation	44
4.2.2 Very weak formulation for point source excitations	44
4.3 Finite Element Discretization	46

4.4	Bayesian framework	47
4.4.1	Continuous posterior moments	48
4.4.2	Computable posterior moments	51
4.5	Numerical experiments	55
4.5.1	The general experimental setup	56
4.5.2	On the selection of the prior and fitted posterior densities	57
4.5.3	2D model: Discretization and sampling error	58
4.5.4	3D problem with data from impedance problem	62
4.5.5	3D problem with data from coupled acoustic-structural problem	64
4.6	On the Markov-Chain Monte Carlo method	69
4.7	Outlook	74
5	Shape optimization for uncertain source location	75
5.1	Basic concepts of PDE-constrained shape optimization	76
5.2	Computation of shape gradients	77
5.3	Shape optimization of rectangular domain to minimize goal functional in certain subdomain	84
5.3.1	Domain transformation and velocity field	85
5.3.2	Goal functional and problem formulation	87
5.3.3	Gradient descent algorithm using Armijo backtracking	87
5.4	Expectation domains for uncertain source location	91
5.5	Conclusion	101
6	Optimized truncation of domains for exterior Helmholtz problems	102
6.1	An approach to approximate the Sommerfeld condition by domain truncation	103
6.1.1	Absorbing boundary conditions	106
6.1.2	Perfectly matched layer	107
6.1.3	Residuals for non-perpendicular incoming waves	108
6.1.4	The Poynting vector for plane waves and the fundamental solution	110
6.2	Numerical comparison of contour and standard circular truncation	111
6.2.1	Scattering problems	112
6.2.2	Problem with point sources as Dirichlet data	116
6.3	Conclusions	118
7	Conclusions and Outlook	119

List of Figures

1.1	Contents of this thesis.	3
2.1	Unique continuation principle illustrated for the Helmholtz problem in a two-dimensional domain, based on figure 1 in [50].	16
3.1	Level difference and phase difference of $Z_{\text{in}} = \frac{p(0)}{q}$ and $Z_{\text{in,ref}} = \frac{p_{\text{ref}}(0)}{q}$ and $Z_{\text{tr}} = \frac{p(L)}{q}$ and $Z_{\text{tr,ref}} = \frac{p_{\text{ref}}(L)}{q}$. The discrete solution p of (3.8) is computed with $N = 4 \max(1 \text{ m} \cdot \ell / \lambda^2, 1)$ elements for a typical area function $S(x)$ and eardrum impedance Z_d . The reference solution p_{ref} is computed with $N_{\text{ref}} = 5000$ elements. The error is uniformly bounded within the frequency range 100 Hz to 20 kHz.	25
3.2	Solution for the Horn equation with $f = 6000$ Hz with variable area function and constant area function using linear finite elements (left) and associated area functions (right).	26
3.3	Mesh of the ear canal of Subject 5 cut at the first bend. The ear canal was rotated such that both the entrance and the eardrum (marked faces) are visible.	27
3.4	Eardrum impedances types (i) and (ii) for \tilde{Z}_{ED} that were used to compute the reference data. Type (iii) is not shown due to the large magnitude that is constant at approximately 458 dB with zero phase.	28
3.5	Results for the original parameter fitting method for Subject 5 and impedance model (ii). Solutions to each of the twelve different initial parameter sets are depicted by a black line respectively. Left: Area function. The rear part represents the cone as part of the impedance model, see discussion in Section 3.2. Center: Input impedance Z_{in} . Right: Transfer impedance Z_{tr}	30
3.6	Parameter fitting may lead to negative values of the area function. Results for Subject 3 and impedance model (i). Solutions to each of the twelve different initial parameter sets are depicted by a black line respectively. Left: Area function. The rear part represents the cone as part of the impedance model, see discussion in Section 3.2. Center: Input impedance Z_{in} . Right: Transfer impedance Z_{tr}	31

List of Figures

3.7	Left: Results incorporating penalty term J_1 for Subject 3 and impedance model (i) for twelve different initial parameter sets. Parameter fitting may lead to unrealistic ear canal geometries due to large increases in the area function near the eardrum. Center: Results incorporating penalty terms J_1 and J_2 for Subject 3 and impedance model (i) for twelve different initial parameter sets. Parameter fitting may lead to largely overestimating the length of the ear canal. Right: Results incorporating penalty terms J_1 , J_2 and prior estimating of the ear canal length ℓ for Subject 3 and impedance model (i) for twelve different initial parameter sets. Parameter fitting leads to a realistic area function.	32
3.8	Ear canal of Subject 9 and impedance model (i) as example for a case of high frequency behavior that cannot be reproduced with the one-dimensional model. The last minimum in the entrance and transfer impedance data gets very low. Including high frequencies in the parameter fitting very likely influences precision for lower frequencies.	33
3.9	Ear canal of Subject 9 and impedance model (i) when only using data for frequencies up to 10 kHz. Improvements in the lower frequency range, especially up to 8 kHz can be observed in comparison to Figure 3.8.	34
3.10	Validation for the parameter fitting considering differences of the transfer impedance for frequencies for linearly distributed frequencies up to 20 kHz considering all data sets. Straight solid line: 5 dB or 45° difference. Straight dashed line: 3 dB or 22.5° difference. Blue lines: 5 and 95 quantile. Red line in between: Mean. Dashed gray lines: Frequencies used during the parameter fitting.	35
3.11	Validation function J_{val} depending on number of Fourier coefficients in area function.	36
3.12	Validation for the parameter fitting considering differences of the transfer impedance for frequencies for up to 10 kHz. Straight solid line: 5 dB or 45° difference. Straight dashed line: 3 dB or 22.5° difference. Blue lines: 5 and 95 quantile. Red line in between: Mean. Dashed gray lines: Frequencies used during the parameter fitting.	37
3.13	Validation for the parameter fitting considering differences of the transfer impedance for frequencies for up to 20 kHz excluding Subject 9 that showed unusual behavior for high frequencies. Straight solid line: 5 dB or 45° difference. Straight dashed line: 3 dB or 22.5° difference. Blue lines: 5 and 95 quantile. Red line in between: Mean. Dashed gray lines: Frequencies used during the parameter fitting.	37
3.14	Results for the ear canal area functions for all ten subjects and all three impedance models 10 kHz.	38
3.15	Estimattted impedances at the eardrum for different underlying model data: (i) Hudde (ii) two-resonator (iii) rigid.	39
4.1	Domain for model problem in 2D. Black dots indicate the grid of possible microphone positions.	55

4.2 Discretization error for statistical parameters of $Z^{(1)}$ (left) and $Z^{(2)}$ (right) for $f = 50$ Hz. Note that the absolute errors are shown. Thus, the error curves belonging to the parameters of the lognormal distribution are lower. 59

4.3 Sampling error for statistical parameters of $Z^{(1)}$ (left) and $Z^{(2)}$ (right) for $f = 50$ Hz. Note that the absolute errors are shown. Thus, the error curves belonging to the parameters of the lognormal distribution are lower. 60

4.4 Prior density and density given by estimated expected value and standard deviation for $f = 50$ Hz for $Z^{(1)}$ (left) and $Z^{(2)}$ (right). 60

4.5 Prior density and density given by estimated expected value and standard deviation for $f = 100$ Hz for $Z^{(1)}$ (left) and $Z^{(2)}$ (right). 61

4.6 Absolute value of the reference solution with $Z_{\text{ref}}^{(1)} = 400 - 700i$ and $Z_{\text{ref}}^{(2)} = 500 + 800i$ (left) and the reconstructed solution with the most likely acoustic impedance value during the sampling process $Z^{(1)} \approx 427 - 697i$ and $Z^{(2)} \approx 583 + 860i$ (right) for $f = 50$ Hz. The source is located at $(1, 1)$. The red marks are the measurement positions. 62

4.7 Domain for model problem in 3D. 62

4.8 Maximum log-likelihood for the impedance problem. The thin lines correspond to the individual runs. 63

4.9 Estimated expected value (real part left, imaginary part right) of the impedance for the impedance problem for all 20 runs. The black dashed line indicates the reference impedance value. The red line is the mean over all runs. Thin lines correspond to individual runs. 63

4.10 Most likely impedance (real part left, imaginary part right) for the impedance problem for all 20 runs. The black dashed line indicates the reference impedance value. The red line is the mean over all runs. Thin lines correspond to individual runs. 64

4.11 Prior density and density given by estimated expected value and standard deviation for $f = 25$ Hz (left) and $f = 95$ Hz (right). 65

4.12 Eigenfrequencies of coupled problem, pure impedance problem (sound hard at $\Gamma_R^{(2)}$) and for the glass wall (window) decoupled from the room acoustics (boundary conditions were set to be free at the large front and back surfaces and fixed at the edges of the window). 66

4.13 Maximum log-likelihood for the coupled problem with eigenfrequencies (real part). The thin lines correspond to the individual runs. 67

4.14 The reference solution that produces artificial measurement data (left) and the likelihood maximizer computed by the algorithm (right) in dB (re 20 μPa) for $f = 51.5$ Hz. 67

4.15 The reference solution that produces artificial measurement data (left) and the likelihood maximizer computed by the algorithm (right) in dB (re 20 μPa) for $f = 54.5$ Hz. 68

4.16 The reference solution that produces artificial measurement data (left) and the likelihood maximizer computed by the algorithm (right) in dB (re 20 μPa) for $f = 69$ Hz. 68

List of Figures

4.17	Samples drawn during the Metropolis-Hastings algorithm for Cases 1-4 with different starting samples $Z^{(0)}$ and χ . The height of the points coincide with the computed posterior $\theta(Z, y)\pi_0(Z)$. The posterior is scaled such that the maximum is 1.	73
4.18	True and estimated posterior for the different Cases 1-4, scaled such that the maximum value is 1.	74
5.1	Domain to problem (5.4). G is the subdomain of Ω in which the solution p_Ω to (5.4) is supposed to minimize the goal functional. The small red circle illustrates the sound source, i.e., the support of f . The large red circle shows possible source locations for Section 5.4. The boundary Γ_R in red is the part of the boundary that is transformed during the shape optimization.	85
5.2	Domain transformation at the bottom boundary of a rectangular domain.	86
5.3	Discretization error of the goal functional J for different wave numbers k (left) and the shape derivative dJ for $k = 2$ (right) with respect to mesh size h . The reference was computed on a very fine mesh with $h_{\text{ref}} \approx 0.00035$.	89
5.4	Convergence of geometry parameters t for $t_{\text{data}} = (0.1, 0, 0, 0, 0)$ (left) and goal functional J for different t_{data} (right) with respect to the iteration in the optimization algorithm for $k = 2$	90
5.5	Transformation of domains for different numbers of iterations in the optimization algorithm for $k = 2$ and $t_{\text{data}} = (0.1, 0, 0, 0, 0)$. Left: Whole domain. Right: Zoom-in on transformed boundary.	90
5.6	Domain deviation for Vorob'ev and parametric domain with respect to sample size for different wave number k	93
5.7	Vorob'ev and parametric domain for different number of samples in the optimization algorithm for $k = 8$. Left: Whole domain. Right: Zoom-in on transformed boundary. The reference solution was computed with high sample size of $M = 512$	94
5.8	Solution on different domains with source location $s = (0.75, 1.8)$ and $k = 2$. Top left: Initial domain. Top right: Parametric domain. Bottom left: Vorob'ev domain. Bottom right: Reference domain (image restricted to the same size as the other domains).	95
5.9	Solution on different domains with source location $s = (0.8, 1.85)$ and $k = 2$. Top left: Initial domain. Top right: Parametric domain. Bottom left: Vorob'ev domain. Bottom right: Reference domain (image restricted to the same size as the other domains).	95
5.10	Goal functional with respect to source location for $k = 2$. Top left: Initial domain. Top right: Parametric domain. Bottom left: Vorob'ev domain. Bottom right: Reference domain.	96
5.11	Solution on different with source location $s = (0.75, 1.8)$ and $k = 3.25$. Top left: Initial domain. Top right: Parametric domain. Bottom left: Vorob'ev domain. Bottom right: Reference domain (image restricted to the same size as the other domains).	97

5.12 Solution on different with source location $s = (0.8, 1.85)$ and $k = 3.25$.
 Top left: Initial domain. Top right: Parametric domain. Bottom left:
 Vorob'ev domain. Bottom right: Reference domain (image restricted to
 the same size as the other domains). 97

5.13 Goal functional with respect to source location for $k = 3.25$. Top left:
 Initial domain. Top right: Parametric domain. Bottom left: Vorob'ev
 domain. Bottom right: Reference domain. 98

5.14 Solution on different with source location $s = (0.75, 1.8)$ and $k = 6.25$.
 Top left: Initial domain. Top right: Parametric domain. Bottom left:
 Vorob'ev domain. Bottom right: Reference domain (image restricted to
 the same size as the other domains). 99

5.15 Solution on different with source location $s = (0.8, 1.85)$ and $k = 6.25$.
 Top left: Initial domain. Top right: Parametric domain. Bottom left:
 Vorob'ev domain. Bottom right: Reference domain (image restricted to
 the same size as the other domains). 99

5.16 Goal functional with respect to source location for $k = 6.25$. Top left:
 Initial domain. Top right: Parametric domain. Bottom left: Vorob'ev
 domain. Bottom right: Reference domain. 100

5.17 Average functional $\bar{J}_{k,k'}$ over k' . Top left: Optimized for each k individ-
 ually, i.e., $k = k'$. Top right: Domain optimized for $k = 1.75$. Bottom
 left: Domain optimized for $k = 3.25$. Bottom right: Domain optimized
 for $k = 4.75$ 101

6.1 Domain of the exterior Helmholtz problem with indicated possible trun-
 cation. 104

6.2 Fundamental solutions for the Helmholtz equation in two and three spatial
 dimensions. 105

6.3 Domain with additional layer for absorption. 108

6.4 Residual at the boundary for the impedance boundary condition and the
 C-ABC in 2D and 3D (for one angle) with respect to incidence angle. . . 109

6.5 Residual at the boundary for the impedance boundary condition (left)
 and C-ABC (right) in 3D with respect to two incidence angles. 109

6.6 Circular scatterer: Complex argument (top) and absolute value (bottom)
 of the solution p on original domain, contour domain and area-equivalent
 domain for $f = 1478$ Hz. The red circle indicates the domain Ω_s 112

6.7 Relative L^2 -error $\frac{\|p-p_{\text{ref}}\|_{L^2(\Omega)}}{\|p_{\text{ref}}\|_{L^2(\Omega)}}$ and $\frac{\|p-p_{\text{ref}}\|_{L^2(\Omega_s)}}{\|p_{\text{ref}}\|_{L^2(\Omega_s)}}$ on the whole domain and
 a small circular domain around the circular scatterer, respectively, with
 respect to frequency for impedance and C-ABC on the contour and area-
 equivalent domains. 113

6.8 Rectangular scatterer: Complex argument (top) and absolute value (bot-
 tom) of the solution p on original domain, contour domain and area-
 equivalent domain for $f = 1478$ Hz. The red circle indicates the domain
 Ω_s 114

List of Figures

6.9 Kite-shaped scatterer: Complex argument (top) and absolute value (bottom) of the solution p on original domain, contour domain and area-equivalent domain for $f = 1478$ Hz. The red circle indicates the domain Ω_s . Note that the original domain is chosen larger ($r = 2.5$ m) since otherwise it was not possible to find a continuous contour line inside the domain. The small comparison domain Ω_s is also slightly larger with radius 0.8 m to fully enclose the scatterer. 115

6.10 Relative L^2 -error $\frac{\|p-p_{\text{ref}}\|_{L^2(\Omega)}}{\|p_{\text{ref}}\|_{L^2(\Omega)}}$ and $\frac{\|p-p_{\text{ref}}\|_{L^2(\Omega_s)}}{\|p_{\text{ref}}\|_{L^2(\Omega_s)}}$ on the whole domain and a small circular domain around the rectangular scatterer with respect to frequency for impedance and C-ABC on the contour and area-equivalent domains. 115

6.11 Relative L^2 -error $\frac{\|p-p_{\text{ref}}\|_{L^2(\Omega)}}{\|p_{\text{ref}}\|_{L^2(\Omega)}}$ and $\frac{\|p-p_{\text{ref}}\|_{L^2(\Omega_s)}}{\|p_{\text{ref}}\|_{L^2(\Omega_s)}}$ on the whole domain and a small circular domain around the kite-shaped scatterer, respectively, with respect to frequency for impedance and C-ABC on the contour and area-equivalent domains. 116

6.12 Point sources. Complex argument (top) and absolute value (bottom) of solution on original domain, contour domain and area-equivalent domain for $f = 1478$ Hz. The red circle indicates the domain Ω_s 117

6.13 Relative L^2 -error $\frac{\|p-p_{\text{ref}}\|_{L^2(\Omega)}}{\|p_{\text{ref}}\|_{L^2(\Omega)}}$ and $\frac{\|p-p_{\text{ref}}\|_{L^2(\Omega_s)}}{\|p_{\text{ref}}\|_{L^2(\Omega_s)}}$ on the whole domain and a small circular domain around the circle that surrounds the point sources, respectively, with respect to frequency for impedance and C-ABC on the contour and area-equivalent domains. 117

List of Tables

3.1	Parameters used for the generation of data using the two-resonator model.	28
3.2	Basic estimate with lower and upper bounds of the parameters of the ear canal area function and the two-resonator impedance model used in the one-dimensional surrogate model. The decibel values for impedance levels $L_{0,1}$ and $L_{0,2}$ refers to dB re 1 Pa · s/m ³ .	29
4.1	Estimated expectation for various the Cases 1-4 for different χ and starting sample $Z^{(0)}$ (in $\frac{Pa \cdot s}{m^3}$).	71
4.2	Estimated variance for various the Cases 1-4 for different χ and starting sample $Z^{(0)}$ (in $\frac{Pa \cdot s}{m^3}$).	72

Chapter 1

Introduction

Acoustic wave propagation can be described via the wave equation

$$\Delta_x P(x, t) = \frac{1}{c^2} \frac{\partial^2 P(x, t)}{\partial t^2}, \quad (1.1)$$

where P is the complex-valued time-dependent pressure, c is the speed of sound in the medium, x is the spatial variable and t is time. Often, wave propagation is studied in time-harmonic settings. This way, it can be analyzed for specific frequencies isolated. For this the ansatz¹

$$P(x, t) = p(x)e^{i\omega t}$$

is used, where $\omega = 2\pi f$ is the radian frequency with respect to frequency f . i is the imaginary unit. Substituting this in the wave equation (1.1) leads to

$$\begin{aligned} \Delta_x p(x)e^{i\omega t} &= \frac{1}{c^2} (i\omega)^2 p(x)e^{i\omega t} \\ \Rightarrow \Delta p(x) &= - \underbrace{\frac{\omega^2}{c^2}}_{=: k^2} p(x) \end{aligned}$$

and thus leading to the Helmholtz equation

$$-\Delta p(x) - k^2 p(x) = 0$$

with wave number k . In this thesis we study numerical methods for harmonic wave propagation in acoustics. For this we consider the one-dimensional Webster's horn equation and the Helmholtz equation in two and three space dimensions. The time-harmonic version of Webster's horn equation [109] to model the pressure p in a horn (or ear canal) is given as the following boundary value problem (BVP)

$$\begin{aligned} -\frac{\partial}{\partial x} \left(S(x) \frac{\partial p}{\partial x} \right) - k^2 S(x) p(x) &= 0, \quad x \in (0, L), \\ S(0) p'(0) &= g, \\ S(L) p'(L) + i\alpha p(L) &= 0. \end{aligned} \quad (1.2)$$

¹This convention seems to be prevalent in the applications that we deal with in Chapters 3-5, see e.g. [70, 81, 108], and is also used in the commercial software COMSOL. There also exists a different convention with regard to the sign in the exponent that leads to the ansatz $P(x, t) = p(x)e^{-i\omega t}$. This ansatz is dominant in the community with respect to the contents of Chapter 6, which is why we use a different ansatz in that chapter.

Here, S denotes the area function (of the horn or ear canal). At $x = 0$ a source is assumed (incoming sound at the ear canal entrance) and at $x = L$ some reflecting wall (reflection and absorption of the ear drum). The coefficient α describes reflectance and absorption. In the following chapters α will usually have the form $\alpha = \frac{\omega\rho}{Z}$ where ρ is the density of the medium (typically air) and Z is the complex-valued surface impedance consisting of the real part (acoustic resistance) and the imaginary part (acoustic reactance). Note that for $Z = \rho c$ the Robin boundary condition becomes (for $S \equiv 1$)

$$p'(L) + ikp(L) = 0$$

which is equivalent to full absorption, i.e., no reflection for a plane wave p , i.e., let $p(x) = e^{-ikx}$, then

$$p'(L) + ikp(L) = -ike^{-ikL} + ike^{-ikL} = 0.$$

We will now introduce the Helmholtz equation in two and three dimensions. Let $\Omega \subset \mathbb{R}^d$, $d = 2, 3$. The Helmholtz equation is given as

$$\begin{aligned} -\Delta p - k^2 p &= f && \text{in } \Omega \\ p &= p_D && \text{on } \Gamma_D \\ \frac{\partial p}{\partial n} &= g && \text{on } \Gamma_N \\ \frac{\partial p}{\partial n} + i\alpha p &= 0 && \text{on } \Gamma_R \end{aligned} \tag{1.3}$$

Here f denotes a source in the domain. Homogeneous Dirichlet and Neumann conditions model a sound-soft or sound-hard boundary. In these cases either the pressure p or its normal derivative, i.e., the velocity is zero. In scattering problems with a sound-soft scatterer we often have $p_D = -p_{\text{inc}}$, where p_{inc} describes the pressure of an incoming wave. That way the total field, i.e., the sum of scattered and incoming wave, has vanishing pressure at the boundary and thus is modeled as sound-soft. The Robin boundary condition at Γ_R describes a mix of absorption and reflection depending on the parameter α .

The overall goal of this thesis is to enhance the accuracy of acoustic simulations, see Figure 1.1 for an overview of the contents of this thesis. This will be done in different ways: Identifying parameters of geometry and those used in the partial differential equations (1.2) and (1.3) and optimizing the shape of the domain to minimize a goal functional or derive improved discretized models. To tackle these tasks the thesis is structured as follows: In Chapter 2 we revisit preliminaries of functional analysis and the theory of partial differential equations as well as their discretization with the finite element method (FEM). In this chapter the problems (1.2) and (1.3) are stated in weak formulation and well-posedness, i.e., existence and uniqueness of the solution, is shown for the infinite- and finite-dimensional, i.e., discretized, case. In Chapter 3 we consider the problem of estimating the ear canal transfer function. This is a highly important topic in the hearing aid research. The acoustic wave propagation in ear canals can be modeled by Webster's horn equation (1.2). However, since the individual shape of the

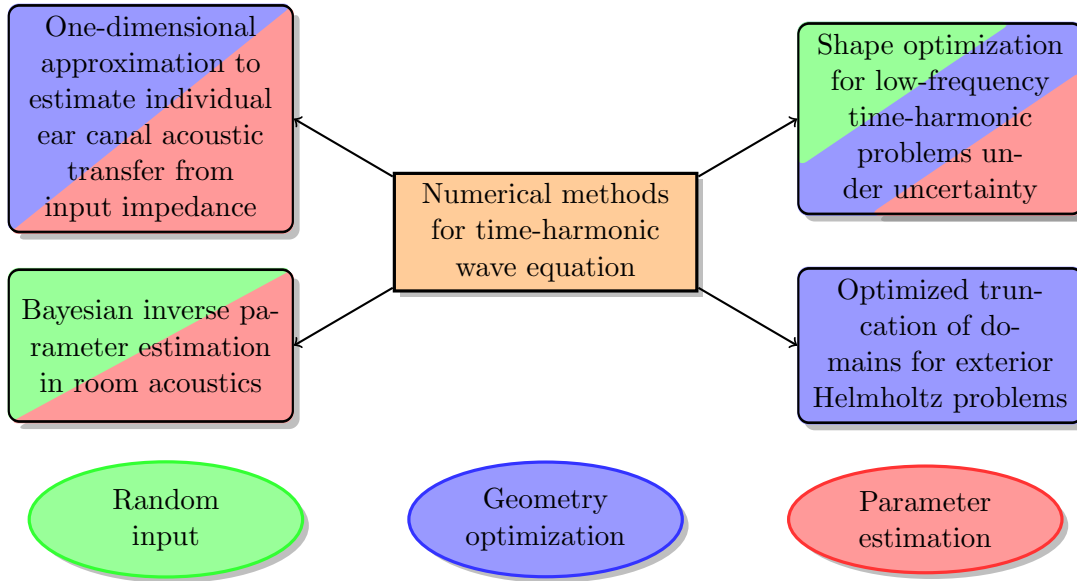


Figure 1.1: Contents of this thesis.

ear canal and exact behavior of the ear drum is unknown without elaborate measurements we need to estimate the parameters used in (1.2), namely the area function S , ear canal length L and acoustic impedance Z . Given measured data at the ear canal entrance we develop the framework to find the unknown parameters and estimate the ear canal transfer impedance.

In reality acoustic measurements, or measurements in general, are polluted by measurement errors. This error can have many sources, like noise or uncertain shapes and parameters. In Chapter 4 we address the estimation of parameters from acoustic measurements in a different setting. This time we consider a room-acoustics problem where we aim to find the acoustic impedance of a wall surface. Again, we do this by using measurements, however here we assume these are perturbed by noise. Hence the deterministic approach to estimate the parameter is not suitable. Instead we consider a Bayesian approach where we also assume the acoustic impedance to be a random variable and hence can study its statistics based on the random noise in the measurements.

Uncertainty does not only arise in the terms of noisy measurements. It can also come from the unknown location of a source. This problem is considered in Chapter 5. Here we assume the location of a sound source to be uncertain. The aim will be to optimize the shape of the domain in a certain way, such that a goal functional is minimized. Due to the uncertainty of the source location, we need to integrate the uncertainty in the optimizing procedure which is why we introduce expectation domains and evaluate these by comparing them to an initial domain and the truth solution.

The shape of the domain plays a role also in a rather different part of acoustic simulations. In exterior Helmholtz problems we aim to approximate a solution in an unbounded spatial domain. In this free space setting the acoustic waves decay and fulfill the Som-

merfeld radiation condition²

$$\left| \frac{\partial p}{\partial r} + ikp \right| = o(r^{-(d-1)/2}),$$

where d is the space dimension. However due to the nature of finite elements we have to truncate the domain somehow. Usually the domain is just reduced by a simple shape as artificial truncation boundary like a circle or rectangle in 2D or a sphere or cuboid in 3D and the boundary is imposed with an absorbing boundary condition, eventually of higher order, or an additional layer that absorbs the wave artificially is added. In Chapter 6 we consider a different approach by imposing a low order boundary condition but in return truncate the domain in a different way to achieve higher accuracy results. Finally we give conclusions and an outlook in Chapter 7 .

The numerical experiments performed in the Chapters 3-6 were computed either on a local machine (Intel i7-7700HQ CPU at 2.80 GHz, 16 GB of RAM) or a high-performance cluster (until 2023: HPC Cluster CARL³, starting 2023: HPC cluster ROSA⁴), due to larger available memory needed for solving the underlying system of equations numerically or the need of parallelization due to large amount of simulations. Since the computational time was not focused on in this thesis the exact machine is not stated in each chapter. If not stated differently, the numerical experiments in Chapters 3-6 are done with an own implementation in `MATLAB`, including the finite element code. Due to the indefiniteness of the Helmholtz equation iterative solvers usually perform poorly [42]. That is why in the numerical experiments we used direct solvers, specifically the backslash operator of `MATLAB`. This generally leads to solving the system of equations with LU-decomposition using the *Unsymmetric MultiFrontal PACKage* with automatic reordering (UMFPACK, [34]).

²For the different time convention the sign changes.

³located at the University of Oldenburg (Germany), funded by the DFG under INST 184/157-1 FUGG

⁴located at the University of Oldenburg (Germany), funded by the DFG under INST 184/225-1 FUGG

Chapter 2

Preliminaries

2.1 Introduction

Before diving into the applications in later chapters we need to consider some fundamentals of functional analysis, such as Sobolev spaces and weak formulations, and the theory of partial differential equations (PDEs) concerning existence and uniqueness. The contents of this chapter are mainly based on established references in the field of elliptic PDEs, Finite Element Method and their applications to wave propagation like the Helmholtz equation [21, 54, 62, 67, 92]. Important definitions and theorems will be stated in order to explain the existence and uniqueness of the solutions of the considered PDEs.

In practical applications, PDEs are often posed on complex domains where smooth solutions may not exist. This can be due to non-smooth boundaries of the domain or varying parameters. Hence, solutions in the classical sense, i.e., that are differentiable, might not exist. To obtain reasonable results nonetheless usually the notion of weak solutions is used. These are solutions that are in general not differentiable in the classical sense, but differentiable in the weak sense. Many numerical methods for solving PDEs, such as the Finite Element Method, are also based on the weak formulation. They lead to approximations of solutions even when classical smoothness is not guaranteed. In the following, if not further defined, we assume that $\Omega \subset \mathbb{R}^d$ is a bounded Lipschitz domain.

Definition 2.1 (Multi-index, [54, p.34]). $\alpha \in \mathbb{N}_0^n, n \in \mathbb{N}$, is called multi-index of length $|\alpha|$, where

$$|\alpha| = \alpha_1 + \dots + \alpha_n.$$

D^α is the α -fold partial differential operator

$$D^\alpha = \frac{\partial^{|\alpha|}}{\partial x_1^{\alpha_1} \partial x_2^{\alpha_2} \dots \partial x_n^{\alpha_n}}.$$

As usual for $u, v \in L^2(\Omega)$ we write the scalar product

$$(u, v)_{L^2(\Omega)} := \int_{\Omega} uv \, dx$$

and hence the norm

$$\|u\|_{L^2(\Omega)} := \sqrt{(u, u)_{L^2(\Omega)}} = \left(\int_{\Omega} |u|^2 \, dx \right)^{\frac{1}{2}}.$$

Definition 2.2 (Weak derivative, [54, Definition 6.20]). Let $u \in L^2(\Omega)$. We say, u has a weak derivative $v := D^\alpha u \in L^2(\Omega)$ if

$$(w, v)_{L^2(\Omega)} = (-1)^{|\alpha|} (D^\alpha w, u)_{L^2(\Omega)} \quad \text{for all } w \in C_0^\infty(\Omega),$$

where

$$C_0^\infty(\Omega) := \{u \in C^\infty(\Omega) : \text{supp } u \subset\subset \Omega\}.$$

The corresponding spaces are the Sobolev spaces.

Definition 2.3 (Sobolev space [54, Chapter 6.2.2]). Let $k \in \mathbb{N}_0$. Let $H^k(\Omega) \subset L^2(\Omega)$ be the set of all functions having weak derivatives $D^\alpha u \in L^2(\Omega)$ for all $|\alpha| \leq k$:

$$H^k(\Omega) = \{u \in L^2(\Omega) : D^\alpha u \in L^2(\Omega) \text{ for } |\alpha| \leq k\}$$

The Sobolev space with functions vanishing on (part of) the boundary is defined as

$$H_\Gamma^k(\Omega) = \left\{ u \in H^k(\Omega) : u \Big|_\Gamma = 0 \right\}$$

for $\Gamma \subset \partial\Omega$.

To formulate the problems (1.2) and (1.3) in terms of the weak formulation, i.e., in Sobolev spaces, we need sesquilinear forms.

Definition 2.4 (Sesquilinear form, antilinear functional, [54]). Let V_1 and V_2 be normed linear spaces. $b : V_1 \times V_2 \rightarrow \mathbb{C}$ is called a sesquilinear form if it is linear in the first and antilinear in the second argument, i.e., for $u, u_1, u_2 \in V_1$, $v, v_1, v_2 \in V_2$ and $\lambda \in \mathbb{C}$

$$\begin{aligned} b(\lambda u_1 + u_2, v) &= \lambda b(u_1, v) + b(u_2, v), \\ b(u, \lambda v_1 + v_2) &= \bar{\lambda} b(u, v_1) + b(u, v_2). \end{aligned}$$

The sesquilinear form b is called continuous (or bounded) if

$$b(u, v) \leq C_{cont} \|u\|_{V_1} \|v\|_{V_2} \quad \text{for all } u \in V_1 \text{ and } v \in V_2.$$

A functional $\ell : V_1 \rightarrow \mathbb{C}$ is called antilinear if

$$\ell(\lambda v_1 + v_2) = \bar{\lambda} \ell(v_1) + \ell(v_2).$$

The antilinear functional ℓ is called continuous (or bounded) if

$$|\ell(v)| \leq C_{\ell, cont} \|v\|_{V_1} \quad \text{for all } v \in V_1.$$

In the weak formulation we generally seek functions $u \in V$ to solve

$$b(u, v) = \ell(v) \quad \forall v \in V, \tag{2.1}$$

where V is $H^1(\Omega)$ or its subspace, e.g., $H_\Gamma^1(\Omega)$.

2.2 Uniqueness and existence of solutions to elliptic second order BVPs

We derive these in detail for the classical formulations (1.2) and (1.3) in Sections 2.2.1 and 2.2.2, respectively. For example, the special case of (1.3)

$$\begin{aligned} -\Delta p - k^2 p &= f & \text{in } \Omega \\ \frac{\partial p}{\partial n} + ikp &= 0 & \text{on } \partial\Omega \end{aligned} \quad (2.2)$$

has the weak formulation: Find $p \in H^1(\Omega)$ such that

$$\int_{\Omega} \nabla p \cdot \nabla \bar{q} \, dx - k^2 \int_{\Omega} p \bar{q} \, dx + ik \int_{\partial\Omega} p \bar{q} \, ds = \int_{\Omega} f \bar{q} \, dx \quad \forall q \in H^1(\Omega). \quad (2.3)$$

Under certain conditions on the space dimension d and the Sobolev index s the Sobolev spaces can be embedded in the continuously differentiable functions. Here, s does not need to be a natural number. For the definition of Sobolev spaces with real-valued index s we refer to [2, 54].

Theorem 2.5 (Sobolev embedding, [54, Theorem 6.48]). $H^s(\mathbb{R}^d) \subset C^k(\mathbb{R}^d)$ holds for $k \in \mathbb{N}_0$, $s > k + \frac{d}{2}$ and $H^s(\mathbb{R}^d) \subset C^t(\mathbb{R}^d)$ for $0 < t \notin \mathbb{N}$, $s \geq t + \frac{d}{2}$.

To deal with boundary terms we need the trace inequality. Here $\gamma : H^1(\Omega) \rightarrow H^{\frac{1}{2}}(\Gamma)$ denotes the trace operator from the domain Ω to its boundary Γ . The trace operator γ is linear and continuous for a Lipschitz domain Ω [54, Theorem 6.58].

Theorem 2.6 (Trace inequality, [22, Theorem 1.6.6]). *Suppose that Ω is a Lipschitz domain. Then there is a constant $C_\gamma > 0$ such that*

$$\|\gamma u\|_{L^2(\partial\Omega)} \leq C_\gamma \|u\|_{L^2(\Omega)}^{\frac{1}{2}} \|u\|_{H^1(\Omega)}^{\frac{1}{2}}.$$

2.2 Uniqueness and existence of solutions to elliptic second order BVPs

This section follows the explanations of standard works like [22, 54], and specifically for indefinite problems through the works of [62, 50, 97], to explain the existence and uniqueness of the solutions to the problems (1.2) and (1.3).

It will be convenient to introduce the notion of a Gelfand triple.

Definition 2.7 (Gelfand triple, [54, (6.36)]). *Let U and V be Hilbert spaces. Then*

$$V \subset U \subset V' \quad (V \subset U \text{ continuously and densely embedded})$$

where $V' := L(V, \mathbb{C})$ is the dual space to V , is called Gelfand triple.

Remark 2.8. In this thesis usually $V = H^1(\Omega)$ (or $V = H_\Gamma^1(\Omega)$) and $U = L^2(\Omega)$. The dual space to $H^1(\Omega)$ is $H^1(\Omega)' \subset H^{-1}(\Omega) = H_{\partial\Omega}^1(\Omega)'$. For the exact definition and

meaning of this space see for example [2]. For the well-posedness one often finds, that the right hand side f needs to be in $H^1(\Omega)'$ (or $H^1_{\Gamma}(\Omega)'$). In the applications in this thesis, f is usually in $L^2(\Omega)$ (admitting a smoother solution) with the exception of Chapter 4, where f is the Dirac-Delta distribution, which is in general, i.e., for $d > 1$, not even in $H^{-1}(\Omega)$: The following only

$$\left| \int_{\Omega} \delta(x)u(x) dx \right| = |u(0)| < \infty$$

holds for continuous $u \in C^0(\Omega)$. However not even all $u \in H^1(\Omega)$ are continuous: For example $u(x) = \log(|\log|x||)$ is not continuous but an element of $H^1(\Omega)$ for $\Omega = B_{0,1}(0) \subset \mathbb{R}^d, d > 1$.

The well-posedness of many variational formulations, e.g., diffusion or linear elasticity problems, is shown by using the V -ellipticity and the famous lemma of Lax-Milgram.

Definition 2.9 (V -ellipticity, [54, Definition 6.96]). *A (real valued) bilinear form a is said to be V -elliptic if it is continuous on $V \times V$ and there is a constant C_E such that*

$$a(x, x) \geq C_E \|x\|_V^2 \quad \forall x \in V \text{ with } C_E > 0.$$

A complex-valued sesquilinear form b is said to be V -elliptic if it is continuous on $V \times V$ and there is a constant C_E such that

$$|b(x, x)| \geq C_E \|x\|_V^2 \quad \forall x \in V \text{ with } C_E > 0.$$

Lemma 2.10 (Lax-Milgram, [22, Theorem 2.7.7]). *If a is V -elliptic and bounded, then the corresponding linear operator A is invertible, i.e., for all linear functionals $\ell : V \rightarrow \mathbb{R}$ there exists a unique solution for the problem*

$$a(u, v) = \ell(v) \quad \forall v \in V.$$

However, the standard variational formulation for the Helmholtz equation, see e.g. (2.3) or later (2.13), is not V -elliptic for all wave numbers k , although one can construct V -elliptic formulations [79]. To show the well-posedness (at least for the standard variational formulation) additional tools are necessary. For these indefinite problems the Gårding inequality takes over the role of V -ellipticity. Note that in some works V -ellipticity is already called V -coercivity. In this thesis coercivity is defined as fulfilling the Gårding inequality as in the following definition.

Definition 2.11 (Coercivity/Gårding inequality, [54, Definition 6.105],[62, (2.4.15)]). *Let $V \subset U \subset V'$ be a Gelfand triple. A sesquilinear form $b : V \times V \rightarrow \mathbb{C}$ is called V -coercive if it is continuous and the following Gårding inequality holds:*

$$|b(x, x) + C_K \|x\|_U^2| \geq C_E \|x\|_V^2 \quad \forall x \in V \text{ with } C_K, C_E > 0. \quad (2.4)$$

Just as the coercivity is a generalization of the ellipticity, the inf-sup condition is the generalization to the lemma of Lax and Milgram. Here we use a formulation based on the ones used in [54] and [62] which is based on [12].

2.2 Uniqueness and existence of solutions to elliptic second order BVPs

Theorem 2.12 (inf-sup condition, [12]). *Let V_1 and V_2 be Hilbert spaces. Assume that a sesquilinear form $b : V_1 \times V_2 \rightarrow \mathbb{C}$ is continuous. Let further $\ell : V_2 \rightarrow \mathbb{C}$ be a bounded antilinear functional. Then there exists a unique solution $u_0 \in V_1$ such that*

$$b(u_0, v) = \ell(v), \quad \forall v \in V_2,$$

if and only if the two following conditions hold

(i) *inf-sup condition:*

$$\exists \beta > 0 : \beta \leq \sup_{0 \neq v \in V_2} \frac{|b(u, v)|}{\|u\|_{V_1} \|v\|_{V_2}}, \quad \forall 0 \neq u \in V_1,$$

(ii) *transposed inf-sup condition:*

$$\sup_{0 \neq u \in V_1} |b(u, v)| > 0, \quad \forall 0 \neq v \in V_2.$$

The solution satisfies

$$\|u_0\|_{V_1} \leq \frac{1}{\beta} \|\ell\|_{V_2'}.$$

Theorem 2.13 (Fredholm's alternative, [62, p. 51]). *Let $V \subset U \subset V'$ be a Gelfand triple with compact embedding $V \subset U$. Let $b : V \times V \rightarrow \mathbb{C}$ be a V -coercive sesquilinear form. Then either*

$$b(u, v) = \ell(v) \quad \forall v \in V$$

has a unique solution $u \in V$ for all antilinear functionals $\ell : V \rightarrow \mathbb{C}$ or

$$b(u, v) = 0 \quad \forall v \in V$$

has a non-trivial solution $u \in V$.

Remark 2.14. Fredholm's alternative essentially states that existence follows from uniqueness.

As stated above, we are usually interested in $V \subseteq H^1(\Omega)$ and $U = L^2(\Omega)$. Hence, to use Fredholm's alternative we need a compact embedding $H^1(\Omega) \subset L^2(\Omega)$. The embedding theorem by Rellich states the compact embedding in the case of a bounded Lipschitz domain Ω . The theorem dates back to 1930 in Rellich's original work [91] or to Kondrachov in 1945 [68] in a more general context. The statement can be found in a more modern setting in various textbooks, e.g., [43, 5, 2, 66].

Theorem 2.15 (Compact Sobolev embedding). *For a Lipschitz domain Ω the embedding $H^1(\Omega) \subset L^2(\Omega)$ is compact.*

To make use of Fredholm's alternative one needs to show the uniqueness of the solution to conclude the existence. For this one often uses the unique continuation principle (see [71, Ch. 4.3]): If the solution to the homogeneous problem satisfies homogeneous Cauchy-data at part of the boundary, it can be extended by zero and one can conclude that the function itself is zero in the whole domain. For the case of Helmholtz problems (with variable coefficients, i.e., the Horn equation is also included) this was shown in [50].

Theorem 2.16 (Unique continuation principle, [50, Theorem 2.1]). *Suppose $a \in L^\infty(\Omega, [a_{\min}, a_{\max}])$ is real-valued with $0 < a_{\min} \leq a_{\max} < \infty$. Let $u \in H^1(\Omega)$ satisfy the homogeneous Helmholtz equation*

$$\int_{\Omega} a \nabla u \cdot \nabla \bar{v} + ku\bar{v} \, dx = 0$$

for all $v \in H^1(\Omega)$. Then: If u vanishes on a ball B of positive radius, with $\bar{B} \subset \Omega$, it follows that u vanishes identically in Ω .

In the following the two main differential equations in this thesis are considered: The horn equation, i.e. one-dimensional Helmholtz equation with variable coefficient and the Helmholtz equation (in two and three dimensions). For each the uniqueness and existence of the solution is shown using the prior theorems and some more specific tools and proofs. First the horn equation is considered. Second the two- and three-dimensional Helmholtz equation, which can be dealt with in a similar fashion.

2.2.1 Time-harmonic horn equation

The first problem we consider here is Webster's horn equation in a time-harmonic setting. For this we first repeat the strong formulation (1.2): Find $p \in C^2([0, L])$ such that

$$-\frac{d}{dx} \left(S(x) \frac{dp}{dx}(x) \right) - k^2 S(x) p(x) = 0 \quad x \in (0, L), \quad (2.5)$$

$$S(0)p'(0) = g, \quad (2.6)$$

$$S(L)p'(L) + i\alpha p(L) = 0, \quad (2.7)$$

where $S \in L^\infty([0, L], [S_{\min}, S_{\max}])$, $0 < S_{\min} < S_{\max} < \infty$ and $\alpha \in \mathbb{C}$. In applications α will often be of the form $\alpha = \frac{\omega \rho}{Z}$ where Z is the acoustic surface impedance, see also Chapter 3. Note, that other boundary conditions, like Dirichlet, are also possible. Essentially, to guarantee existence and uniqueness for all wave numbers k , we need the impedance/Robin boundary condition with $\text{Re}(\alpha) \neq 0$, as we will see in the following. First we derive the weak formulation to this problem. For this multiply Equation (2.5) by the complex conjugate of a test function $q \in H^1([0, L])$ and integrate by parts:

$$\begin{aligned} 0 &= \int_0^L \left[-\frac{d}{dx} (S(x)p'(x)) - k^2 S(x)p(x) \right] \bar{q}(x) \, dx \\ &= \int_0^L \left[-\frac{d}{dx} (S(x)p'(x)) \right] \bar{q}(x) \, dx - \int_0^L k^2 S(x)p(x)\bar{q}(x) \, dx \\ &= \int_0^L S(x)p'(x)\bar{q}'(x) \, dx - [S(x)p'(x)\bar{q}(x)]_0^L - \int_0^L k^2 S(x)p(x)\bar{q}(x) \, dx \end{aligned}$$

2.2 Uniqueness and existence of solutions to elliptic second order BVPs

Inserting the boundary conditions leads to

$$\begin{aligned}
0 &= \int_0^L S(x)p'(x)\bar{q}'(x) dx + i\alpha p(L)\bar{q}(L) + g\bar{q}(0) - \int_0^L k^2 S(x)p(x)\bar{q}(x) dx \\
&\Leftrightarrow \int_0^L S(x)p'(x)\bar{q}'(x) dx + i\alpha p(L)\bar{q}(L) - \int_0^L k^2 S(x)p(x)\bar{q}(x) dx = -g\bar{q}(0) \\
&\Leftrightarrow b(p, q) = \ell(q)
\end{aligned}$$

with sesquilinear form

$$b(p, q) = \int_0^L S(x)p'(x)\bar{q}'(x) dx + i\alpha p(L)\bar{q}(L) - \int_0^L k^2 S(x)p(x)\bar{q}(x) dx$$

and antilinear form

$$\ell(q) = -g\bar{q}(0).$$

The problem in weak formulation reads: Find $p \in H^1([0, L])$ such that

$$b(p, q) = \ell(q) \quad \forall q \in H^1([0, L]). \quad (2.8)$$

To show that problem (2.8) is well-defined, we aim to show that the sesquilinear form b is coercive and show that the solution to the problem is unique. Fredholm's alternative then yields the existence. Finally, using the inf-sup theorem we get continuous dependence on the data g .

We start by showing that the Gårding inequality (2.4) is fulfilled. Let $q \in H^1(\Omega)$, then

$$\begin{aligned}
&|b(q, q) + C_K \|q\|_{L^2([0, L])}^2| \\
&= \left| \int_0^L S(x)|q'|^2 dx + i\alpha|q(L)|^2 - k^2 \int_0^L S(x)|q|^2 dx + C_K \int_0^L |q|^2 dx \right| \\
&\geq \int_0^L S(x)|q'|^2 dx - \operatorname{Im}(\alpha)|q(L)|^2 + (C_K - k^2 \max_{x \in [0, L]} S(x)) \int_0^L |q|^2 dx \\
&\geq \min_{x \in [0, L]} S(x) \int_0^L |q'|^2 dx - \operatorname{Im}(\alpha)|q(L)|^2 + (C_K - k^2 \max_{x \in [0, L]} S(x)) \int_0^L |q|^2 dx,
\end{aligned}$$

where the first inequality comes from just taking the real part and a large enough C_K which will be specified in the following. If $\operatorname{Im}(\alpha) \leq 0$ we can simply choose $C_K = k^2 \max_{x \in [0, L]} S(x) + 1$ and the Gårding inequality (2.4) is fulfilled with $C_E = \min \left(\min_{x \in [0, L]} S(x), 1 \right)$. If $\operatorname{Im}(\alpha) > 0$ we need to be more careful. Let $j(x) = \frac{2}{L}x - 1$ and

notice, that

$$\begin{aligned}
|q(L)|^2 &\leq |q(L)|^2 + |q(0)|^2 \\
&= \int_0^L (q\bar{q}j)' dx = \int_0^L |q|^2 j'(x) dx + \int_0^L (q\bar{q}' + q'\bar{q}) j(x) dx \\
&\leq \int_0^L \frac{2}{L} |q|^2 dx + \int_0^L |q\bar{q}'| dx + \int_0^L |q'\bar{q}| dx \\
&\leq \frac{2}{L} \left(\int_0^L |q|^2 dx \right)^{\frac{1}{2}} \left(\int_0^L |q|^2 dx \right)^{\frac{1}{2}} + 2 \left(\int_0^L |q|^2 dx \right)^{\frac{1}{2}} \left(\int_0^L |q'|^2 dx \right)^{\frac{1}{2}} \\
&\leq 2 \left(\frac{1}{L} + 1 \right) \|q\|_{L^2([0,L])} \|q\|_{H^1([0,L])}.
\end{aligned}$$

Note that, this corresponds to the one-dimensional trace inequality. This can be further estimated as

$$2 \left(\frac{1}{L} + 1 \right) \|q\|_{L^2([0,L])} \|q\|_{H^1([0,L])} \leq 2\varepsilon \left(\frac{1}{L} + 1 \right) \|q\|_{L^2([0,L])}^2 + \frac{1}{2\varepsilon} \left(\frac{1}{L} + 1 \right) \|q\|_{H^1([0,L])}^2,$$

for some $\varepsilon > 0$. In terms of the Gårding inequality this leads to

$$\begin{aligned}
&|b(q, q) + C_K \|q\|_{L^2([0,L])}^2| \\
&\geq \min_{x \in [0,L]} S(x) \int_0^L |q'|^2 dx - \text{Im}(\alpha) |q(L)|^2 + (C_K - k^2 \max_{x \in [0,L]} S(x)) \int_0^L |q|^2 dx \\
&\geq \min_{x \in [0,L]} S(x) \|q\|_{H^1([0,L])}^2 - 2\varepsilon \text{Im}(\alpha) \left(\frac{1}{L} + 1 \right) \|q\|_{L^2([0,L])}^2 \\
&\quad - \frac{1}{2\varepsilon} \text{Im}(\alpha) \left(\frac{1}{L} + 1 \right) \|q\|_{H^1([0,L])}^2 + (C_K - k^2 \max_{x \in [0,L]} S(x)) \|q\|_{L^2([0,L])}^2 \\
&= \left[\min_{x \in [0,L]} S(x) - \frac{\text{Im}(\alpha)}{2\varepsilon} \left(\frac{1}{L} + 1 \right) \right] \|q\|_{H^1([0,L])}^2 \\
&\quad + \left[C_K - k^2 \max_{x \in [0,L]} S(x) - \min_{x \in [0,L]} S(x) - 2\varepsilon \text{Im}(\alpha) \left(\frac{1}{L} + 1 \right) \right] \|q\|_{L^2([0,L])}^2.
\end{aligned}$$

The constants ε and C_K can be chosen such that the term in front of the H^1 -norm is positive and the term in front of the L^2 -norm vanishes: Choose

$$\varepsilon = \frac{\text{Im}(\alpha)}{\min_{x \in [0,L]} S(x)} \left(\frac{1}{L} + 1 \right) \quad \text{and}$$

$$C_K = \min_{x \in [0,L]} S(x) + k^2 \max_{x \in [0,L]} S(x) + 2 \frac{\text{Im}(\alpha)^2}{\min_{x \in [0,L]} S(x)} \left(\frac{1}{L} + 1 \right)^2,$$

2.2 Uniqueness and existence of solutions to elliptic second order BVPs

then we get

$$\min_{x \in [0, L]} S(x) - \frac{\operatorname{Im}(\alpha)}{2\varepsilon} \left(\frac{1}{L} + 1 \right) = \frac{1}{2} \min_{x \in [0, L]} S(x), \quad \text{and}$$

$$C_K - k^2 \max_{x \in [0, L]} S(x) - \min_{x \in [0, L]} S(x) - 2\varepsilon \operatorname{Im}(\alpha) \left(\frac{1}{L} + 1 \right) = 0.$$

Hence, the Gårding inequality holds with $C_E = \frac{1}{2} \min_{x \in [0, L]} S(x)$. Fredholm's alternative, i.e., Theorem 2.13, states that existence of the solution follows from uniqueness. Hence, the next step in showing the well-posedness of problem (2.8) is to show the uniqueness of the solution. Assume p_1 and p_2 both solve (2.8). Let $w := p_1 - p_2$. Then

$$b(w, q) = 0 \quad \forall q \in H^1([0, L]).$$

To show uniqueness, we need to prove $w = 0$. The idea is to use the unique continuation principle for this matter. Considering only the imaginary part and setting $q = w$ leads to

$$0 = \operatorname{Im}(b(w, w)) = \operatorname{Re}(\alpha) |w(L)|^2.$$

Now, since $\operatorname{Re}(\alpha) > 0$, we must have $w(L) = 0$ and due to the impedance boundary condition also $w'(L) = 0$. We can extend w to the interval $[0, L + \delta]$ by zero, i.e.,

$$w^*(x) = \begin{cases} w(x), & x \in [0, L] \\ 0, & x \in [L, L + \delta]. \end{cases}$$

Extending S as S^* such that $S^* \geq S_{\min}^* > 0$ on $[0, L + \delta]$, w^* is the solution to

$$\int_0^{L+\delta} S^*(x) w^{*'}(x) \bar{q}'(x) dx - \int_0^{L+\delta} k^2 S^*(x) w^*(x) \bar{q}(x) = 0 \quad \forall q \in H^1([0, L + \delta]).$$

Since $w^* = 0$ on $[L, L + \delta]$, $w^* = 0$ on the all $[0, L + \delta]$ due to the unique continuation principle. Hence, p is unique and as a consequence from Fredholm's alternative also exists. Theorem 2.12 now concludes that the solution p satisfies

$$\|p\|_{H^1([0, L])} \leq c|g|.$$

Note that here g is a constant. Even if it was a function, the boundary part the function g lives on is only one single point.

2.2.2 Helmholtz equation in 2D/3D

Showing the well-posedness of the Helmholtz equation in two and three dimensions is rather similar to the case of the horn equation in one dimension. First revisit the strong

formulation of equation (1.3) from the introduction. Let $\Omega \subset \mathbb{R}^d$, $d = 2, 3$, a Lipschitz domain and $\partial\Omega = \overline{\Gamma_D} \cup \overline{\Gamma_N} \cup \overline{\Gamma_R}$. Find $p \in C^2(\Omega)$ such that

$$-\Delta p - k^2 p = f \quad x \in \Omega \quad (2.9)$$

$$p = p_D \quad \text{on } \Gamma_D \quad (2.10)$$

$$\frac{\partial p}{\partial n} = g \quad \text{on } \Gamma_N \quad (2.11)$$

$$\frac{\partial p}{\partial n} + i\alpha p = 0 \quad \text{on } \Gamma_R, \quad (2.12)$$

where $\alpha \in L^\infty(\Gamma_R)$ piecewise constant, $\text{Re}(\alpha) \neq 0$ and Γ_R has positive Lebesgue measure. For simplicity, we assume that either $\text{Im}(\alpha) \leq 0$ or $\text{Im}(\alpha) > 0$ on Γ_R . This way we do not need to consider the case of $\text{Im}(\alpha)$ switching the sign, which lets us avoid splitting the boundary part Γ_R further in that follows and reduce the discussion to two cases only. However, this simplification is not needed as can easily be checked. In fact, in Chapter 4 we consider a problem where we have negative $\text{Im}(\alpha)$ on one part of the boundary and positive $\text{Im}(\alpha)$ on another part. We assume $p_D = 0$. However, later we show that we can assume $p_D \in H^{\frac{1}{2}}(\Gamma_D)$ as long as Ω is Lipschitz [54, Ch. 7.3]. To get the weak formulation we again multiply the equation with the complex conjugate of a test function $q \in H_{\Gamma_D}^1(\Omega) := \{v \in H^1(\Omega) : v|_{\Gamma_D} = 0\}$ and integrate over the domain:

$$\begin{aligned} 0 &= \int_{\Omega} [-\Delta p - k^2 p] \bar{q} - f \bar{q} \, dx \\ &= \int_{\Omega} \nabla p \cdot \nabla \bar{q} \, dx - \int_{\Gamma_N} \frac{\partial p}{\partial n} \bar{q} \, ds - \int_{\Gamma_R} \frac{\partial p}{\partial n} \bar{q} \, ds - \int_{\Omega} k^2 p \bar{q} \, dx - \int_{\Omega} f \bar{q} \, dx \\ &= \int_{\Omega} \nabla p \cdot \nabla \bar{q} \, dx - \int_{\Gamma_N} g \bar{q} \, ds + \int_{\Gamma_R} i\alpha p \bar{q} \, ds - \int_{\Omega} k^2 p \bar{q} \, dx - \int_{\Omega} f \bar{q} \, dx, \end{aligned}$$

leading to $b(p, q) = \ell(q)$ with

$$\begin{aligned} b(p, q) &= \int_{\Omega} \nabla p \cdot \nabla \bar{q} \, dx + \int_{\Gamma_R} i\alpha p \bar{q} \, ds - \int_{\Omega} k^2 p \bar{q} \, dx \quad \text{and} \\ \ell(q) &= \int_{\Omega} f \bar{q} \, dx + \int_{\Gamma_N} g \bar{q} \, ds. \end{aligned}$$

The weak formulation reads: Find $p \in H_{\Gamma_D}^1(\Omega)$ such that for all $q \in H_{\Gamma_D}^1(\Omega)$:

$$b(p, q) = \ell(q). \quad (2.13)$$

The first step to the well-posedness is again to show that b is coercive, i.e., the Gårding inequality holds:

$$\begin{aligned} |b(q, q) + C_K \|q\|_{L^2(\Omega)}| &= \left| \int_{\Omega} |\nabla q|^2 \, dx + \int_{\Gamma_R} i\alpha |q|^2 \, ds - k^2 \int_{\Omega} |q|^2 \, dx + C_K \int_{\Omega} |q|^2 \, dx \right| \\ &\geq |q|_{H^1(\Omega)}^2 - \int_{\Gamma_R} \text{Im}(\alpha) |q|^2 \, ds + (C_K - k^2) \|q\|_{L^2(\Omega)}^2 \end{aligned}$$

2.2 Uniqueness and existence of solutions to elliptic second order BVPs

Now if $\text{Im}(\alpha) \leq 0$ on Γ_R one can simply leave out the term and have coercivity with $C_K = k^2 + 1$. Otherwise we use the trace inequality (Theorem 2.6)

$$\begin{aligned} \int_{\Gamma_R} \text{Im}(\alpha)|q|^2 ds &\leq \sup_{x \in \Gamma_R} \text{Im}(\alpha(x)) \|q\|_{L^2(\Gamma_R)}^2 \\ &\leq \sup_{x \in \Gamma_R} \text{Im}(\alpha(x)) \|q\|_{L^2(\partial\Omega)}^2 \\ &\leq C_\gamma \sup_{x \in \Gamma_R} \text{Im}(\alpha(x)) \|q\|_{L^2(\Omega)} \|q\|_{H^1(\Omega)} \end{aligned}$$

Now the product of the norms can be split into two parts for some $\varepsilon > 0$:

$$\sup_{x \in \Gamma_R} \text{Im}(\alpha(x)) \|q\|_{L^2(\Omega)} \|q\|_{H^1(\Omega)} \leq \sup_{x \in \Gamma_R} \text{Im}(\alpha(x)) \left(2\varepsilon \|q\|_{L^2(\Omega)}^2 + \frac{1}{2\varepsilon} \|q\|_{H^1(\Omega)}^2 \right).$$

Inserting this above leads to

$$\begin{aligned} &|q|_{H^1(\Omega)}^2 - \int_{\Gamma_R} \text{Im}(\alpha)|q|^2 ds + (C_K - k^2) \|q\|_{L^2(\Omega)}^2 \\ &\geq |q|_{H^1(\Omega)}^2 - \sup_{x \in \Gamma_R} \text{Im}(\alpha(x)) \left(2\varepsilon \|q\|_{L^2(\Omega)}^2 + \frac{1}{2\varepsilon} \|q\|_{H^1(\Omega)}^2 \right) + (C_K - k^2) \|q\|_{L^2(\Omega)}^2 \\ &= \left[1 - \frac{\sup_{x \in \Gamma_R} \text{Im}(\alpha(x))}{2\varepsilon} \right] \|q\|_{H^1(\Omega)}^2 + \left[C_K - k^2 - 1 - 2\varepsilon \sup_{x \in \Gamma_R} \text{Im}(\alpha(x)) \right] \|q\|_{L^2(\Omega)}^2 \\ &\geq C_E \|q\|_{H^1(\Omega)}^2 \end{aligned}$$

for $C_E = \frac{1}{2}$, $\varepsilon = \sup_{x \in \Gamma_R} \text{Im}(\alpha(x))$ and $C_K = k^2 + 1 + 2\varepsilon \sup_{x \in \Gamma_R} \text{Im}(\alpha(x))$. Hence, the sesquilinear form is coercive. To show well-posedness of problem (2.13) it is now enough to show uniqueness, since the existence follows from Theorem 2.13. Let p_1 and p_2 be solutions of (2.13) and let $w = p_1 - p_2$. Then w solves

$$b(w, q) = 0 \Leftrightarrow \int_{\Omega} \nabla w \cdot \nabla \bar{q} dx + \int_{\Gamma_R} i\alpha w \bar{q} ds - k^2 \int_{\Omega} w \bar{q} dx = 0.$$

Considering only the imaginary part and $v = w$ gives

$$\text{Im}(b(w, w)) = \int_{\Gamma_R} \text{Re}(\alpha)|w|^2 ds = 0.$$

Since $\text{Re}(\alpha) \neq 0$ on Γ_R and also on a subset $\tilde{\Gamma} \subset \Gamma_R$ with positive measure, we have $w = 0$ on $\tilde{\Gamma}$ and due to the Robin boundary condition also $\frac{\partial w}{\partial n} = 0$ on $\tilde{\Gamma}$. Now let w^* be the extension of w on Ω^* where $\Omega \subset \Omega^*$ and $\tilde{\Gamma} \subset \Omega^*$, see Figure 2.1, by extending $w = 0$ on $\Omega^* \setminus \Omega$. Then w^* solves

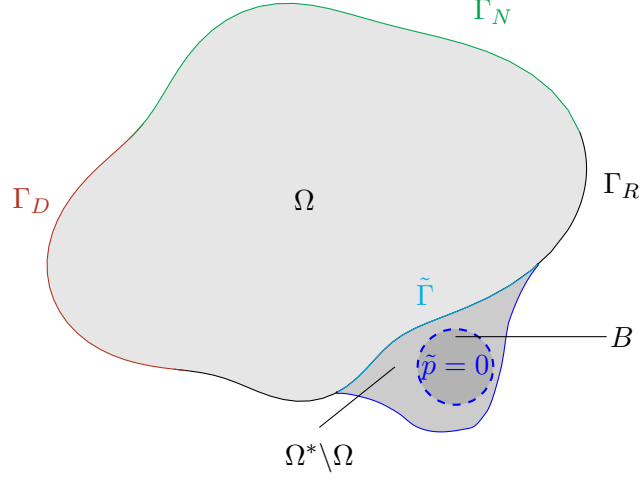


Figure 2.1: Unique continuation principle illustrated for the Helmholtz problem in a two-dimensional domain, based on figure 1 in [50].

$$\int_{\Omega^*} \nabla w^* \cdot \nabla \bar{q} \, dx - k^2 \int_{\Omega^*} w^* \bar{q} \, dx = 0$$

for all $q \in H_{\Gamma_D}^1(\Omega^*)$. Since $w^* = 0$ on a ball $B \subset \Omega^*$, due to the unique continuation principle, $w^* = 0$ in Ω^* and, hence, $w = 0$. Thus, $p_1 = p_2$. Therefore, the solution to (2.13) is unique. From Fredholm's alternative it follows that p also exists. Theorem 2.12 then states the stability with respect to the data, i.e.,

$$\|p\|_{H^1(\Omega)} \leq c \left(\|f\|_{H^{-1}(\Omega)} + \|g\|_{H^{-\frac{1}{2}}(\Gamma_N)} \right). \quad (2.14)$$

If $0 \neq p_D \in H^{\frac{1}{2}}(\Gamma_D)$, then there exists an extension $\tilde{p}_D \in H^1(\Omega)$ such that $\tilde{p}_D|_{\Gamma_D} = p_D$ [54, Remark 7.20]. Let $w \in H_{\Gamma_D}^1$ be the solution to

$$b(w, q) = \ell(q) - b(\tilde{p}_D, q) \quad \forall q \in H_{\Gamma_D}^1(\Omega).$$

Then $p = \tilde{p}_D + w$ solves

$$b(p, q) = \ell(q) \quad \forall q \in H_{\Gamma_D}^1(\Omega)$$

with $p|_{\Gamma_D} = p_D$. Thus, the analysis above also applies for the non-homogeneous Dirichlet conditions. The stability estimate (2.14) becomes (with possibly a different constant c)

$$\|p\|_{H^1(\Omega)} \leq c \left(\|f\|_{H^{-1}(\Omega)} + \|g\|_{H^{-\frac{1}{2}}(\Gamma_N)} + \|p_D\|_{H^{\frac{1}{2}}(\Gamma_D)} \right).$$

In case of convex Ω or smooth boundary the solution p is in $H^2(\Omega)$ if $f \in L^2(\Omega)$, $g \in H^{1/2}(\Gamma_N)$ and $p_D \in H^{3/2}(\Gamma_D)$, and also a change in boundary condition (from

Neumann/Robin to Dirichlet) is only happening at a boundary angle smaller or equal than 90 degrees. In this case the following regularity estimate holds [52, 32, 51]

$$\|p\|_{H^2(\Omega)} \leq C_{reg} \left(\|f\|_{L^2(\Omega)} + \|g\|_{H^{1/2}(\Gamma_N)} + \|p_D\|_{H^{3/2}(\Gamma_D)} \right). \quad (2.15)$$

2.3 Discretization using finite elements

In this section we discuss the discretization in terms of finite dimensional spaces and discuss the associated convergence theory. In the numerical experiments in this thesis we use linear and quadratic finite elements.

2.3.1 Finite element space

For the one-dimensional case we divide the interval $\Omega = [a, b]$ into uniform subintervals $T_i = [x_i, x_{i+1}]$, $i = 0, \dots, N - 1$, of length $h = \frac{1}{N}$. We define the finite element space $V_h \subset V$ as globally continuous on $[a, b]$ and piecewise linear (or quadratic) in each T_i . The basis consists of piecewise linear (or quadratic) functions with $\varphi_i(x_j) = \delta_{ij}$.

In the case of $\Omega \subset \mathbb{R}^d$, $d = 2, 3$, we discretize the problem using a quasi-uniform family of triangulations $\{\mathcal{T}_h\}_{h>0}$ of Ω . Each element $T \in \mathcal{T}_h$ is a triangle or tetrahedron with diameter h_T , and the diameter of the largest ball contained in T is denoted by ρ_T . The maximum diameter of all elements in \mathcal{T}_h is the mesh size, $h := \max_{T \in \mathcal{T}_h} h_T$. We assume the triangulations $\{\mathcal{T}_h\}_{h>0}$ to be shape regular, i.e., we assume there exist constants $c_1, c_2 > 0$, such that for all $T \in \mathcal{T}_h$ and for all $h > 0$

$$\frac{h_T}{\rho_T} \leq c_1, \quad \frac{h}{h_T} \leq c_2.$$

We then define the finite element space V_h on the triangulation \mathcal{T}_h . The functions in V_h are globally continuous on Ω and piecewise linear (or quadratic) in each $T \in \mathcal{T}_h$, such as in the one-dimensional case. The basis of V_h is made of piecewise linear (or quadratic) functions φ_i with $\varphi_i(x_j) = \delta_{ij}$. For the quadratic elements one typically defines additional nodes x_i in the center of the interval (1D) or the center of the edges of the triangle (2D) or tetrahedron (3D), see for example [26] for details on the definition on standard finite elements. The discrete weak formulation of (2.1) is: Find $u_h \in V_h$ such that for all $v_h \in V_h$

$$b(u_h, v_h) = \ell(v_h), \quad (2.16)$$

where b and ℓ are the same as in the infinite dimensional case.

2.3.2 Approximation in V_h

In the discrete setting for indefinite problem we need to state the inf-sup condition for the discrete spaces, since in contrast to the lemma of Lax-Milgram, it does not need to hold for subspaces of V . The subspaces W_1 and W_2 can be thought of the finite element spaces defined previously.

Definition 2.17 (Discrete inf-sup condition, [62]). *Let V_1 and V_2 be Hilbert spaces and $W_1 \subset V_1$, $W_2 \subset V_2$ proper subspaces. Let $b : V_1 \times V_2 \rightarrow \mathbb{C}$ be a continuous sesquilinear form. If b satisfies*

$$\exists \beta_h > 0 : \quad \beta_h \leq \sup_{0 \neq v \in W_2} \frac{|b(u, v)|}{\|u\| \|v\|}, \quad \forall 0 \neq u \in W_1 \quad (2.17)$$

and also the transposed condition

$$\sup_{0 \neq u \in W_1} |b(u, v)| > 0, \quad \forall 0 \neq v \in W_2. \quad (2.18)$$

Then there exists a unique element $u_h \in W_1$ such that

$$b(u_h, v) = f(v), \quad \forall v \in W_2.$$

The Ritz-Galerkin solution of the discrete problem (2.1) is quasi-optimal, i.e., out of all functions of V_h its error from the continuous solution is the minimum up to a multiplicative constant. This result dates back to C ea [30] in 1964 for the symmetric and V -elliptic case, e.g. for the Laplace or linear elasticity problem, the general case was analyzed first by Birkhoff, Schulz and Varga [18] in 1968.

Theorem 2.18 ([54, Theorem 8.21]). *Let $V_h \subset V$ be a finite-dimensional subspace of V . Let $b : V \times V \rightarrow \mathbb{C}$ be a continuous sesquilinear form and suppose the discrete inf-sup condition (2.17) is fulfilled with β_h and also the transposed discrete inf-sup condition (2.18) holds. Let $u_h \in V_h$ be the Ritz-Galerkin solution of (2.16). Then*

$$\|u - u_h\| \leq \left(1 + \frac{C_{cont}}{\beta_h}\right) \inf_{v_h \in V_h} \|u - v_h\|_V.$$

If b is symmetric and V -elliptic, the estimate can be improved to

$$\|u - u_h\| \leq \sqrt{\frac{C_{cont}}{\beta_h}} \inf_{v_h \in V_h} \|u - v_h\|_V.$$

A variant of the following theorem can be found in [22], where $\ell(v) = (f, v)_{L^2(\Omega)}$.

Theorem 2.19. *Let $b : H^1(\Omega) \times H^1(\Omega) \rightarrow \mathbb{C}$ be a continuous sesquilinear form. Let b fulfill the G arding inequality (2.4). Assume the problem*

$$b(u, v) = \ell(v) \quad \forall v \in H_{\Gamma_D}^1(\Omega)$$

and its adjoint

$$b(v, u) = (u - u_h, v) =: \ell_{adjoint}(v) \quad \forall v \in H_{\Gamma_D}^1(\Omega),$$

where u_h is defined below, to be H^2 -regular, i.e., it holds especially (2.15) (or similarly depending on the boundary conditions) with corresponding smoothness on the data. Assume further that for some $C_{int} > 0$

$$\inf_{v_h \in V_h} \|v - v_h\|_{H^1(\Omega)} \leq C_{int} h |v|_{H^2(\Omega)} \quad \text{for all } v \in H_{\Gamma_D}^1(\Omega). \quad (2.19)$$

2.3 Discretization using finite elements

Then there exists a unique $u_h \in V_h$ such that for $h > 0$ sufficiently small

$$b(u_h, v_h) = \ell(v_h) \quad \forall v_h \in V_h$$

and

$$\|u - u_h\|_{H^1(\Omega)} \leq C \inf_{v_h \in V_h} \|u - v_h\|_{H^1(\Omega)} \leq C_A h |u|_{H^2(\Omega)}.$$

Proof. Assume that problem (2.1) has a solution $u_h \in V_h$. Then for all $v_h \in V_h$

$$b(u_h, v_h) = b(u, v_h) = \ell(v_h)$$

and hence $b(u - u_h, v_h) = 0$ (this property is also called *Galerkin orthogonality*). Using Gårding's inequality we get

$$\alpha \|u - u_h\|_{H^1(\Omega)}^2 \leq |b(u - u_h, u - u_h) + K \|u - u_h\|_{L^2(\Omega)}^2|.$$

To bound the L^2 -norm of the error $u - u_h$ one uses a standard duality argument also known as Nitsche's trick. Let $w \in H^1(\Omega)$ be the solution to the adjoint problem

$$b(v, w) = (u - u_h, v) = \ell_{\text{adjoint}}(v) \quad \forall v \in H_{\Gamma_D}^1(\Omega).$$

Then

$$\|u - u_h\|_{L^2(\Omega)}^2 = (u - u_h, u - u_h)_{L^2(\Omega)} = \ell_{\text{adjoint}}(u - u_h) = b(u - u_h, w).$$

Choose $w_h \in V_h$ such that

$$\|w - w_h\|_{H^1(\Omega)} \leq C_{\text{int}} h |w|_{H^2(\Omega)}.$$

This is possible due to assumption in (2.19). Since $b(u - u_h, v_h) = 0$ for all $v_h \in V_h$ we have

$$\begin{aligned} b(u - u_h, w) &= b(u - u_h, w - w_h) \leq C_{\text{cont}} \|u - u_h\|_{H^1(\Omega)} \|w - w_h\|_{H^1(\Omega)} \\ &\leq C_{\text{cont}} C_{\text{int}} h \|u - u_h\|_{H^1(\Omega)} |w|_{H^2(\Omega)} \\ &\leq C_{\text{cont}} C_{\text{int}} C_{\text{reg}} h \|u - u_h\|_{H^1(\Omega)} \|u - u_h\|_{L^2(\Omega)}. \end{aligned}$$

Hence

$$\|u - u_h\|_{L^2(\Omega)} \leq C_{\text{cont}} C_{\text{int}} C_{\text{reg}} h \|u - u_h\|_{H^1(\Omega)}.$$

Inserting this in the equation above, and using again Galerkin orthogonality for the first term, leads to

$$\begin{aligned} \alpha \|u - u_h\|_{H^1(\Omega)}^2 &\leq C_{\text{cont}} \|u - u_h\|_{H^1(\Omega)} \|u - v_h\|_{H^1(\Omega)} \\ &\quad + h^2 K C_{\text{cont}}^2 C_{\text{int}}^2 C_{\text{reg}}^2 \|u - u_h\|_{H^1(\Omega)}^2 \\ \Rightarrow (\alpha - h^2 K C_{\text{cont}}^2 C_{\text{int}}^2 C_{\text{reg}}^2) \|u - u_h\|_{H^1(\Omega)} &\leq C_{\text{cont}} \|u - v_h\|_{H^1(\Omega)} \end{aligned}$$

for all $v_h \in V_h$. For $h < h_0 := \frac{\alpha^{\frac{1}{2}}}{(2K)^{\frac{1}{2}} C_{cont} C_{int} C_{reg}}$ this leads to

$$\alpha \|u - u_h\|_{H^1(\Omega)} \leq 2C_{cont} \|u - v_h\|_{H^1(\Omega)} \quad \forall v_h \in V_h.$$

Using the assumption in (2.19), this can be further expressed as

$$\alpha \|u - u_h\|_{H^1(\Omega)} \leq 2C_{cont} \inf_{v_h \in V_h} \|u - v_h\|_{H^1(\Omega)} \leq 2C_{cont} C_{int} h |u|_{H^2(\Omega)}, \quad (2.20)$$

hence u_h converges to u for $h > h_0$. The existence and uniqueness of u_h , which is equivalent in the finite-dimensional space V_h , is seen as follows: If the solution were not unique, then there would be a nontrivial solution $u_h \in V_h$ with $a(u_h, v_h) = 0$ for all $v_h \in V_h$. However, for the homogeneous problem one has $u = 0$, due to the stability estimate (2.14) of the continuous case (and also because we know that for the continuous case the solution exists and is unique if it fulfills the Gårding inequality in V). Hence, Equation (2.20) becomes

$$\alpha \|u_h\|_{H^1(\Omega)} \leq 2C_{cont} \inf_{v_h \in V_h} \|v_h\|_{H^1(\Omega)} = 0$$

and therefore also $u_h = 0$. □

Remark 2.20. The assumption in (2.19) typically needs an interpolation operator $\mathcal{I} : H_{\Gamma_D}^1(\Omega) \rightarrow V_h$. For $v \in H^2(\Omega)$ one can use the Lagrange-Interpolation operator to show this inequality. However, in the case of $v \notin H^2(\Omega)$, v is not necessarily continuous. Hence, we might not be able to evaluate it in the interpolation points. The interpolation operator of Scott and Zhang [100] solves this issue as it does not need point evaluations. With this operator we get

$$\inf_{v_h \in V_h} \|v - v_h\|_{H^s(\Omega)} \leq C_{int} h^s |v|_{H^{1+s}(\Omega)} \quad \text{for all } v \in H_{\Gamma_D}^s$$

for $s > 1$. Hence we can prove convergence analogously even for $u \in H^s(\Omega)$, $1 < s < 2$, although the convergence rate suffers.

The proof also shows that for V -elliptic sesquilinear (or bilinear) forms the condition $h < h_0$ is not needed, since $K = 0$ in that case. Existence and uniqueness of the discrete solution in the V -elliptic case follows from the Lax-Milgram Lemma directly anyway, since it still holds if it was fulfilled for the continuous case. This is in contrast to the inf-sup condition where the discrete version does not follow directly from the continuous case. However, the discrete inf-sup condition is fulfilled if the sesquilinear form is also coercive for sufficiently small h .

In acoustic engineering applications one usually suggests choosing h dependent on the wave number. Common rules of thumb are ten elements per wavelength in the case of linear finite elements or six elements per wavelength in the case of quadratic finite elements. However, works on k -explicit stability estimates and convergence theory have shown that this does not hold for large k , see for example [74, 11, 57, 25, 76, 50]. In the numerical experiments in this thesis we usually followed the rule of thumb of ten elements per wavelength. This seemed to be sufficient in these cases.

In the case of higher regularity of the solution u faster convergence can be achieved by using higher order polynomials as ansatz functions, see, e.g., [22] for details.

Chapter 3

Using a one-dimensional finite-element approximation of Webster's horn equation to estimate individual ear canal acoustic transfer from input impedances

The contents of this chapter have been published in [112]. Mainly minor parts are changed in this chapter with respect to the publication to give more context to the other contents of the thesis. The author of this thesis is the first author of this publication and has made major contributions to the development of the method, the writing and the numerical experiments (with the exception of the data preparation in Section 3.3).

3.1 Introduction

Humans have individually shaped ear canals which will individually influence the sound transfer from the ear canal entrance to the eardrum. In many applications such as hearing aids or insert earphones, one is interested in the sound pressure at the eardrum, however, it is often not practical to measure it directly. Therefore, it is desirable to be able to individually predict the eardrum sound pressure from measurements at the entrance to the ear canal. One possibility is to measure the acoustic impedance, i.e., the ratio of sound pressure and volume velocity, at the entrance of the ear canal. The goal is then to estimate the transfer impedance, i.e., the ratio of the eardrum sound pressure to the volume velocity at the entrance, because one can then use input and transfer impedances together with a source model to individually predict the eardrum pressure, see e.g. [19].

A useful one-dimensional equation to study this behavior is Webster's horn equation [109], describing the sound pressure in a horn, i.e., a tube with varying diameter. In order to solve Webster's equation for the sound pressure at different positions along the ear canal, an area function which describes the area along the ear canal is needed. If three-dimensional ear canal geometries are given, a curved center axis and an associated area function can be computed, using, for instance, the method proposed in [105]. In most cases, such data is, however, not available. Alternatively, area functions can be estimated from acoustic impedances or reflectances measured at the entrance of the individual ear canal.

In a number of publications, the phase of the reflectance was used to estimate the transfer impedance and area function [61, 19, 89, 96, 95, 103]. As an example, in [61] the optimization was done by an electro-acoustic model and a gradient method to approximate the radius function for a measured (or simulated) input reflectance. Given reference pressure values at the eardrum, the pressure was transformed back to the entrance for individual ear canals. A chain matrix, optimized using reflectance data then lead to accurate results for the radius function and the pressure at the drum for frequencies up to 16 kHz.

Another approach using a reflectance-based method was considered in [89] where the aim was to reproduce the ear canal cross-sectional area. Specifically, a time-domain reflectance was calculated and the inverse solution to the time-domain horn equation was formulated in terms of forward and backward traveling pressure waves to obtain the area function by using a finite difference approximation. The solution to the inverse problem was analyzed for infinite acoustic horns in [90]. In [89] the area function of the inverse solution was applied to measurements made in an ear simulator. The estimated ear canal area function was close to the one of the simulator. Furthermore, the authors estimated the ear canal area function from reflectance measurements on real subjects, assuming the eardrum to be rigid, although the true ear canal area functions were not known. The resulting ear canal area functions looked plausible and similar to other ear canal area functions from the literature. The transfer impedance, however, was not investigated.

In this chapter, we present a different approach based on data of the input impedance in the frequency domain. Working in the frequency domain appears to be more convenient with respect to actual measurement data (i.e., acoustic impedances or reflectances) whose validity will in general be limited to a certain frequency range. Our aim is to estimate the transfer impedance of the individual residual ear canal. To this end, we parameterize the ear canal area function and the acoustic impedance of the eardrum. We solve the horn equation in the frequency domain with linear finite elements and optimize the parameters using the Nelder-Mead method [83] with respect to given data of the input impedance. By doing so, we also obtain estimations of the ear canal area function and the acoustic impedance at the eardrum.

The general idea of the method is described in Section 3.2. The generation of data as input and for validation purposes is explained in Section 3.3. In Section 3.4 the procedure from Section 3.2 will be extended by several adjustments to avoid unrealistic results during the parameter fitting. The final version of our method is validated in Section 3.5 on a variety of ear canal geometries with different eardrum impedance models. Finally, in Section 3.6 conclusions are given.

A MATLAB implementation of the complete method can be found in the supplementary material [110].¹

¹See supplementary material at <https://github.com/nickwulbusch/ear-canal-parameter-fitting-1d> for full MATLAB-Code of the final method.

3.2 Modeling approach and parameter estimation

The main goal of our method is to estimate the transfer impedance Z_{tr} , based on data of the input impedance $Z_{\text{in,data}}$, for individual ear canals. To do this, we use Webster's horn equation, see Section 2.2.1, in the frequency domain as surrogate model of a simplified representation of the pressure distribution in the ear canal,

$$\frac{d}{dx} \left[S(x) \frac{d}{dx} p(x) \right] + k^2 S(x) p(x) = 0 \text{ in } [0, \ell], \quad (3.1a)$$

$$S(0) \frac{dp}{dx}(0) = qi\omega\rho, \quad (3.1b)$$

$$S(\ell) \frac{dp}{dx}(\ell) + \frac{i\omega\rho}{Z_d} p(\ell) = 0. \quad (3.1c)$$

The solution $p(x)$ to this problem denotes the acoustic pressure, $S(x)$ is the area function, $k = \frac{2\pi f}{\lambda}$ the wave number with frequency f and wavelength λ , q the volume velocity, $\omega = 2\pi f$ the angular frequency, ρ the density of air inside the ear canal and Z_d the acoustic impedance of the eardrum. In this setting, the aim is to estimate the transfer impedance $Z_{\text{tr}} = \frac{p(\ell)}{q}$ from given data of the input impedance $Z_{\text{in,data}}$ which in turn is modeled by $Z_{\text{in}} = \frac{p(0)}{q}$ in the one-dimensional surrogate (3.1a)-(3.1c). The area function $S(x)$ and acoustic impedance Z_d at the eardrum are unknown. In the following, these quantities are parameterized and fitted to the given data of the input impedance. This is done through PDE-constraint optimization by minimizing the cost function

$$J_0(Z_{\text{in}}) = \sum_{f \in \mathcal{F}} A \left(\log_{10} \left| \frac{Z_{\text{in}}(f)}{Z_{\text{in,data}}(f)} \right| \right)^2 + B \arg \left(\frac{Z_{\text{in}}(f)}{Z_{\text{in,data}}(f)} \right)^2, \quad (3.2)$$

with weighting parameters A and B . These are chosen as $A = 10$ and $B = 1$. The cost function is thus the weighted sum of the squared differences between model and data of the logarithmic amplitude and the phase in radians. $Z_{\text{in,data}}(f)$ denotes the given data, i.e., the input impedance from the measurement at the entrance of the ear canal for a specific frequency f , whereas $Z_{\text{in}}(f)$ denotes the input impedance from the solution of problem (3.1a)-(3.1c) at the entrance. \mathcal{F} denotes a set of frequencies. Different choices of \mathcal{F} will be discussed in Section 3.4.3. Unknown parameters are involved in the area function $S(x)$, the model for the acoustic impedance at the eardrum Z_d and the length of the ear canal ℓ . The area function is modeled as

$$S(x) := S(x, S_0, \mathbf{c}, \mathbf{s}, \ell) = S_0 + \sum_{m=1}^M c_m \cos\left(\frac{m\pi x}{\ell}\right) + s_m \sin\left(\frac{m\pi x}{\ell}\right). \quad (3.3)$$

The acoustic impedance at the eardrum Z_{ED} is modeled using a two-resonator model, similar to the model described in [106],

$$Z_{\text{ED}} = \left(\frac{1}{10^{L_{0,1}/20 \text{ dB}} (iv_1 Q_1 + 1)} + \frac{1}{10^{L_{0,2}/20 \text{ dB}} (iv_2 Q_2 + 1)} \right)^{-1} \text{ Pa}\cdot\text{s}/\text{m}^3, \quad (3.4)$$

where

$$v_i = \frac{\omega}{2\pi f_{0,i}} - \frac{2\pi f_{0,i}}{\omega}, \quad i = 1, 2, \quad (3.5)$$

and the parameters Q_i , $f_{0,i}$ and $L_{0,i}$ are the quality factor, the resonance frequency and the impedance level at resonance (in dB re 1 Pa·s/m³), respectively. This model is a good compromise between the number of parameters and approximation as compared to more sophisticated models like the model in [60]. It is notably capable of modeling the cadaver measurements in [94] with acceptable accuracy.

Following the suggestion in [59], the innermost part of the ear canal is modeled as a lumped compliance (of a right circular cone of 4 mm length and 2.5 mm radius) acting in parallel with the eardrum impedance,

$$Z_d = \frac{Z_{ED} Z_{vol}}{Z_{ED} + Z_{vol}}, \quad (3.6)$$

where

$$Z_{vol} = \frac{\rho c^2}{i\omega V}, \quad (3.7)$$

Z_{ED} corresponds to the acoustic impedance at the eardrum, c is the speed of sound and V is the volume of the cone. This effectively removes the innermost part from the ear canal geometry.

The parameters used in the definitions of the area function, i.e., $S(x)$ in (3.3) and the acoustic impedance of the eardrum Z_d in (3.6), were fitted using the Nelder-Mead constrained optimization procedure [83, 36]. To this end, equations (3.1a)-(3.1c) were solved numerically by a self-implemented finite-element code in **MATLAB** using linear basis functions and the Simpson quadrature rule to compute the integrals. For this, equation (3.1a) was multiplied by a test function $u(x)$ and integrated over the interval $[0, \ell]$. Changing the signs and integrating by parts lead to the so called weak formulation

$$\int_0^\ell S(x) p'(x) u'(x) dx + \frac{i\omega\rho}{Z_d} p(\ell) u(\ell) - k^2 \int_0^\ell S(x) p(x) u(x) dx = -qi\omega\rho u(0). \quad (3.8)$$

As discussed in Chapter 2 this problem admits a unique solution. To discretize this problem we divided the interval into smaller intervals $[x_{n-1}, x_n]$ with $x_n = \frac{n\ell}{N}$, $n = 1, \dots, N$ for some $N \in \mathbb{N}$. These subintervals are called elements. Next we considered a basis $\{\varphi_n\}_n$ of continuous and piecewise linear functions, where φ_n are hat functions on the corresponding subinterval $[x_{n-1}, x_{n+1}]$ and 0 elsewhere:

$$\varphi_n(x) = \begin{cases} \frac{x-x_{n-1}}{x_n-x_{n-1}}, & \text{if } x \in [x_{n-1}, x_n), n = 1, \dots, N, \\ \frac{x_{n+1}-x}{x_{n+1}-x_n}, & \text{if } x \in [x_n, x_{n+1}], n = 0, \dots, N-1, \\ 0, & \text{else.} \end{cases} \quad (3.9)$$

The discrete solution p_N to (3.8) is written in terms of this basis,

$$p_N(x) = \sum_{n=0}^N c_n \varphi_n(x), \quad (3.10)$$

3.2 Modeling approach and parameter estimation

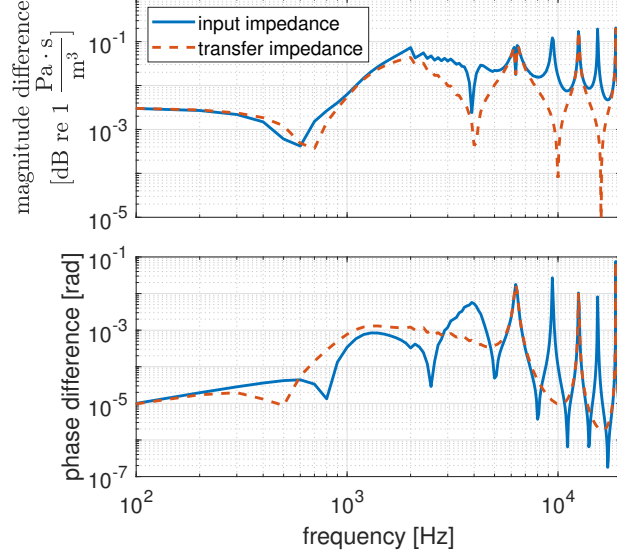


Figure 3.1: Level difference and phase difference of $Z_{\text{in}} = \frac{p(0)}{q}$ and $Z_{\text{in,ref}} = \frac{p_{\text{ref}}(0)}{q}$ and $Z_{\text{tr}} = \frac{p(L)}{q}$ and $Z_{\text{tr,ref}} = \frac{p_{\text{ref}}(L)}{q}$. The discrete solution p of (3.8) is computed with $N = 4 \max(1 \text{ m} \cdot \ell / \lambda^2, 1)$ elements for a typical area function $S(x)$ and eardrum impedance Z_d . The reference solution p_{ref} is computed with $N_{\text{ref}} = 5000$ elements. The error is uniformly bounded within the frequency range 100 Hz to 20 kHz.

where the coefficients c_n are computed by solving the system of linear equations

$$(A - M + R)c = F, \quad (3.11)$$

where

$$A_{ij} = \int_0^\ell S(x) \varphi_j'(x) \varphi_i'(x) dx, \quad (3.12a)$$

$$M_{ij} = k^2 \int_0^\ell S(x) \varphi_j(x) \varphi_i(x) dx, \quad (3.12b)$$

$$R_{NN} = \frac{i\omega\rho}{Z_d}, \quad R_{ij} = 0, \text{ for } i \neq N \neq j, \quad (3.12c)$$

$$F_1 = -qi\omega\rho, \quad F_i = 0, \text{ for } i \neq 0. \quad (3.12d)$$

In the experiments, the number of elements was chosen frequency-dependent as $N = 4 \max(1 \text{ m} \cdot \ell / \lambda^2, 1)$, i.e., the discretization is different for each frequency. In this case the typical "rule of thumb" of 10 elements per wave length is guaranteed. Additionally for the case of the horn equation, the discretization error with respect to a the magnitude and phase seems to be uniformly bounded, see Figure 3.1. The discretization error was computed with respect to a reference solution with $N_{\text{ref}} = 5000$ elements on a uniform

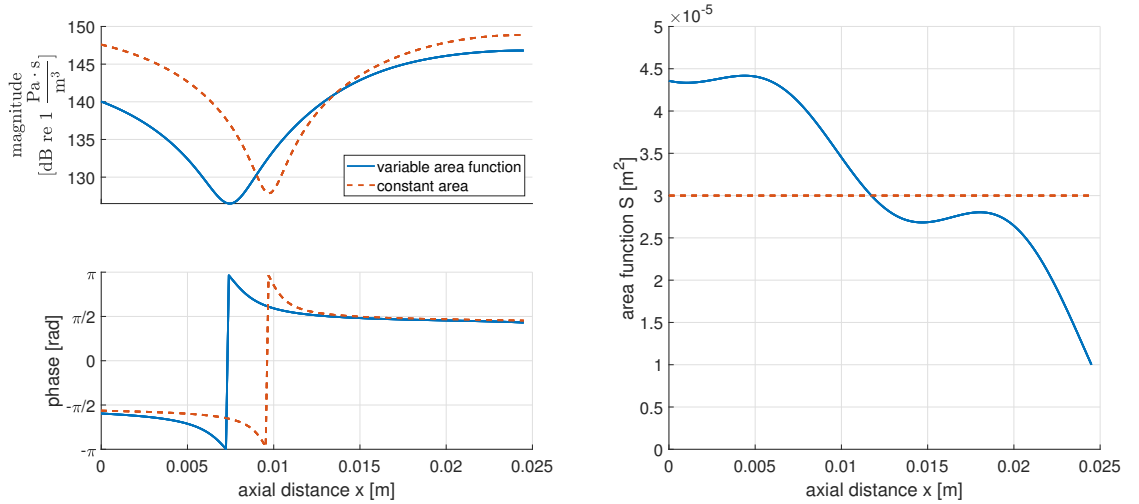


Figure 3.2: Solution for the Horn equation with $f = 6000$ Hz with variable area function and constant area function using linear finite elements (left) and associated area functions (right).

mesh.

Figure 3.2 illustrates an example solution for the weak formulation (3.8) of the horn equation (3.1a)-(3.1c) for a frequency of $f = 6$ kHz, $Z_d = (6.08 + 7.34i) \times 10^7$ Pa·s/m³ and an area function chosen as illustrated in Figure 3.2, i.e., a typical area function for an ear canal. In comparison, the solution to the pure Helmholtz problem, i.e., using a constant area function, is visualized as well to see the impact of the area function.

3.3 Synthetic and validation data preparation

The synthetically generated input impedance and validation data were created by 3D finite-element simulations on geometries from the IHA database [93]. For the simulation, the STL geometry was cut at the first bend of the ear canal. The first bend was determined by computing the center axis of the ear canal using the VMTK toolbox [7]. Then, the coordinates with highest curvature of this center axis in the region of the first bend, which can be visually estimated, was evaluated using the MATLAB function of Mjaavatten [78]. The implementation by Claxton [27] was used to shape the entrance surface with respect to the coordinates of the first bend and the corresponding tangential vectors. This modified geometry was used in COMSOL [28], where the geometries were discretized in a tetrahedral mesh with approximately 70,000-100,000 degrees of freedom, which corresponds to a maximum edge length of 1 mm of an element. The meshes at the eardrum were refined further with maximum edge length of 0.2 mm. As example, the meshed ear canal from Subject 5 is illustrated in Figure 3.3.

The entrance surface was then assumed to vibrate piston-like to provide the excitation of the residual ear canal. Using this set-up, acoustic input impedances for three different

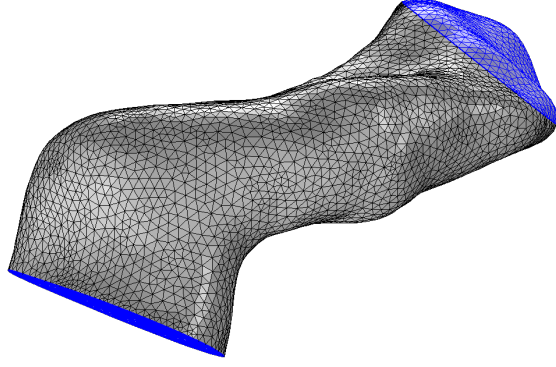


Figure 3.3: Mesh of the ear canal of Subject 5 cut at the first bend. The ear canal was rotated such that both the entrance and the eardrum (marked faces) are visible.

types of impedances at the eardrum were computed at the entrance, by solving the Helmholtz equation,

$$\Delta p_{3D}(\mathbf{x}) + k^2 p_{3D}(\mathbf{x}) = 0 \quad \text{in } \Omega, \quad (3.13a)$$

$$\frac{\partial p_{3D}}{\partial n} = -v_n i \omega \rho \quad \text{on } \Gamma_{\text{entrance}}, \quad (3.13b)$$

$$\frac{\partial p_{3D}}{\partial n} + \frac{i \omega \rho}{\tilde{Z}_{ED} |\Gamma_{\text{drum}}|} p_{3D} = 0 \quad \text{on } \Gamma_{\text{drum}}, \quad (3.13c)$$

$$\frac{\partial p_{3D}}{\partial n} = 0 \quad \text{on } \Gamma_{\text{wall}}, \quad (3.13d)$$

with Ω being the interior of the geometry, $\Gamma_{\text{entrance}} \subset \partial\Omega$ is the surface at the entrance, $\Gamma_{\text{drum}} \subset \partial\Omega$ is the surface that corresponds to the eardrum and Γ_{wall} is the wall of the ear canal. $\frac{\partial}{\partial n}$ denotes the outer normal derivative. Note that comparing Equation (3.1b) and (3.13b) we have different signs, since in (3.1b) the derivative in the one-dimensional model is directed into the interval. v_n is the particle velocity. The input impedance used as input data during the parameter fitting was averaged over the entrance surface Γ_{entrance}

$$Z_{\text{in,data}} = \frac{\frac{1}{|\Gamma_{\text{entrance}}|} \int_{\Gamma_{\text{entrance}}} p_{3D}(\mathbf{x}) d\Gamma_{\text{entrance}}}{|\Gamma_{\text{entrance}}| v_n}.$$

The considered eardrum impedances \tilde{Z}_{ED} are of the following types

- (i) impedance model by Hudde and Engel [60],
- (ii) a two-resonator model as described in (3.4) with parameters given in Table 3.1,
- (iii) (nearly) rigid, i.e., $\tilde{Z}_{ED} \approx 8.4 \times 10^{22} - 8.8 \times 10^{15}i \text{ Pa}\cdot\text{s}/\text{m}^3$.

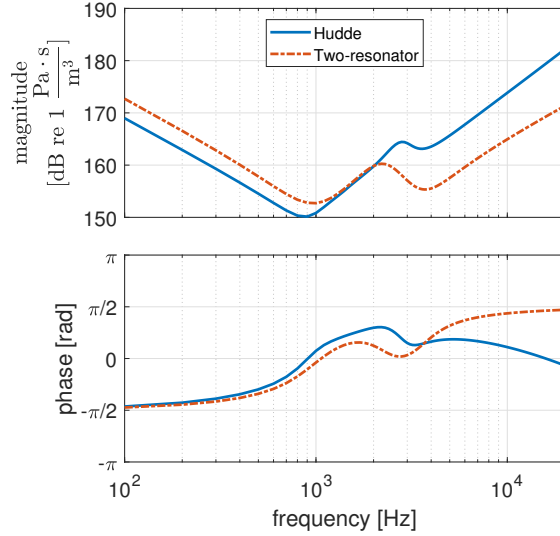


Figure 3.4: Eardrum impedances types (i) and (ii) for \tilde{Z}_{ED} that were used to compute the reference data. Type (iii) is not shown due to the large magnitude that is constant at approximately 458 dB with zero phase.

They are illustrated in Figure 3.4. For the validation in Section 3.5, the transfer impedance $Z_{\text{tr,data}}$ was computed with respect to the umbo, i.e.,

$$Z_{\text{tr,data}} = \frac{p_{3D}(\mathbf{x}_{\text{umbo}})}{|\Gamma_{\text{entrance}}|v_n}.$$

The entrance impedance $Z_{\text{in,data}}$ and transfer impedance $Z_{\text{tr,data}}$ were computed for 200 distinct frequencies linearly distributed in the range between 100 Hz and 20 kHz. A total of 30 data sets, ten subjects with three different impedance models each, were available for testing and validation.

	resonator 1	resonator 2
f_0	1000 Hz	3500 Hz
Q	1.1	1.5
L_0	153 dB re 1 Pa · s/m ³	157 dB re 1 Pa · s/m ³

Table 3.1: Parameters used for the generation of data using the two-resonator model.

3.4 Original parameter fitting and refinement of the method

We began with the basic algorithm and $M = 4$, i.e., four sine and cosine summands in the definition of the area function $S(x)$ in (3.3). The parameter fitting was done with a subset of all available frequencies, more specifically with 25 logarithmically distributed frequencies in the range from 100 Hz to 20 kHz. The parameter constraints were set according to Table 3.2 to ensure that the area function $S(x)$ does not take excessive values,

3.4 Original parameter fitting and refinement of the method

	$S_0[\text{m}^2]$	$\ell[\text{m}]$	c_m				s_m	
upper bound	2×10^{-4}	15×10^{-3}	$2^{-m+2} \times 10^{-5}$				$2^{-m+2} \times 10^{-5}$	
lower bound	10^{-5}	45×10^{-3}	$-2^{-m+2} \times 10^{-5}$				$-2^{-m+2} \times 10^{-5}$	
basic	6×10^{-5}	30×10^{-3}	$(2 \times 10^{-6}, 0, \dots, 0)$				$(0, 0, \dots, 0)$	

	$L_{0,1}[\text{dB}]$	$L_{0,2}[\text{dB}]$	Q_1	Q_2	$f_{0,1}[\text{Hz}]$	$f_{0,2}[\text{Hz}]$	$V[\text{m}^3]$
upper bound	200	$L_{0,1}+40$	10	10	2500	6000	5.23×10^{-8}
lower bound	50	$L_{0,1}+0$	0.3	0.3	500	2500	1.3×10^{-8}
basic	161	$L_{0,1}+20$	1.2	1.2	900	4000	2.62×10^{-8}

Table 3.2: Basic estimate with lower and upper bounds of the parameters of the ear canal area function and the two-resonator impedance model used in the one-dimensional surrogate model. The decibel values for impedance levels $L_{0,1}$ and $L_{0,2}$ refers to dB re $1 \text{ Pa} \cdot \text{s}/\text{m}^3$.

the oscillations of the area function are not unreasonably large and the impedance magnitude at the eardrum corresponds approximately to the expectations from commonly used models (i) and (ii) as in Figure 3.4. To enhance the accuracy, the Nelder-Mead method was used with three restarts, taking the result of the preceding optimization as initialization. Since the Nelder-Mead optimization procedure does not guarantee convergence to a global minimum, the parameter fitting procedure was executed several times with different initial parameters. These were chosen as random perturbation of up to 25% from the basic set of parameters, also depicted in Table 3.2, i.e., for a given parameter α with basic value α_0 ,

$$\alpha_{\text{init}} = \alpha_0 (1 + 0.25\mathcal{U}(-1, 1)),$$

where $\mathcal{U}(-1, 1)$ is the uniform distribution over the interval $(-1, 1)$. In total, twelve different initial parameter sets were considered. Figure 3.5 shows the results obtained with all twelve sets of initial parameters, considering data generated from the geometry of Subject 5 and eardrum impedance model (ii). All twelve initial parameter sets converged to similar results, thus the lines for each model type are very close to each other. The area function $S(x)$ has a similar trend in comparison to the area function computed by the method of [105] which is depicted as data curve in Figure 3.5. The input impedance is fitted well over the whole frequency range and even for the transfer impedance only slight differences between data and model can be observed.

However, this original parameter fitting did not lead to comparably good results for all subjects and all different types of eardrum impedances. To enhance the robustness of the method, several aspects that lead to problems or unrealistic results for individual subjects and eardrum impedance models are considered in the following and possible solution strategies are discussed, implemented and illustrated.

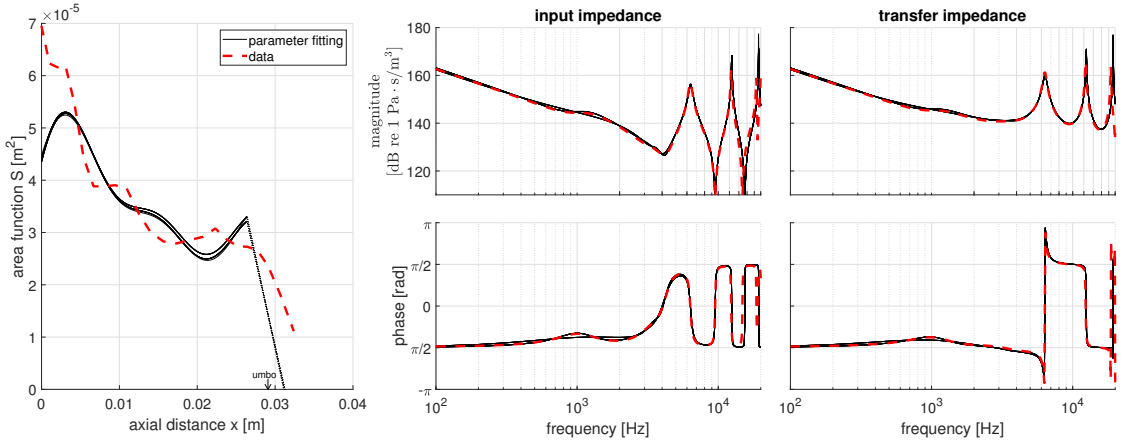


Figure 3.5: Results for the original parameter fitting method for Subject 5 and impedance model (ii). Solutions to each of the twelve different initial parameter sets are depicted by a black line respectively. Left: Area function. The rear part represents the cone as part of the impedance model, see discussion in Section 3.2. Center: Input impedance Z_{in} . Right: Transfer impedance Z_{tr} .

3.4.1 Avoiding negative areas

For some initial parameter sets, the original parameter fitting procedure returns a parameter set where the corresponding area function $S(x)$ takes negative values for some part in the interval $[0, \ell]$. Even though the reference data, i.e., the input impedance, was matched reasonably well, see Figure 3.6, some larger differences can be observed for the transfer impedance. We also note that the initial parameter set largely influences the result, thus the method is not very robust with regard to the initialization. Two possible strategies to prevent negative area function are

- (1) further restriction on the parameters S_0 , c_m and s_m such that the area function S will always be positive,
- (2) adding a penalty term to the cost function that penalizes negative or small values of S .

Here the first strategy is not very practical. It leads to strong restrictions on S_0 in the way that the lower bound needs to be relatively large or the restrictions on c_m and s_m are such that admissible geometries are quite restricted.

The second strategy still keeps a lot of freedom in the geometry-related parameters and will be used in the following. The penalty term is chosen as

$$J_{1,H^{(1)}}(S_0, \mathbf{c}, \mathbf{s}, \ell) = 10^4 \frac{\|\max(H^{(1)} - S(x), 0)\|_\infty}{H^{(1)}}, \quad (3.14)$$

where $\|\cdot\|_\infty$ is the discrete supremum norm. This penalty term penalizes the area function becoming smaller than $H^{(1)}$. We choose $H^{(1)} = 10^{-5} \text{ m}^2$, which is about one half of

3.4 Original parameter fitting and refinement of the method

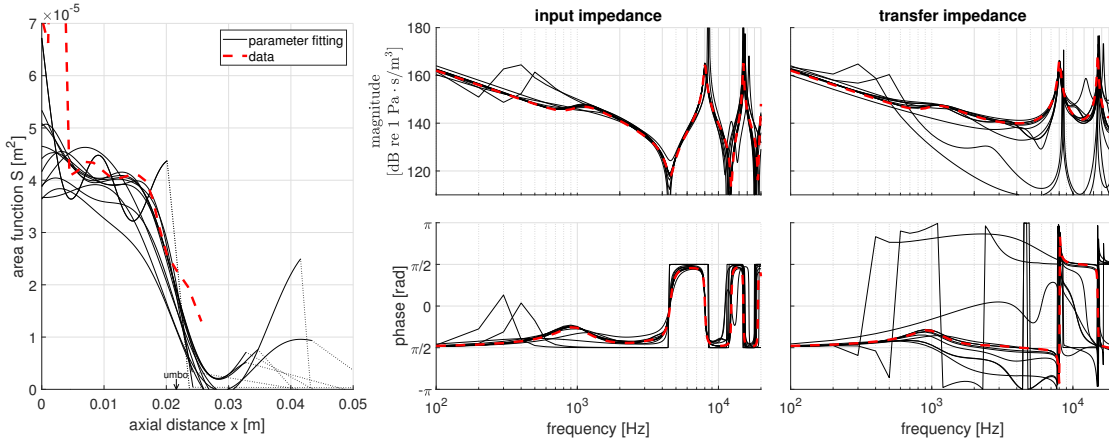


Figure 3.6: Parameter fitting may lead to negative values of the area function. Results for Subject 3 and impedance model (i). Solutions to each of the twelve different initial parameter sets are depicted by a black line respectively. Left: Area function. The rear part represents the cone as part of the impedance model, see discussion in Section 3.2. Center: Input impedance Z_{in} . Right: Transfer impedance Z_{tr} .

the base area of the standard cone with a radius of 2.5 mm.

The updated procedure now usually generates functions that are positive on $[0, \ell]$. If the area still becomes negative then the model-data misfit is probably just too large and a meaningful parameter fitting is not possible with the underlying one-dimensional surrogate model (3.1a)-(3.1c) or the initial values were chosen poorly.

Occasionally the problem arises that the area function steeply increases after reaching the minimum. One case for this behavior is illustrated in Figure 3.7 (left). This is anatomically at least unusual. Therefore, another penalty term is applied that penalizes solutions in which the end of the ear canal is larger than the overall minimum or close to that minimum. This additional penalty term is given as

$$J_{2,H^{(2)}}(S_0, \mathbf{c}, \mathbf{s}, \ell) = 10^4 \left\| \max \left(\frac{S(\ell) - S(x) - H^{(2)}}{|S(x)|}, 0 \right) \right\|_{\infty}. \quad (3.15)$$

The penalty is chosen as $H^{(2)} = 0$ which enforces the minimum of the area function to be at the end of the ear canal. The cost function now becomes

$$J = J_0 + J_{1,H^{(1)}} + J_{2,H^{(2)}}. \quad (3.16)$$

Using the updated cost function J in the parameter fitting leads to more realistic ear canal area functions, see Figure 3.7 (center).

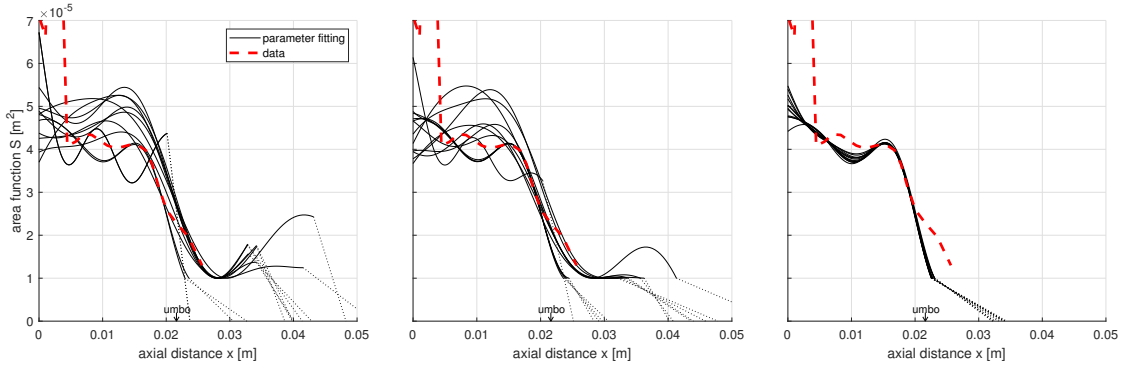


Figure 3.7: Left: Results incorporating penalty term J_1 for Subject 3 and impedance model (i) for twelve different initial parameter sets. Parameter fitting may lead to unrealistic ear canal geometries due to large increases in the area function near the eardrum. Center: Results incorporating penalty terms J_1 and J_2 for Subject 3 and impedance model (i) for twelve different initial parameter sets. Parameter fitting may lead to largely overestimating the length of the ear canal. Right: Results incorporating penalty terms J_1 , J_2 and prior estimating of the ear canal length ℓ for Subject 3 and impedance model (i) for twelve different initial parameter sets. Parameter fitting leads to a realistic area function.

3.4.2 Accommodating long and short ear canals

The length of the ear canal varies for each individual, thus the bounds of ℓ are chosen as $15 \text{ mm} \leq \ell \leq 45 \text{ mm}$ to be able to model short and long ear canals. Arbitrary initial values for ℓ may, however, lead the Nelder-Mead algorithm converge to a local minimum with an inadequate result for the value of ℓ , as can be seen in Figure 3.7 (center). To avoid this, we estimate ℓ in a first step by looking at the first maximum of the input impedance magnitude of the data, see for example Figure 3.6 (center) at around 8 kHz. Assuming a rigidly terminated cylindrical waveguide, the initial length is estimated as

$$\ell_{\text{est}} = \frac{c}{2f_{\text{max}}}, \quad (3.17)$$

where f_{max} corresponds to the frequency where the first maximum of the input impedance magnitude, i.e., the data, is achieved. It turned out that in general the first maximum frequency gave a better result than the first minimum, which is why the length was estimated using Equation (3.17). The ear canal is not a rigidly terminated cylindrical waveguide, but still this is a reasonable first approximation. Using this estimated ℓ_{est} as initial parameter leads to more appropriate results in the numerical simulations. To ensure that the overall length does not vary much from this estimated initial length during the parameter fitting, the bounds for ℓ were redefined to $\ell_{\text{est}} - 3 \text{ mm} \leq \ell \leq \ell_{\text{est}} + 1 \text{ mm}$. The upper bound is stricter since the impedance model already assumes that the ear canal is longer due to the cone at the end representing the innermost part of the ear

canal. These bounds lead to reasonable results for most initial values, see Figure 3.7 (right). Further results using the refined method are discussed in the validation in Section 3.5.

In the following subsection we further discuss the influence of the chosen frequency set for the parameter fitting and the influence of the length of the expansion of the area function.

3.4.3 Influence of the bandwidth and frequency spacing used in the parameter fitting

While the improvements of the prior subsections lead to better results in the parameter fitting, in some cases problems arise at very high frequencies, because some features of the 3D geometry cannot be captured in a one-dimensional model. This means that not for all ear canal shapes good estimations on the transfer impedance for frequencies up to 20 kHz can be expected. An example is illustrated in Figure 3.8. Here, the minimum of the magnitude of the input impedance at approximately 17 kHz is much lower than usual. For this individual, good approximations for high frequencies cannot be achieved using the horn equation. It might therefore be useful to restrict the frequency range during the parameter fitting to get better results regarding the lower frequency part. Restricting the frequency range to frequencies smaller than 10 kHz lead to improvements in the input impedance Z_{in} and transfer impedance Z_{tr} from the parameter fitting, see Figure 3.9.

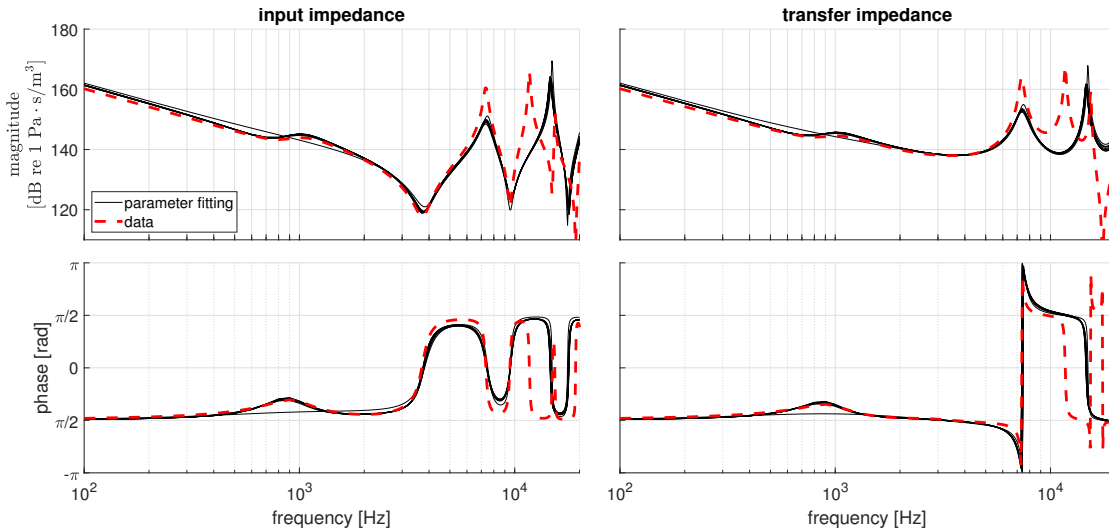


Figure 3.8: Ear canal of Subject 9 and impedance model (i) as example for a case of high frequency behavior that cannot be reproduced with the one-dimensional model. The last minimum in the entrance and transfer impedance data gets very low. Including high frequencies in the parameter fitting very likely influences precision for lower frequencies.

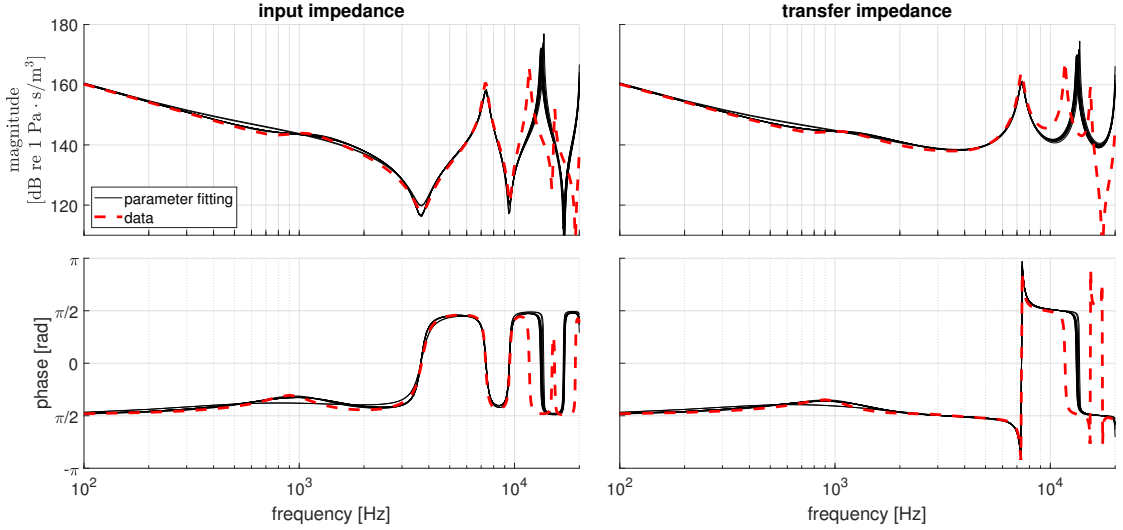


Figure 3.9: Ear canal of Subject 9 and impedance model (i) when only using data for frequencies up to 10 kHz. Improvements in the lower frequency range, especially up to 8 kHz can be observed in comparison to Figure 3.8.

In the following, different choices for frequency subsets are considered. The considered frequency sets were either uniformly or logarithmically distributed (rounded up to the nearest 100 Hz). Figure 3.10 illustrates the validation for uniformly distributed frequencies where the magnitude and phase difference of the transfer impedance was computed with respect to the reference data. For some frequency sets, finer resolutions in the low-frequency range (up to 3 kHz) or the higher frequency range (larger than 3 kHz) were used. Different upper limits were also considered, where the frequency sets were restricted either to frequencies up to 20 kHz or 10 kHz for reasons discussed above. Additionally, for some frequency sets \mathcal{F} , the frequencies that correspond to the maxima and minima of the input impedance magnitude were included, because these are the frequencies where usually the largest error with respect to the data is made and these frequencies are characteristic for the specific ear canal shape. We could observe that the frequency set using logarithmic distribution while additionally including the frequencies corresponding to the maxima and minima of the magnitude of the input impedance results in comparably low function values for the specific frequency range with respect to the validation function

$$J_{\text{val}}(Z_{\text{tr}}) = \sum_{f=100 \text{ Hz}, 200 \text{ Hz}, \dots, 20 \text{ kHz}} A \left| \log_{10} \left| \frac{Z_{\text{tr}}(f)}{Z_{\text{tr,data}}(f)} \right| \right|^2 + B \arg \left(\frac{Z_{\text{tr}}(f)}{Z_{\text{tr,data}}(f)} \right)^2. \quad (3.18)$$

Although other configurations lead to comparable validation function values, plotting the actual difference of the magnitude in dB over the frequency showed that for low frequencies the versions using uniformly distributed frequencies result in slightly worse behavior in the low frequency range with magnitude differences of up to 3 dB in the

3.4 Original parameter fitting and refinement of the method

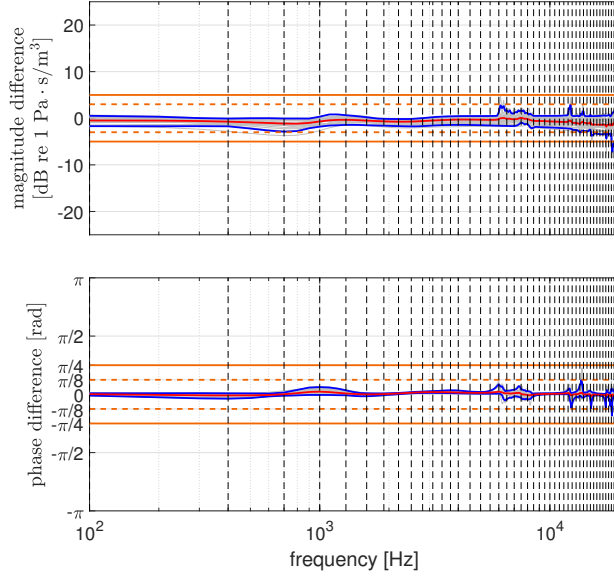


Figure 3.10: Validation for the parameter fitting considering differences of the transfer impedance for frequencies for linearly distributed frequencies up to 20 kHz considering all data sets. Straight solid line: 5 dB or 45° difference. Straight dashed line: 3 dB or 22.5° difference. Blue lines: 5 and 95 quantile. Red line in between: Mean. Dashed gray lines: Frequencies used during the parameter fitting.

frequency range from 100 Hz to 6 kHz, see Figure 3.10 as example, while the logarithmically distributed frequencies only lead to magnitude differences of up to 1.5 dB in this frequency range. This case is discussed and illustrated in the validation in Section 3.5. Consequently, a logarithmic distributed frequency set with maxima and minima frequencies was the choice for the validation in Section 3.5.

Since usually frequencies smaller than 10 kHz are especially of interest, we restrict the frequencies to 10 kHz to improve the results in this range, especially if the pressure distribution in the ear canal exhibits large three-dimensional effects due to the geometry of the ear canal.

3.4.4 Influence of the number of parameters in the area function expansion

In the parameter fittings in the previous sections, the number of geometrical parameters c_i and s_i was always chosen as $M = 4$. In this section, observations on varying number of parameters M are discussed.

Figure 3.11 illustrates the validation function J_{val} from (3.18) computed for varying parameter M . The underlying data for the boxplot are the refined parameter fittings of all ten subjects and all three different impedance models (i)-(iii). We observe only small changes for $M \geq 4$. Thus, due to increasing computational cost in the following

experiments $M = 4$ was chosen as a reasonable compromise between accuracy and computational cost.

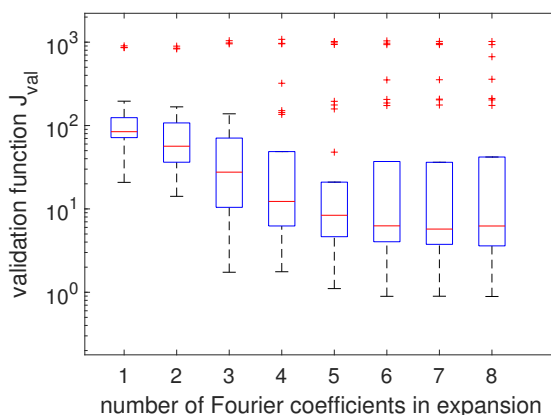


Figure 3.11: Validation function J_{val} depending on number of Fourier coefficients in area function.

3.5 Validation

3.5.1 Transfer impedance

In this section validation results are presented. To this end, ten different ear canals with three different impedance models at the eardrum were considered as discussed in Section 3.3. In Figure 3.12 the transfer impedance level and phase difference between the data and the parameter fitting, i.e.,

$$20 \log_{10} \left(\left| \frac{Z_{tr}}{Z_{tr,data}} \right| \right) \text{ and } \arg \left(\frac{Z_{tr}}{Z_{tr,data}} \right),$$

are plotted. The blue lines indicate the 5% and 95% quantile over the 30 parameter fittings based on 30 data sets, i.e., 10 different subjects and three different impedance models at the eardrum, in total.

The parameter fitting was done for twelve initial parameter sets in all cases. Only the one with the lowest cost function over all 200 frequencies was kept. The results are illustrated in Figure 3.12. In this case the results show magnitude differences of less than 1 dB for all frequencies in the range of up to 7 kHz, and still magnitude differences smaller than 5 dB for frequencies between 7 kHz and 10 kHz. In most cases the magnitude difference is even smaller than 3 dB for frequencies up to 10 kHz. For larger frequencies the differences are very large since only frequencies up to 10 kHz were used in the parameter fitting. Note however, that for most geometries reasonable results were also achieved for higher frequencies, see Figure 3.13.

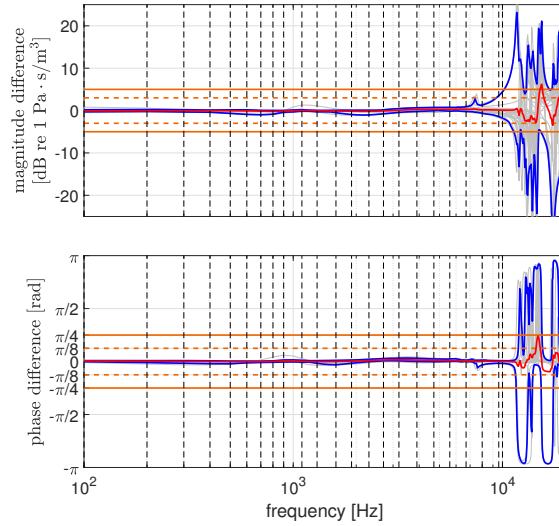


Figure 3.12: Validation for the parameter fitting considering differences of the transfer impedance for frequencies for up to 10 kHz. Straight solid line: 5 dB or 45° difference. Straight dashed line: 3 dB or 22.5° difference. Blue lines: 5 and 95 quantile. Red line in between: Mean. Dashed gray lines: Frequencies used during the parameter fitting.

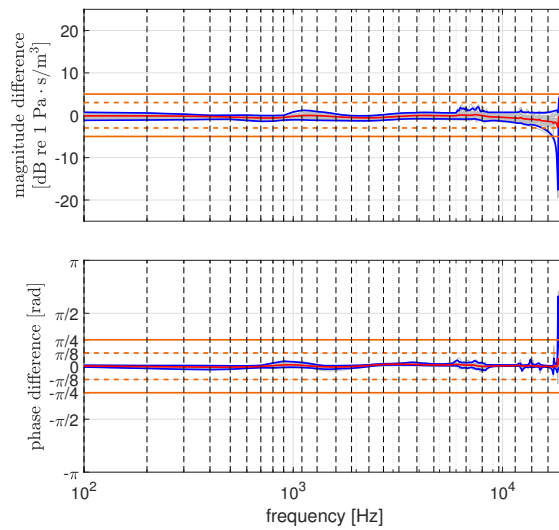


Figure 3.13: Validation for the parameter fitting considering differences of the transfer impedance for frequencies for up to 20 kHz excluding Subject 9 that showed unusual behavior for high frequencies. Straight solid line: 5 dB or 45° difference. Straight dashed line: 3 dB or 22.5° difference. Blue lines: 5 and 95 quantile. Red line in between: Mean. Dashed gray lines: Frequencies used during the parameter fitting.

3.5.2 Ear canal area function

During the parameter fitting, the estimated parameters for the ear canal area function can be used to construct an area function to get an approximate model of the geometry.

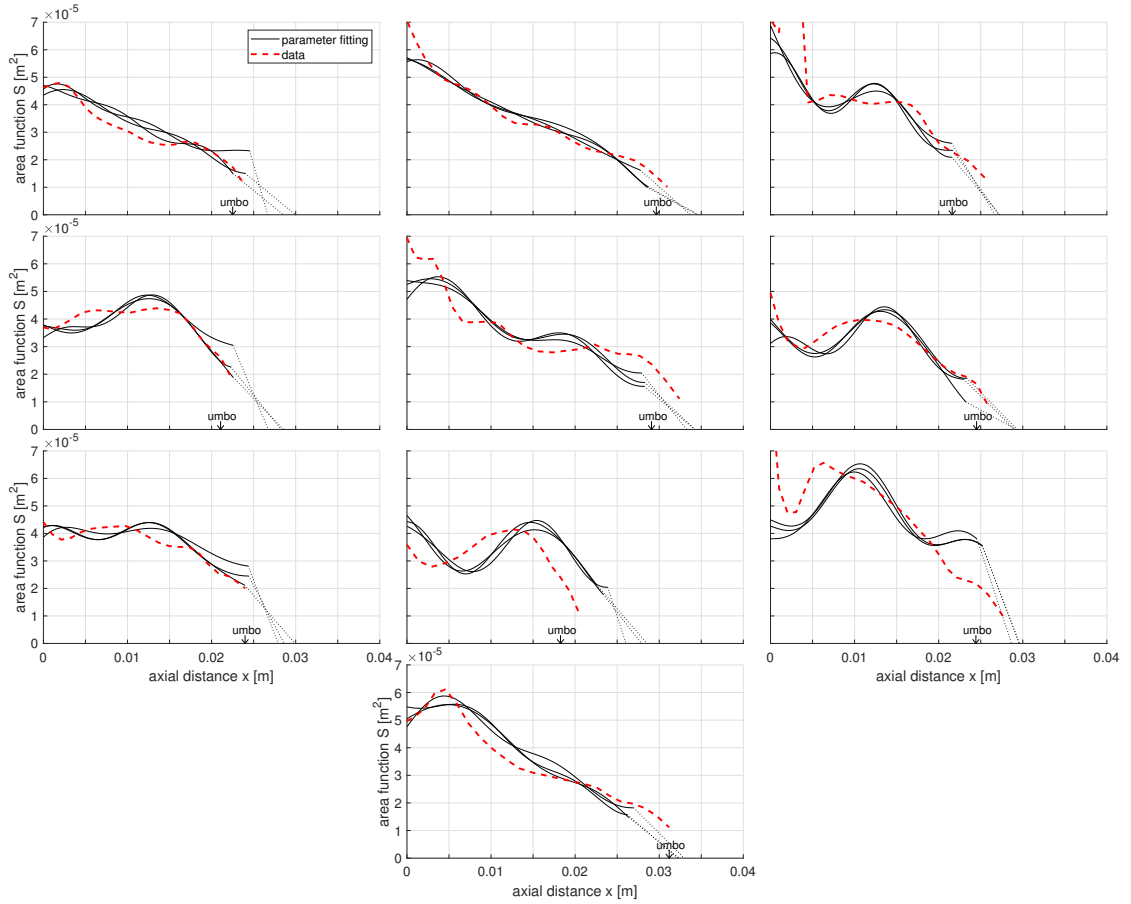


Figure 3.14: Results for the ear canal area functions for all ten subjects and all three impedance models 10 kHz.

In Figure 3.14 area functions taken from the parameter fitting (using logarithmically distributed frequencies up to 10 kHz) are displayed comparing it with the area function computed from the 3D geometry using the method described in [105]. Main features for most ear canals could be reproduced reasonably well. Note that the geometry used for the generation of the data was cut at the first bend of the center axis obtained from using the VMTK toolbox. This center axis differs from the one proposed in [105]. Especially the entrance surface will not be perpendicular to the center axis in [105] which explains the large deviations at the entrance of the area function for some subjects like Subject 3 and Subject 9. Overall, the approximations from the parameter fitting are quite close to the area function generated with the method from [105]. The area functions are also largely unaffected by the impedance model used for the data generation.

3.5.3 Impedance at eardrum

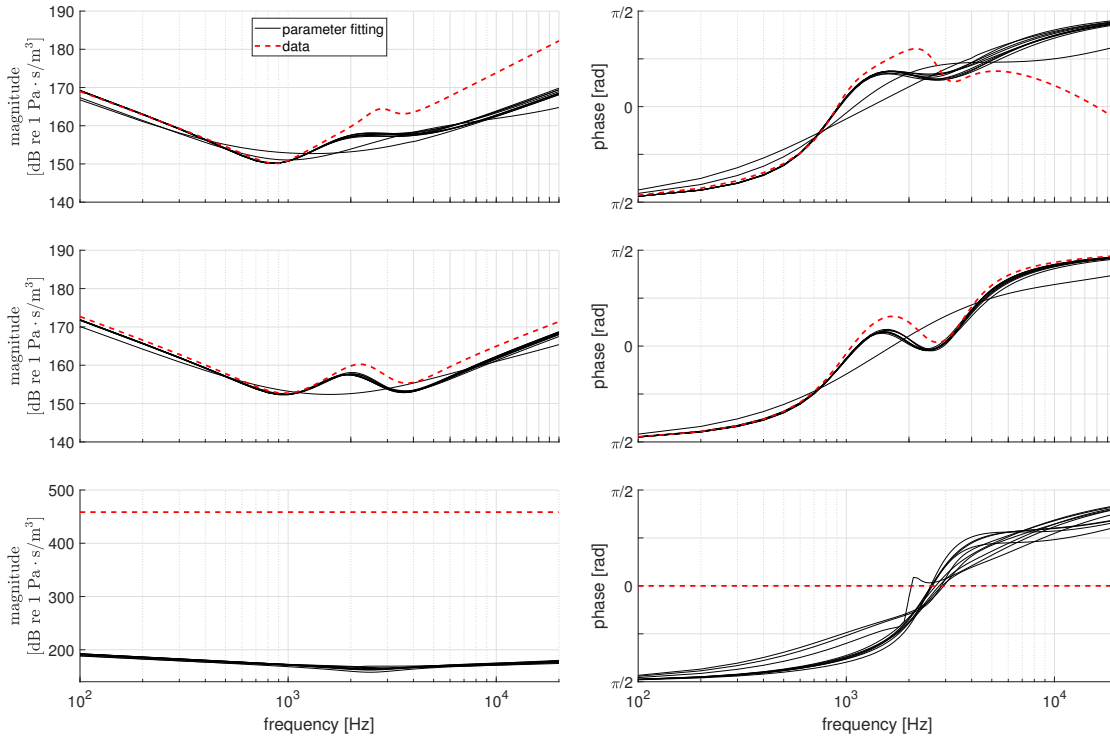


Figure 3.15: Estimated impedances at the eardrum for different underlying model data: (i) Hudde (ii) two-resonator (iii) rigid.

The parameter fitting also lead to an approximation of the impedance at the eardrum. This is illustrated in Figure 3.15. The data of the two-resonator model (ii) can be reconstructed well since this is the impedance model we used in the parameter fitting. The model in [60] is approximated well in the low frequency range. The impedance condition (iii) could not be approximated well since the bounds on the parameters do not allow impedances of such high magnitude. However, one can observe that the magnitude is larger than in the other cases, such that the resulting parameter fitting is closer to the rigid case. In all cases, the true eardrum impedance had a larger magnitude than the estimated one at frequencies above 2 kHz.

3.6 Conclusion

In this chapter a method to estimate the transfer impedance from input impedance is described and validated. Using synthetically generated data the method produces accurate results, especially in the frequency range of 100 Hz to 7 kHz. We can furthermore estimate the ear canal area function and the eardrum impedance, where for the area function the main features of the geometry were recognized. The eardrum impedance was

Chapter 3 Estimating individual ear canal acoustic transfer

estimated well in the low frequency range if the underlying impedance model was fitting. For higher frequencies, however, the eardrum impedance estimation was underestimated in general.

Future work should involve the validation and enhancement of the method using in vivo measurements.

Chapter 4

Bayesian Parameter Identification in Impedance Boundary Conditions for Helmholtz Problems

The contents of this chapter have been published in [111]. Some minor adjustments have been made in this chapter compared to the publication to give more context to the other contents of the thesis. The author of this thesis is the first author of this publication and has made major contributions to the development of the method, proofs, the writing and the numerical experiments (with the exception of the data preparation in Section 4.5.5). The discussion on the Markov Chain Monte Carlo methods in Section 4.6 is new and was not published before.

4.1 Introduction

The acoustic properties of rooms (e.g. recording studios, lecture or concert halls) critically depend on the geometry of the room and acoustic properties of the materials the room boundaries are made of. For example, the size and shape of windows made of glass significantly impact acoustic properties of the room. In order to facilitate virtual room design and to ensure reliable simulations the precise identification of parameters, such as the acoustic impedance of the walls and other constituent materials is crucial. These characteristics are typically measured using standardized methods, e.g. an impedance tube [63, 64] or a reverberation chamber [65].

Frequently it is not possible or not practical to examine isolated pieces of the material. In such a case, one may attempt to identify material parameters by measurements taken within the room itself. Moreover, the actual behavior of the material in the room might be significantly different from measurements done in isolation due to various coupling effects. For these reasons, methods to determine the acoustic impedance from measurements in the room are attractive.

In general, we can classify approaches for parameter identification in inverse problems into two types: classical deterministic and Bayesian approaches. The classical deterministic optimization-based approach involves utilizing an error function and employing methods such as least-squares, potentially with regularization, to solve for the parameter values. The Bayesian approach treats the parameters as random variables and naturally incorporates errors arising from one or more sources and deals with the corresponding

uncertainties.

Previous research in the classical context investigated the deterministic problem to identify the acoustic impedance from measurements in the room. In [87] the authors solved the deterministic inverse problem with boundary element method and Nelder-Mead optimization algorithm. This lead to complex values for the acoustic impedance that best fitted the measured data. In [39] an evolution strategy approach was used for the optimization of the impedance values and the absorption coefficient. Noise was also considered and good results were achieved if the Signal-to-Noise ratio (SNR) was large enough. In [6] the authors considered a related model, where the source of sound is coming from the vibrations of the structure, thus is included in the boundary condition instead of modeling it as a sound source in the interior. They use a genetic global optimization algorithm in combination with Newton's method, which lead to accurate estimations of the acoustic impedance. However, they did not consider any noise.

In practice, measurements are typically perturbed by noise. The information about the noise is naturally built into the Bayesian approach, where the parameters are interpreted as random quantities. The goal of the computation is to approximately compute their statistics. The Bayesian approach [107, 31] has several advantages compared to the classical approach. Firstly, the prior distribution serves as a form of regularization with clear interpretation. In contrast, regularization in the deterministic approach often is somewhat arbitrary [107]. Secondly, the Bayesian inference incorporates inevitable uncertainties directly and transparently [88]. Furthermore, in the deterministic approach, the resulting parameter values are presented with respect to a shared residual value. In contrast, the Bayesian approach yields individual parameter estimates, accompanied by corresponding uncertainty descriptions for each parameter separately [88].

In this chapter we consider the Bayesian approach to estimate the acoustic impedance on specific boundary regions in a room. For this, instead of computing a single (complex) value for the acoustic impedance we interpret the acoustic impedance as a random variable. We compute its statistical moments via ratio estimators and Monte-Carlo sampling to characterize the impedance. We consider the measurement setup of one sound source and several microphones at different positions, which represents the typical measurement procedure. The room acoustic is modeled using the interior Helmholtz equation, i.e., the time-harmonic wave equation, with impedance boundary conditions that represents locally reacting wall impedances. To solve the resulting partial differential equation, we employ the finite element method. We prove well-posedness of our problem and show convergence of the mean squared error for functionals of the acoustic impedance, which includes statistical moments of its real and imaginary part, using Monte Carlo sampling and ratio estimators. In the numerical experiments we consider two different scenarios. In the first scenario we utilize synthetic data generated using the same parametric model that is used for solving the inverse problem, i.e., impedance boundary conditions on the specific boundary regions. In this case the data are consistent with the parametric model and one would expect that the Bayesian algorithm will be able to recover correct parameter values. For this case we demonstrate convergence of the Bayesian algorithm numerically. In the second scenario the synthetic data are generated using a coupled acoustic-structural model where the boundary region is modeled as a glass wall, which

is not locally reacting. Although in general the locally reacting impedance model does not describe the physics of the glass wall well, for some frequency intervals the Bayesian algorithm finds values of acoustic impedance having high likelihood. Outside these frequency ranges, however, the results did not represent the measurement well due to the model-data misfit. We investigate this somewhat surprising behavior and explain it by the local structure of the eigenmodes and the distribution of the resonances.

We also point out that the Bayesian parameter identification for acoustic problems has been also applied in recent works [99, 40]. The short note [99] contains a numerical study of a two-dimensional acoustic problem with a different type of excitation. In [40] the authors consider an acoustical problem of source detection. Here, the uncertainty lies in the source of the Helmholtz equation, i.e., the position, number and amplitude of the sources. The authors adopt a Bayesian framework, mathematically analyzed the problem and proved convergence of the sequential Monte Carlo method, a method to sample directly from the posterior. In our work we are considering the uncertainty in the boundary condition instead of the source and utilize ratio estimators to compute moments of the posterior instead of sequential Monte Carlo.

This chapter is structured as follows. In Section 4.2 we discuss the model Helmholtz equation and review some basic definitions, theorems regarding existence and regularity of the solution and error estimates. In Section 4.3 we discuss the discretization of the problem in a finite element setting and collect convergence estimates required in that follows. In Section 4.4 we introduce the Bayesian setting and analyze the convergence of the proposed algorithm. Section 4.5 shows the numerical experiments where the theoretical error bounds are confirmed if the data are consistent with the model. We also demonstrate the behavior in the case of model-data misfit. In addition to the journal paper [111] version of this chapter in Section 4.6 we also include a discussion on Markov-Chain Monte-Carlo and how it compares to the ratio estimators and posterior estimation studied in [111]. Section 4.7 contains the outlook.

4.2 Preliminaries

We consider an interior Helmholtz problem on a bounded convex polygonal or polyhedral domain $\Omega \subset \mathbb{R}^d$, $d = 2, 3$. The boundary $\Gamma := \partial\Omega$ is decomposed into two disjoint open sets, Γ_N and Γ_R , such that $\Gamma = \overline{\Gamma_N} \cup \overline{\Gamma_R}$. The complex-valued acoustic pressure is then modeled as solution of the problem

$$\begin{cases} -\Delta p - k^2 p & = f & \text{in } \Omega, \\ \frac{\partial p}{\partial n} + \frac{i\omega\rho}{Z} p & = 0 & \text{on } \Gamma_R, \\ \frac{\partial p}{\partial n} & = 0 & \text{on } \Gamma_N, \end{cases} \quad (4.1)$$

with angular frequency ω , density ρ , acoustic impedance Z and wave number $k = \frac{\omega}{c}$, where c is the speed of sound. Here, we assume that Z is bounded with uniformly

positive real part and piecewise constant on a fixed partition $\cup_{i=1}^n \overline{\Gamma_R^{(i)}} = \Gamma_R$, that is

$$Z \in U := \{Z \in L^\infty(\Gamma_R) \mid Z \equiv z_i \in \mathbb{C} \text{ on } \Gamma_R^{(i)} \text{ with } \operatorname{Re}(z_i) \geq C > 0\}. \quad (4.2)$$

Note that $\operatorname{Re}(Z) \neq 0$ on some portion of the boundary is a sufficient condition for the well-posedness of (4.1). However, in the practically relevant case of a passive surface absorbing energy $\operatorname{Re}(Z)$ is strictly positive.

4.2.1 Weak formulation

The *weak formulation* is obtained by multiplying the Equation (4.1) by the complex conjugate of a test function $q \in H^1(\Omega)$ and integrating over Ω . The weak formulation reads: Find $p \in H^1(\Omega)$ such that for all $q \in H^1(\Omega)$

$$\int_{\Omega} \nabla p \cdot \nabla \bar{q} \, dx + \int_{\Gamma_R} \frac{i\omega\rho}{Z} p \bar{q} \, ds - k^2 \int_{\Omega} p \bar{q} \, dx = \int_{\Omega} f \bar{q} \, dx. \quad (4.3)$$

We define the sesquilinear form $b : H^1(\Omega) \times H^1(\Omega) \mapsto \mathbb{C}$ and antilinear form $\ell : H^1(\Omega) \rightarrow \mathbb{C}$ as follows

$$b(p, q) := \int_{\Omega} \nabla p \cdot \nabla \bar{q} \, dx + \int_{\Gamma_R} \frac{i\omega\rho}{Z} p \bar{q} \, ds - k^2 \int_{\Omega} p \bar{q} \, dx, \quad (4.4)$$

$$\ell(q) := \int_{\Omega} f \bar{q} \, dx. \quad (4.5)$$

As discussed in Chapter 2 the weak formulation (4.3) is well-posed for $f \in L^2(\Omega)$. However, in the experiments, a point source is assumed as the sound source. Therefore, the right-hand side f is modeled as a Dirac delta distribution δ^s located at a point s in the interior of Ω . The theory for the weak formulation does not guarantee well-posedness in this case, hence the so-called “very weak formulation” is used instead. Additionally, we define source and measurement domain that are distinct from each other, such that source and microphone positions are not too close to each other or to the boundary.

Definition 4.1 (Source and measurement domain, cf. [40, Definition 2.5]). *For $\kappa > 0$ the source domain $\Omega_\kappa \subset \Omega$ is a set satisfying $\operatorname{dist}(\Omega_\kappa, \Gamma) > \kappa$. The measurement domain is defined as*

$$M_\kappa := \{x \in \Omega : \operatorname{dist}(x, \Omega_\kappa) > \kappa \text{ and } \operatorname{dist}(x, \Gamma) > \kappa\}.$$

4.2.2 Very weak formulation for point source excitations

Let $s \in \Omega_\kappa$ be the location of the point source. The *very weak formulation* of (4.3) with Dirac delta right hand side is given by: Find $G_Z^s \in L^2(\Omega)$ such that

$$\int_{\Omega} G_Z^s (-\Delta \bar{q}) \, dx - k^2 \int_{\Omega} G_Z^s \bar{q} \, dx = \bar{q}(s), \quad (4.6)$$

for all $q \in \{q \in H^2(\Omega) : \frac{\partial q}{\partial n} + \frac{i\omega\rho}{Z} q = 0 \text{ on } \Gamma_R \text{ and } \frac{\partial q}{\partial n} = 0 \text{ on } \Gamma_N\}$. Since the solution G_Z^s depends on s and Z , we explicitly track this dependency in the notation. The right

hand side of the equation comes as a result of the defining property of the Dirac delta distribution, i.e.,

$$\int_{\Omega} \delta^s(x) \bar{q} \, dx = \bar{q}(s).$$

The following Proposition is a variation of Proposition 2.8 in [40]. The main difference is that here, we show Lipschitz continuity of G_Z^s with respect to Z .

Proposition 4.2 (cf. [40, Proposition 2.8]). *The very weak formulation (4.6) has a unique solution $G_Z^s \in L^2(\Omega)$ for any $s \in \Omega_\kappa$. Additionally there exists a constant $C_\kappa > 0$ depending on Z and κ but not on s such that*

$$\|G_Z^s\|_{H^2(M_\kappa)}, \|G_Z^s\|_{W^{2,\infty}(M_\kappa)} \leq C_\kappa \quad \text{for all } s \in \Omega_\kappa. \quad (4.7)$$

For $Z \in U$ the constant C_κ can be chosen independently of Z . Furthermore, there exists a constant $\tilde{C}_\kappa > 0$, such that for all $z \in M_\kappa$ it holds that

$$|G_{Z^{(1)}}^s(z) - G_{Z^{(2)}}^s(z)| \leq \tilde{C}_\kappa \|Z^{(1)} - Z^{(2)}\|_{L^\infty(\Gamma_R)}$$

for all piecewise constant $Z^{(1)}, Z^{(2)}$ with $\text{Re}(Z^{(1)}), \text{Re}(Z^{(2)}) \geq C > 0$.

Proof. Let Φ^s be the fundamental solution of the Helmholtz operator, that is

$$\Phi^s(z) := \begin{cases} \frac{2}{\pi} Y_0(k\|s-z\|), & \text{if } d = 2, \\ \frac{\exp(-k\|s-z\|)}{4\pi\|s-z\|}, & \text{if } d = 3, \end{cases} \quad (4.8)$$

where Y_0 is the Bessel function of second kind and zero order, see e.g. [33, 104]. Let p_Z^s be the unique weak solution of

$$\begin{aligned} -\Delta p_Z^s - k^2 p_Z^s &= 0 && \text{in } \Omega, \\ \frac{\partial p_Z^s}{\partial n} + \frac{i\omega\rho}{Z} p_Z^s &= -\frac{\partial \Phi^s}{\partial n} - \frac{i\omega\rho}{Z} \Phi^s && \text{on } \Gamma_R, \\ \frac{\partial p_Z^s}{\partial n} &= -\frac{\partial \Phi^s}{\partial n} && \text{on } \Gamma_N, \end{aligned}$$

i.e., $p_Z^s \in H^1(\Omega)$ is the unique solution of

$$\begin{aligned} \int_{\Omega} \nabla p_Z^s \cdot \nabla \bar{q} \, dx + \int_{\Gamma_R} \frac{i\omega\rho}{Z} p_Z^s \bar{q} \, d\Gamma_R - k^2 \int_{\Omega} p_Z^s \bar{q} \, dx \\ = - \int_{\Gamma_R} \left[\frac{i\omega\rho}{Z} \Phi^s + \frac{\partial \Phi^s}{\partial n} \right] \bar{q} \, d\Gamma_R - \int_{\Gamma_N} \frac{\partial \Phi^s}{\partial n} \bar{q} \, d\Gamma_N \end{aligned}$$

for all $q \in H^1(\Omega)$. Thus, the solution G_Z^s of (4.6) can be written as

$$G_Z^s = \Phi^s + p_Z^s. \quad (4.9)$$

Similarly as discussed in Section 2.2.2, in [15, Lemma 3.1, Theorem 3.3, Chapter 3.2] the existence and uniqueness of p_Z^s and hence of G_Z^s was proven, by showing that p_Z^s satisfies Gårding's inequality and thus the problem satisfies the Fredholm alternative, i.e., existence is a consequence of uniqueness which was shown in [15, Lemma 3.1]. Following [15], since Ω is convex, the H^2 -estimate is given by

$$\|p_Z^s\|_{H^2(\Omega)} \leq C \left[\left\| \frac{\partial \Phi^s}{\partial n} + \frac{i\omega\rho}{Z} \Phi^s \right\|_{H^{\frac{1}{2}}(\Gamma_R)} + \left\| \frac{\partial \Phi^s}{\partial n} \right\|_{H^{\frac{1}{2}}(\Gamma_N)} \right],$$

where the fundamental solution Φ^s and its derivatives are bounded uniformly in x for $\|x - s\| > \kappa$, see [40, proof of Theorem 2.8]. The $W^{2,\infty}$ -estimate $\|p_Z^s\|_{W^{2,\infty}(M_\kappa)} < C_\kappa$ was proven in [15, Lemma 3.4]. Tracking the constants in the proof of [15, Lemma 3.4] C_κ can be chosen independently of Z if $\frac{1}{Z}$ is bounded, which is the case for $\text{Re}(Z) \geq C > 0$.

It remains to show the Lipschitz continuity in Z . The Sobolev embedding [2, Theorem 4.12] implies that $H^2(M_\kappa) \subset C(M_\kappa)$ for $d = 2, 3$. Thus, for $z \in M_\kappa$

$$|G_{Z^{(1)}}^s(z) - G_{Z^{(2)}}^s(z)| \leq \|G_{Z^{(1)}}^s - G_{Z^{(2)}}^s\|_{C(M_\kappa)} \leq \tilde{C} \|G_{Z^{(1)}}^s - G_{Z^{(2)}}^s\|_{H^2(M_\kappa)}.$$

Now observe that for $Z^{(1)}, Z^{(2)} \in \mathbb{C}$ with $\text{Re}(Z^{(1)}), \text{Re}(Z^{(2)}) \geq C > 0$ we have

$$\begin{aligned} \|G_{Z^{(1)}}^s - G_{Z^{(2)}}^s\|_{H^2(M_\kappa)} &\leq \|p_{Z^{(1)}}^s - p_{Z^{(2)}}^s\|_{H^2(M_\kappa)} \leq \|p_{Z^{(1)}}^s - p_{Z^{(2)}}^s\|_{H^2(\Omega \setminus \Omega_\kappa)} \\ &\leq C_1 \left[\left\| \frac{i\omega\rho}{Z^{(1)}} \Phi^s + \frac{\partial \Phi^s}{\partial n} - \left(\frac{i\omega\rho}{Z^{(2)}} \Phi^s + \frac{\partial \Phi^s}{\partial n} \right) \right\|_{H^{1/2}(\Gamma_R)} \right] \\ &= C_1 \left\| i\omega\rho \left(\frac{1}{Z^{(1)}} - \frac{1}{Z^{(2)}} \right) \Phi^s \right\|_{H^{1/2}(\Gamma_R)}, \end{aligned}$$

where the right-hand side admits the following upper bound

$$\begin{aligned} C_1 \left\| i\omega\rho \left(\frac{1}{Z^{(1)}} - \frac{1}{Z^{(2)}} \right) \Phi^s \right\|_{H^{1/2}(\Gamma_R)} &\leq C_2 |\omega\rho| \|\Phi^s\|_{H^2(\Omega \setminus \Omega_\kappa)} \left\| \frac{1}{Z^{(1)}} - \frac{1}{Z^{(2)}} \right\|_{L^\infty(\Gamma_R)} \\ &\leq C_3 \left\| \frac{Z^{(2)} - Z^{(1)}}{Z^{(1)}Z^{(2)}} \right\|_{L^\infty(\Gamma_R)} \\ &\leq \tilde{C}_\kappa \|Z^{(1)} - Z^{(2)}\|_{L^\infty(\Gamma_R)}. \end{aligned}$$

□

4.3 Finite Element Discretization

In our approach, we discretize the problem using a quasi-uniform family of triangulations $\{\mathcal{T}_h\}_{h>0}$ of Ω . Each element $T \in \mathcal{T}_h$ is a triangle or tetrahedron with diameter h_T , and the diameter of the largest ball contained in T is denoted by ρ_T . The maximum diameter of all elements in \mathcal{T}_h is the mesh size, $h := \max_{T \in \mathcal{T}_h} h_T$. We assume the triangulations

$\{\mathcal{T}_h\}_{h>0}$ to be shape regular, i.e., we assume there exist constants $c_1, c_2 > 0$, such that for all $T \in \mathcal{T}_h$ and for all $h > 0$

$$\frac{h_T}{\rho_T} \leq c_1, \quad \frac{h}{h_T} \leq c_2.$$

We then define the finite element space V_h on the triangulation \mathcal{T}_h . The functions in V_h are globally continuous on Ω and piecewise linear in each $T \in \mathcal{T}_h$. The basis of V_h is made of piecewise linear (or quadratic) functions φ_i with $\varphi_i(x_j) = \delta_{ij}$. The discrete weak formulation of (2.1) is: Find $p_h \in V_h$ such that for all $q_h \in V_h$

$$b(p_h, q_h) = \ell(q_h), \quad (4.10)$$

where b is given as in (4.4). The antilinear functional

$$\ell(q_h) = \bar{q}_h(s)$$

as in the very weak formulation (4.6). Notice that even for the point source excitation f the weak formulation (4.10) is well posed on V_h , and thus can be used for the numerical approximation of (4.6). The following theorem states pointwise convergence of these approximations.

Theorem 4.3 (cf. [40, Theorem 2.14]). *Let $Z \in U$. Let $G_{Z,h}^s \in V_h$ be the discrete solution to (4.10) with $\ell(q) = \bar{q}(s)$. Then for any $h \in (0, h_0]$, $z \in M_\kappa$ and $s \in \Omega_\kappa$ there exist $h_0, C_\kappa > 0$ such that*

$$|G_Z^s(z) - G_{Z,h}^s(z)| \leq C_\kappa |\ln h| h^2$$

Proof. See appendix of [40]. The proof requires the bound $\|G_Z^s\|_{W^{2,\infty}(M_\kappa)} < C_\kappa$ independently of Z , which has been shown in Proposition 4.2. \square

Proposition 4.4. *There exist $h_0, C_\kappa > 0$ such that for all $z \in M_\kappa$ and for all $h \in (0, h_0]$ the discrete solution mapping $G_{Z_1,h}^s(z) : U \rightarrow \mathbb{C}$ is Lipschitz continuous in Z , that is*

$$|G_{Z_1,h}^s(z) - G_{Z_2,h}^s(z)| \leq C_\kappa \|Z_1 - Z_2\|_{L^\infty(\Gamma_R)}.$$

Proof. The proof is similar to the continuous case in Proposition 4.2 by replacing Green's function with its discrete version. \square

4.4 Bayesian framework

Since measurements are typically corrupted by noise, it is reasonable to work with models that take noise into account. In what follows we interpret the impedance Z as random variable and estimate its statistical moments using the Bayesian approach and the ratio estimators. This provides quantitative information on the sensitivity of the parameter with respect to the data, for example if the variance of Z is large, then multiple values and/or (large) regions are candidates for the true parameter value. If, however, the variance is very low, then only a small region in the domain of Z produces accurate results if the underlying model is a good representation for the data.

4.4.1 Continuous posterior moments

Let $\mathcal{F} : U \rightarrow H^1(\Omega)$ and $\mathcal{O} : H^1(\Omega) \rightarrow \mathbb{C}^m$ denote the forward map and observation operator, respectively, where $m \in \mathbb{N}$. The composition of both operators, denoted by $\mathcal{G} = \mathcal{O} \circ \mathcal{F} : U \rightarrow \mathbb{C}^m$, is given by

$$\mathcal{G}(Z) = (G_Z^s(x_1), G_Z^s(x_2), \dots, G_Z^s(x_m))^\top.$$

The problem is to determine an unknown element $Z \in U$ from noisy observations

$$y = \mathcal{G}(Z) + \eta, \quad (4.11)$$

where η is a realization of a multivariate complex normal distributed random variable $\mathcal{CN}(0, \Gamma, C)$ with a Hermitian and non-negative covariance matrix Γ and symmetric relation matrix C . The corresponding density of such a random variable is proportional to

$$\rho_\eta \propto \exp\left(-\frac{1}{2}\|z\|_\Sigma^2\right), \quad \forall z \in \mathbb{C}^m,$$

where $\Sigma \in \mathbb{C}^{2m \times 2m}$ is a positive definite complex matrix given by

$$\Sigma = \begin{pmatrix} \Gamma & C \\ \overline{C} & \overline{\Gamma} \end{pmatrix} \quad \text{and} \quad \|z\|_\Sigma^2 := \begin{pmatrix} \overline{z}^\top & z^\top \end{pmatrix} \Sigma^{-1} \begin{pmatrix} z \\ \overline{z} \end{pmatrix}.$$

We assume Z to be distributed according to a prior measure ν_0 on (U, \mathcal{B}) , where \mathcal{B} is the Borel σ -algebra. Bayes' Theorem gives the following relation for the Radon-Nikodym derivative of the posterior measure ν^y with respect to the prior measure ν_0 (see, e.g., [107, Theorem 6.31]):

$$\frac{d\nu^y}{d\nu_0}(Z) = \frac{\theta(Z, y)}{\Lambda(y)}, \quad (4.12)$$

where

$$\theta(Z, y) = \exp(-\Psi(Z, y)), \quad (4.13)$$

$$\Psi(Z, y) = \frac{1}{2}\|y - \mathcal{G}(Z)\|_\Sigma^2, \quad (4.14)$$

$$\Lambda(y) = \mathbb{E}_{\nu_0}[\theta(Z, y)]. \quad (4.15)$$

Here, θ is called the *likelihood*, Ψ the *potential*, $\log \theta = -\Psi$ the *log-likelihood* and Λ is a normalization constant. The expectation $\mathbb{E}_\nu[\phi]$ of a function $\phi : U \rightarrow \mathbb{R}$ with respect to a measure ν on (U, \mathcal{B}) is defined as

$$\mathbb{E}_\nu[\phi] = \int_U \phi(Z) d\nu(Z). \quad (4.16)$$

Remark 4.5. Since the potential $\Psi(Z, y)$ is nonnegative, the likelihood $\theta(Z, y)$ can only take values between 0 and 1 and the value 1 is only attained if the measurement data y exactly match the value $\mathcal{G}(Z)$. This is only possible if (i) the parametric model exactly

match the data y and (ii) the measurements contain no noise. The strength of the noise and the number of observation points clearly impact what can be treated as “a high value of the likelihood”. In particular, for the experimental setting of Section 4.5.4 we will see that log-likelihood values of $\log \theta(Z, y) \sim -10$ (and larger) can be seen as high.

Let $\phi : U \rightarrow \mathbb{R}$ be a ν_0 -measurable functional. If the posterior measure ν^y is well-defined (see Theorem 4.10 below), then, according to (4.12), the expected value of $\phi(Z)$ under the posterior measure can be expressed as

$$\mathbb{E}_{\nu^y}[\phi(Z)] = \frac{Q(y)}{\Lambda(y)}, \quad (4.17)$$

where the normalization constant $\Lambda(y)$ has been defined in (4.15) and

$$Q(y) = \mathbb{E}_{\nu_0}[\theta(Z, y)\phi(Z)]. \quad (4.18)$$

Notice that the posterior expectation $\mathbb{E}_{\nu^y}[\phi(Z)]$ is a ratio of two expectations with respect to the prior measure. A computable version of (4.17), see (4.25) below, is called a *ratio estimator*. Later we will chose $\phi(Z) = \operatorname{Re}(Z)^k$ or $\phi(Z) = \operatorname{Im}(Z)^k$ to compute k -th moments of the real or imaginary part of Z , respectively. From now on let ν_0 be a measure on (U, \mathcal{B}) .

The aim of the remainder of this subsection is to show that the posterior measure is well-defined.

Definition 4.6. Let ν be a measure on (U, \mathcal{B}) and $k \geq 1$. We say $\phi \in L^k_\nu(U)$ if

$$\|\phi\|_{L^k_\nu(U)} = \begin{cases} \left(\int_U |\phi(Z)|^k d\nu \right)^{\frac{1}{k}}, & 1 \leq k < \infty, \\ \operatorname{ess\,sup}_{Z \in U} |\phi(Z)|, & k = \infty \end{cases} \quad (4.19)$$

is finite.

Proposition 4.7. The operator \mathcal{G} is ν_0 -measurable and bounded, i.e.,

$$\|\mathcal{G}(Z)\|_\Sigma \leq K.$$

Proof. The measurability and the boundedness follow from the continuity and boundedness of $G_Z^s(z)$ in Z for all measurement positions $z \in M_\kappa$ from Proposition 4.2. Note that K depends on Z or more precisely on $\frac{1}{Z}$. But $\frac{1}{Z}$ is bounded since we assume $Z \in U$, hence K can be chosen independently of Z . \square

The following lemma states some properties of the potential that are needed to show that the posterior ν^y is well-defined. The statements are analogous to Lemma 3.6 in [40], but address the impedance parameter Z which is the focus of our work.

Lemma 4.8. The potential Ψ and the prior measure ν_0 satisfy:

(i) There exists a constant $K > 0$ such that

$$0 \leq \Psi(Z, y) \leq K + \|y\|_\Sigma^2, \quad \text{for all } Z \in U, y \in \mathbb{C}^m.$$

(ii) For every $y \in \mathbb{C}^m$ the map $\Psi(\cdot, y) : U \rightarrow \mathbb{R}$ is ν_0 -measurable.

(iii) For every $\varrho > 0$ there exists a constant $C_\varrho > 0$ such that

$$|\Psi(Z, y_1) - \Psi(Z, y_2)| \leq C_\varrho \|y_1 - y_2\|_\Sigma$$

for all $Z \in U$ and for all $y_1, y_2 \in B_\varrho(0) := \{y \in \mathbb{R}^m : \|y\|_2 < \varrho\}$.

Proof. (i) The lower bound follows from the definition of the potential (4.14), whereas the upper bound is a consequence the triangle inequality and Proposition 4.7 since

$$\Psi(Z, y) = \frac{1}{2} \|y - \mathcal{G}(Z)\|_\Sigma^2 \leq \|y\|_\Sigma^2 + \|\mathcal{G}(Z)\|_\Sigma^2 \leq \|y\|_\Sigma^2 + K.$$

(ii) Follows from the measurability of \mathcal{G} and the continuity of $\Psi(\cdot, y)$.

(iii) We have

$$\begin{aligned} \Psi(Z, y_1) - \Psi(Z, y_2) &= \frac{1}{2} \|y_1 - \mathcal{G}(Z)\|_\Sigma^2 - \frac{1}{2} \|y_2 - \mathcal{G}(Z)\|_\Sigma^2 \\ &= \frac{1}{2} (y_1 - \mathcal{G}(Z), y_1 - y_2)_\Sigma + \frac{1}{2} (y_1 - y_2, y_2 - \mathcal{G}(Z))_\Sigma \end{aligned}$$

Now, by Cauchy-Schwarz and the triangle inequality we continue as

$$\begin{aligned} |\Psi(Z, y_1) - \Psi(Z, y_2)| &\leq \frac{1}{2} \|y_1 - y_2\|_\Sigma (\|y_1 - \mathcal{G}(Z)\|_\Sigma + \|y_2 - \mathcal{G}(Z)\|_\Sigma) \\ &\leq \|y_1 - y_2\|_\Sigma \left(\|\mathcal{G}(Z)\|_\Sigma + \frac{1}{2} \|y_1\|_\Sigma + \frac{1}{2} \|y_2\|_\Sigma \right) \\ &\leq C_\varrho \|y_1 - y_2\|_\Sigma, \end{aligned}$$

where the last inequality holds since $\mathcal{G}(Z)$ is bounded and $y_1, y_2 \in B_\varrho(0)$. □

To show the well-posedness of the posterior ν^y it is essential to show the following bounds on the normalization constant $\Lambda(y)$.

Lemma 4.9. *For the normalization constant $\Lambda(y)$ there exists $\alpha > 0$ such that*

$$\alpha \exp(-\|y\|_\Sigma^2) \leq \Lambda(y) \leq 1 \quad \text{for all } y \in \mathbb{C}^m.$$

Proof. The upper bound follows directly from the definition (4.15) of $\Lambda(y)$

$$\Lambda = \mathbb{E}_{\nu_0} [\theta(Z, y)] = \int_U \theta(Z, y) d\nu_0(Z) = \int_U \exp(-\Psi(Z, y)) d\nu_0(Z) \leq 1,$$

since ν_0 is a probability measure on U and Ψ is nonnegative. For the lower bound we use property (ii) from Lemma 4.8 to get

$$\Lambda = \int_U \exp(-\Psi(Z, y)) d\nu_0(Z) \geq \int_U \exp(-(K + \|y\|_\Sigma^2)) d\nu_0(Z) = \alpha \exp(-\|y\|_\Sigma^2)$$

with $\alpha := \exp(-K)$. □

We can now state the well-posedness of the posterior ν^y and the existence of moments in the following theorem. The proof of the following theorem is partially based upon Theorem 15 in [31], where the authors show that the posterior measure is well-defined under more general assumptions.

Theorem 4.10. *Let $y \in \mathbb{C}^m$ be a fixed set of measurements. The posterior defined in (4.12) is well defined. Furthermore, if $\phi \in L_{\nu_0}^p(U)$ then $\phi \in L_{\nu^y}^p(U)$ for all $1 \leq p \leq \infty$ and a fixed y .*

Proof. We show that the Radon-Nikodym derivative (4.12) is bounded for all $Z \in U$. This follows since $\theta(Z, y) \leq 1$ and $\Lambda(y)$ is uniformly positive for $Z \in U$, cf. Lemma 4.9. To show that $\phi \in L_{\nu_0}^p(U)$ implies $\phi \in L_{\nu^y}^p(U)$ we observe by (4.17) that

$$\|\phi\|_{L_{\nu^y}^p(U)}^p = \mathbb{E}_{\nu^y} [|\phi|^p] = \frac{1}{\Lambda(y)} \mathbb{E}_{\nu_0} [|\phi|^p \theta(\cdot, y)] \leq \frac{1}{\Lambda(y)} \|\phi\|_{L_{\nu_0}^p(U)}^p < \infty,$$

since $\theta(Z, y) \leq 1$ and $\Lambda(y)$ is uniformly positive for $Z \in U$ by Lemma 4.9. \square

Note that the expected value of ϕ under the posterior measure ν^y is stable with respect to the data, i.e.,

$$\|\mathbb{E}_{\mu^{y_1}}[\phi] - \mathbb{E}_{\mu^{y_2}}[\phi]\|_U \leq c \|y_1 - y_2\|_\Sigma.$$

This can be shown by the means of the Hellinger distance

$$d_{\text{Hell}}(\mu^1, \mu^2) := \left(\int_U \frac{1}{2} \left(\left(\frac{d\mu^1}{d\nu} \right)^{\frac{1}{2}} - \left(\frac{d\mu^2}{d\nu} \right)^{\frac{1}{2}} \right)^2 d\nu \right)^{\frac{1}{2}} \quad (4.20)$$

using the properties of the potential proven in Lemma 4.8. See [31, Theorem 16] and [107, Lemma 6.37] for the details.

4.4.2 Computable posterior moments

In practice, the weak formulation is discretized and solved approximately. A discretization naturally introduces perturbation of the forward map $\mathcal{F} : U \rightarrow V$. To extend the Bayesian framework to this setting, we introduce the discrete forward map $\mathcal{F}_h : U \rightarrow V_h$, which now depends on the discretization parameter h . For a Finite Element discretization from Section 4.3 h stands for the mesh size. We can then define the discrete version of the operator \mathcal{G} introduced in Section 4.4 as $\mathcal{G}_h := \mathcal{O} \circ \mathcal{F}_h : U \rightarrow \mathbb{C}^m$. To adapt the likelihood, potential, and normalization constant to the discrete setting, we define

$$\theta_h(Z, y) = \exp(-\Psi_h(Z, y)), \quad Q_h(y) = \mathbb{E}_{\nu_0}[\theta_h(Z, y)\phi(Z)], \quad (4.21)$$

$$\Psi_h(Z, y) = \frac{1}{2} \|y - \mathcal{G}_h(Z)\|_\Sigma^2, \quad \Lambda_h(y) = \mathbb{E}_{\nu_0}[\theta_h(Z, y)]. \quad (4.22)$$

Remark 4.11. The discrete potential Ψ_h satisfies the same properties as Ψ given in Lemma 4.8 in the continuous case, where the constants and sets are independent of h [40, Theorem 4.3]. Furthermore, Lemma 4.9 also holds for the discrete normalization constant Λ_h .

If the Finite Element approximation converges, one expects that the size of perturbations $\mathcal{G} - \mathcal{G}_h$ and $\Psi - \Psi_h$ become smaller as $h \rightarrow 0$. The following two lemmas quantify this statement in a precise way. Their proofs are analogous to the corresponding results in [40], but with the focus on the random impedance parameter Z .

Lemma 4.12 (cf. [40, Lemma 4.1]). *There exist $h_0, C > 0$ such that for every $h \in (0, h_0]$ and every $Z \in U$ the discrete observation operator \mathcal{G}_h satisfies*

$$\|\mathcal{G}_h(Z)\|_\Sigma \leq C \quad \text{and} \quad (4.23)$$

$$\|\mathcal{G}(Z) - \mathcal{G}_h(Z)\|_\Sigma \leq C |\ln h| h^2. \quad (4.24)$$

Furthermore, \mathcal{G}_h is ν_0 -measurable.

Proof. From Theorem 4.3 we have

$$|G_Z^s(z) - G_{Z,h}^s(z)| \leq C_\kappa |\ln h| h^2, \quad \text{for all } z \in M_\kappa$$

with $C_\kappa > 0$ independent of Z and h . Since \mathcal{G} and \mathcal{G}_h are just point evaluations of G_Z^s and $G_{Z,h}^s$, (4.24) holds (with a different constant that does not depend on h). Further we have by the triangle inequality

$$\|\mathcal{G}_h(Z)\|_\Sigma \leq \|\mathcal{G}_h(Z) - \mathcal{G}(Z)\|_\Sigma + \|\mathcal{G}(Z)\|_\Sigma$$

which proves the boundedness of \mathcal{G}_h since $\|\mathcal{G}(Z)\|_\Sigma$ is bounded due to Proposition 4.7. The ν_0 -measurability follows from the continuity of $G_{Z,h}^s$ with respect to Z shown in Corollary 4.4. \square

Lemma 4.13 (cf. [40, Lemma 4.2]). *There exist $C, h_0 > 0$ such that for every $h \in (0, h_0]$ the discrete potential Ψ_h satisfies for all $Z \in U$, $y \in \mathbb{C}^m$*

$$|\Psi(Z, y) - \Psi_h(Z, y)| \leq C (1 + \|y\|_\Sigma) |\ln h| h^2.$$

Proof. Acting as in the proof of Lemma 4.8 (iii) we get

$$\begin{aligned} \Psi(Z, y) - \Psi_h(Z, y) &= \frac{1}{2} \|y - \mathcal{G}(Z)\|_\Sigma^2 - \frac{1}{2} \|y - \mathcal{G}_h(Z)\|_\Sigma^2 \\ &= \frac{1}{2} (y - \mathcal{G}(Z), \mathcal{G}_h(Z) - \mathcal{G}(Z))_\Sigma + \frac{1}{2} (\mathcal{G}_h(Z) - \mathcal{G}(Z), y - \mathcal{G}_h(Z))_\Sigma. \end{aligned}$$

Thus, by the triangle and the Cauchy-Schwarz inequality we get

$$\begin{aligned} |\Psi(Z, y) - \Psi_h(Z, y)| &\leq \|\mathcal{G}_h(Z) - \mathcal{G}(Z)\|_\Sigma \left(\|y\|_\Sigma + \frac{1}{2} \|\mathcal{G}(Z)\|_\Sigma + \frac{1}{2} \|\mathcal{G}_h(Z)\|_\Sigma \right) \\ &\leq C (1 + \|y\|_\Sigma) |\ln h| h^2, \end{aligned}$$

where we have used Proposition 4.7 and Lemma 4.12 in the last step. \square

Remark 4.14. Lemma 4.12 and Lemma 4.13 imply that (see also [31, Theorem 17] for a generalization of this): There exists $h_0 > 0$ such that the posterior measure ν_h^y is well-defined for $h \in (0, h_0]$. The posterior measure ν_h^y converges to ν^y with respect to the Hellinger distance

$$d_{\text{Hell}}(\nu^y, \nu_h^y) \leq C |\ln h| h^2.$$

This can be shown with the same arguments as in Chapter 4.2 in [31].

To make the posterior expectation (4.17) fully computable, we replace the prior expectations by a computable approximation. We use for simplicity the standard Monte Carlo method, i.e., the empirical mean

$$E_N[X] = \frac{1}{N} \sum_{i=1}^N X^i.$$

for independent and identically distributed samples X^1, \dots, X^N of X . Possible more sophisticated alternatives are, e.g., Quasi Monte Carlo methods [101, 84, 69] and Multilevel Monte Carlo methods [56, 49, 13]. However, the Multilevel Monte Carlo methods might have only restricted advantage here, because for Helmholtz problems the discretization needs to be comparably fine even on the lowest level in comparison to, e.g., the Laplace equation. The fully computable ratio estimator is now given by

$$\frac{\widehat{Q}_{h,N}}{\widehat{\Lambda}_{h,N}} := \frac{E_N[Q_h]}{E_N[\Lambda_h]}. \quad (4.25)$$

The following theorem states the convergence of the ratio estimator in the mean-square sense with respect to the prior measure.

Theorem 4.15. *Let $\phi \in L_{\nu_0}^2(U)$. Then*

$$\text{MSE} \left(\frac{\widehat{Q}_{h,N}}{\widehat{\Lambda}_{h,N}} \right) := \mathbb{E}_{\nu_0} \left[\left(\frac{Q}{\Lambda} - \frac{\widehat{Q}_{h,N}}{\widehat{\Lambda}_{h,N}} \right)^2 \right] \leq C \left(h^4 |\ln h|^2 + \frac{1}{N} \right).$$

Proof. For the MSE the following holds

$$\begin{aligned} \text{MSE} \left(\frac{\widehat{Q}_{h,N}}{\widehat{\Lambda}_{h,N}} \right) &= \mathbb{E}_{\nu_0} \left[\left(\frac{Q}{\Lambda} - \frac{\widehat{Q}_{h,N}}{\widehat{\Lambda}_{h,N}} \right)^2 \right] = \mathbb{E}_{\nu_0} \left[\left(\frac{Q\widehat{\Lambda}_{h,N} - Q\Lambda + Q\Lambda - \widehat{Q}_{h,N}\Lambda}{\Lambda\widehat{\Lambda}_{h,N}} \right)^2 \right] \\ &\leq 2\mathbb{E}_{\nu_0} \left[\left(\frac{Q(\widehat{\Lambda}_{h,N} - \Lambda)}{\Lambda\widehat{\Lambda}_{h,N}} \right)^2 \right] + 2\mathbb{E}_{\nu_0} \left[\left(\frac{(Q - \widehat{Q}_{h,N})\Lambda}{\Lambda\widehat{\Lambda}_{h,N}} \right)^2 \right] \\ &= 2\mathbb{E}_{\nu_0} \left[\left(\frac{Q}{\Lambda\widehat{\Lambda}_{h,N}} \right)^2 (\widehat{\Lambda}_{h,N} - \Lambda)^2 \right] + 2\mathbb{E}_{\nu_0} \left[\frac{1}{\widehat{\Lambda}_{h,N}^2} (Q - \widehat{Q}_{h,N})^2 \right] \end{aligned}$$

Since $Q = \mathbb{E}_{\nu_0}[\theta(\cdot, y)\phi] \leq \mathbb{E}_{\nu_0}[|\phi|]$, we know that Q is bounded if $\phi \in L^1_{\nu_0}(U)$. Moreover, Lemma 4.9 and Lemma 4.11 imply that for a fixed $y \in \mathbb{C}^m$ Λ and $\widehat{\Lambda}_{h,N}$ are bounded from below uniformly in $Z \in U$. Thus, the following estimate holds

$$\text{MSE} \left(\frac{\widehat{Q}_{h,N}}{\widehat{\Lambda}_{h,N}} \right) \leq C(y, \kappa) \left(\mathbb{E}_{\nu_0} \left[\left(\widehat{\Lambda}_{h,N} - \Lambda \right)^2 \right] + \mathbb{E}_{\nu_0} \left[\left(Q - \widehat{Q}_{h,N} \right)^2 \right] \right).$$

Here, the last expression is well defined, since $\phi \in L^2_{\nu_0}(U)$. The following Lemma 4.16 concludes the proof by showing the convergence results for

$$\mathbb{E}_{\nu_0} \left[\left(Q - \widehat{Q}_{h,N} \right)^2 \right].$$

The convergence for the other summand, i.e., the MSE of Λ , follows since Λ corresponds to a special case of Q with $\phi \equiv 1$. \square

The following lemma concludes the proof of Theorem 4.15 by analyzing the MSE for Q . This is done by splitting the MSE into bias and variance and showing convergence of these quantities.

Lemma 4.16. *For the MSE the following splitting holds*

$$\text{MSE}(\widehat{Q}_{h,N}) = \mathbb{E}_{\nu_0} \left[\left(Q - \widehat{Q}_{h,N} \right)^2 \right] = \text{Bias}(\widehat{Q}_{h,N})^2 + \text{Var}(\widehat{Q}_{h,N}) \quad (4.26)$$

where

$$\text{Bias}(\widehat{Q}_{h,N}) = |Q - \mathbb{E}_{\nu_0}[\widehat{Q}_{h,N}]| \leq C_B h^2 |\ln h|, \quad (4.27)$$

$$\text{Var}(\widehat{Q}_{h,N}) = \mathbb{E}_{\nu_0} \left[\left(Q_h - \widehat{Q}_{h,N} \right)^2 \right] \leq \frac{C_V}{N} \quad (4.28)$$

and constants C_B and C_V independent of h and N .

Proof. Observe that

$$\text{MSE}(\widehat{Q}_{h,N}) = \mathbb{E}_{\nu_0} \left[\left(Q - \widehat{Q}_{h,N} \right)^2 \right] = \mathbb{E}_{\nu_0} \left[\left(Q - Q_h \right)^2 \right] + \mathbb{E}_{\nu_0} \left[\left(Q_h - \widehat{Q}_{h,N} \right)^2 \right]$$

since Q and Q_h are deterministic and therefore

$$\mathbb{E}_{\nu_0} \left[\left(Q - Q_h \right) \left(Q_h - \widehat{Q}_{h,N} \right) \right] = \left(Q - Q_h \right) \left(Q_h - \mathbb{E}_{\nu_0} \left[\widehat{Q}_{h,N} \right] \right) = 0,$$

where we used that $\widehat{Q}_{h,N}$ is an unbiased estimator of Q_h . This implies (4.26) since Q and $Q_h = \mathbb{E}_{\nu_0}[\widehat{Q}_{h,N}]$ are deterministic. The estimate (4.27) follows from Lemma 4.13 and the Lipschitz continuity of $\exp(-\cdot)$ on $[0, \infty)$, since

$$\begin{aligned} \text{Bias}(\widehat{Q}_{h,N}) &= \left| \mathbb{E}_{\nu_0} [Q - Q_h] \right| \leq \mathbb{E}_{\nu_0} \left[|\phi(Z)| |\theta(Z, y) - \theta_h(Z, y)| \right] \\ &\leq \mathbb{E}_{\nu_0} [|\phi(Z)|] \sup_{Z \in \text{supp}(\nu_0)} |\Psi(Z, y) - \Psi_h(Z, y)| \\ &\leq C \mathbb{E}_{\nu_0} [\phi(Z)] (1 + \|y\|_{\Sigma}) h^2 |\ln h|. \end{aligned}$$

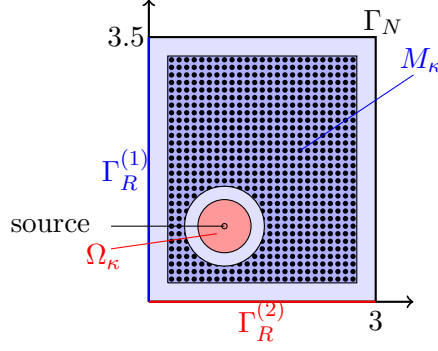


Figure 4.1: Domain for model problem in 2D. Black dots indicate the grid of possible microphone positions.

Concerning the variance, we observe

$$\begin{aligned} \text{Var}(\widehat{Q}_{h,N}) &= \mathbb{E}_{\nu_0} \left[\left(\mathbb{E}_{\nu_0} [\phi(Z)\theta_h(Z, y)] - E_N [\phi(Z)\theta_h(Z, y)] \right)^2 \right] \\ &= \mathbb{E}_{\nu_0} \left[\left(\frac{1}{N} \sum_{i=1}^N \left(\phi(Z^i)\theta_h(Z^i, y) - \mathbb{E}_{\nu_0} [\phi(Z^i)\theta_h(Z^i, y)] \right) \right)^2 \right], \end{aligned}$$

where Z^i are independent copies of Z . This implies

$$\begin{aligned} \text{Var}(\widehat{Q}_{h,N}) &= \frac{1}{N^2} \mathbb{E}_{\nu_0} \left[\left(\sum_{i=1}^N \phi(Z^i)\theta_h(Z^i, y) - \mathbb{E}_{\nu_0} [\phi(Z^i)\theta_h(Z^i, y)] \right)^2 \right] \\ &= \frac{1}{N} \mathbb{E}_{\nu_0} \left[(\phi(Z)\theta_h(Z, y) - \mathbb{E}_{\nu_0} [\phi(Z)\theta_h(Z, y)])^2 \right] \leq \frac{C_V}{N}. \end{aligned}$$

Since $\theta_h(Z) \leq 1$ for all $Z \in U$, the last inequality is satisfied with $C_V = \mathbb{E}_{\nu_0} [\phi(Z)^2]$. This implies (4.28) and concludes the proof thereby. \square

4.5 Numerical experiments

In this section, we demonstrate the numerical performance of our approach using various model problems in two and three space dimensions. In all experiments the aim is to determine the complex-valued acoustic impedance parameter $Z = Z_R + iZ_I$ and thereby fit the impedance boundary condition

$$\frac{\partial p}{\partial n} + \frac{i\omega\rho}{Z} p = 0 \quad \text{on } \Gamma_R \quad (4.29)$$

at the part of the boundary $\Gamma_R \subset \partial\Omega$. The parameter Z is assumed to be constant (in Section 4.5.3 piecewise constant) on Γ_R .

4.5.1 The general experimental setup

We consider a convex room $\Omega \subset \mathbb{R}^d$, which is either a rectangle for $d = 2$ or a cuboid for $d = 3$, with a fixed sound point source at s within the source domain $\Omega_\kappa \subset \Omega$ and m microphones placed at m different locations x_1, \dots, x_m within the measurement domain $M_\kappa \subset \Omega \setminus \Omega_\kappa$. The m measurement positions are randomly chosen in M_κ , based on a regular grid with L points in the room, see Figure 4.1. We draw m samples from a discrete uniform distribution with sample space $\{1, \dots, L\}$, where the indices of points that are too close (i.e., the distance between them is smaller than κ) to the source or boundary $\partial\Omega$ are excluded. To ensure consistency across experiments, the sound source location remains the same for a fixed experimental scenario. The computational algorithm is outlined as Algorithm 1.

- (1) For a given source of acoustic excitation get noisy measurements $y = (y_1, \dots, y_m)$, where y_j is the point value of the acoustic pressure $p(x_j)$ at a point in the measurement domain $x_j \in M_\kappa$.
- (2) Describe the a priori knowledge of the parameter Z by the prior ν_0 with density π_0 .
- (3) Draw N independent samples Z^1, \dots, Z^N of the parameter Z distributed according to the prior density π_0 .
- (4) For each sample Z^i solve numerically the model problem (4.1) with the local impedance boundary condition on Γ_R . Collect the point values $\mathcal{G}_h(Z^i) = (p_h(x_1), \dots, p_h(x_m))$, where p_h is the deterministic numerical solution of (4.1) for $Z = Z^i$.
- (5) Evaluate the likelihood $\theta_h(Z^i, y)$ of the sample Z^i according to (4.21), (4.22).
- (6) Evaluate the posterior mean and the variance of $Z_* \in \{Z_R, Z_I\}$ by the ratio estimator (4.25), i.e., $\widehat{\Lambda}_{h,N} = \frac{1}{N} \sum_{i=1}^N \theta_h(Z^i, y)$ and

$$\begin{aligned} \widehat{\mathcal{M}}_y^1[Z_*]_{h,N} &= \frac{1}{\widehat{\Lambda}_{h,N}} \left(\frac{1}{N} \sum_{i=1}^N Z_*^i \theta_h(Z_*^i, y) \right), \\ \widehat{\mathcal{M}}_y^2[Z_*]_{h,N} &= \frac{1}{\widehat{\Lambda}_{h,N}} \left(\frac{1}{N} \sum_{i=1}^N (Z_*^i - \widehat{\mathcal{M}}_y^1[Z_*]_{h,N})^2 \theta_h(Z^i, y) \right). \end{aligned} \tag{4.30}$$

Algorithm 1: Bayesian parameter identification

Steps (3)–(6) can be realized consecutively or in parallel, depending of the available computer architecture.

Note that computed posterior moments (4.30) are random variables themselves. In particular, their values change for different samples Z^i of Z . To demonstrate the validity

of Theorem 4.15 we repeat (3)–(6) multiple times to estimate the mean square error (MSE); see Section 4.5.3 below. In the other examples we fit a particular probability density π^y to reproduce the posteriori moments (4.30) and discuss the outcomes.

Clearly, the idealized local impedance boundary condition (4.29) does not always correctly describe the sound radiation and absorption at Γ_R . For significant model-data misfit, one would naturally expect failure of the Bayesian algorithm. In Section 4.5.5 we demonstrate that the inconsistency of the parametric model is not always detected, i.e., for certain frequencies our algorithm finds values of Z having high likelihood, even when the impedance condition (4.29) does not capture the physics at Γ_R . As we will see, the reasons for this somewhat unexpected behaviour are related to the actual microphone positions and the distribution of the eigenmodes of the physical model and their local structure.

It is natural that the demonstration of the effects related to consistency or inconsistency of the particular data sets $y = (y_1, \dots, y_m)$ and the parametric model (4.29) require full control over the generation and reproducibility of the noisy data y . That is why synthetic data generated from computer simulations are used in our experiments and not real measurements. We remark however, that our algorithm is designed to work with real measurements.

4.5.2 On the selection of the prior and fitted posterior densities

As already mentioned above, the impedance parameter $Z = Z_R + iZ_I$ describes a passive absorbing surface. Mathematically this means $Z_R > 0$, whereas Z_I is constraint-free. In other words, Z can take values on the right complex half-plane. This justifies the selection of the lognormal prior density for Z_R and the normal prior density for Z_I , that is

$$\log Z_R \sim \mathcal{N}(\mu_R, \gamma_R^2) \quad \text{and} \quad Z_I \sim \mathcal{N}(\mu_I, \gamma_I^2) \quad (4.31)$$

for the means μ_R, μ_I and standard deviations γ_R, γ_I . Notice that according to (4.31) the real part Z_R is not uniformly positive, as opposed to the requirement $Z_R \geq C > 0$ imposed in the previous sections by assuming $Z \in U$, defined in (4.2). However, we have not detected any significant change in the performance of our algorithm related to the presence of the uniform positivity condition, and therefore work with the model (4.31) in what follows. The joint probability density function is given by (see [44])

$$\pi_0(Z_R, Z_I) = \frac{1}{2\pi\gamma_R\gamma_I} \frac{1}{Z_R} \exp\left(-\frac{(\log Z_R - \mu_R)^2}{2\gamma_R^2} - \frac{(Z_I - \mu_I)^2}{2\gamma_I^2}\right).$$

Without additional knowledge apart from the first two moments nothing can be said about the shape of the posterior density. The following numerical experiments confirm this choice in the sense that the expected value and maximum of the estimated density are close to the reference value. Similarly as π_0 , the posterior density should be supported in the right half-plane. In view of these arguments, we approximate the posterior density π^y by

$$\hat{\pi}^y(Z_R, Z_I) = \frac{1}{2\pi\hat{\gamma}_R\hat{\gamma}_I} \frac{1}{Z_R} \exp\left(-\frac{(\log Z_R - \hat{\mu}_R)^2}{2\hat{\gamma}_R^2} - \frac{(Z_I - \hat{\mu}_I)^2}{2\hat{\gamma}_I^2}\right), \quad (4.32)$$

where the parameters $\hat{\mu}_R, \hat{\mu}_I, \hat{\gamma}_R, \hat{\gamma}_I$ are fitted to reproduce the posterior moments (4.30) by

$$\begin{aligned}\hat{\mu}_R &= \log \left(\frac{\widehat{\mathcal{M}}_{\nu^y}^1[Z_R]_{h,N}^2}{\sqrt{\widehat{\mathcal{M}}_{\nu^y}^2[Z_R]_{h,N} + \widehat{\mathcal{M}}_{\nu^y}^1[Z_R]_{h,N}^2}} \right), & \hat{\mu}_I &= \widehat{\mathcal{M}}_{\nu^y}^1[Z_I]_{h,N}, \\ \hat{\gamma}_R &= \sqrt{\log \left(1 + \frac{\widehat{\mathcal{M}}_{\nu^y}^2[Z_R]_{h,N}}{\widehat{\mathcal{M}}_{\nu^y}^1[Z_R]_{h,N}} \right)}, & \hat{\gamma}_I &= \sqrt{\widehat{\mathcal{M}}_{\nu^y}^2[Z_I]_{h,N}}.\end{aligned}\tag{4.33}$$

Note that all quantities with a hat $\hat{\cdot}$ depend on the discretization and sampling parameters h and N . For brevity, we will not explicitly track these parameters in the notation. Although there is no indication that $\hat{\pi}^y$ is close to π^y , we will see in Section 4.5.3 that the maximum of $\hat{\pi}^y$ reproduces the reference value of Z surprisingly well if the data $y = (y_1, \dots, y_m)$ are consistent with the impedance model (4.29).

4.5.3 2D model: Discretization and sampling error

To validate the results from the previous sections we consider the model problem in a two-dimensional room of 3 m width and 3.5 m length, i.e., $\Omega := [0, 3] \times [0, 3.5] \subset \mathbb{R}^2$:

$$\begin{cases} -\Delta p - k^2 p &= f & \text{in } \Omega, \\ \frac{\partial p}{\partial n} + \frac{i\omega\rho}{Z^{(1)}} p &= 0 & \text{on } \Gamma_R^{(1)}, \\ \frac{\partial p}{\partial n} + \frac{i\omega\rho}{Z^{(2)}} p &= 0 & \text{on } \Gamma_R^{(2)}, \\ \frac{\partial p}{\partial n} &= 0 & \text{on } \Gamma_N. \end{cases}\tag{4.34}$$

Here, the boundary $\partial\Omega$ of Ω is split into three disjoint parts $\Gamma_R^{(1)} = \{(x_1, x_2) \in \partial\Omega : x_1 = 0\}$, $\Gamma_R^{(2)} = \{(x_1, x_2) \in \partial\Omega : x_2 = 0\}$ and $\Gamma_N = \partial\Omega \setminus (\Gamma_R^{(1)} \cup \Gamma_R^{(2)})$, see Figure 4.1. We assume that the acoustic impedances $Z^{(1)} = Z_R^{(1)} + iZ_I^{(1)}$ and $Z^{(2)} = Z_R^{(2)} + iZ_I^{(2)}$, $Z_R^{(\ell)}, Z_I^{(\ell)} \in \mathbb{R}$ for $\ell = 1, 2$, are constant on the specific part of the boundary. The point source $f = \delta^s$ is located at $s = (1, 1) \in \Omega_\kappa$. The data are computed by numerically solving problem (4.34) with reference acoustic impedance values, namely $Z_{\text{ref}}^{(1)} = 400 - 700i$ and $Z_{\text{ref}}^{(2)} = 500 + 800i$, evaluating the solution at $m = 4$ measurement positions and adding artificial noise, i.e., $y = \mathcal{G}(Z_{\text{ref}}) + \eta$, where $\eta \sim \mathcal{CN}(0, \Sigma, 0)$. Σ is a diagonal matrix with entries $\sigma_k^2 = \sigma_0^2$, $k = 1, \dots, 2m$, where $\sigma_0 = 0.02$. This means that the log-likelihood can be expected to be of the order of $-m$ if the sampling and discretization errors are neglected, since then $\mathbb{E}_{\nu_0}[\log \theta] = \mathbb{E}_{\nu_0}[-\frac{1}{2}\|\eta\|_\Sigma^2] = -m$. The prior distribution was chosen as described in Section 4.5.2 with $\log Z_R^{(1)} \sim \mathcal{N}(\mu_R^{(1)}, \gamma_R^{(1)2})$, $Z_I^{(1)} \sim \mathcal{N}(\mu_I^{(1)}, \gamma_I^{(1)2})$, $\log Z_R^{(2)} \sim \mathcal{N}(\mu_R^{(2)}, \gamma_R^{(2)2})$ and $Z_I^{(2)} \sim \mathcal{N}(\mu_I^{(2)}, \gamma_I^{(2)2})$ with $\mathbb{E}[Z_R^{(1)}] = 300$, $\mathbb{E}[Z_I^{(1)}] = -600$, $\mathbb{E}[Z_R^{(2)}] = 600$, $\mathbb{E}[Z_I^{(2)}] = 900$ and $\text{Var}(Z_R^{(1)}) = \text{Var}(Z_I^{(1)}) = \text{Var}(Z_R^{(2)}) = \text{Var}(Z_I^{(2)}) =$

200^2 , i.e., $\mu_R^{(1)} \approx 5.52$, $\mu_I^{(1)} = -600$, $\mu_R^{(2)} \approx 6.34$, $\mu_I^{(2)} = 900$, $\gamma_R^{(1)} \approx 0.61$, $\gamma_I^{(1)} = 200$, $\gamma_R^{(2)} \approx 0.32$ and $\gamma_I^{(2)} = 200$.

To confirm the theoretical convergence rates from Theorem 4.15 we compute $\widehat{M}_{\nu y}^1[Z_*^{(\ell)}]$ and $\widehat{M}_{\nu y}^2[Z_*^{(\ell)}]$, i.e., we use $\phi(Z_*^{(\ell)}) = Z_*^{(\ell)}$ or $\phi(Z_*^{(\ell)}) = (Z_*^{(\ell)} - \widehat{M}_{\nu y}^1[Z_*^{(\ell)}])^2$ in Theorem 4.15. These let us compute the estimates for $\widehat{\mu}_R^{(\ell)}, \widehat{\gamma}_R^{(\ell)}, \widehat{\mu}_I^{(\ell)}$ and $\widehat{\gamma}_I^{(\ell)}$ with equations (4.33).

First, consider the discretization error, i.e., $|\mu_*^{(\ell)} - \widehat{\mu}_*^{(\ell)}|$ and $|\gamma_*^{(\ell)} - \widehat{\gamma}_*^{(\ell)}|$, $\ell = 1, 2$, where we recall that $\widehat{\mu}_*^{(\ell)}$ and $\widehat{\gamma}_*^{(\ell)}$ depend on the discretization parameters h, N . For the estimation $N = 2^{16}$ samples are drawn. The exact expected values $\mu_*^{(\ell)}$ and $\gamma_*^{(\ell)}$, $\ell = 1, 2$, are approximated on a small grid with $h = \frac{c/f}{10 \cdot 2^5} \approx 0.021$ m for reference. The error visualized in Figure 4.2 is averaged over 20 runs, i.e., different set of drawn samples, while the positions of the measurements and the noise (and therefore the data y) stay fixed for all runs. As seen from Figure 4.2, the convergence behaviour confirms the theoretically predicted convergence rates in Theorem 4.15.

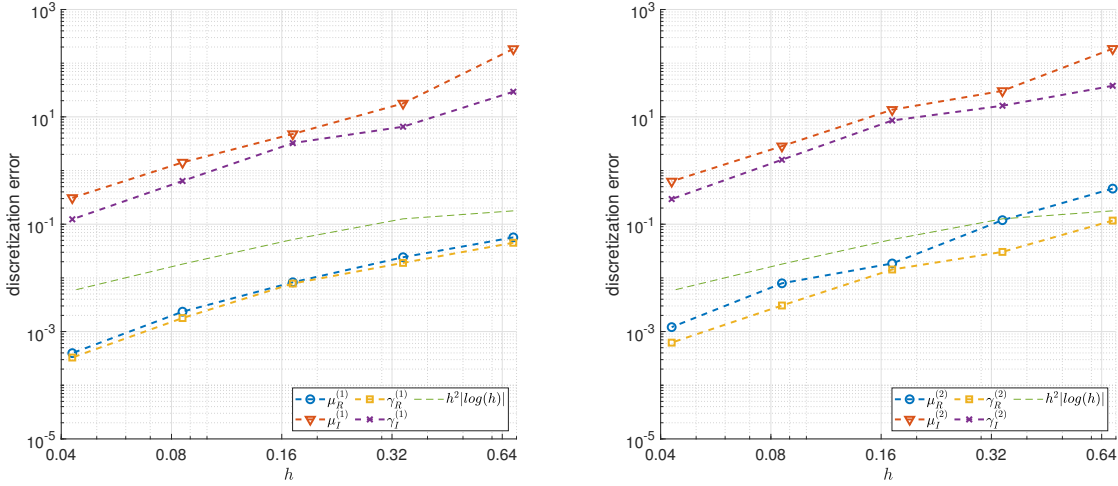


Figure 4.2: Discretization error for statistical parameters of $Z^{(1)}$ (left) and $Z^{(2)}$ (right) for $f = 50$ Hz. Note that the absolute errors are shown. Thus, the error curves belonging to the parameters of the lognormal distribution are lower.

Next, we address the sampling error. The exact values are approximated with large sample size of $N = 2^{16}$. The computations for the sampling error were all done on a grid with mesh size $h = \frac{c/f}{20} \approx 0.34$ m and frequency $f = 50$ Hz. In Figure 4.3 the sampling error is averaged over 20 runs. We observe the convergence rate of $\frac{1}{\sqrt{N}}$ as expected from Theorem 4.15.

Given the estimations on the first and second moments of $Z_R^{(\ell)}$ and $Z_I^{(\ell)}$, $\ell = 1, 2$, we can approximate the posterior density π^y by $\widehat{\pi}^y$ defined in Equation (4.32) as described in Section 4.5.2. For $N = 2^{16}$ samples and $h = \frac{c/f}{20}$ we again compute the estimators given in (4.33). In Figures 4.4 and 4.5 we compare the approximate posterior density $\widehat{\pi}^y$ with the prior density for 50 Hz and 100 Hz, respectively. We observe that the peak of

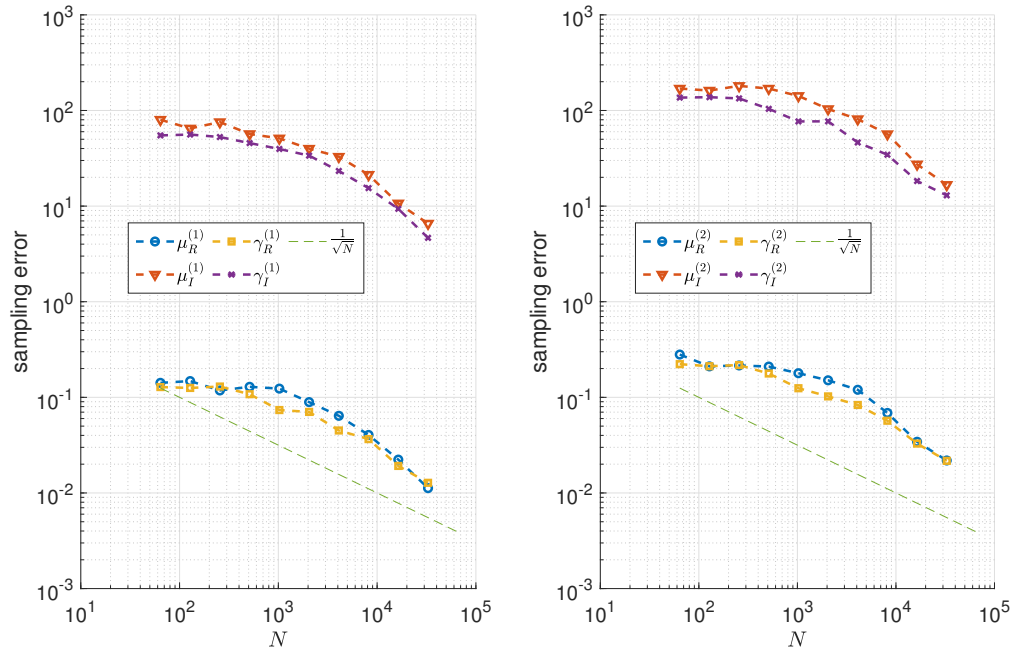


Figure 4.3: Sampling error for statistical parameters of $Z^{(1)}$ (left) and $Z^{(2)}$ (right) for $f = 50$ Hz. Note that the absolute errors are shown. Thus, the error curves belonging to the parameters of the lognormal distribution are lower.

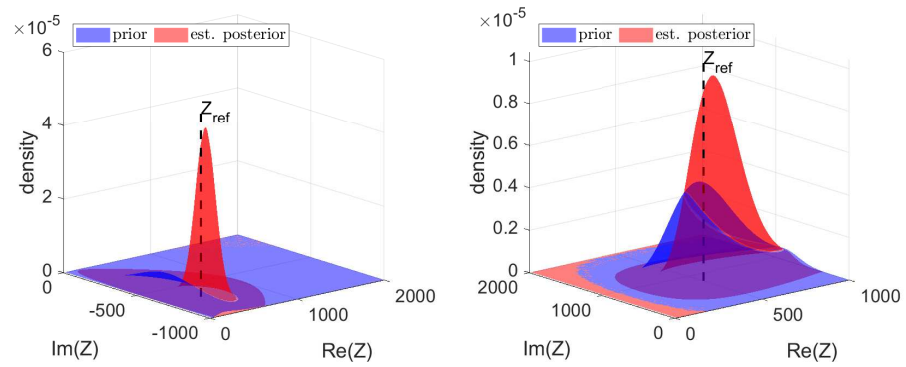


Figure 4.4: Prior density and density given by estimated expected value and standard deviation for $f = 50$ Hz for $Z^{(1)}$ (left) and $Z^{(2)}$ (right).

the density function $\hat{\pi}^y$ is closer to the true underlying value than the peak of π_0 , and the variance reduces. Consequently, we obtain a sharper estimate for the impedance than the initial prior. Instead of only pointing out the single best value for the impedance fitting the data, we get a density plot that shows a whole domain of reasonable parameter combinations under the assumption that certain noise is present. Note that for the

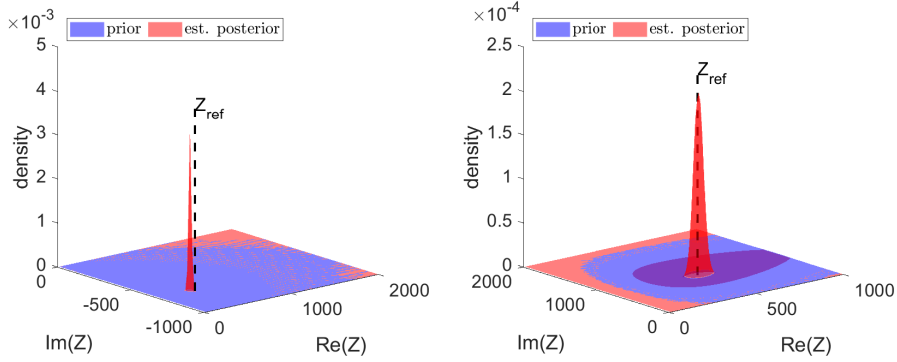


Figure 4.5: Prior density and density given by estimated expected value and standard deviation for $f = 100$ Hz for $Z^{(1)}$ (left) and $Z^{(2)}$ (right).

real part, the peak of the density is lower than the expected value as it should be for the lognormal distribution. Thus, the expected value as a single parameter is rather insufficient to provide the best estimate for the impedance: the expected value and the standard deviation, or a fitted distribution, as we propose here, result in a more complete and informative estimate.

Our result can be optionally utilized in several ways to design further simulations (e.g., acoustic modeling of another room with a wall made from the same material, or a room with a set of acoustic obstacles inside it). If the aim is to use a single deterministic value of the estimated acoustic impedance that best fits the data, one should rather use the value that maximizes the likelihood. If the focus is in the further probabilistic parameter modeling (e.g., further Bayesian simulations), the estimated statistical moments and the fitted distribution can be used instead.

Figure 4.6 shows an example of solution plots with marked source and receiver positions for $f = 50$ Hz. The solution plot the data was generated from, i.e., the solution to problem (4.34) using the reference values $Z_{\text{ref}}^{(1)} = 400 - 700i$ and $Z_{\text{ref}}^{(2)} = 500 + 800i$ in the left panel, looks very similar to the simulation with the estimated impedance value \hat{Z} in the right panel. The latter was chosen as the sample Z^i for which the likelihood θ_h was largest, i.e.,

$$\hat{Z} := \arg \max_{Z^i, i=1, \dots, N} \theta_h(Z^i, y).$$

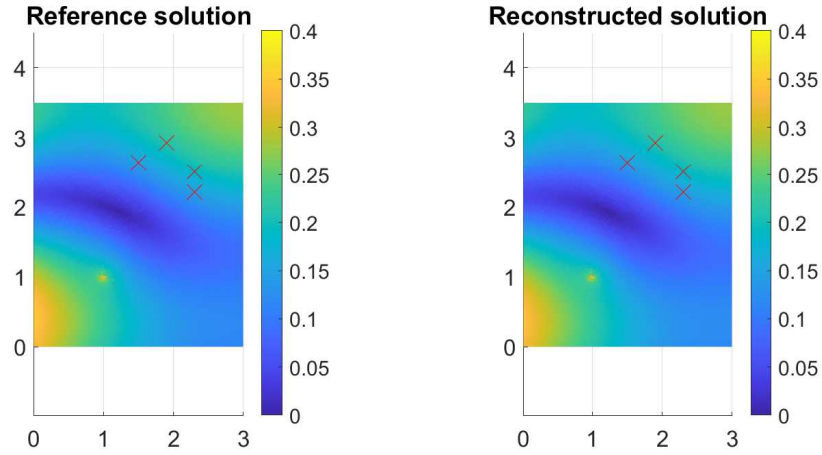


Figure 4.6: Absolute value of the reference solution with $Z_{\text{ref}}^{(1)} = 400 - 700i$ and $Z_{\text{ref}}^{(2)} = 500 + 800i$ (left) and the reconstructed solution with the most likely acoustic impedance value during the sampling process $Z^{(1)} \approx 427 - 697i$ and $Z^{(2)} \approx 583 + 860i$ (right) for $f = 50$ Hz. The source is located at $(1, 1)$. The red marks are the measurement positions.

4.5.4 3D problem with data from impedance problem

We again consider the model problem (4.34). However this time we consider a room in three dimensions with width 3 m, length 3.5 m and height 2.5 m, i.e., $\Omega := [0, 3] \times [0, 3.5] \times [0, 2.5] \subset \mathbb{R}^3$, $\Gamma_R^{(1)} = \{(x_1, x_2, x_3) \in \partial\Omega : x_1 = 0\}$, $\Gamma_R^{(2)} = \{(x_1, x_2, x_3) \in \partial\Omega : x_2 = 0\}$ and $\Gamma_N = \partial\Omega \setminus (\Gamma_R^{(1)} \cup \Gamma_R^{(2)})$, see Figure 4.7. Here $Z^{(1)} = 500 - 800i$ is assumed to be known and only moments of an unknown $Z^{(2)}$ are computed. The point source $f = \delta^s$ is located at $s = (1, 1, 1) \in \Omega_\kappa$. In the experiments the artificial measurements y are generated by

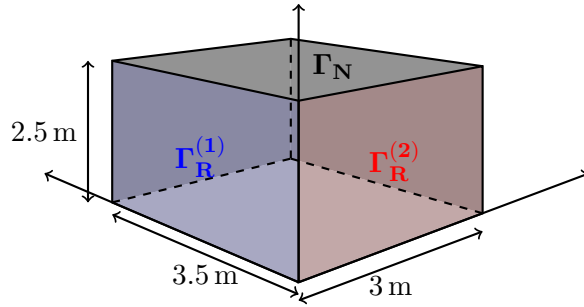


Figure 4.7: Domain for model problem in 3D.

solving problem (4.34) with $Z^{(2)} = Z_{\text{ref}} = 500 + 800i$, evaluating the solution at $m = 16$ measurement positions and adding noise, i.e., $y = \mathcal{G}(Z_{\text{ref}}) + \eta$, where $\eta \sim \mathcal{CN}(0, \Sigma, 0)$. Here Σ is a diagonal matrix with entries $\sigma_k^2 = \sigma_0^2$, $k = 1, \dots, 2m$. The variance of the

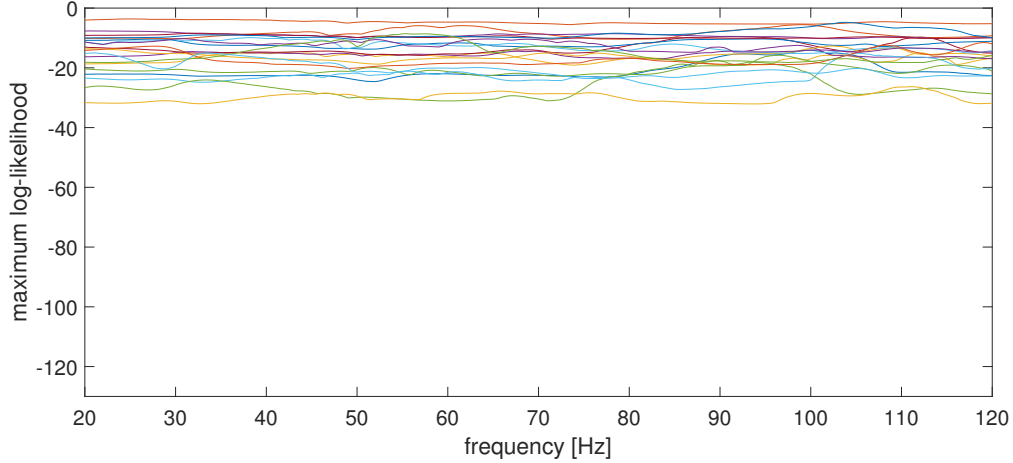


Figure 4.8: Maximum log-likelihood for the impedance problem. The thin lines correspond to the individual runs.

noise is given by $\sigma_0 = 0.02$. For each run m measurement positions are randomly placed in M_κ with $\kappa = \frac{1}{2}$, i.e., in contrast to the 2D experiments in the previous section, the receiver positions and noise change from run to run. This allows us to observe behavior that is not depending on specific measurement positions. The prior distribution is chosen as described in Section 4.5.2 with $\log Z_R^{(2)} \sim \mathcal{N}(4000, 10000^2)$ and $Z_I^{(2)} \sim \mathcal{N}(0, 30000^2)$. For frequencies from 20 Hz to 120 Hz in steps of 0.5 Hz we estimate the expected value

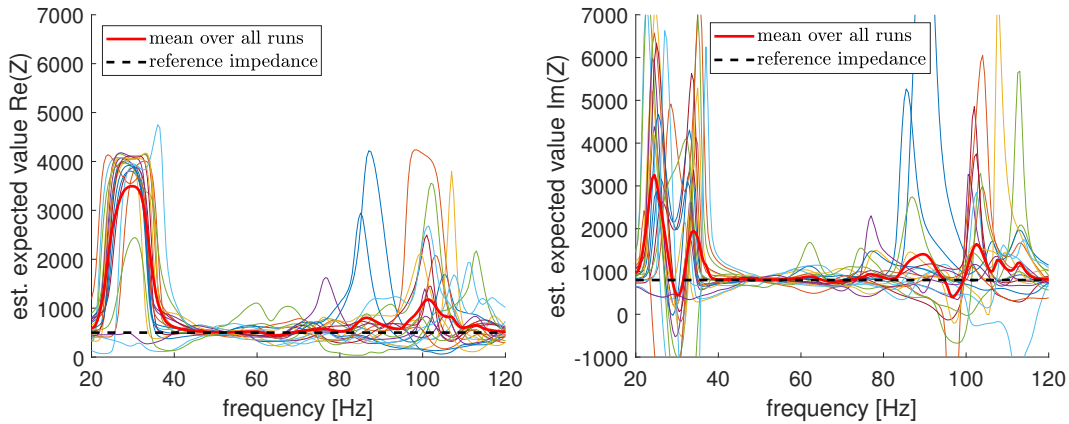


Figure 4.9: Estimated expected value (real part left, imaginary part right) of the impedance for the impedance problem for all 20 runs. The black dashed line indicates the reference impedance value. The red line is the mean over all runs. Thin lines correspond to individual runs.

and variance for the posterior of $Z_R^{(2)}$ and $Z_I^{(2)}$ in the same way as outlined above. Here we take $N = 2^{14}$ samples and choose the mesh width as $h = \min(\frac{c}{f}, 0.5)$. We

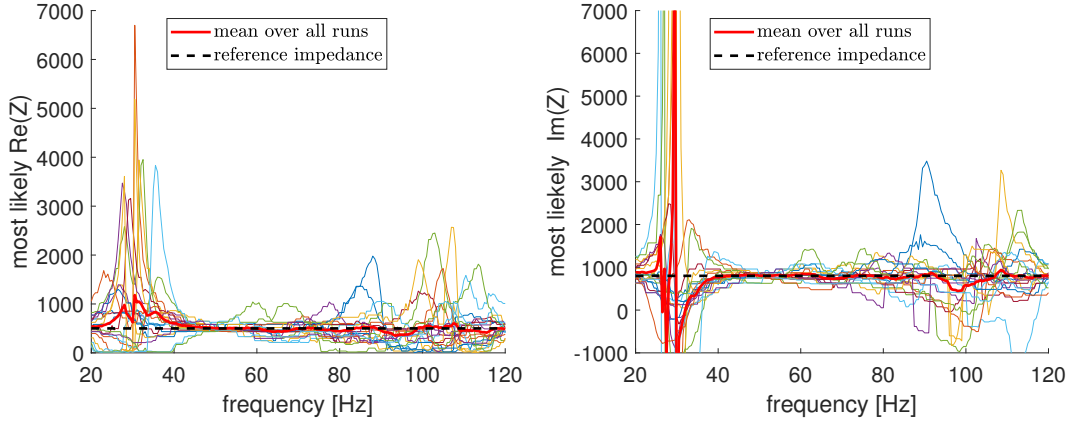


Figure 4.10: Most likely impedance (real part left, imaginary part right) for the impedance problem for all 20 runs. The black dashed line indicates the reference impedance value. The red line is the mean over all runs. Thin lines correspond to individual runs.

observe that parameters with high likelihoods are detected. In Figure 4.8 we show the maximum of the log-likelihood achieved from samples during the Monte Carlo sampling, i.e., $\max \theta_h(Z^i, y)$. The estimated expected values, i.e., $\widehat{\mathcal{M}}_y^1[Z_*^{(2)}]_{h,N}$, are close to the true underlying parameter values of $Z^{(2)}$ for most frequencies, see Figure 4.9. In the lower frequency range of 20 Hz to 40 Hz we observe rather large fluctuations around the reference value. In this frequency range the solution of (4.34) seems to be less dependent on the acoustic impedance $Z^{(2)}$ and hence impedance values $Z^{(2)}$ with large magnitude still lead to high likelihood values. The samples Z^i with largest likelihood, i.e.,

$$\widehat{Z} := \arg \max_{Z^i, i=1, \dots, N} \theta_h(Z^i, y),$$

the best fitting parameter-pairs, are visualized in Figure 4.10. For the low frequency range we observe that for some runs the impedance is estimated badly, however we see good approximation for most runs. The prior density π_0 together with the estimated posterior density $\widehat{\pi}^y$ given by the estimated parameters are visualized for two selected frequencies in Figure 4.11. The prior density looks flat, since its variance is large. The estimated posterior, however, has smaller variance and leads to a suitable estimate of the reference impedance.

4.5.5 3D problem with data from coupled acoustic-structural problem

In this section we again consider the 3D version of the problem (4.34) as before, but this time the data was generated in COMSOL MULTIPHYSICS by solving a coupled acoustic-structural problem, where instead of an impedance boundary condition at $\Gamma_R^{(2)}$ a model of a glass wall is considered. In particular, this means that this part of the boundary is not locally reacting.

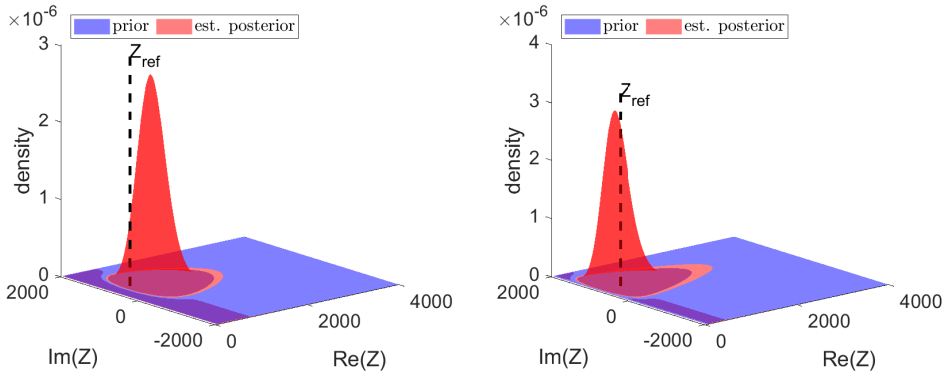


Figure 4.11: Prior density and density given by estimated expected value and standard deviation for $f = 25$ Hz (left) and $f = 95$ Hz (right).

The model to estimate moments of the posterior distribution remains the pure impedance problem as before. Hence the model used to approximate the data are different from the one that is used to generate the data, and thus, leads to a significant *model-data misfit*. In this section we investigate how well the data can be estimated by the locally reacting impedance model (4.29) and whether the inconsistency of the model and the data can be detected by the simulations. The remaining experimental setup including the domain, prior, noise, source position and microphone positions are the same as in Section 4.5.4. In fact, the same samples Z^i drawn in the previous subsection and the corresponding observations $\mathcal{G}_h(Z^i)$ can be recycled here again. Only the data y changes and hence only the likelihood θ_h has to be evaluated again to compute the approximate moments in (4.33).

Inspecting the maximum log-likelihood in the frequency range 20-120 Hz in Figure 4.13, we observe that for some frequencies its value gets very negative for *all* samples Z^i in each of the 20 runs. This is the consequence of the model-data misfit. Nevertheless for some frequency ranges the algorithm detects well fitting impedance values from the parametric model.

To further study this behavior we compute the eigenfrequencies for the coupled problem, the glass wall itself and the impedance problem (4.34) (with sound hard $\Gamma_R^{(2)}$, i.e., for $|Z^{(2)}| \rightarrow \infty$). The eigenfrequencies are shown in Figure 4.12. Notice, that for the glass wall the eigenfrequencies are real, but for the discretized coupled and impedance problem the eigenfrequencies are complex-valued with small imaginary part due to the boundary condition at $\Gamma_R^{(1)}$. Comparing the real part of the eigenfrequencies of the coupled problem with those from the glass wall itself we observe that their locations coincide quite well with only small shifts, in particular the real parts of eigenfrequencies of the impedance problem are only slightly smaller than the ones from the coupled problem. Comparing the eigenfrequencies with small imaginary part, i.e., those close to purely real frequencies, with the maximum likelihood, see Figure 4.13, we observe the follow-

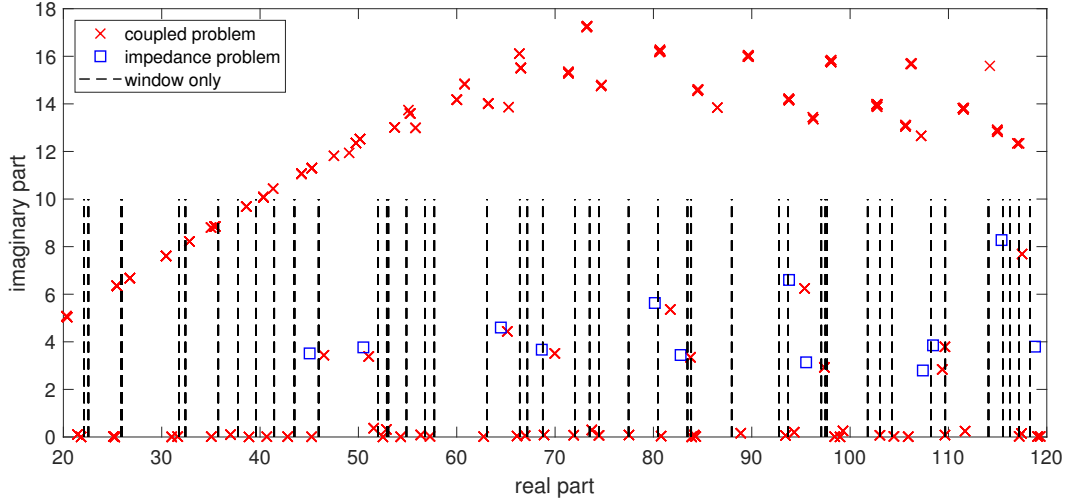


Figure 4.12: Eigenfrequencies of coupled problem, pure impedance problem (sound hard at $\Gamma_R^{(2)}$) and for the glass wall (window) decoupled from the room acoustics (boundary conditions were set to be free at the large front and back surfaces and fixed at the edges of the window).

ing: If the likelihood vanishes there are also eigenfrequencies nearby. If the frequency is far from any eigenfrequency the coupled problem behaves similar to the impedance problem. We also notice that for some eigenfrequencies the log-likelihood $\log \theta_h$ is still of a similar magnitude as in the case of Section 4.5.4. In Figures 4.14–4.16 we demonstrate the pressure (in dB) for different frequencies for the reference solution of the coupled problem (i.e., the solution from which the artificial data have been generated), and the solution of (4.34), where the value of the impedance $Z^{(2)}$ is the sample having the highest likelihood θ_h . To illustrate three typical types of behaviour over the frequency range 20–120 Hz we focus on the three representative values $f = 51.5$ Hz, $f = 54.5$ Hz and $f = 69$ Hz. As seen in Figure 4.13, these frequencies are close to the eigenfrequencies of the coupled problem. In general, we observe that for some eigenfrequencies the solution in the interior is much more affected by the behaviour of the glass wall than for others.

For $f = 51.5$ Hz a very low maximum log-likelihood was observed for all runs, see Figure 4.13. In the left panel of Figure 4.14 we can clearly see the eigenmodes at the glass wall and that the reference solution in the interior of the domain is affected by its behaviour. In contrast, the solution plot for the locally reacting impedance boundary condition for the likelihood maximizer does not show oscillations for this frequency value, see the right panel of Figure 4.14. Therefore, the simulation is not capable to fit the data and the model-data misfit can be clearly detected from the low values of the likelihood.

For $f = 54.5$ Hz we again observe the eigenmodes on the glass wall for the reference solution in the left panel of Figure 4.15. However this time the algorithm is able to determine impedance parameters that fit the data well and result in high values of the likelihood. A closer inspection of the reference solution and the likelihood maximizer in

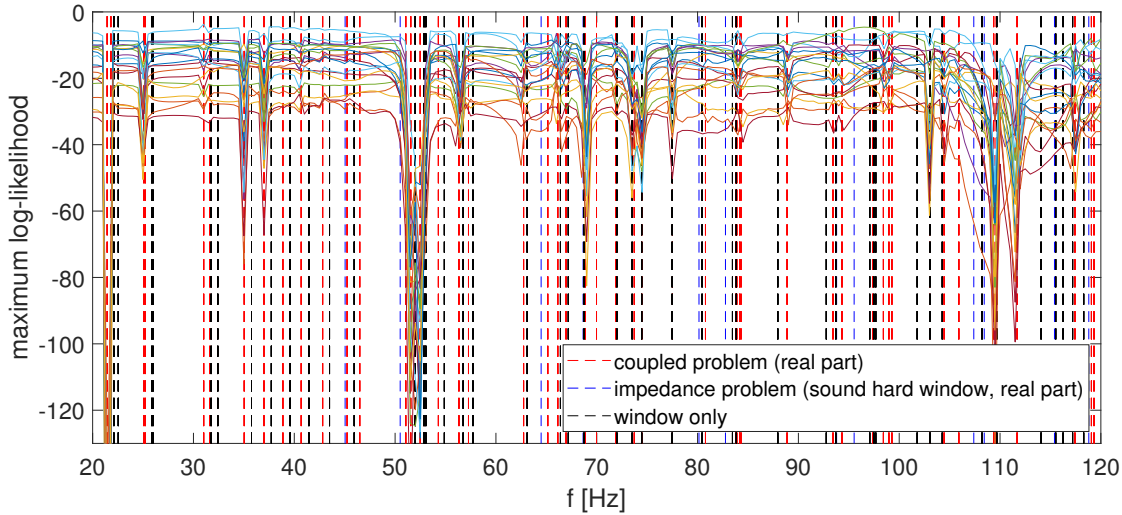


Figure 4.13: Maximum log-likelihood for the coupled problem with eigenfrequencies (real part). The thin lines correspond to the individual runs.

the left and right panels of Figure 4.15 show the similar structure in the interior of the domain, whereas the boundary behaviour is quite different. Here, the glass wall eigenmode is quite localized near the boundary, so that the oscillations cannot be detected by the microphones located in the interior of the domain. In this case, the algorithm does not detect the model-data misfit.

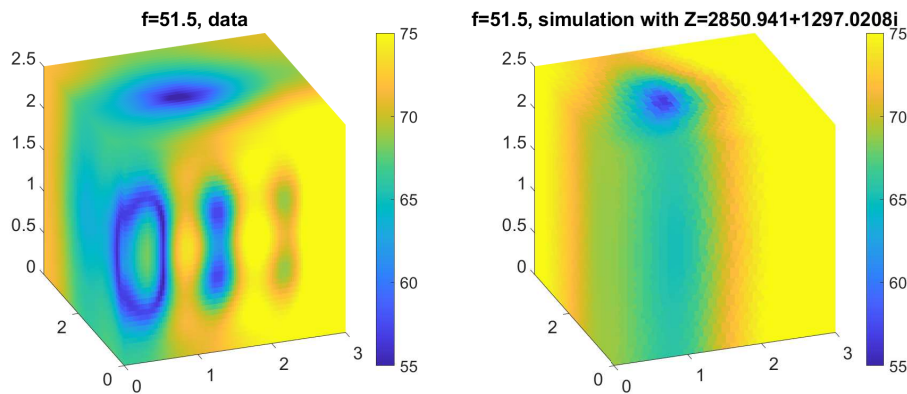


Figure 4.14: The reference solution that produces artificial measurement data (left) and the likelihood maximizer computed by the algorithm (right) in dB (re $20 \mu\text{Pa}$) for $f = 51.5$ Hz.

In contrast to the two typical cases discussed above, the frequency $f = 69$ Hz exhibits an intermediate behaviour, see Figure 4.16. The eigenmode of the glass wall is again quite localized near the boundary. The algorithm, however, fails to identify the impedance parameter with the same likelihood as for $f = 54.5$ Hz. In Figure 4.13 we see, however,

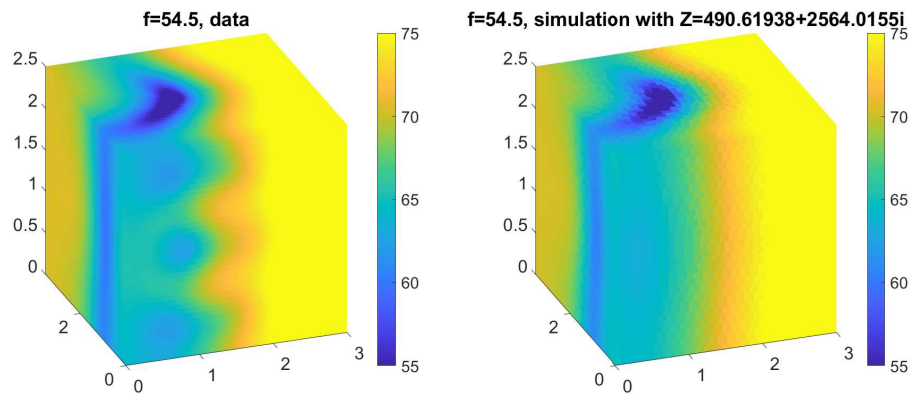


Figure 4.15: The reference solution that produces artificial measurement data (left) and the likelihood maximizer computed by the algorithm (right) in dB (re $20 \mu\text{Pa}$) for $f = 54.5$ Hz.

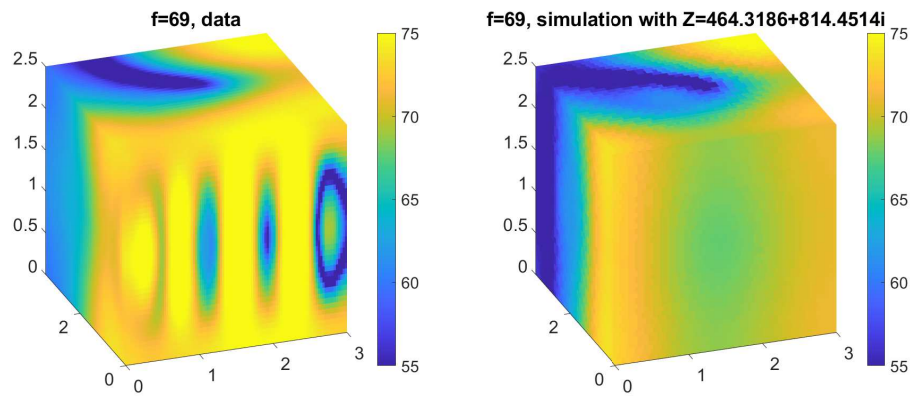


Figure 4.16: The reference solution that produces artificial measurement data (left) and the likelihood maximizer computed by the algorithm (right) in dB (re $20 \mu\text{Pa}$) for $f = 69$ Hz.

that the likelihood drop is not so dramatic as around $f = 51.5$ Hz. As a consequence, we can see clear differences in the solution close to $\Gamma^{(2)}$, but a more similar qualitative (but not quantitative!) behaviour for parts away from this part of the boundary.

4.6 On the Markov-Chain Monte Carlo method

In the preceding sections, we sampled from the prior distribution ν_0 and computed the likelihood θ . By multiplying these two, we obtained values of the posterior (up to a constant). However, direct sampling from the posterior distribution was not possible. A class of methods, namely the Metropolis-Hastings (MH) Markov-Chain Monte Carlo (MCMC) methods can overcome this problem and allow direct sampling from the posterior [77, 55, 38]. For this, a new sample Z_p is drawn relative to the last sample $Z^{(n)}$, where $Z^{(n)}$ is the n -th sample, using a random step. This is done by a proposal distribution q . It is often chosen as $q \sim \mathcal{N}(Z^{(n)}, \chi^2)$. This is why we choose q such that $\text{Re}(Z_p) \sim \mathcal{N}(\text{Re}(Z_p), \chi^2)$ and $\text{Im}(Z_p) \sim \mathcal{N}(\text{Im}(Z_p), \chi^2)$. The (non-normalized) posterior of the proposal sample Z_p , i.e., $\pi^y(Z_p) \sim \theta(Z_p, y)\pi_0(Z_p)$, and the last sample $Z^{(n)}$, i.e., $\pi^y(Z^{(n)}) \sim \theta(Z^{(n)}, y)\pi_0(Z^{(n)})$, are compared by computing the ratio $r = \min\left(\frac{\pi^y(Z_p)q(Z_p|Z^{(n)})}{\pi^y(Z^{(n)})q(Z^{(n)}|Z_p)}, 1\right)$, and the new sample is either accepted or rejected based on the value of r and a uniformly distributed random variable $u \sim \mathcal{U}[0, 1]$, see also Algorithm 2. Due to the symmetry of the normal distribution we have $q(Z_p|Z^{(n)}) = q(Z^{(n)}|Z_p)$ [88]. Hence the ratio r reduces to $r = \min\left(\frac{\pi^y(Z_p)}{\pi^y(Z^{(n)})}, 1\right)$.

Result: Samples from the posterior distribution
Input : maximum number of iterations N ,
initial sample $Z^{(0)} \in \mathbb{C}$,
standard deviation χ of proposal distribution
Output: N samples

```

1 for  $n=0:N-1$  do
2   Draw sample  $Z_p$  from the proposal distribution  $q(Z_p|Z^{(n)})$ 
3   compute ratio  $r = \min\left(\frac{\pi^y(Z_p)q(Z_p|Z^{(n)})}{\pi^y(Z^{(n)})q(Z^{(n)}|Z_p)}, 1\right)$ ;
4   draw  $u \in [0, 1]$  from uniform distribution
5   if  $r \geq u$  then
6     |  $Z^{(n+1)} = Z_p$ 
7   else
8     |  $Z^{(n+1)} = Z^{(n)}$ 
9   end
10 end

```

Algorithm 2: Metropolis-Hastings algorithm, based on [88].

At the first glance, this method seems to be superior to the ratio estimators discussed earlier, since we can directly sample from the posterior and hence can also compute its moments. Thus, we are not in need a low-parametric posterior density estimation as proposed in the previous sections, but can directly sample from the posterior if needed

for other problems. However, there are also some drawbacks. First, Metropolis-Hastings does not allow for *parallel* sampling, because every sample is dependent on the previous sample. Second, if we want to compute likelihoods or moments for different number or location of observations, in the ratio estimator setting we could have just stored the observation at different locations and compute the likelihood and the moments afterwards using an arbitrary subset of these observations. In the Metropolis-Hastings algorithm the positions and number of the observations directly influence the next sample. Hence for each scenario we would have to redo the entire sampling process.

While these limitations may not be crucial for all applications, we computed likelihoods for twenty different runs, i.e., different microphone positions and noise realizations in this chapter. For these runs we only had to solve the three-dimensional problem once per sample and could reuse it in the other runs. For Metropolis-Hastings this would not be possible and the sampling process would need to be repeated for each variation.

We consider four different cases to compare ratio estimators and the Metropolis-Hastings algorithm for different values of χ and starting samples $Z^{(0)}$ (in the following Z does correspond to $Z^{(2)}$ in Section 4.5.4, to not be confused with the Metropolis-Hastings samples):

Case 1: Impedance data with $Z = 500 + 800i$, $f = 50$ Hz; this is the same impedance assumed as in the experiments above.

Case 2: Impedance data with $Z = 5000 + 8000i$, $f = 50$ Hz; the higher modulus models a wall that is nearly sound hard.

Case 3: Data from coupled problem, $f = 44.5$ Hz; this corresponds to a case with rather high likelihood.

Case 4: Data from coupled problem, $f = 52.5$ Hz; this corresponds to a case where the model-misfit is apparent.

Often the step size is initially chosen as $\chi = \chi_0 := \frac{2.38}{\sqrt{n_p}}$ if the posterior is depending on n_p variables [48]. However, in this application we noticed, that the step size is too small to really explore the posterior. For all cases we observe the data at $M = 16$ positions, assume the standard deviation of the noise to be $\sigma_0 = 0.02$ and use the same prior as in Section 4.5.4.

Tables 4.1 and 4.2 show the estimated expectation and variance using ratio estimators, i.e., $\mu_R^{(RE)}$, $\mu_I^{(RE)}$, $\gamma_R^{(RE)2}$ and $\gamma_I^{(RE)2}$, and Metropolis-Hastings algorithm, i.e., $\mu_R^{(MH)}$, $\mu_I^{(MH)}$, $\gamma_R^{(MH)2}$ and $\gamma_I^{(MH)2}$, for different χ and starting samples $Z^{(0)}$. The true moments $\mu_R^{(post)}$, $\mu_I^{(post)}$, $\gamma_R^{(post)2}$ and $\gamma_I^{(post)2}$ are computed by first identifying where the posterior function is significantly larger than zero and then computing the respective integral over that area numerically using a deterministic quadrature. When the starting sample is poorly chosen and χ is small then sometimes the Metropolis-Hastings algorithm has a long burn-in phase. Due to this, in some sampling processes, we changed

χ	case	$Z^{(0)}$	$\mu_R^{(RE)}$	$\mu_I^{(RE)}$	$\mu_R^{(MH)}$	$\mu_I^{(MH)}$	$\mu_R^{(post)}$	$\mu_I^{(post)}$
$\chi_0 \times 1000$	1	100+1i	595.0	778.2	4347.3	1224.0	547.5	774.1
$\chi_0 \times 100$		100+1i			689.7	797.8		
$\chi_0 \times 100$		500+800i			690.7	811.9		
$\chi_0 \times 10$		500+800i			550.4	776.5		
χ_0		500+800i			549.9	780.4		
$\chi_0 \times 1000$	2	100+1i	4081.0	16610	5655.7	18195	3974.6	16297
$\chi_0 \times 100$		100+1i			4124.3	16116		
$\chi_0 \times 100$		5000+8000i			3704.2	16543.7		
$\chi_0 \times 10$		5000+8000i			5631.7	10961		
χ_0		5000+8000i			5093.1	8242.9		
$\chi_0 \times 1000$	3	100+1i	387.2	3256.5	4365	4784.1	419.4	3247.1
$\chi_0 \times 100$		100+1i			504.2	3274.3		
$\chi_0 \times 100$		400+3000i			508.2	3305.4		
$\chi_0 \times 10$		400+3000i			423.3	3262.4		
χ_0		400+3000i			455.5	3247.5		
$\chi_0 \times 1000$	4	100+1i	1370.1	-750.3	5022.6	-2227.9	1430.5	-742.2
$\chi_0 \times 100$		100+1i			1480.0	-753.2		
$\chi_0 \times 100$		1500-600i			1490.5	-771.8		
$\chi_0 \times 10$		1500-600i			1429.7	-711.8		
χ_0		1500-600i			1475.6	-555.9		

Table 4.1: Estimated expectation for various the Cases 1-4 for different χ and starting sample $Z^{(0)}$ (in $\frac{Pa \cdot s}{m^3}$).

the initial sample to one that is close to the maximum of the respective posterior. In case of large χ the estimated expectations are not very accurate. This is due to the fact, that only few samples will be in the area where the posterior is large. This should, however, improve with larger sample size. This is a similar behavior as for the Monte Carlo sampling for the ratio estimators in the case of a prior with large variance. For Case 2 we observe that the result for the expectation is at least at a comparable magnitude as $\mu_R^{(post)}$ or $\mu_I^{(post)}$. This is due to the large variance that the posterior in this case has, see the corresponding picture in Figure 4.17. On the other hand $\mu_I^{(MH)}$ is significantly underestimated for this case if χ is small. For most configurations, however, the expectations are reliably estimated and comparable with the results from the ratio estimators. We can conclude that different values of χ are better suited for different cases.

The variance estimation shows more variability. For large χ the variance is generally overestimated a lot by the Metropolis-Hastings algorithm. However, if χ is too small than the variance will be underestimated. The results are only comparable to the ones we get from the ratio estimators if χ is chosen well, which is case-dependent. Finding an optimal χ is in the need of tuning or adapting χ during the algorithm, see, e.g., [53]. Figure 4.17 illustrates the samples drawn during the Metropolis-Hastings algorithm for the different configurations with the exception of the optimized starting value $Z^{(0)}$

χ	case	$Z^{(0)}$	$\gamma_R^{(RE)2}$	$\gamma_I^{(RE)2}$	$\gamma_R^{(MH)2}$	$\gamma_I^{(MH)2}$	$\gamma_R^{(post)2}$	$\gamma_I^{(post)2}$
$\chi_0 \times 1000$	1	100+1i	6.91e2	2.58e3	1.01e7	1.13e7	5.24e2	5.22e2
$\chi_0 \times 100$		100+1i			1.09e5	1.12e5		
$\chi_0 \times 100$		500+800i			1.11e5	1.14e5		
$\chi_0 \times 10$		500+800i			1.38e3	1.25e3		
χ_0		500+800i			3.89e2	3.78e2		
$\chi_0 \times 1000$	2	100+1i	1.14e7	2.85e7	2.25e7	6.07e7	9.05e6	2.13e7
$\chi_0 \times 100$		100+1i			7.89e6	1.57e7		
$\chi_0 \times 100$		5000+8000i			5.19e6	1.10e7		
$\chi_0 \times 10$		5000+8000i			2.87e5	1.72e6		
χ_0		5000+8000i			5.53e3	1.37e4		
$\chi_0 \times 1000$	3	100+1i	1.90e4	9.34e3	2.12e7	1.96e7	1.15e4	1.32e4
$\chi_0 \times 100$		100+1i			8.17e4	1.64e5		
$\chi_0 \times 100$		400+3000i			8.58e4	1.14e5		
$\chi_0 \times 10$		400+3000i			1.43e4	1.17e4		
χ_0		400+3000i			1.83e3	9.09e3		
$\chi_0 \times 1000$	4	100+1i	1.04e4	1.46e4	2.03e7	1.70e7	1.47e4	2.08e4
$\chi_0 \times 100$		100+1i			1.25e5	1.31e5		
$\chi_0 \times 100$		1500-600i			1.23e5	1.17e5		
$\chi_0 \times 10$		1500-600i			1.46e4	1.49e4		
χ_0		1500-600i			6.29e2	1.53e3		

Table 4.2: Estimated variance for various the Cases 1-4 for different χ and starting sample $Z^{(0)}$ (in $\frac{Pa \cdot s}{m^3}$).

and $\chi = \chi_0 \times 100$. This configuration essentially results in the same picture as with $Z^{(0)} = 100 + 1i$, but without the burn-in phase. We observe that large χ leads to many samples with very low posterior values, while small χ might (as in Cases 2-4) fail to fully explore the posterior. Therefore, further sampling would not be representative for the true posterior (only for very large sample size), since it would be biased to one side of the peak. Comparison with the true (discrete) posterior, i.e., $\pi_h^y(Z) \sim \pi_0(Z)\theta_h(Z)$ and the estimated posterior density $\hat{\pi}^y$ constructed from the ratio estimators, see Figure 4.18, shows that the estimated posteriors are reasonable approximations of the true posterior and could be used for further uncertainty quantification.

In conclusion, the (plain) Metropolis-Hastings is a viable alternative to the ratio estimators if χ is chosen well. This, however, requires some expert knowledge or trial phase, which we also did not assume for the ratio estimators. For example, both methods would lead to better approximations with less samples for a prior that is more focused on one particular area. For the purpose of the previous sections, we intentionally chose a prior with large variance to avoid bias. Further, the computational cost of Metropolis-Hastings will be significantly larger when computing moments for different positions and number of measurements as well as for different data and noise realizations. In such cases, the ratio estimator framework is superior in terms of reusability of samples. The

largest advantage of the Metropolis-Hastings algorithm lies in the fact that it can actually sample from the true posterior (if parameters were chosen correctly). Depending on the actual application the accuracy of the posterior or the computational cost might be more important or feasible. Therefore the method needs to be chosen based on the considered application.

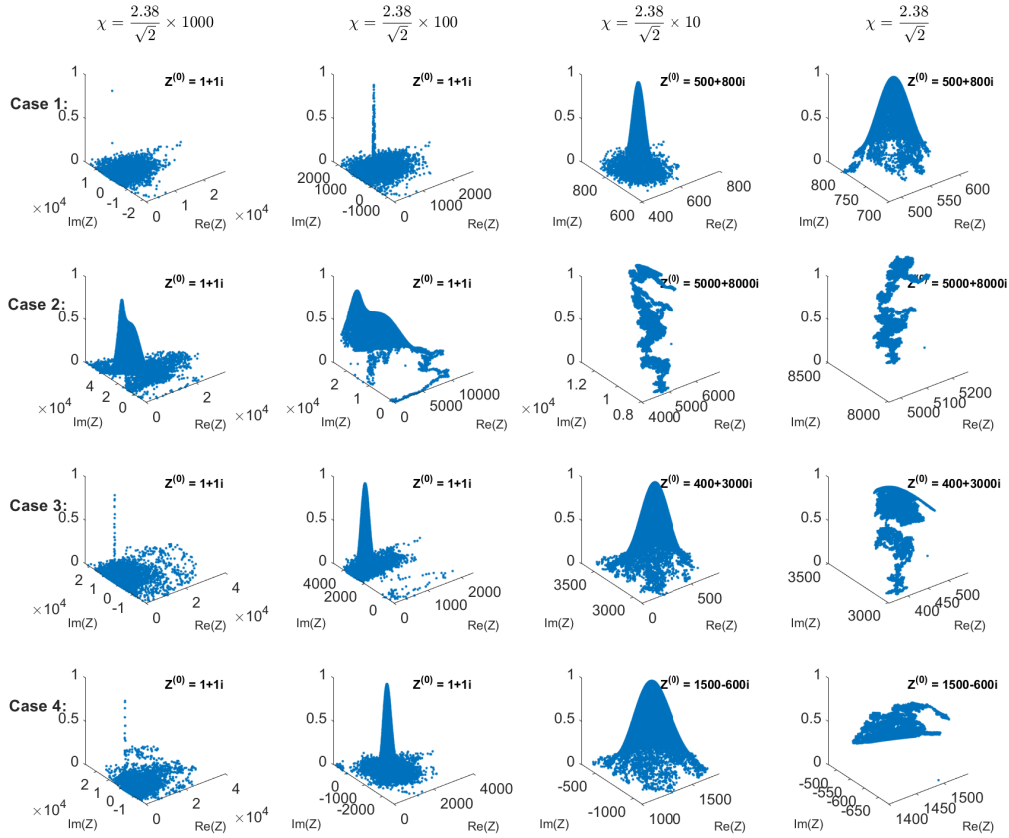


Figure 4.17: Samples drawn during the Metropolis-Hastings algorithm for Cases 1-4 with different starting samples $Z^{(0)}$ and χ . The height of the points coincide with the computed posterior $\theta(Z, y)\pi_0(Z)$. The posterior is scaled such that the maximum is 1.

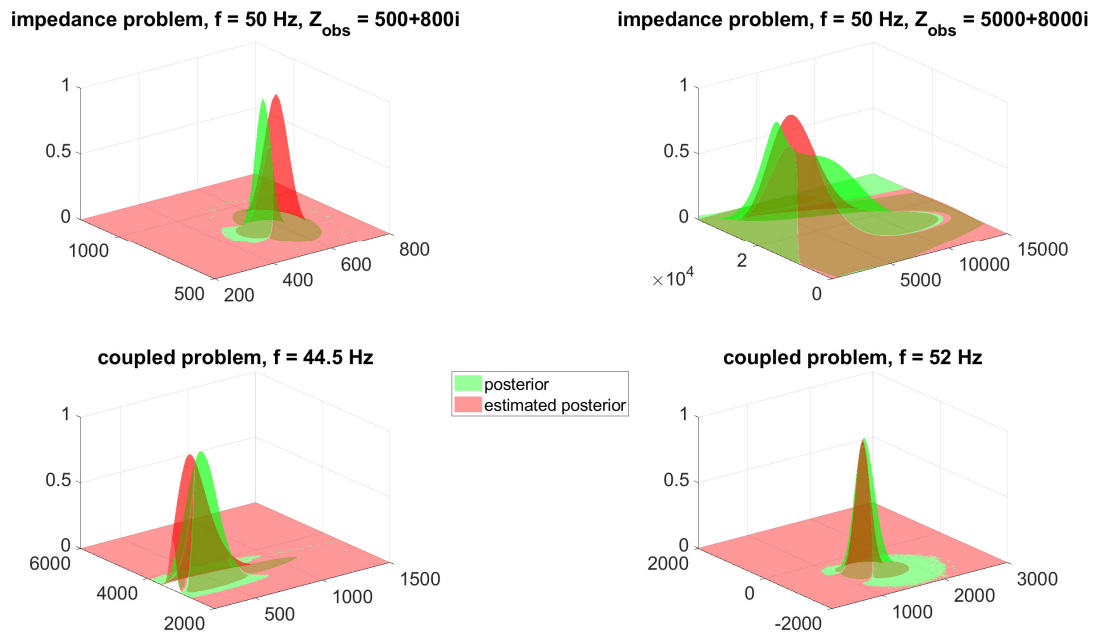


Figure 4.18: True and estimated posterior for the different Cases 1-4, scaled such that the maximum value is 1.

4.7 Outlook

From this point a lot of other extensions are possible. For once, estimating higher moments for the posterior density and computing parametric density functions with those is a way to include properties like skewness in the resulting function.

Another possible extension is to replace the scalar-valued parametric impedance boundary condition by a more general parametric model, e.g., represented by a Karhunen–Loève expansion, or a non-local boundary condition. In this case a lot more parameters would need to be estimated, depending on the goal.

Another thread is the analysis of further intelligent sampling methods like multilevel Monte Carlo or Quasi Monte Carlo (as done in [98] for the elliptic problem), advanced Markov Chain / sequential Monte Carlo method (as done in [40] for uncertainty in the right hand side of the Helmholtz equation) or even Multilevel Markov Chain Monte Carlo Algorithms [37, 72].

Chapter 5

Shape optimization for low-frequency time-harmonic problems under uncertain source location

Shape and topology optimization are fields of classical but also on-going research in particular for engineering applications. For example, a common objective is to design structures with certain properties while minimizing material usage. In shape optimization the goal is to optimize the geometry of some structure to minimize a potential goal functional. On top of that topology optimization also allows change in the topology, such as different numbers of holes. For an overview on current methods and applications we refer to [4, 10]. In this chapter we restrict the research on shape optimization.

Often in shape optimization problems the problem is related to partial differential equations (PDEs) and such the shape optimization relies on solving these equations. In this case shape optimization is used together with a PDE solving method like finite elements.

Due to the rising interest in uncertainty quantification and also the advancements in computational technology, that make elaborate computations possible, shape optimization is nowadays often considered including random inputs or constraints, see e.g., [3, 29, 46].

In this chapter we consider again an interior time-harmonic wave propagation problem, in particular we consider shape optimization with a partial differential equation constraint which is the Helmholtz equation in two dimensions. Let $\Omega \subset \mathbb{R}^2$ be a Lipschitz domain with $\partial\Omega = \overline{\Gamma_N} \cup \overline{\Gamma_R}$ with $|\Gamma_R| \neq \emptyset$. The aim is to minimize a goal functional

$$J(\Omega) = \int_{\Omega} j(p) dx \quad (5.1)$$

under the constrained that p solves the following problem:

$$\begin{aligned} -\Delta p - cp &= f && \text{in } \Omega \\ \frac{\partial p}{\partial n} &= 0 && \text{on } \Gamma_N \\ \frac{\partial p}{\partial n} + i\alpha p &= 0 && \text{on } \Gamma_R \end{aligned} \quad (5.2)$$

For $c > 0$ this leads to the Helmholtz problem discussed in several chapters before. For $c = 0$ this is the inhomogeneous diffusion problem and for $c < 0$ we arrive at the

reaction-convection problem. We assume that $c \in \mathbb{R}$ and $\alpha \in \mathbb{C}$ with $\operatorname{Re}(\alpha) \neq 0$ and the support of $f \in L^2(\Omega)$ lies strictly in Ω .

The following sections are structured as follows: In Section 5.1 we revisit basic concepts of (deterministic) PDE-constrained shape optimization. In Section 5.2 we compute the shape gradients related to the problem (5.1). Sections 5.3 and 5.4 deal with concrete numerical examples. In Section 5.3 we do shape optimization for the deterministic setting while in Section 5.4 we introduce randomness in the source location and define and study expectation domains and domain deviation for this problem.

5.1 Basic concepts of PDE-constrained shape optimization

The aim of shape optimization is to transform the domain Ω such that a shape functional $J(\Omega, u)$ is minimized. As transformation we define the map

$$T_t(V) : \mathbb{R}^2 \rightarrow \mathbb{R}^2.$$

We assume that T_t is defined by a small perturbation $\theta \in C^{0,1}(\overline{\mathbb{R}^2}, \mathbb{R}^2)$, i.e., Lipschitz continuous, in the sense that it can be written as $T_t(x) = x + t\theta(x)$. To this perturbation we can associate [35, Ch. 2, Ch. 9] a vector field $V \in (C^0([0, \tau]); C^1(\mathbb{R}^2, \mathbb{R}^2))$, i.e., continuous in t and differentiable in space, such that $\frac{dT_t(V)}{dt} = V(t) \circ T_t(V)$ and $T_0(V) = I$. We define perturbations of the domain Ω as $\Omega_t := T_t(V)(\Omega)$.

In optimization we often make use of gradients of the goal functional with respect to the free parameters. Here, these parameters are associated with the geometry/shape of the domain and hence we want to use the so-called *shape derivatives*.

Definition 5.1 (Eulerian derivative, [102, Definition 2.19]). *For a vector field $V \in (C^0([0, \tau]); C^1(\mathbb{R}^2, \mathbb{R}^2))$ the Eulerian derivative of J at Ω in the direction of V is defined as*

$$dJ(\Omega; V) = \lim_{t \rightarrow 0} \frac{J(\Omega_t) - J(\Omega)}{t}. \quad (5.3)$$

Definition 5.2 (Shape differentiability, [102, Definition 2.20]). *The functional $J(\Omega)$ is shape differentiable at Ω if*

- (i) *there exists the Eulerian derivative $dJ(\Omega; V)$ for all directions V ,*
- (ii) *the mapping $V \rightarrow dJ(\Omega; V)$ is linear and continuous from $(C^0([0, \tau]); C^1(\mathbb{R}^2, \mathbb{R}^2))$ into \mathbb{R} .*

The following lemma computes the Eulerian derivative for $J(\Omega)$ being the integral of the characteristic function of Ω .

Lemma 5.3. *Let*

$$J(\Omega_t) = \int_{\Omega_t} dx.$$

Then

$$dJ(\Omega_t) = \int_{\Omega} \operatorname{div} V(0) dx.$$

Proof. Change of variables with $x = T_t(x)$ leads to

$$J(\Omega_t) = \int_{\Omega_t} dx = \int_{\Omega} |\det DT_t(x)| dx = \int_{\Omega} \det DT_t(x) dx,$$

since $\det DT_t(x) > 0$ for small $t \geq 0$, because $\det(DT_0(x)) = 1$. Using Jacobi's formula [73] we can compute the derivative of $\det DT_t(x)$ in t :

$$\begin{aligned} \left. \frac{d}{dt} \det DT_t(x) \right|_{t=0} &= \det(DT_t(x)) \operatorname{tr} \left(DT_t(x)^{-1} \frac{dDT_t(x)}{dt} \right) \Big|_{t=0} \\ &= \det(DT_t(x)) \operatorname{tr} (DT_t(x)^{-1} DV(t, T_t(x))) \Big|_{t=0} \\ &= \operatorname{div} V(0, x). \end{aligned}$$

Hence

$$\begin{aligned} dJ(\Omega; V) &= \lim_{t \rightarrow 0} \frac{J(\Omega_t) - J(\Omega)}{t} \\ &= \lim_{t \rightarrow 0} \frac{1}{t} \left(\int_{\Omega_t} dx - \int_{\Omega} dx \right) \\ &= \lim_{t \rightarrow 0} \frac{1}{t} \left(\int_{\Omega} \det DT_t(x) - 1 dx \right) \\ &= \int_{\Omega} \lim_{t \rightarrow 0} \frac{\det DT_t(x) - \det DT_0(x)}{t} dx \\ &= \int_{\Omega} \operatorname{div} V(0, x) dx. \end{aligned}$$

□

To deal with the upcoming boundary integrals we need the following lemma dealing with the integral transformation on the boundary.

Lemma 5.4 ([102, Proposition 2.47, Lemma 2.49]). *Let $f \in L^1(\Gamma_t)$ and $\omega_t = \|\det(DT_t)DT_t^{-\top} \cdot n\|_2$. Then*

$$\int_{\Gamma_t} f(s) ds = \int_{\Gamma} (f \circ T_t)(s) \omega_t(s) ds.$$

The derivative of ω with respect to t in $t = 0$ is given by

$$\left. \frac{d}{dt} \omega_t(s) \right|_{t=0} = \operatorname{div} V(0, s) - (DV(0, s)n) \cdot n.$$

5.2 Computation of shape gradients

As we will see in Proposition 5.7 we need the derivative of the solution p_{Ω_t} of problem (5.2) (on Ω_t instead of Ω) with respect to t . This is the notion of the *material derivative*.

Definition 5.5 (Material derivative, [102, Definition 2.71]). *The material derivative of $p \in H^s(\Omega)$ is $\mathring{p}_\Omega(V) \in H^s(\Omega)$ defined by*

$$\mathring{p}_\Omega(V) = \lim_{t \rightarrow 0} \frac{1}{t} (p_{\Omega_t} \circ T_t(V) - p_\Omega).$$

Using the material derivative we can motivate the shape derivative. Consider the shape functional $J(\Omega) = \int_\Omega p_\Omega dx$. Then

$$\begin{aligned} dJ(\Omega; V) &= \lim_{t \rightarrow 0} \frac{J(\Omega_t) - J(\Omega)}{t} \\ &= \lim_{t \rightarrow 0} \frac{1}{t} \left(\int_{\Omega_t} p_{\Omega_t} dx - \int_\Omega p_\Omega dx \right) \\ &= \lim_{t \rightarrow 0} \frac{1}{t} \left(\int_\Omega [p_{\Omega_t} \circ T_t](x) \det DT_t(x) dx - \int_\Omega p_\Omega \det DT_0(x) dx \right) \\ &= \int_\Omega \frac{d}{dt} ([p_{\Omega_t} \circ T_t](x) \det DT_t(x)) \Big|_{t=0} dx \\ &= \int_\Omega \underbrace{p'_\Omega(x) + \nabla p_\Omega(x)^\top V(0, x)}_{=\mathring{p}_\Omega(x)} + p_\Omega(x) \operatorname{div} V(0, x) dx, \end{aligned}$$

where in the last step the product and chain rule were used and p'_Ω is the shape derivative defined in the following:

Definition 5.6 (Shape derivative, [102, Definition 2.85]). *Let $\mathring{p}_\Omega(V) \in H^s(\Omega)$ be the material derivative to $p_\Omega \in H^s(\Omega)$ and $\nabla p_\Omega \cdot V(0) \in H^s(\Omega)$. Then the shape derivative of p_Ω in the direction V is defined by*

$$p'_\Omega(V) := \mathring{p}_\Omega(V) - \nabla p_\Omega \cdot V(0).$$

Taking test and trial functions from $H^1(\Omega)$ we can formulate the weak formulation of problem (5.2): Find $p \in H^1(\Omega)$ such that

$$\int_\Omega \nabla p \cdot \nabla \bar{q} dx - c \int_\Omega p \bar{q} dx + i\alpha \int_{\Gamma_R} p \bar{q} ds = \int_\Omega f \bar{q} dx \quad \forall q \in H^1(\Omega). \quad (5.4)$$

This problem has a unique solution as discussed in Chapter 2. If $c < 0$ the problem is even $H^1(\Omega)$ -elliptic.

The aim is to optimize the shape such that the goal functional

$$J(\Omega) = \int_\Omega j(p) dx \quad (5.5)$$

is minimized under the constraint that problem (5.2), or more precisely (5.4), is fulfilled. To do this we want to use a gradient descent algorithm. For this we need the derivatives of the goal functional with respect to the shape parameters t . Hence, the Eulerian

derivatives of problem (5.1) need to be computed. In Proposition 5.7 and in Proposition 5.8 we further derive the shape derivative in terms of boundary integral expressions only. The statements of Proposition 5.7 and 5.8 can be found in a similar way in [86], however the proof given here varies.

Proposition 5.7. *Let Ω be Lipschitz. The Eulerian derivative of the shape functional (5.1) constrained to (5.4) can be written as*

$$\begin{aligned} dJ(\Omega) &= \int_{\Omega} \left[\operatorname{div}V(0) - DV(0)^\top - DV(0) \right] \nabla p_{\Omega} \cdot \nabla u \, dx - c \int_{\Omega} p_{\Omega} u \operatorname{div}V(0) \, dx \\ &+ i\alpha \int_{\Gamma} p_{\Omega} u [\operatorname{div}V(0) - DV(0)n \cdot n] \, ds - \int_{\Omega} \nabla f^\top V(0) u \, dx \\ &- \int_{\Omega} f \operatorname{div}V(0) u \, dx + \int_{\Omega} j(p_{\Omega}) \operatorname{div}V(0) \, dx, \end{aligned} \quad (5.6)$$

where $u \in H^1(\Omega)$ is the adjoint solution to p_{Ω} defined through the weak formulation of

$$\begin{aligned} -\Delta u - cu &= -j'(p_{\Omega}) && \text{in } \Omega, \\ \frac{\partial u}{\partial n} + i\alpha u &= 0 && \text{on } \Gamma_R, \\ \frac{\partial u}{\partial n} &= 0 && \text{on } \Gamma_N. \end{aligned}$$

Proof. Consider $J(\Omega)$ on a parameterized domain Ω_t given by

$$J(\Omega_t) = \int_{\Omega_t} j(p_{\Omega_t}) \, dx = \int_{\Omega} j(p_{\Omega_t} \circ T_t) \det DT_t \, dx,$$

where p_{Ω_t} is the solution of (5.4) with Ω_t instead of Ω , Γ_N and Γ_R respectively. By the product rule, the Eulerian derivative is then given by

$$dJ(\Omega) = \lim_{t \rightarrow 0} \frac{J(\Omega_t) - J(\Omega)}{t} = \int_{\Omega} j'(p_{\Omega}) \dot{p}_{\Omega} \, dx + \int_{\Omega} j(p_{\Omega}) \operatorname{div}V(0) \, dx. \quad (5.7)$$

To compute the first term we need to be able to compute the material derivative \dot{p}_{Ω} . For this, consider the weak formulation (5.4), but on the transformed domain Ω_t . It reads: Find $p_{\Omega_t} \in H^1(\Omega_t)$ such that

$$\int_{\Omega_t} \nabla p_{\Omega_t} \cdot \nabla \bar{q} \, dx - c \int_{\Omega_t} p_{\Omega_t} \bar{q} \, dx + i\alpha \int_{\Gamma_{R,t}} p_{\Omega_t} \bar{q} \, ds = \int_{\Omega_t} f \bar{q} \, dx$$

for all $q \in H^1(\Omega_t)$. Transforming the integrals to Ω , see Lemma 5.4 for the boundary integral, leads to

$$\begin{aligned} &\int_{\Omega} \nabla (p_{\Omega_t} \circ T_t) DT_t^{-1} DT_t^{-\top} \nabla (\bar{q} \circ T_t) \det DT_t \, dx \\ &- c \int_{\Omega} (p_{\Omega_t} \circ T_t) (\bar{q} \circ T_t) \det DT_t \, dx + i\alpha \int_{\Gamma_R} (p_{\Omega_t} \circ T_t) (\bar{q} \circ T_t) \omega_t \, ds \\ &= \int_{\Omega} (f \circ T_t) (\bar{q} \circ T_t) \det DT_t \, dx. \end{aligned}$$

Since q is an arbitrary function in $H^1(\Omega_t)$ we can substitute $\bar{q} \circ T_t$ by $w \in H^1(\Omega)$. Taking the derivative in $t = 0$ on both sides leads to

$$\begin{aligned}
 & \int_{\Omega} \nabla \dot{p}_{\Omega} \cdot \nabla w \, dx - \int_{\Omega} [DV(0)^{\top} + DV(0)] \nabla p_{\Omega} \cdot \nabla w \, dx + \int_{\Omega} \nabla p_{\Omega} \cdot \nabla w \operatorname{div} V(0) \, dx \\
 & - c \int_{\Omega} \dot{p}_{\Omega} w \, dx - c \int_{\Omega} p_{\Omega} w \operatorname{div} V(0) \, dx \\
 & + i\alpha \int_{\Gamma_R} \dot{p}_{\Omega} w \, ds + i\alpha \int_{\Gamma_R} p_{\Omega} w [\operatorname{div} V(0) - DV(0)n \cdot n] \, ds \\
 & = \int_{\Omega} \nabla f^{\top} V(0) w \, dx + \int_{\Omega} f \operatorname{div} V(0) w \, dx.
 \end{aligned}$$

Rewriting this in order to have the sesquilinear form with respect to \dot{p} on the left hand side gives

$$\begin{aligned}
 & \int_{\Omega} \nabla \dot{p}_{\Omega} \cdot \nabla w \, dx - c \int_{\Omega} \dot{p}_{\Omega} w \, dx + i\alpha \int_{\Gamma_R} \dot{p}_{\Omega} w \, ds \\
 & = \int_{\Omega} [DV(0)^{\top} + DV(0)] \nabla p_{\Omega} \cdot \nabla w \, dx - \int_{\Omega} \nabla p_{\Omega} \cdot \nabla w \operatorname{div} V(0) \, dx \\
 & + c \int_{\Omega} p_{\Omega} w \operatorname{div} V(0) \, dx - i\alpha \int_{\Gamma_R} p_{\Omega} w [\operatorname{div} V(0) - DV(0)n \cdot n] \, ds \\
 & + \int_{\Omega} \nabla f^{\top} V(0) w \, dx + \int_{\Omega} f \operatorname{div} V(0) w \, dx.
 \end{aligned} \tag{5.8}$$

Note that this is already a weak formulation to find the material derivative \dot{p}_{Ω} . Next, we introduce the adjoint problem:

$$-\Delta u - cu = -j'(p_{\Omega}) \quad \text{in } \Omega \tag{5.9}$$

$$\frac{\partial u}{\partial n} + i\alpha u = 0 \quad \text{on } \Gamma_R \tag{5.10}$$

$$\frac{\partial u}{\partial n} = 0 \quad \text{on } \Gamma_N, \tag{5.11}$$

which has the following weak formulation: Find $u \in H^1(\Omega)$ such that for all $v \in H^1(\Omega)$:

$$\int_{\Omega} \nabla u \cdot \nabla \bar{v} \, dx - c \int_{\Omega} u \bar{v} \, dx + i\alpha \int_{\Gamma_R} u \bar{v} \, ds = - \int_{\Omega} j'(p_{\Omega}) \bar{v} \, dx. \tag{5.12}$$

Choosing $\bar{v} = \dot{p}_{\Omega}$ in (5.12) and using (5.8) leads to

$$\begin{aligned}
 & \int_{\Omega} j'(p_{\Omega}) \dot{p}_{\Omega} \, dx = - \int_{\Omega} \nabla u \cdot \nabla \dot{p}_{\Omega} \, dx + c \int_{\Omega} u \dot{p}_{\Omega} \, dx - i\alpha \int_{\Gamma_R} u \dot{p}_{\Omega} \, ds \\
 & = \int_{\Omega} [\operatorname{div} V(0) - DV(0)^{\top} - DV(0)] \nabla p_{\Omega} \cdot \nabla u \, dx - c \int_{\Omega} p_{\Omega} u \operatorname{div} V(0) \, dx \\
 & + i\alpha \int_{\Gamma_R} p_{\Omega} u [\operatorname{div} V(0) - DV(0)n \cdot n] \, ds - \int_{\Omega} \nabla f^{\top} V(0) u \, dx - \int_{\Omega} f \operatorname{div} V(0) u \, dx.
 \end{aligned}$$

Inserting this in (5.7) finally gives the following expression for $dJ(\Omega)$:

$$\begin{aligned}
 dJ(\Omega) &= \int_{\Omega} \left[\operatorname{div}V(0) - DV(0)^\top - DV(0) \right] \nabla p_{\Omega} \cdot \nabla u \, dx - c \int_{\Omega} p_{\Omega} u \operatorname{div}V(0) \, dx \\
 &\quad + i\alpha \int_{\Gamma_R} p_{\Omega} u [\operatorname{div}V(0) - DV(0)n \cdot n] \, ds - \int_{\Omega} \nabla f^\top V(0) u \, dx \\
 &\quad - \int_{\Omega} f \operatorname{div}V(0) u \, dx + \int_{\Omega} j(p) \operatorname{div}V(0) \, dx.
 \end{aligned} \tag{5.13}$$

□

If the boundary is smooth enough and admits a solution in $H^2(\Omega)$ one can formulate the derivative in terms of integrals over the boundary only. This leads to more efficient computation of the shape derivative $dJ(\Omega, V)$.

Proposition 5.8. *If Ω is smooth enough, such that $p_{\Omega}, u \in H^2(\Omega)^1$ with N corners $a_i, i = 1, \dots, N$ on $\Gamma_R = \cup_{i=1}^N \Gamma_{R,i}$, where $\Gamma_{R,i}$ itself has no corners for all i and a_1 and a_N are the transition points from Γ_R to Γ_N , we can further express (5.6) as a boundary form*

$$\begin{aligned}
 dJ(\Omega) &= \int_{\partial\Omega} (\nabla p_{\Omega} \cdot \nabla u) (V(0) \cdot n) \, ds + i\alpha \int_{\Gamma_R} (-2i\alpha p_{\Omega} u + \kappa p_{\Omega} u) (V(0) \cdot n) \, ds \\
 &\quad - c \int_{\partial\Omega} p_{\Omega} u (V(0) \cdot n) \, ds - \int_{\partial\Omega} p_{\Omega} (fV(0) \cdot n) \, ds + \int_{\partial\Omega} j(p_{\Omega}) (V(0) \cdot n) \, ds \\
 &\quad + \sum_{i=1}^N p_{\Omega}(a_{i+1}) u(a_{i+1}) V(0, a_{i+1}) \cdot \tau^-(a_{i+1}) - p_{\Omega}(a_i) u(a_{i+}) V(0, a_i) \cdot \tau^+(a_i),
 \end{aligned} \tag{5.14}$$

Where κ is the mean curvature and

$$\begin{aligned}
 \tau^-(a_{i+1}) &= \lim_{x \rightarrow a_{i+1}, x \in \Gamma_i} \tau(x) \\
 \tau^+(a_i) &= \lim_{x \rightarrow a_i, x \in \Gamma_i} \tau(x)
 \end{aligned}$$

and τ is the tangential field.

Proof. In the following the terms in (5.6) are considered separately. Integration by parts

¹See the discussion in Chapter 2 when the solution to the Helmholtz problem admits a solution in $H^2(\Omega)$.

on the first term leads to the following calculations.

$$\begin{aligned}
 & \int_{\Omega} \left[\operatorname{div} V(0) - DV(0)^{\top} - DV(0) \right] \nabla p_{\Omega} \cdot \nabla u \, dx \\
 &= \int_{\Omega} \operatorname{div} V(0) \nabla p_{\Omega} \cdot \nabla u \, dx - \int_{\Omega} DV(0)^{\top} \nabla p_{\Omega} \cdot \nabla u \, dx - \int_{\Omega} DV(0) \nabla p_{\Omega} \cdot \nabla u \, dx \\
 &= \int_{\partial\Omega} (\nabla p_{\Omega} \cdot \nabla u) (V(0) \cdot n) \, ds - \int_{\Omega} V(0) \cdot \nabla (\nabla p_{\Omega} \cdot \nabla u) \, dx \\
 &\quad - \left[\int_{\partial\Omega} (V(0) \cdot \nabla p_{\Omega}) \frac{\partial u}{\partial n} \, ds - \int_{\Omega} \Delta u (V(0) \cdot \nabla p_{\Omega}) \, dx - \int_{\Omega} \nabla u \cdot H_p V(0) \, dx \right] \\
 &\quad - \left[\int_{\partial\Omega} (V(0) \cdot \nabla u) \frac{\partial p_{\Omega}}{\partial n} \, ds - \int_{\Omega} \Delta p (V(0) \cdot \nabla u) \, dx - \int_{\Omega} \nabla p_{\Omega} \cdot H_u V(0) \, dx \right] \\
 &= \int_{\partial\Omega} (\nabla p_{\Omega} \cdot \nabla u) (V(0) \cdot n) \, ds - \int_{\partial\Omega} (V(0) \cdot \nabla p_{\Omega}) \frac{\partial u}{\partial n} \, ds + \int_{\Omega} \Delta u (V(0) \cdot \nabla p_{\Omega}) \, dx \\
 &\quad - \int_{\partial\Omega} (V(0) \cdot \nabla u) \frac{\partial p_{\Omega}}{\partial n} \, ds + \int_{\Omega} \Delta p_{\Omega} (V(0) \cdot \nabla u) \, dx,
 \end{aligned} \tag{5.15}$$

where $H_p = \nabla(\nabla p_{\Omega})^{\top}$ and $H_u = \nabla(\nabla u)^{\top}$ are the Hessians of p_{Ω} and u , respectively. Next, we consider the second term in (5.13):

$$\begin{aligned}
 & \int_{\Omega} p_{\Omega} u \operatorname{div} V(0) \, dx = \int_{\partial\Omega} p_{\Omega} u (V(0) \cdot n) \, ds - \int_{\Omega} V(0) \cdot \nabla (p_{\Omega} u) \, dx \\
 &= \int_{\partial\Omega} p_{\Omega} u (V(0) \cdot n) \, ds - \int_{\Omega} (V(0) \cdot \nabla p_{\Omega}) u \, dx - \int_{\Omega} (V(0) \cdot \nabla u) p_{\Omega} \, dx.
 \end{aligned} \tag{5.16}$$

For the terms with respect to the right hand side f in (5.6) it holds that

$$\begin{aligned}
 & \int_{\Omega} \nabla f \cdot V(0) u \, dx + \int_{\Omega} f \operatorname{div} V(0) u \, dx = \int_{\Omega} \operatorname{div} (f V(0)) u \, dx \\
 &= \int_{\partial\Omega} u f (V(0) \cdot n) \, ds - \int_{\Omega} f V(0) \cdot \nabla u \, dx
 \end{aligned} \tag{5.17}$$

Finally, the integral involving j leads to

$$\int_{\Omega} j(p_{\Omega}) \operatorname{div} V(0) \, dx = \int_{\partial\Omega} j(p_{\Omega}) (V(0) \cdot n) \, ds - \int_{\Omega} j'(p_{\Omega}) (V(0) \cdot \nabla p_{\Omega}) \, dx. \tag{5.18}$$

Inserting equations (5.15)-(5.18) into (5.13) then leads to

$$\begin{aligned}
 J'(\Omega) &= \int_{\partial\Omega} (\nabla p_{\Omega} \cdot \nabla u) (V(0) \cdot n) \, ds - \int_{\partial\Omega} (V(0) \cdot \nabla p_{\Omega}) \frac{\partial u}{\partial n} \, ds + \int_{\Omega} \Delta u (V(0) \cdot \nabla p_{\Omega}) \, dx \\
 &\quad - \int_{\partial\Omega} (V(0) \cdot \nabla u) \frac{\partial p_{\Omega}}{\partial n} \, ds + \int_{\Omega} \Delta p_{\Omega} (V(0) \cdot \nabla u) \, dx - c \int_{\partial\Omega} p_{\Omega} u (V(0) \cdot n) \, ds \\
 &\quad + c \int_{\Omega} (V(0) \cdot \nabla p_{\Omega}) u \, dx + c \int_{\Omega} (V(0) \cdot \nabla u) p_{\Omega} \, dx \\
 &\quad + i\alpha \int_{\Gamma_R} p_{\Omega} u [\operatorname{div} V(0) - DV(0)n \cdot n] \, ds - \int_{\partial\Omega} u f (V(0) \cdot n) \, ds \\
 &\quad + \int_{\Omega} f V(0) \cdot \nabla u \, dx + \int_{\partial\Omega} j(p_{\Omega}) (V(0) \cdot n) \, ds - \int_{\Omega} j'(p_{\Omega}) (V(0) \cdot \nabla p_{\Omega}) \, dx.
 \end{aligned}$$

5.2 Computation of shape gradients

Now, since $-\Delta u - cu = -j'(p_\Omega)$ and $-\Delta p_\Omega - cp_\Omega = f$ on Ω (in the weak sense) this becomes

$$\begin{aligned} dJ(\Omega) &= \int_{\partial\Omega} (\nabla p_\Omega \cdot \nabla u) (V(0) \cdot n) \, ds - \int_{\partial\Omega} (V(0) \cdot \nabla p_\Omega) \frac{\partial u}{\partial n} \, ds \\ &\quad - \int_{\partial\Omega} (V(0) \cdot \nabla u) \frac{\partial p_\Omega}{\partial n} \, ds - c \int_{\partial\Omega} p_\Omega u (V(0) \cdot n) \, ds \\ &\quad + i\alpha \int_{\Gamma_R} p_\Omega u [\operatorname{div} V(0) - DV(0)n \cdot n] \, ds \\ &\quad - \int_{\partial\Omega} u (fV(0) \cdot n) \, ds + \int_{\partial\Omega} j(p_\Omega) V(0) \cdot n \, ds. \end{aligned}$$

Inserting the boundary conditions for p_Ω and u restricts the integral to Γ_R if the normal derivative of p_Ω or u is part of the integrand:

$$\begin{aligned} dJ(\Omega) &= \int_{\partial\Omega} (\nabla p_\Omega \cdot \nabla u) (V(0) \cdot n) \, ds + i\alpha \int_{\Gamma_R} (V(0) \cdot \nabla p_\Omega) u \, ds \\ &\quad + i\alpha \int_{\Gamma_R} (V(0) \cdot \nabla u) p_\Omega \, ds - c \int_{\partial\Omega} p_\Omega u (V(0) \cdot n) \, ds \\ &\quad + i\alpha \int_{\Gamma_R} p_\Omega u [\operatorname{div} V(0) - DV(0)n \cdot n] \, ds \\ &\quad - \int_{\partial\Omega} u (fV(0) \cdot n) \, ds + \int_{\partial\Omega} j(p_\Omega) V(0) \cdot n \, ds. \end{aligned}$$

The integrals over Γ_R can be further simplified making use of the product rule and using the identity $\operatorname{div}_\Gamma V(0) = \operatorname{div}_\Gamma V_\tau(0) + \kappa V(0) \cdot n$, cf. [35, Ch. 9, Eq. 5.22].

$$\begin{aligned} &i\alpha \int_{\Gamma_R} (V(0) \cdot \nabla p_\Omega) u \, ds + i\alpha \int_{\Gamma_R} (V(0) \cdot \nabla u) p_\Omega \, ds + i\alpha \int_{\Gamma_R} p_\Omega u [\operatorname{div} V(0) - DV(0)n \cdot n] \, ds \\ &= i\alpha \int_{\Gamma_R} V(0) \cdot \nabla (p_\Omega u) + p_\Omega u \operatorname{div}_\Gamma V(0) \, ds \\ &= i\alpha \int_{\Gamma_R} V(0) \cdot \left(\frac{\partial(p_\Omega u)}{\partial n} n + \frac{\partial(p_\Omega u)}{\partial \tau} \tau \right) + p_\Omega u (\operatorname{div}_\Gamma V_\tau(0) + \kappa (V(0) \cdot n)) \, ds. \end{aligned}$$

Reordering the terms we get

$$\begin{aligned} &i\alpha \int_{\Gamma_R} (V(0) \cdot n) \left(\frac{\partial(p_\Omega u)}{\partial n} + \kappa p_\Omega u \right) + (V(0) \cdot \tau) \frac{\partial(p_\Omega u)}{\partial \tau} + p_\Omega u \operatorname{div}_\Gamma V_\tau(0) \, ds \\ &= i\alpha \int_{\Gamma_R} (V(0) \cdot n) \left(\frac{\partial(p_\Omega u)}{\partial n} + \kappa p_\Omega u \right) + \operatorname{div}_\Gamma (V_\tau(0) p_\Omega u) \, ds \end{aligned}$$

Inserting the Robin boundary condition for p_Ω and u again and using Stokes formula [102, Ch. 3.8] on each piecewise smooth boundary part $\Gamma_{R,i}$, if $\Gamma_R = \cup_{i=1}^N \Gamma_{R,i}$, on the

second expression leads to

$$\begin{aligned}
 & i\alpha \int_{\Gamma_R} (V(0) \cdot n) \left(\frac{\partial(p_\Omega u)}{n} + \kappa p_\Omega u \right) + \operatorname{div}_\Gamma (V_\tau(0) p_\Omega u) \\
 &= i\alpha \int_{\Gamma_R} V(0) \cdot n (-2i\alpha p_\Omega u + \kappa p_\Omega u) ds \\
 &+ \sum_{i=1}^N p_\Omega(a_{i+1}) u(a_{i+1}) V(0, a_{i+1}) \cdot \tau^-(a_{i+1}) - p_\Omega(a_i) u(a_i) V(0, a_i) \cdot \tau^+(a_i).
 \end{aligned}$$

This finally leads to

$$\begin{aligned}
 dJ(\Omega) &= \int_{\partial\Omega} (\nabla p_\Omega \cdot \nabla u) V(0) \cdot n ds + i\alpha \int_\Gamma (-2i\alpha p_\Omega u + \kappa p_\Omega u) (V(0) \cdot n) ds \\
 &- c \int_{\partial\Omega} p_\Omega u (V(0) \cdot n) ds - \int_{\partial\Omega} u (f V(0) \cdot n) ds + \int_{\partial\Omega} j(p_\Omega) V(0) \cdot n ds \\
 &+ \sum_{i=1}^N p_\Omega(a_{i+1}) u(a_{i+1}) V(0, a_{i+1}) \cdot \tau^-(a_{i+1}) - p_\Omega(a_i) u(a_i) V(0, a_i) \cdot \tau^+(a_i)
 \end{aligned}$$

□

Note that, if the boundary has no corners the sum over the corner points vanish with the exception of the points that correspond to the transition from Γ_R to Γ_N . In the case of $\partial\Omega = \Gamma_R$ all corner expressions vanish for smooth boundary. In the following section we will see that, for considered problem there, the sum vanishes, since the boundary Γ_R will be chosen smooth and at the transition points the velocity field is 0.

5.3 Shape optimization of rectangular domain to minimize goal functional in certain subdomain

In this section we want to apply the theory above to a particular shape optimization problem. For this we define the right hand side f in (5.2) as a source in a small area in the domain Ω :

$$f(x) = \begin{cases} \exp\left(-\frac{r^2}{\|x-s\|^2-r^2}\right) & \|x-s\| < r, \\ 0 & \text{else,} \end{cases} \quad (5.19)$$

where s is the center of the source. We assume s and r such that $\operatorname{supp} f \subset \overset{\circ}{\Omega}$. The domain for this model problem is illustrated in Figure 5.1. The problem is: For a given data p_G in $G \subset \Omega$, find boundary Γ_R s.t. the difference of solution p_Ω of (5.4) and p_G in $G \subset \Omega$ is minimized. We assume that the domain can only be changed at the bottom boundary. We consider $c = k^2 > 0$, i.e. the Helmholtz equation with wave number k . Here we can interpret the problem as follows: Imagine the domain Ω is a room, e.g., a concert hall or theater room. The top part, where the source is located, could be the stage, while G is the area for the audience. Assuming the performer is mainly at one position s how does the bottom boundary need to look to achieve a certain experience for the audience?

5.3 Shape optimization of rectangular domain to minimize goal functional in certain subdomain

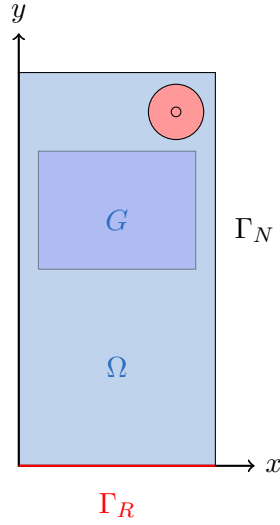


Figure 5.1: Domain to problem (5.4). G is the subdomain of Ω in which the solution p_Ω to (5.4) is supposed to minimize the goal functional. The small red circle illustrates the sound source, i.e., the support of f . The large red circle shows possible source locations for Section 5.4. The boundary Γ_R in red is the part of the boundary that is transformed during the shape optimization.

5.3.1 Domain transformation and velocity field

We consider the domain Ω in Figure 5.1, in particular $\Omega = [0, 1] \times [0, y_{max}]$. As mentioned before we assume a source at the top and only change the bottom boundary such that the goal function is minimized. For this we assume the following parametrization of the lower boundary Γ_R :

$$\gamma(t) = \sum_{\ell=1}^L t_\ell \sin(\ell\pi x). \quad (5.20)$$

Note that $\gamma(0) = \gamma(1) = 0$. We define the transformation T_t in the following way:

$$T_t(x, y) = \left(\begin{array}{c} x \\ y + \left(\frac{y_{max}-y}{y_{max}} \right) \sum_{\ell=1}^L t_\ell \sin(\pi\ell x) \end{array} \right) \quad (5.21)$$

It is visualized in Figure 5.2. Note that here $t \in \mathbb{R}^L$ is a vector. This means that the transformation T_t is a superposition of L transformations. The inverse of T_t is given as

$$T_t^{-1}(\tilde{x}, \tilde{y}) = \left(\begin{array}{c} \tilde{x} \\ \frac{\tilde{y} - \sum_{\ell=1}^L t_\ell \sin(\pi\ell\tilde{x})}{1 - \frac{\sum_{\ell=1}^L t_\ell \sin(\pi\ell\tilde{x})}{y_{max}}} \end{array} \right). \quad (5.22)$$

The derivative of T_t by each t_j , $j = 1, \dots, L$, separately is given via

$$\frac{\partial T}{\partial t_j}(x, y) = \begin{pmatrix} 0 \\ \sin(\pi j x) \frac{y_{max} - y}{y_{max}} \end{pmatrix}. \quad (5.23)$$

Thus, V_j , $j = 1, \dots, L$ can be written as

$$V_j(x, y, t) = \frac{\partial T}{\partial t_j} \circ T_t^{-1}(x, y) = \begin{pmatrix} 0 \\ \sin(\pi j x) \left(1 - \frac{y - \sum_{\ell=1}^L t_\ell \sin(\pi \ell x)}{y_{max} - \sum_{\ell=1}^L t_\ell \sin(\pi \ell x)} \right) \end{pmatrix}. \quad (5.24)$$

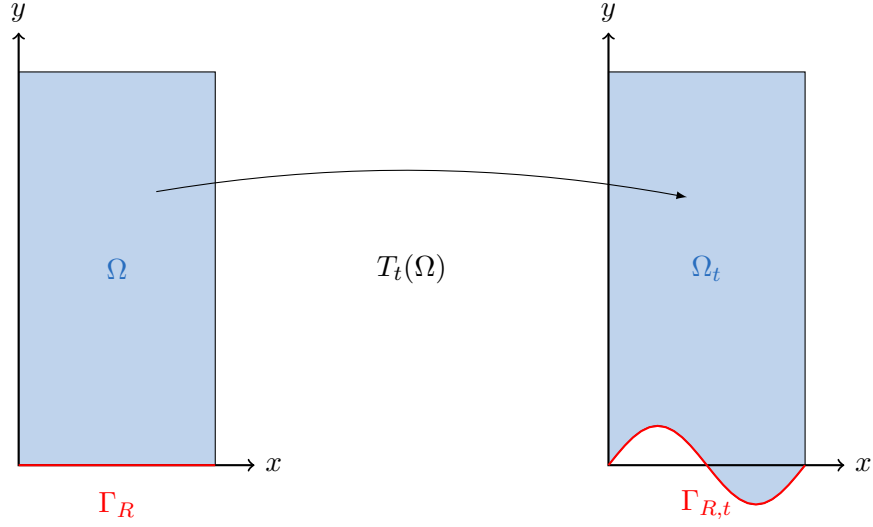


Figure 5.2: Domain transformation at the bottom boundary of a rectangular domain.

The normal field n at the transformed bottom boundary $\Gamma_{R,t} = T_t(\Gamma_R)$ is given by

$$n(x, y) = \frac{1}{\sqrt{\left(\sum_{\ell=1}^L t_\ell \ell \pi \cos(\pi \ell x)\right)^2 + 1}} \begin{pmatrix} \sum_{\ell=1}^L t_\ell \ell \pi \cos(\pi \ell x) \\ -1 \end{pmatrix}. \quad (5.25)$$

The mean curvature κ is then given by (compare [102, Def. 2.52],[102, Eq. 2.143])

$$\kappa = \operatorname{div}_{\Gamma} n = \operatorname{div} n - ((Dn)n, n)_{\mathbb{R}^2},$$

which coincides here with the curvature of the graph $y = \sum_{\ell=1}^L t_\ell \sin(\pi \ell x)$ given by

$$\kappa = \frac{y''}{(1 + y'^2)^{\frac{3}{2}}} = \frac{-\sum_{\ell=1}^L t_\ell \ell^2 \pi^2 \sin(\pi \ell x)}{\left(1 + \left(\sum_{\ell=1}^L t_\ell \ell \pi \cos(\pi \ell x)\right)^2\right)^{\frac{3}{2}}}.$$

5.3 Shape optimization of rectangular domain to minimize goal functional in certain subdomain

5.3.2 Goal functional and problem formulation

The goal is to optimize the boundary Γ_R such that the solution p fits p_G as good as possible in G w.r.t. some goal functional. As a goal functional we choose

$$J(\Omega) = J(\Gamma_R) = \frac{1}{2} \int_G (p_\Omega - p_G)^2 dx, \quad (5.26)$$

where p_Ω is the solution to (5.4). The optimization problem then reads:

Given data p_G find the minimizer $\Gamma_{R,t}$ of

$$\min_{\Gamma_{R,t}} J(\Gamma_{R,t}), \quad \text{where } p_{\Omega_t} \in H^1(\Omega_t) \text{ is the solution of}$$

$$\int_{\Omega_t} \nabla p_{\Omega_t} \cdot \nabla \bar{q} dx - k^2 \int_{\Omega_t} p_{\Omega_t} \bar{q} dx + i\alpha \int_{\Gamma_{R,t}} p_{\Omega_t} \bar{q} ds \quad (5.27)$$

$$= \int_{\Omega_t} f \bar{q} dx, \quad \text{for all } \bar{q} \in H^1(\Omega_t).$$

5.3.3 Gradient descent algorithm using Armijo backtracking

In order to find the minimum $J = J(\Gamma_{R,t})$ and the corresponding parameters $t = (t_1, \dots, t_L)$ of the parametrization of $\Gamma_{R,t}$ we use a gradient descent algorithm. Let β_0 be the (initial) step size. Given an initial vector $t^{(1)}$, for $n = 1, 2, \dots$ compute

$$t^{(n+1)} = t^{(n)} - \beta_0 dJ(t^{(n)}), \quad (5.28)$$

where

$$dJ(t^{(n)}) = \begin{pmatrix} dJ(\Omega_{t^{(n)}}; V_1) \\ \vdots \\ dJ(\Omega_{t^{(n)}}; V_L) \end{pmatrix}. \quad (5.29)$$

<p>Result: Find minimizer domain Ω_t given by parameter t</p> <p>Input : maximum number of iterations N, starting configuration $t \in \mathbb{R}^L$, Armijo-parameters: β_0, ρ, σ</p> <p>Output: final configuration t</p> <pre style="margin: 0;"> 1 for $n=1:N$ do 2 <i>Computation of primal and dual solution:</i> 3 transform domain: $\Omega \rightarrow \Omega_t$; 4 compute p_{Ω_t}; 5 compute u; 6 <i>Computation of shape derivative w.r.t. certain velocity fields V_j:</i> 7 for $j=1:L$ do 8 compute $dJ_j = dJ(\Omega_{t^{(n)}}; V_j)$; 9 end 10 compute J_n; 11 <i>Armijo backtracking</i> 12 set $\beta = \beta_0$; 13 compute p and u with $t - \beta \frac{dJ}{\ dJ\ }$; 14 compute J_{temp} with $t - \beta \frac{dJ}{\ dJ\ }$; 15 while $J_{temp} > J_n - \sigma \beta dJ^T dJ / \ dJ\$ do 16 $\beta = \rho \beta$; 17 compute p_{Ω_t} and u with $t - \beta \frac{dJ}{\ dJ\ }$; 18 compute J_{temp} with $t - \beta \frac{dJ}{\ dJ\ }$; 19 end 20 <i>Update t:</i> 21 $t = t - \beta \frac{dJ}{\ dJ\ }$ 22 end </pre>
--

Algorithm 3: Deterministic shape optimization algorithm using the Armijo-rule.

The shape derivatives $dJ_j := dJ(\Omega_{t^{(n)}}; V_j)$ can be computed using formula (5.14). Note that at the corners we have $V_j(a_i) = 0$, hence the corner expressions vanish. The full shape optimization algorithm is given in Algorithm 3. Obvious extensions such as reusing p_{Ω_t} from line 17 instead of computing it again in line 4 and stopping criteria have been implemented. The gradient step is done with the Armijo rule [9], i.e., a line search method where the step gets smaller if the Armijo condition

$$J(t^{(n)} + \beta d^{(n)}) \leq J(t^{(n)}) + \sigma \beta dJ(t^{(n)})d^{(n)} \quad (5.30)$$

is not fulfilled. Here, $\beta > 0$ denotes the step size which gets multiplied by the control parameter $\rho \in (0, 1)$ if the condition (5.30) is not fulfilled, i.e., the step size gets smaller. $d^{(n)}$ denotes the step direction, i.e., $d^{(n)} = -\frac{dJ}{\|dJ\|}$. The control parameter $\sigma \in (0, 1)$ usually is a small number. Since J is bounded from below by 0, the rule is well-defined, i.e., the line search will stop after a finite number of iterations during the **while** loop

5.3 Shape optimization of rectangular domain to minimize goal functional in certain subdomain

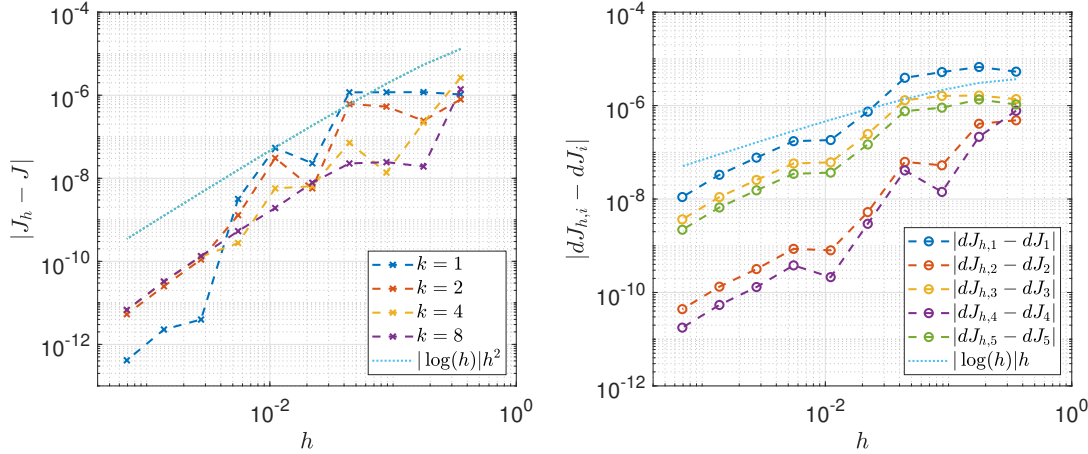


Figure 5.3: Discretization error of the goal functional J for different wave numbers k (left) and the shape derivative dJ for $k = 2$ (right) with respect to mesh size h . The reference was computed on a very fine mesh with $h_{\text{ref}} \approx 0.00035$.

[85, 47]. For the numerical simulations we chose $\beta_0 = 1$, $\rho = 0.5$ and $\sigma = 10^{-2}$. We stop the algorithm if the step size becomes too small, i.e., if $\beta < 10^{-4}$ or a maximum number of iterations $N = 500$ is reached. To prevent the boundary to transform such that parts of G lie outside the domain Ω_t we also stop the algorithm when the boundary parameterization γ from Equation (5.20) takes values larger than 0.95.²

First we study numerically the properties of Algorithm 3 in terms of discretization error of J and dJ_j . For this we generate data by setting $t_{\text{data}} = (0.1, 0, 0, 0, 0)$, i.e., $L = 5$, to construct a reference domain by transforming the domain $\Omega = [0, 1] \times [0, 2]$ using the transformation map $T_{t_{\text{data}}}$. The coefficient α in (5.4) is set to $\alpha = \frac{\omega \rho}{Z}$, with $\omega = 2\pi f = kc$, $c = 340$, $\rho = 1.2$ and $Z = 500 + 800i$ such that $\alpha \approx (0.229 - 0.367i)k$. We compute a reference solution J on a very fine mesh with $h_{\text{ref}} \approx 0.00035$. We compute J and dJ_j , $j = 1, \dots, 5$ for $t = (0, 0, 0, 0, 0)$ for different mesh widths h . Figure 5.3 illustrates the resulting discretization error $|J - J_h|$ and $|dJ_j - dJ_{j,h}|$. We observe convergence rates of $|\log h|h^2$ for J and $|\log h|h$ for dJ . The convergence rate for J can be expected and proven by similar arguments as in Theorem 4.3 in Chapter 4 which is based on [15, Theorem 4.2]. The convergence rate for dJ was proven in [86].

Next we want to consider the behavior J and the parameters t_j , $j = 1, \dots, 5$ during the optimization Algorithm 3. Since the data was generated with the same model that we use in Algorithm 3, i.e., the same source location s , coefficient α and also the domain can be resolved by the transformation T_t with a specific $t = t_{\text{data}}$, J would vanish for $t \rightarrow t_{\text{data}}$. Figure 5.4 illustrates the behavior of the parameters t_j , $j = 1, \dots, 5$. We observe that the parameters are not converging to t_{data} . This is because the gradient descent algorithm is not able to find the global, but only a local minimum. However, on the right hand side of Figure 5.4 we can see that the functional J decreases significantly.

²This only happened regularly for the case $k = 1.75$ and sometimes for $k = 1.5$ in Section 5.4 when different source locations were used.

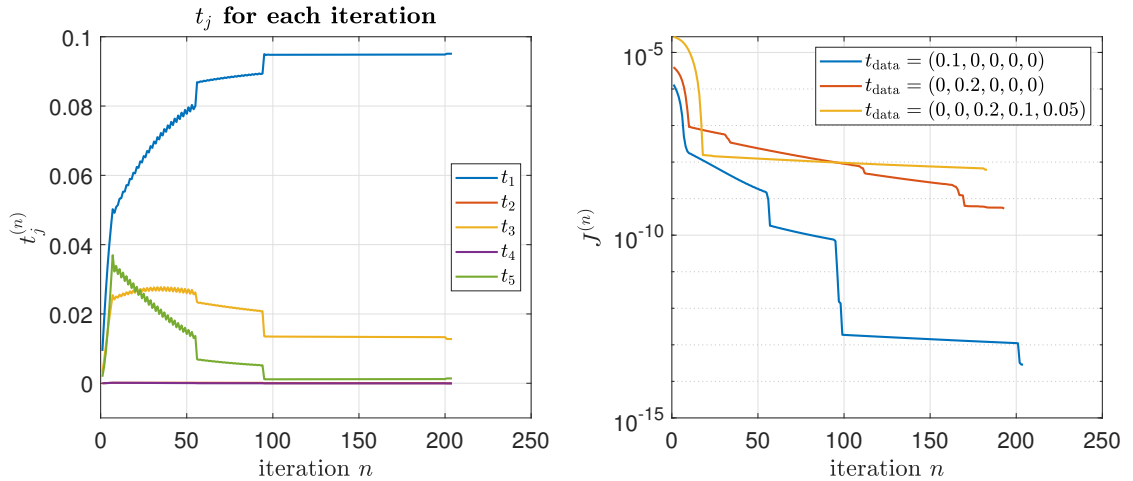


Figure 5.4: Convergence of geometry parameters t for $t_{\text{data}} = (0.1, 0, 0, 0, 0)$ (left) and goal functional J for different t_{data} (right) with respect to the iteration in the optimization algorithm for $k = 2$.

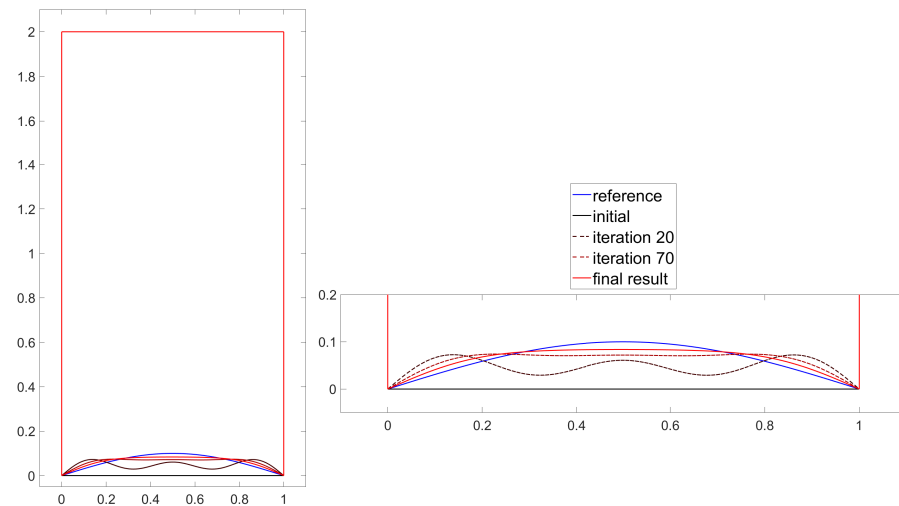


Figure 5.5: Transformation of domains for different numbers of iterations in the optimization algorithm for $k = 2$ and $t_{\text{data}} = (0.1, 0, 0, 0, 0)$. Left: Whole domain. Right: Zoom-in on transformed boundary.

The different lines indicate different parameter sets t_{data} used to generate the data. The blue line corresponds to the case $t_{\text{data}} = (0.1, 0, 0, 0, 0)$. We can observe a decrease of the functional J from around 10^{-6} to 10^{-8} in the first approx. 20 iterations and down to 10^{-13} after approx. 200 iterations for the case $t_{\text{data}} = (0.1, 0, 0, 0, 0)$. Afterwards

the Armijo-step becomes too small and the algorithm stops. We also observe that the goal functional changes only in tiny steps between the iterations 100 to 200. This leads to the assumption that J has some kind of valley where the algorithm is only slowly moving forward.

Figure 5.5 illustrates how the boundary actually changes during the iteration. We observe after a relatively “wavy” boundary after 20 iterations, that becomes less oscillating after 70 iterations. The final result is already rather similar to the reference.

5.4 Expectation domains for uncertain source location

In the next step we assume uncertain location of the source in the sense that a source location in a particular region is expected, but it is not certain. This could be, for example, uncertain location of a performer or loud speaker in a theater. The aim is to construct so-called *expectation domains*, i.e., an average of the optimized domains, using Algorithm 3 with the goal functional J defined in (5.1), for random source locations s . For the sampling we use the Monte Carlo method. We consider two different expectation domains: *parametric expectation* and *Vorob’ev expectation*. For the parametric expectation $\mathbb{E}_{\mathcal{P}}[\Omega(s)]$ we take the expected values for the single parameters $t_j, j = 1, \dots, 5$, in the boundary transformation. The Vorob’ev domain $\mathbb{E}_{\mathcal{V}}[\Omega(s)]$ will be defined in what follows. First we need to define the *coverage function* ζ which is the expectation of the indicator function.

Definition 5.9 (Coverage function, [80, Chapter 2.2.2]). *Let $\Omega(s)$ be the optimized domain for the random source location s . The coverage function ζ is defined as the average of the indicator function.*

$$\mathbb{E}[\chi_{\Omega(s)}(x)] = \mathbb{P}\{x \in \Omega(s)\} =: \zeta(x)$$

The Vorob’ev expectation is defined in the following way:

Definition 5.10 (Vorob’ev expectation, [80, Definition 2.2.3]). *The Vorob’ev expectation $\mathbb{E}_{\mathcal{V}}[\Omega(s)]$ is defined as the set $\{\zeta \geq b\}$ for some fixed $b \in [0, 1]$ which is determined from the equation $\mathbb{E}\mu(\Omega(s)) = \mu(\{\zeta \geq b\})$ if this equation has a solution. Or, in general, from the condition*

$$\mu(\{\zeta \geq a\}) \leq \mathbb{E}\mu(\Omega(s)) \leq \mu(\{\zeta \geq b\})$$

for all $a > b$.

The following algorithm describes how the expectation domains are computed:

Result: Find parametric and Vorob'ev expectation

Input : maximum number of samples M ,
 parameters for Algorithm 3: maximum number of iterations N ,
 starting configuration $t \in \mathbb{K}$, Armijo-parameters: α, ρ, σ

Output: Parametric and Vorob'ev expectation

- 1 **for** $m=1:M$ **do**
- 2 draw source position sample s from specified distribution;
- 3 compute optimal parameters $t^{(m)}$ using Algorithm 3 using specified input parameters for the drawn sample s ;
- 4 **end**
- 5 *Parametric domain*
- 6 $t_{\text{parametric}} = \frac{1}{M} \sum_{m=1}^M t^{(m)}$;
- 7 *Vorob'ev domain*
- 8 compute volume of $\Omega_{t^{(m)}}$ for each $t^{(m)}$, $m = 1, \dots, M$;
- 9 compute coverage function ζ ;
- 10 find Vorob'ev domain according to Definition 5.10;

Algorithm 4: Algorithm to find parametric and Vorob'ev domain.

To measure the difference between two domains we define the *domain deviation*.

Definition 5.11 (Domain deviation). *Let $D_1, D_2 \subset \mathbb{R}^2$ be two domains. The domain deviation between D_1 and D_2 is defined as*

$$Dev(D_1, D_2) = \int_{\mathbb{R}^2} |\chi_{D_1} - \chi_{D_2}| dx.$$

We consider different data that does not match the model defined in the previous section (i.e., initial domain $\Omega = [0, 1] \times [0, 2]$ and coefficient $\alpha \approx (0.229 - 0.367i)k$ in Equation (5.4)). In particular, for the data generation we consider the solution p_{data} to problem (5.4), but in the domain $[0, 1] \times [-3, 2]$, i.e. $\Gamma_{R, \text{data}} = [0, 1] \times \{-3\}$. The source location is chosen as $s_{\text{data}} = [0.75, 1.8]$. The coefficient in the Robin boundary condition for the data is set to $\alpha_{\text{data}} = k$. As we will discuss in more detail in Chapter 6, this is an approximation for an absorbing boundary condition, in particular a plane wave in direction y would be fully absorbed by this, i.e., there is no reflection. Since the domain is now also larger in y -direction the wave will be close to a plane wave at boundary $\Gamma_{R, \text{data}}$ and hence this is a reasonable approximation for an unbounded strip domain, i.e., as if Γ_R were not existent. The problem now becomes to transform Γ_R such that the solution to problem (5.4) approximates the solution p_{data} in this unbounded strip domain in G , i.e., $p_G = p_{\text{data}}|_G$. We consider uncertain source position now. Hence the optimization Algorithm 4 is used: For each sample we take a random location for the source uniformly distributed inside the circle $B_{0,1}(0.75, 1.8)$, i.e., $s = (r \cos(\phi) + 0.75, r \sin(\phi) + 1.8)$ with r^2 sampled from $\mathcal{U}[0, 0.01]$ and ϕ sampled from $\mathcal{U}[0, 2\pi]$. We are interested in the sampling

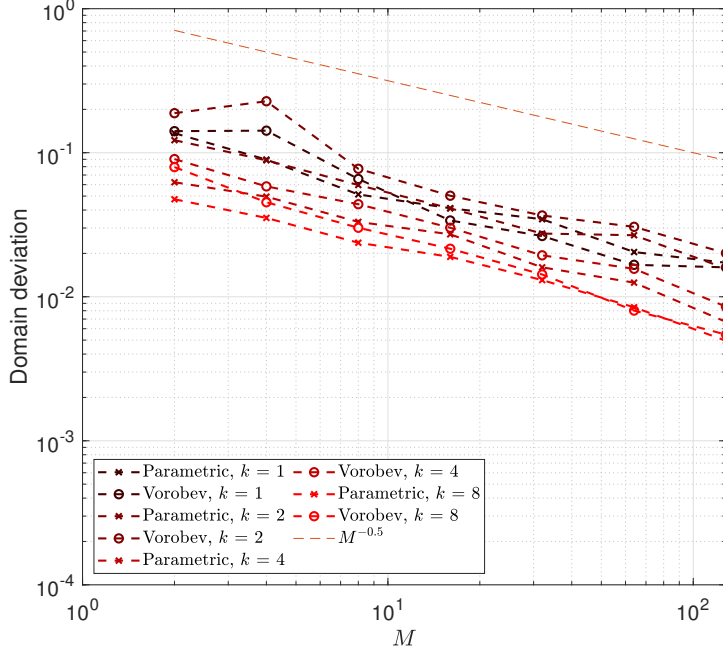


Figure 5.6: Domain deviation for Vorob'ev and parametric domain with respect to sample size for different wave number k .

error for the parametric and Vorob'ev domain. For this we consider

$$\mathbb{E}[Dev(\mathbb{E}_*[\Omega(s)], E_{*,M}[\Omega(s)])], \quad (5.31)$$

where $* \in \{\mathcal{P}, \mathcal{V}\}$, where the sampling averages $E_{\mathcal{P},M}[\Omega(s)]$ and $E_{\mathcal{V},M}[\Omega(s)]$ are computed by taking the empirical mean of M samples to compute $t_{parametric}$ (see Algorithm 4) and constructing the corresponding parametric domain or using M samples to construct the Vorob'ev domain according to Definition 5.10, respectively. The exact expectations are estimated by larger sample size $M = 512$. The outer expectation is again approximated by taking the mean over $M_{outer} = 10$ runs, where one run consists of M samples. Figure 5.6 shows the domain deviation with respect to the number of samples for different wave numbers k . We observe the typical Monte Carlo convergence rate of $M^{-\frac{1}{2}}$. We visualize in Figure 5.7 the Vorob'ev and parametric domain the boundary for different number of samples compared to the reference.

By now we have studied the convergence of Algorithms 3 and 4. In the following we consider the actual domains and corresponding solutions p on these domains for some particular wave numbers. In Figures 5.8, 5.11 and 5.14 we visualize the solution of the optimization problem (5.27) for $k = 2, 3.25$ and 6.25 for source location $s = (0.75, 1.8)$ in the initial domain, i.e., $t = (0, 0, 0, 0, 0)$, the parametric domain, the Vorob'ev domain and the data domain, i.e., $[0, 1] \times [-3, 2]$. In Figures 5.8, 5.9, 5.11, 5.12, 5.14 and 5.15 we show the reference solution values (i.e. the solution to the problem with $\alpha = \alpha_{data}$) restricted to $[0, 1] \times [-2, 2]$ (for Figures 5.8 and 5.9) or $[0, 1] \times [-1, 2]$ (for Figures 5.11,

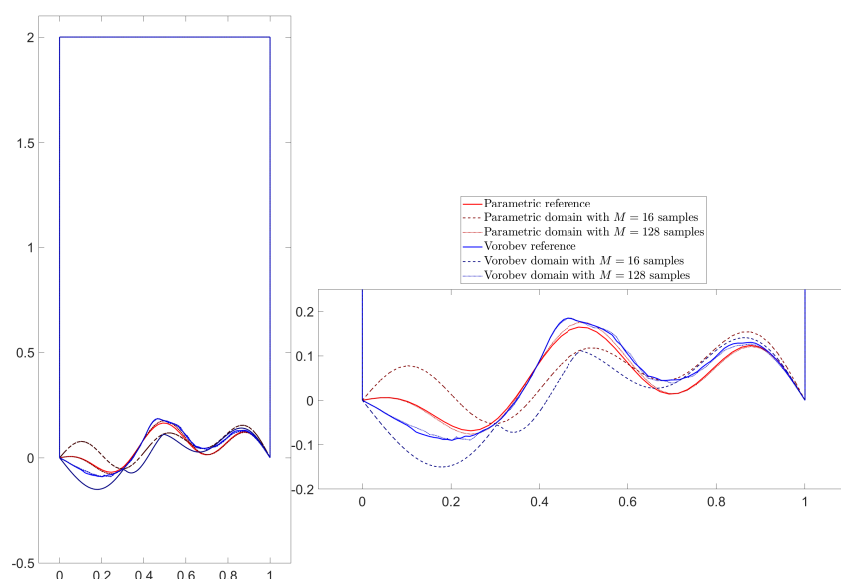


Figure 5.7: Vorob'ev and parametric domain for different number of samples in the optimization algorithm for $k = 8$. Left: Whole domain. Right: Zoom-in on transformed boundary. The reference solution was computed with high sample size of $M = 512$.

5.12, 5.14 and 5.15) instead of the full data domain $[0, 1] \times [-3, 2]$ for the sake of better visual comparison. For $k = 2$ we can see in Figure 5.8 that the transformation, for both, the parametric and the Vorob'ev domain, enlarges the initial rectangle significantly. The solution for these domains is similar to p_G in G . This is a significant improvement compared to the initial domain, where the real part and the absolute value of the solution differ significantly from p_G in G . In Figure 5.9 we changed the source position to $(0.8, 1.85)$. This does not result in significant change in the solution since the wavelength for $k = 2$ is π and therefore relatively large. In general a small change in the location does not lead to a big difference in the solution in this case. Figure 5.10 shows the goal functional J computed on the initial, parametric, Vorob'ev and data domain for $k = 2$ depending on the center of the source. We observe that for the initial domain, J is nearly constant for all possible source locations. For the parametric and Vorob'ev domain we see that setting the source location at the extremes of the possible positions, we get higher values for J , especially in the y -direction. This is similar for the data domain, although more pronounced, since technically a value of $J = 0$ should be reached in the center of the circle. Note also the different color scales with respect to the initial domain. The goal functional values for the parametric and Vorob'ev domain became significantly smaller.

5.4 Expectation domains for uncertain source location

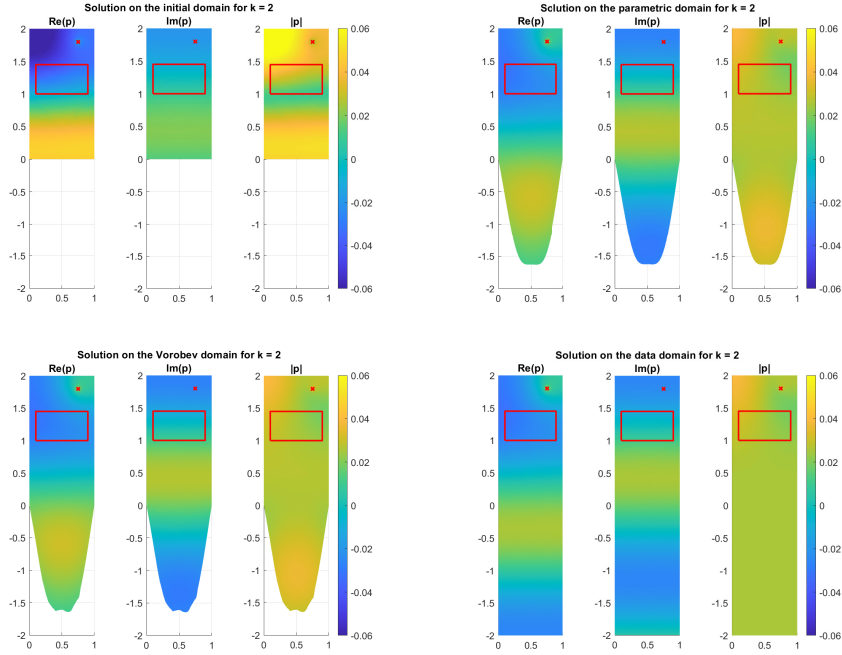


Figure 5.8: Solution on different domains with source location $s = (0.75, 1.8)$ and $k = 2$. Top left: Initial domain. Top right: Parametric domain. Bottom left: Vorob'ev domain. Bottom right: Reference domain (image restricted to the same size as the other domains).

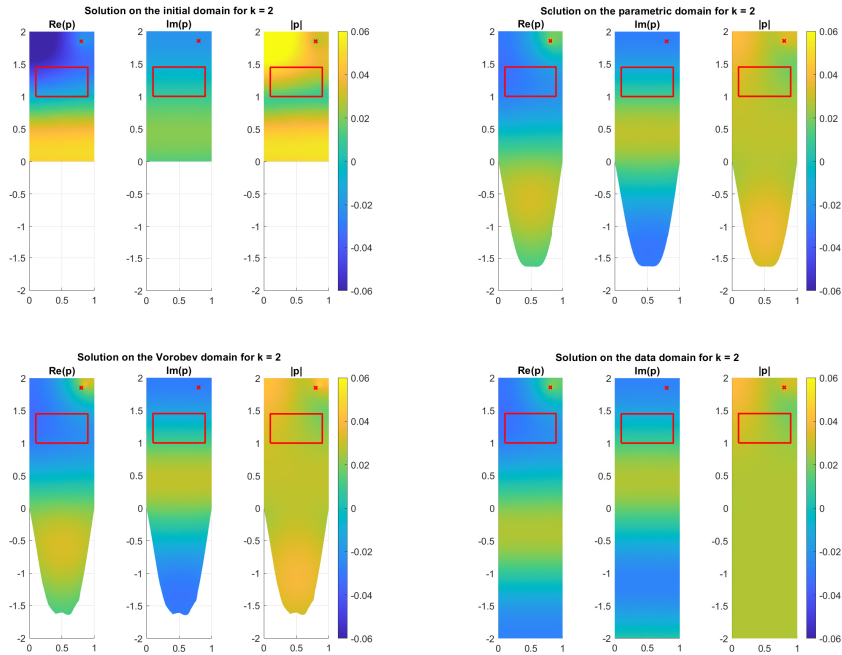


Figure 5.9: Solution on different domains with source location $s = (0.8, 1.85)$ and $k = 2$. Top left: Initial domain. Top right: Parametric domain. Bottom left: Vorob'ev domain. Bottom right: Reference domain (image restricted to the same size as the other domains).

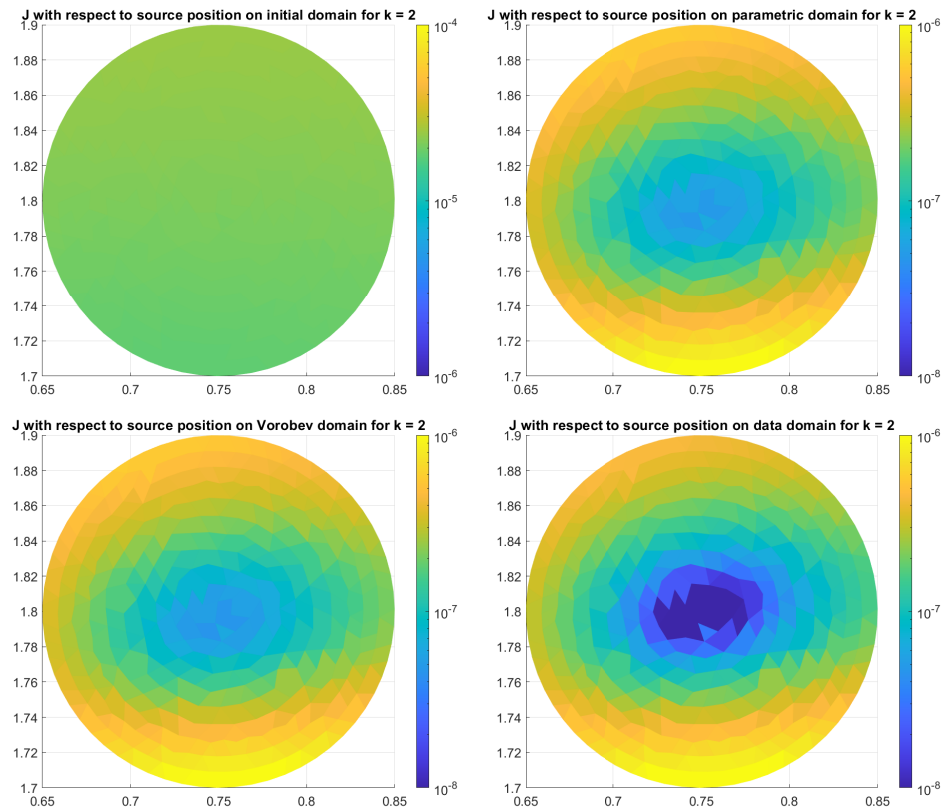


Figure 5.10: Goal functional with respect to source location for $k = 2$. Top left: Initial domain. Top right: Parametric domain. Bottom left: Vorob'ev domain. Bottom right: Reference domain.

Figure 5.11 illustrates the results for $k = 3.25$. Here the domain has changed in a very different way than in the case of $k = 2$. There is a significant difference in the solutions on the initial domain and the Vorob'ev or parametric domain, where the solutions on the latter two are rather similar. In Figure 5.12 we change the source position again. Here the solution plot changes more. While the overall structure of the solution is similar, the maximum magnitudes (i.e., the yellow areas for $|p|$) are more pronounced. This is due to the fact that the source is now closer to the corner and reflections enhance the magnitude of the solution. Note that this is also true for the data domain. Remember that the goal for all source locations is to approximate the solution on the data domain with source location $s = (0.75, 1.8)$. Since even for the data domain the solution varies in G for varying source location, we cannot expect the parametric or Vorob'ev domain to achieve better results there. In Figure 5.13 we observe that the goal functional J is small only when the x -position of the source is close to 0.75, i.e., the mean of the source locations. The reason is probably due to the fact that the wavelength approximately equals the width of the domain, so there is a strong dependence on the x -position of the source.

5.4 Expectation domains for uncertain source location

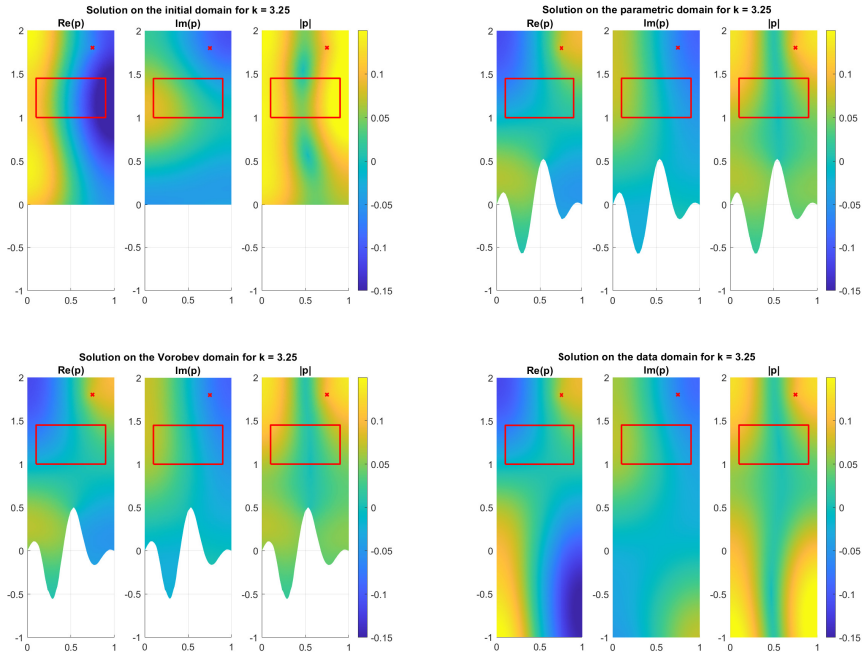


Figure 5.11: Solution on different with source location $s = (0.75, 1.8)$ and $k = 3.25$. Top left: Initial domain. Top right: Parametric domain. Bottom left: Vorob'ev domain. Bottom right: Reference domain (image restricted to the same size as the other domains).

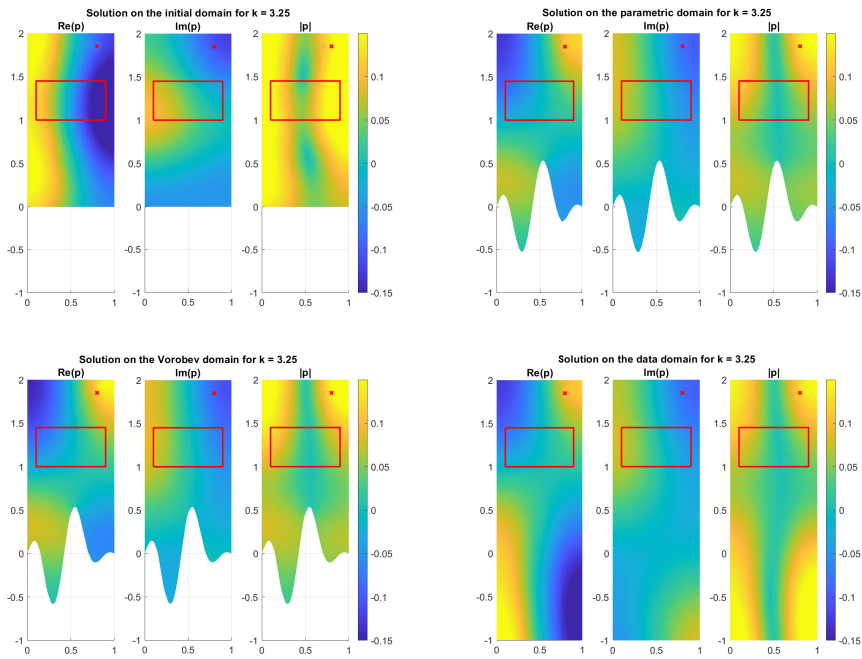


Figure 5.12: Solution on different with source location $s = (0.8, 1.85)$ and $k = 3.25$. Top left: Initial domain. Top right: Parametric domain. Bottom left: Vorob'ev domain. Bottom right: Reference domain (image restricted to the same size as the other domains).

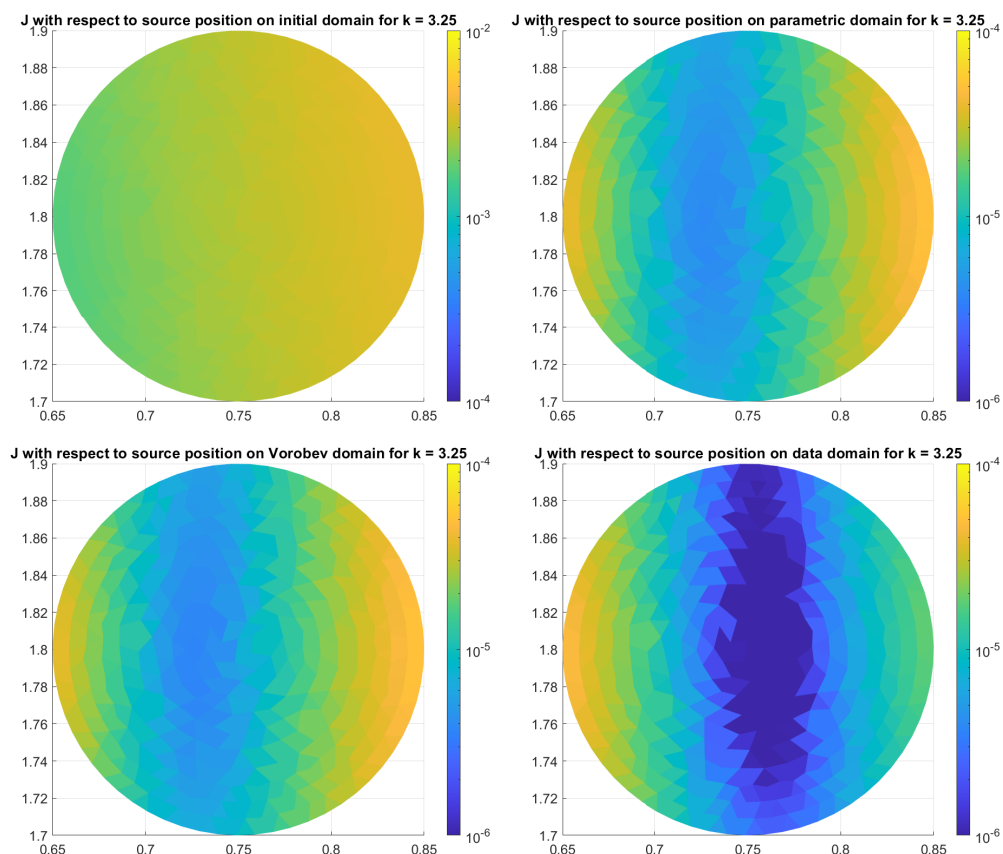


Figure 5.13: Goal functional with respect to source location for $k = 3.25$. Top left: Initial domain. Top right: Parametric domain. Bottom left: Vorob'ev domain. Bottom right: Reference domain.

Lastly, we consider the wave number $k = 6.25$ in Figures 5.14 and 5.15 as representative of the higher wave numbers. In this case (as with most other higher wave numbers) we see no improvement compared to the initial domain. In fact, visually it seems even worse. When the source location is set closer to the corner the magnitude of the solution increases significantly in all domains. This does not mean that the deterministic optimization has failed, but rather that the optimal domain is highly source location dependent, and hence some expectation domains fail to achieve low goal functional values for varying source locations. In Figure 5.16 we again observe the functional J over the source position and see that the source position significantly influences J . Note that we actually use the same color scaling for all domains here. This again illustrates that for high wave numbers no improvement is achieved. For such high wave numbers we cannot expect source location independent optimization since for smaller wavelengths (i.e., higher wave numbers) point values of the solution become increasingly sensitive with respect to changes of the source location.

5.4 Expectation domains for uncertain source location

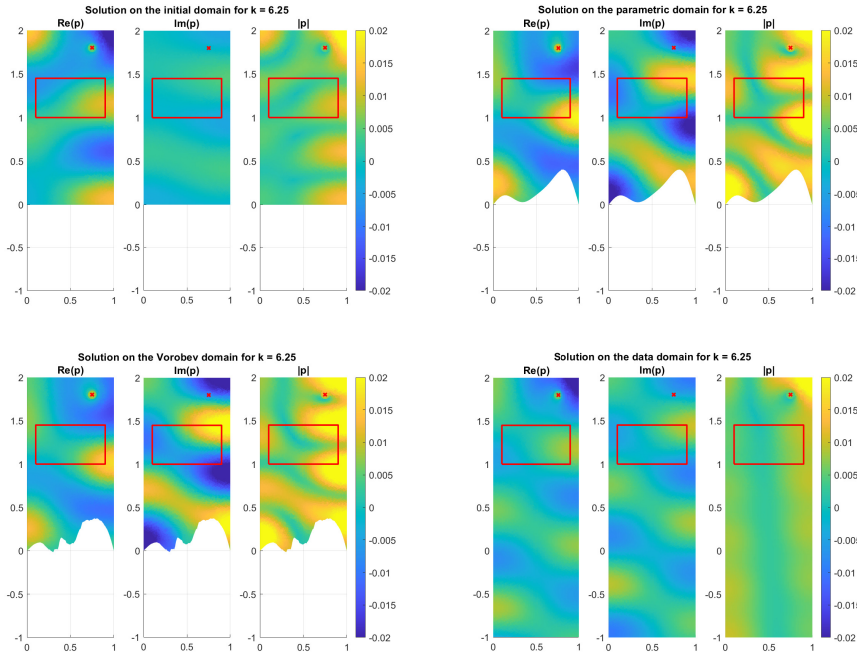


Figure 5.14: Solution on different with source location $s = (0.75, 1.8)$ and $k = 6.25$. Top left: Initial domain. Top right: Parametric domain. Bottom left: Vorob'ev domain. Bottom right: Reference domain (image restricted to the same size as the other domains).

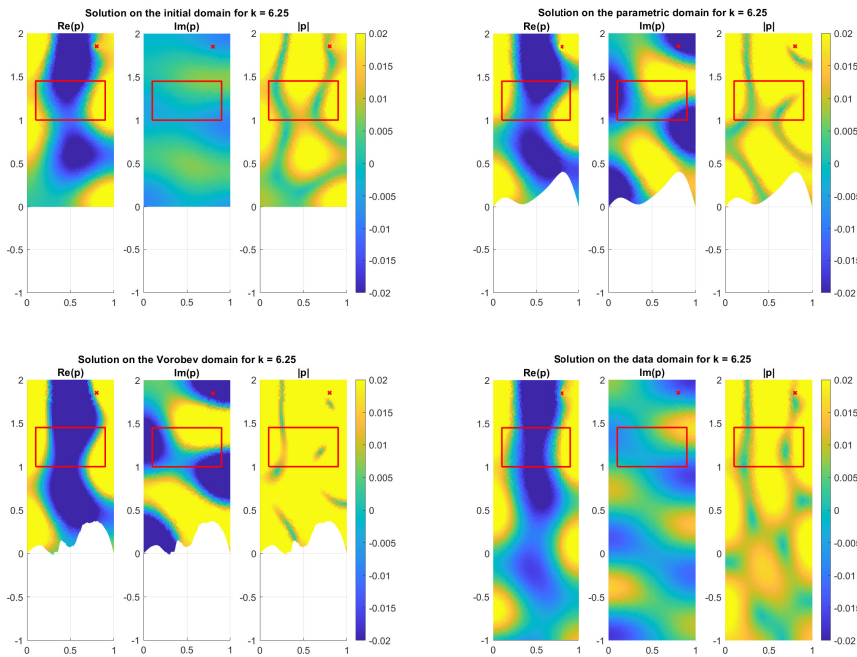


Figure 5.15: Solution on different with source location $s = (0.8, 1.85)$ and $k = 6.25$. Top left: Initial domain. Top right: Parametric domain. Bottom left: Vorob'ev domain. Bottom right: Reference domain (image restricted to the same size as the other domains).

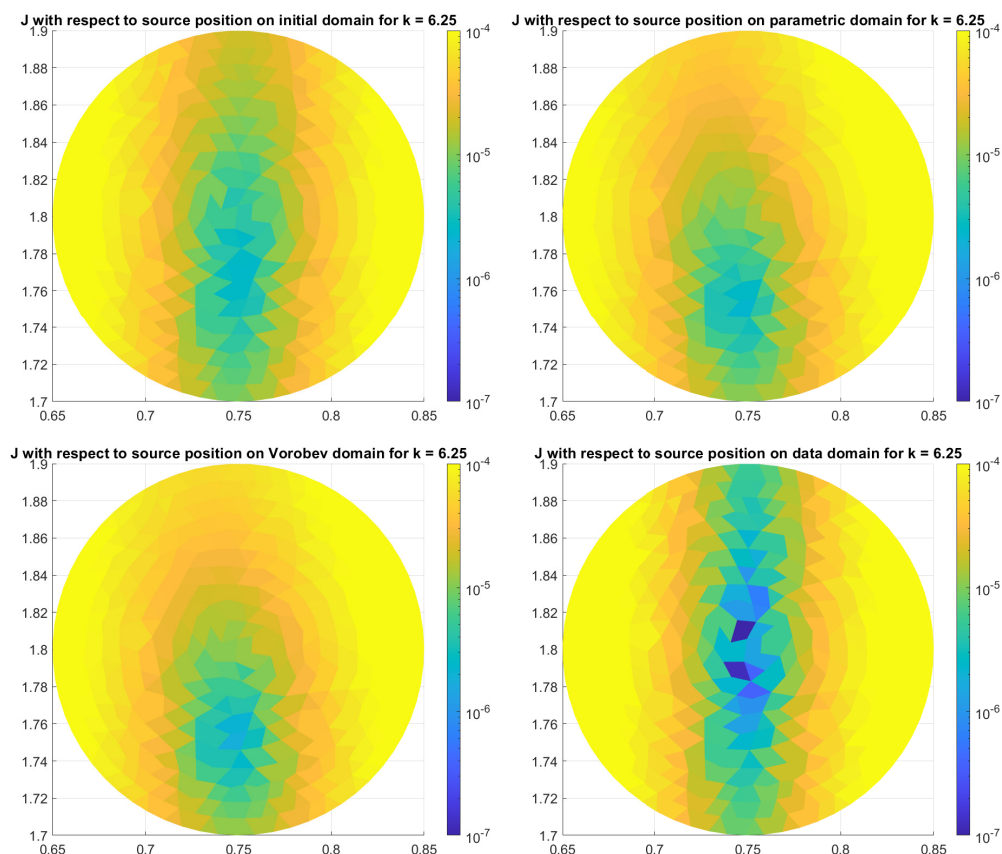


Figure 5.16: Goal functional with respect to source location for $k = 6.25$. Top left: Initial domain. Top right: Parametric domain. Bottom left: Vorob'ev domain. Bottom right: Reference domain.

By now we have observed whether the goal functional is very sensitive to changes in source location. In the following we study the sensitivity of the above results with respect to changes in the wave number. The reference wave number will be denoted as k , whereas k' stands for the perturbed value. Figure 5.17 illustrates the average value $\bar{J}_{k,k'}$ of $J_{k,k'}$ over all sound source locations, i.e.,

$$\bar{J}_{k,k'} = \int_{B_{0.1}(0.75,1.8)} J_{k,k'}(s) ds,$$

that is the integral of the plots visualized in Figures 5.10, 5.13 and 5.16 in the case of $k = k'$. Here $J_{k,k'}$ denotes the goal functional computed for k' over the domain corresponding to k (either initial, parametric, Vorob'ev or data domain, where the first and last are the same for all wave numbers). In the first panel of Figure 5.17 we observe that the average goal functional for both expectation domains is less than or equal to the initial domain when computed for the wave number for which the domain is

computed, i.e., $k = k'$. The other three panels show the average goal functional $\bar{J}_{k,k'}$ for $k = 2, 3.25$ and 4.75 . We can observe that for $k = 2$ and $k = 4.75$ the average goal functional decreases not only for $k' = k$ but also for a small neighborhood, e.g., in the case of $k = 2$ we observe improvements for $k' \in [1, 3]$ and for $k = 4.75$ we observe improvements compared to the initial domain for $k' \in [4, 6]$. Interestingly we even have $\bar{J}_{2,1.75} < \bar{J}_{1.75,1.75}$. This is due to the fact that the optimization procedure had to be stopped early for $k = 1.75$ since the bottom boundary got too high and intruded the subdomain G . For $k = 3.25$ no improvements in the respective neighborhood are visible.

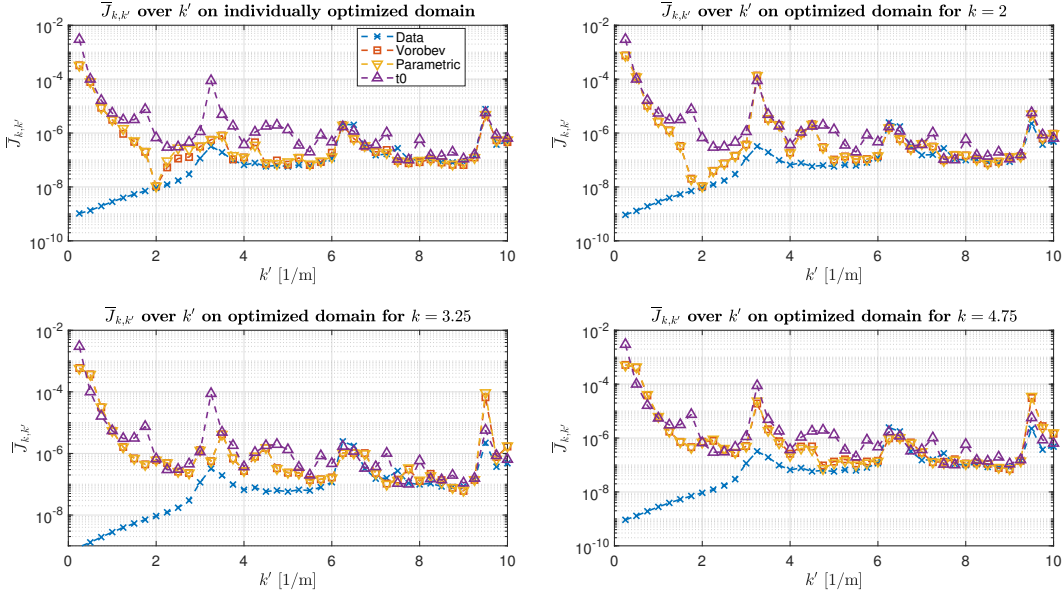


Figure 5.17: Average functional $\bar{J}_{k,k'}$ over k' . Top left: Optimized for each k individually, i.e., $k = k'$. Top right: Domain optimized for $k = 1.75$. Bottom left: Domain optimized for $k = 3.25$. Bottom right: Domain optimized for $k = 4.75$.

5.5 Conclusion

In this chapter we considered a PDE-constrained shape optimization problem. We considered a deterministic setting in which the PDE-constraint was a Helmholtz problem with fixed source. In this case we observed that a corresponding goal functional could be minimized using a gradient descent algorithm. For the uncertain setting, the PDE-constraint was a Helmholtz problem with uncertain source location. Using two different kind of expectation domains we were able to observe improvements in the goal functional for individual wave numbers. The improvements became smaller or even vanished for higher wave number since the wavelength is significantly smaller then. This leads to high sensitivity with respect to the source location. The improvements for the lower wave numbers partially transferred to neighboring wave numbers.

Chapter 6

Optimized truncation of domains for exterior Helmholtz problems

The accurate modeling of wave propagation in unbounded domains is a central challenge in various fields, including acoustics, electromagnetic, and seismology. Exterior Helmholtz problems, which arise frequently in these contexts, require the appropriate handling of radiation conditions to ensure solutions are physically accurate. In particular wave propagation in free space is decaying as

$$p = \mathcal{O}(r^{-\frac{d-1}{2}}). \quad (6.1)$$

The Sommerfeld radiation condition¹

$$\left| \frac{dp}{dr} - ikp \right| = o(r^{-\frac{d-1}{2}}) \quad (6.2)$$

is crucial in this respect, as it governs the asymptotic behavior of waves at infinity [62, 23, 82].

A typical exterior Helmholtz problem is the scattering problem. We consider the following exterior Dirichlet problem in $\mathbb{R}^d \setminus \Omega_{\text{sca}}$, $d = 2, 3$, where Ω_{sca} is a Lipschitz domain with boundary Γ_{sca} , for the upcoming discussion:

$$\begin{aligned} -\Delta p - k^2 p &= 0 && \text{in } \mathbb{R}^d \setminus \Omega_{\text{sca}}, \\ p &= -p_{\text{inc}} && \text{on } \Gamma_{\text{sca}}, \\ \left| \frac{dp}{dr} - ikp \right| &= o(r^{-\frac{d-1}{2}}), && \text{for } |r| \rightarrow \infty. \end{aligned} \quad (6.3)$$

Assuming the scatterer is a circle with radius a and the incoming wave p_{inc} is a plane wave coming from direction θ_{inc} , see Figure 6.1, given by

$$p_{\text{inc}} = p_0 e^{ika \sin(\theta_{\text{inc}} - \theta)}, \quad p_0 \in \mathbb{C}, \quad (6.4)$$

the analytic solution can be derived explicitly [20], in polar coordinates, as

$$p(r, \theta) = -p_{\text{inc}} \sum_{n=-\infty}^{\infty} \frac{J_n(ka)}{H_n^{(1)}(ka)} H_n^{(1)}(kr) e^{in(\theta_{\text{inc}} - \theta)}, \quad (6.5)$$

¹Note that, as discussed in the introduction, the time-convention $e^{-i\omega t}$ is used in this chapter. This leads to some changes in the sign, for example for the Robin boundary or Sommerfeld condition and the plane wave, as well as the fundamental solution.

6.1 An approach to approximate the Sommerfeld condition by domain truncation

where J_n are the Bessel functions of first kind and order n and $H_n^{(1)}$ the Hankel-function of first kind and order n . Note that here, following the conventions in [20], angle θ_{inc} of the plane incident wave is defined as coming from the top for $\theta_{\text{inc}} = 0$. Hence, an incoming wave from the right is realized by $\theta_{\text{inc}} = \frac{3\pi}{2}$. To derive the solution one uses polar coordinates, separation of variables and results in the context of Bessel functions [1], see [20] for details.

In general, however, analytical solutions the scattering problems like (6.3) with arbitrary scatterer are not analytically solvable. Hence, numerical methods need to be applied. To solve the exterior Helmholtz problem in practice different strategies can be used. The boundary element method is a natural way to deal with the unbounded domain and is a well-studied method to solve the Helmholtz equation [58, 23, 17, 24]. Another approach is the finite element method (FEM). However, the unbounded nature of the domain necessitates truncation for numerical computations, raising the question of how to best approximate these conditions within a finite computational framework.

Traditional strategies for handling truncation include the use of absorbing boundary conditions (ABCs) [14], Dirichlet-to-Neumann (DtN) mappings [75, 45], and perfectly matched layers (PMLs) [16]. These techniques, while effective, often involve trade-offs between computational cost and implementation complexity. This chapter explores an approach to truncating the computational domain, addressing these challenges from a different perspective. By adapting the domain's geometry to the contours of the solution's complex argument, the incidence angles of waves on the artificial boundary are minimized, leading to improved absorption and reduced reflection.

In this chapter we consider a rather simple boundary condition and choose the shape of the boundary such that good absorption behavior is observed. In the following section we want to motivate this approach, and in particular shortly revisit established methods (Sections 6.1.1 and 6.1.2) and introduce the Poynting vector (Section 6.1.4). In Section 6.2 we present results from numerical experiments for different shapes of the scatterer. In Section 6.3 we give final conclusions and remarks.

6.1 An approach to approximate the Sommerfeld condition by domain truncation

The simplest idea to approximate the Sommerfeld radiation condition is to just use the impedance boundary condition with $Z = \rho c$, i.e., setting the left-hand side of the Sommerfeld condition to zero. Considering a plane wave hitting a wall or boundary perpendicularly one observes that this condition is exactly the one one needs to fully absorb the wave:

$$\begin{aligned} p &= \exp(ik(n \cdot x)), & \frac{\partial p}{\partial n} &= ik \exp(ik(n \cdot x))n, \\ \frac{\partial p}{\partial n} - ikp &= 0. \end{aligned} \tag{6.6}$$

If the plane wave hits the boundary in a different angle there is a non-decaying residual,

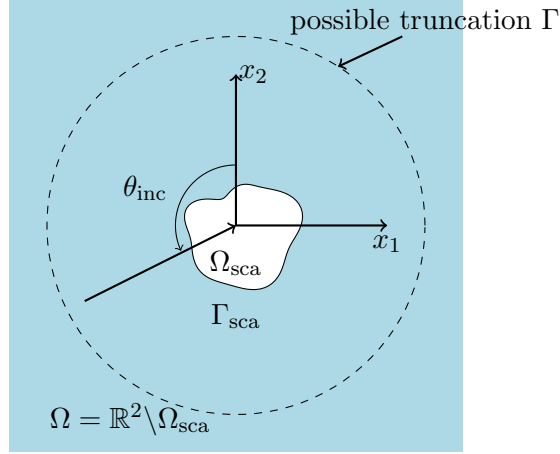


Figure 6.1: Domain of the exterior Helmholtz problem with indicated possible truncation.

since the plane wave itself is not decaying, hence it is not a suitable starting point for the considerations of exterior wave problems. However, we observed total absorption for perpendicular incoming waves. To go one step further we now consider the fundamental solution to the Helmholtz problem in two and three space dimensions, see e.g. [62],

$$\Psi_{2D}(x) = \frac{i}{4} H_0^{(1)}(k|x|), \quad \Psi_{3D}(x) = \frac{\exp(ik|x|)}{4\pi|x|}, \quad (6.7)$$

see Figure 6.2 for a visualization of these functions. Inserting these in the left hand side of the Sommerfeld condition (6.2) will give us insight on the error for a truncated domain, i.e., imposing the impedance boundary condition for finite r instead of the Sommerfeld condition for $r \rightarrow \infty$. To compute this we need the directional derivatives of Ψ_{2D} and Ψ_{3D} , respectively. The partial derivative of Ψ_{2D} is given by (see, e.g., [8] for properties of the Hankel functions)

$$\frac{\partial}{\partial x_j} \Psi_{2D}(x) = -\frac{i}{4} H_1^{(1)}(k|x|) \frac{kx_j}{|x|}, \quad j = 1, 2.$$

Hence the directional derivative in direction $n \in \mathbb{R}^2$ is

$$\frac{\partial}{\partial n} \Psi_{2D}(x) = -\frac{i}{4} H_1^{(1)}(k|x|) k \frac{x \cdot n}{|x|}. \quad (6.8)$$

And for $n = \frac{x}{|x|}$ we get

$$\frac{\partial}{\partial n} \Psi_{2D}(x) = -\frac{i}{4} k H_1^{(1)}(k|x|).$$

The Sommerfeld condition then leads to

$$\frac{\partial \Psi_{2D}}{\partial n}(x) - ik\Psi_{2D}(x) = -\frac{ik}{4} H_1^{(1)}(k|x|) + \frac{k}{4} H_0^{(1)}(k|x|). \quad (6.9)$$

6.1 An approach to approximate the Sommerfeld condition by domain truncation

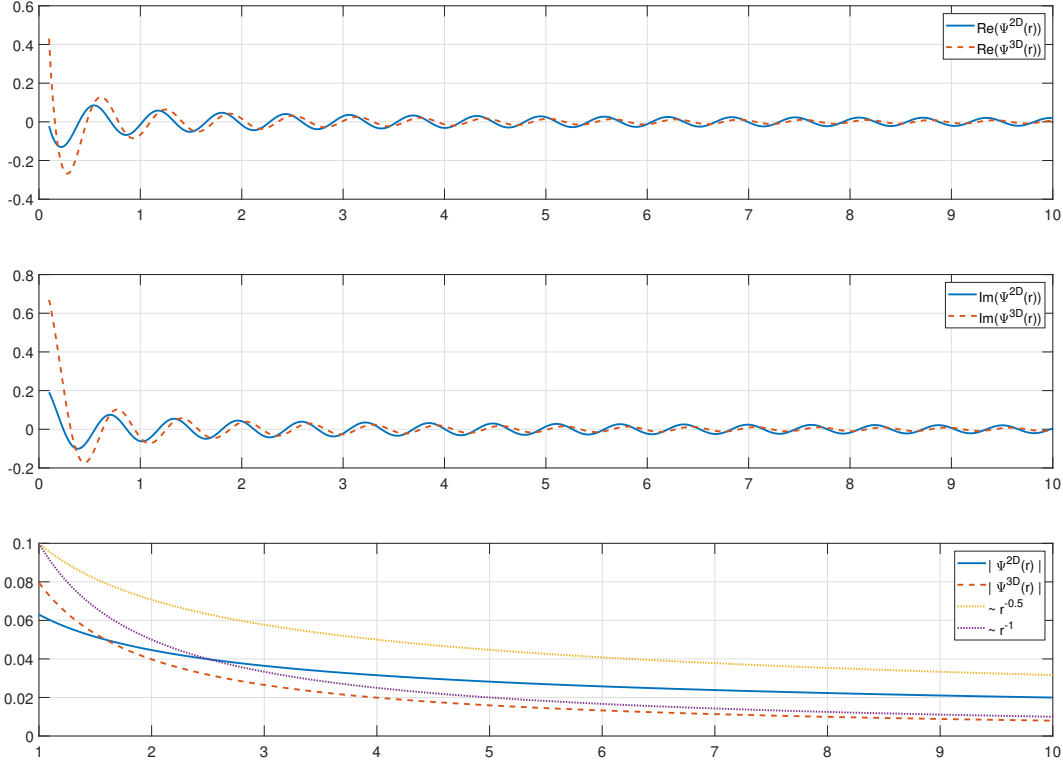


Figure 6.2: Fundamental solutions for the Helmholtz equation in two and three spatial dimensions.

Analogously for the three-dimensional fundamental solution we get

$$\begin{aligned}
 \frac{\partial}{\partial x_j} \Psi_{3D}(x) &= \frac{\exp(ik|x|) ik \frac{2x_j}{2|x|} 4\pi|x| - \exp(ik|x|) 4\pi \frac{2x_j}{2|x|}}{16\pi^2|x|^2} \\
 &= \frac{4\pi ikx_j \exp(ik|x|) - \frac{4\pi x_j}{|x|} \exp(ik|x|)}{16\pi^2|x|^2} \\
 &= \frac{\exp(ik|x|) \left(ikx_j - \frac{x_j}{|x|} \right)}{4\pi|x|^2}, \quad j = 1, 2, 3.
 \end{aligned}$$

Which leads to the directional derivative in direction n

$$\frac{\partial}{\partial n} \Psi_{3D}(x) = \frac{\exp(ik|x|) \left(ik(x \cdot n) - \frac{x \cdot n}{|x|} \right)}{4\pi|x|^2}. \quad (6.10)$$

Thus, for the radial direction $n = \frac{x}{|x|}$:

$$\begin{aligned}\frac{\partial}{\partial n}\Psi_{3D}(x) &= \frac{\exp(ik|x|)(ik|x| - 1)}{4\pi|x|^2} \\ &= \Psi_{3D}(x)\left(ik - \frac{1}{|x|}\right).\end{aligned}\tag{6.11}$$

Inserting this into the Sommerfeld condition gives

$$\frac{\partial\Psi_{3D}(x)}{\partial n} - ik\Psi_{3D}(x) = -\frac{1}{|x|}\Psi_{3D}(x).\tag{6.12}$$

As the Sommerfeld condition implies and the computations for the fundamental solution show, the simple impedance boundary condition

$$\frac{\partial p}{\partial n} - ikp = 0$$

is a reasonable approximation for the Sommerfeld condition on a bounded domain if the boundary is far away from the source, or, in the two-dimensional case, the wave number k is large, since the residuals in (6.9) and (6.12) are decaying in x (and k in case of (6.9)). However, from the three-dimensional case we can already deduce that there are improved boundary conditions since

$$\frac{\partial p}{\partial n} - \left(ik - \frac{1}{|x|}\right)p = 0$$

would reproduce exact absorption if p is the fundamental solution and the normal derivative is the radial derivative with respect to the source location of p , e.g., if p is a point source in 0 and the bounded domain is a circle. Indeed, similar boundary conditions and boundary conditions of higher order have been developed.

6.1.1 Absorbing boundary conditions

In the literature many ways to improve the simple impedance boundary condition as radiation condition have been considered and derived. For example in [41] they were derived using the Dirichlet-to-Neumann-operator. The Dirichlet-to-Neumann-operator itself is non-local. While leading to high accuracy it is costly to compute. Hence, other approximation techniques are needed. In [14] the authors considered micro-local approximation, which yielded to superior accuracy in contrast to the impedance boundary condition. However, for higher order conditions these will get more and more tedious to implement and are often not available in most common commercial or free software. In [14] only two-dimensional conditions were derived, however the authors state, that they see no hindrance for doing similar derivations in three dimensions. In that follows only the simple impedance boundary condition and the so called curvature absorbing boundary condition (C-ABC) will be considered. These are given by

$$\frac{\partial}{\partial n}p - ikp = 0 \text{ on } \Gamma\tag{6.13}$$

6.1 An approach to approximate the Sommerfeld condition by domain truncation

and

$$\begin{cases} \frac{\partial}{\partial n}p - ikp + \frac{\kappa}{2}p = 0 \text{ on } \Gamma, & d = 2, \\ \frac{\partial}{\partial n}p - ikp + \kappa p = 0 \text{ on } \Gamma, & d = 3. \end{cases} \quad (6.14)$$

The latter is still of Robin-type, whereas higher order ABCs involve more complex expressions like the Laplace-Beltrami-operator and even higher order derivatives. In the following section an idea to improve the accuracy, using only the simple boundary conditions, is presented. We observe that the curvature boundary condition (6.14) for the three-dimensional case is identical with the one in our prior calculations if the domain is a ball, since its the curvature of a sphere of radius r is given as $\kappa = \frac{1}{r}$. Another way to deal with the truncation of the domain is the addition of an absorbing layer that prevents the reflection of the wave at the boundary: Perfectly matched layer.

6.1.2 Perfectly matched layer

In this section an implementation of the PML following the ideas of [16] is shortly introduced. It will be used in the numerical experiments to compute a reference solution if no analytic solution is available.

The truncated computational domain is wrapped by a square or rectangular domain (note that this domain does not need to be rectangular, we chose this here for an easy overview and implementation), where an absorption layer is introduced. An absorption function lowers the solution value to zero till the boundary. The idea is that no reflection can occur in this case. In the example of the scattering problem (6.3) the domain can be viewed as in Figure 6.3. Here Ω denotes the usual physical domain, whereas Ω_{PML} is the absorbing layer. The union of both we just call $\tilde{\Omega} = \Omega \cup \Omega_{\text{PML}}$. The problem states (for convenience of the notation we use $(x, y) \in \mathbb{R}^2$ here):

$$\begin{aligned} \frac{1}{\gamma_x} \frac{\partial}{\partial x} \left(\frac{1}{\gamma_x} \frac{\partial p}{\partial x} \right) + \frac{1}{\gamma_y} \frac{\partial}{\partial y} \left(\frac{1}{\gamma_y} \frac{\partial p}{\partial y} \right) + k^2 p &= 0 & \text{in } \tilde{\Omega}, \\ p &= p_0 & \text{on } \Gamma_{\text{sca}}, \\ p &= 0 & \text{on } \Gamma_D. \end{aligned} \quad (6.15)$$

The functions γ_x and γ_y are given by

$$\begin{aligned} \gamma_x(x) &= \begin{cases} 1, & \text{if } |x| < a, \\ 1 + \frac{i}{\omega} \sigma_x(|x|), & \text{if } a \leq |x| < a^*, \end{cases} \\ \gamma_y(y) &= \begin{cases} 1, & \text{if } |y| < b, \\ 1 + \frac{i}{\omega} \sigma_y(|y|), & \text{if } b \leq |y| < b^*. \end{cases} \end{aligned} \quad (6.16)$$

Note that there are no impedance boundary conditions or other absorbing boundary conditions necessary anymore. The PML layer is the substitute for this. In the interior of Ω the functions γ_x and γ_y are constant to one, hence the first line in equation (6.15) becomes the usual Helmholtz equation. In [16] several absorbing functions σ_x and σ_y and

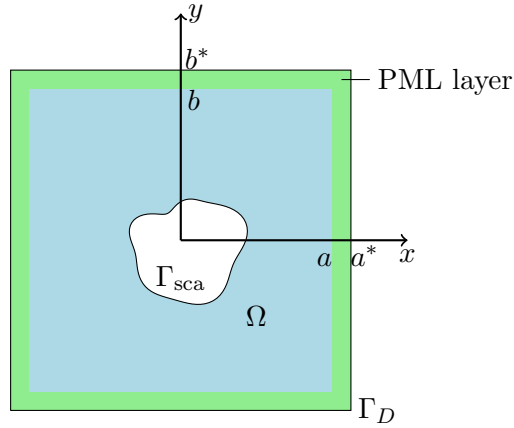


Figure 6.3: Domain with additional layer for absorption.

parameters β were considered. For the implementation here the continuous functions with linear denominator are chosen, i.e.,

$$\sigma_x(x) = \frac{\beta}{a^* - x} - \frac{\beta}{a^* - a}, \quad \sigma_y(y) = \frac{\beta}{b^* - y} - \frac{\beta}{b^* - b} \quad (6.17)$$

with $\beta = c$, where $c = 340$ is the speed of sound (in m/s). In practice this method usually achieves very good results in terms of absorption. However, it increases the computational domain by a layer and how to choose the parameters used in the formulation is not totally clear and depends on the problem.

6.1.3 Residuals for non-perpendicular incoming waves

We have seen, that for a plane wave the impedance boundary condition is exact for a plane wave and that for the 3D case the curvature absorbing boundary condition is exact for the fundamental solution if the wave in both cases hits the boundary perpendicular. If the direction, however, is not perpendicular to the boundary we get larger reflection, i.e., the wave is less absorbed. For this we again consider the plane wave first and the fundamental solutions afterwards. Let θ be the angle between n and m where n is the outer normal derivative of the boundary. Assume $-\frac{\pi}{2} < \theta < \frac{\pi}{2}$, since otherwise the wave does not hit the boundary. m can be written as

$$m = Rn, \quad \text{where} \\ R = \begin{pmatrix} \cos(\theta) & -\sin(\theta) \\ \sin(\theta) & \cos(\theta) \end{pmatrix}$$

$$p(x) = \exp(ik(m \cdot x)), \quad \frac{\partial p}{\partial n}(x) = ikp(x)(m \cdot n), \\ \frac{\partial p}{\partial n}(x) - ikp(x) = (Rn \cdot n - 1)ikp(x). \quad (6.18)$$

6.1 An approach to approximate the Sommerfeld condition by domain truncation

For the plane wave we can directly see that the right-hand side of (6.18) is largest if Rn is close to being perpendicular to n (in terms of magnitude). This case leads to the worst model error if we enforce the impedance boundary condition. We can do similar calculations for the fundamental solutions in two and three dimensions using the directional derivatives computed in (6.8) and (6.10). We illustrate the residual of the impedance boundary condition and the curvature boundary condition for the fundamental solutions in Figures 6.4 and 6.5, where the domains are a ball in their respective dimension, i.e., the curvature at the boundary is given by $\frac{1}{r}$ with a radius of $r = 1$. We observe that for angles $\theta > 0.5$, i.e., angles larger than approx. 30° , both boundary conditions lead to similar errors. For small incident angle the curvature absorbing boundary condition leading to smaller residuals, i.e., better absorption.

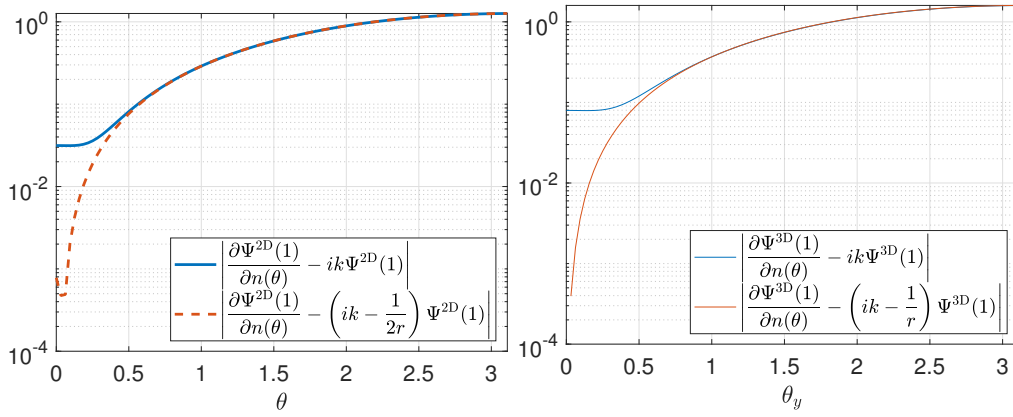


Figure 6.4: Residual at the boundary for the impedance boundary condition and the C-ABC in 2D and 3D (for one angle) with respect to incidence angle.

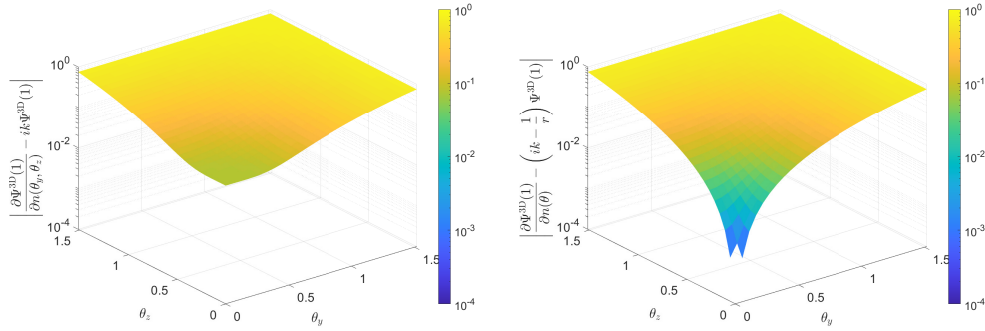


Figure 6.5: Residual at the boundary for the impedance boundary condition (left) and C-ABC (right) in 3D with respect to two incidence angles.

6.1.4 The Poynting vector for plane waves and the fundamental solution

These findings suggest that one can approximate problem (6.3) quite well if the incident angle of the wave is close to perpendicular. It is however unclear how exactly this incident angle is defined for an arbitrary solution to the Helmholtz problem. We are grateful to Prof. Dr. Andrea Moiola for suggesting that we use the so-called *Poynting vector*²:

$$S(p) := \operatorname{Re} \left(\frac{1}{ik} \bar{p} \nabla p \right).$$

We can observe that for the plane wave (and the fundamental solution) this coincides with the wave direction: Let $p(x) = \exp(ikx \cdot d)$, then

$$S(p) = \operatorname{Re} \left(\frac{1}{ik} \exp(-ikx \cdot d) \exp(ikx \cdot d) ikd \right) = d.$$

Hence, the Poynting vector is indeed the propagation direction for a plane wave. Next consider the two-dimensional fundamental solution

$$\begin{aligned} S(\Psi_{2D}) &= \operatorname{Re} \left(\frac{1}{ik} \frac{-i}{4} \overline{H_0^{(1)}(k|x|)} \frac{-i}{4} H_1^{(1)}(k|x|) \frac{k}{|x|} x \right) \\ &= \operatorname{Re} \left(\frac{i}{16} \overline{H_0^{(1)}(k|x|)} H_1^{(1)}(k|x|) \right) \frac{x}{|x|} \\ &= -\operatorname{Im} \left(\frac{1}{16} \overline{H_0^{(1)}(k|x|)} H_1^{(1)}(k|x|) \right) \frac{x}{|x|}, \end{aligned}$$

which is proportional to the wave direction x , since $\overline{H_0^{(1)}(k|x|)} H_1^{(1)}(k|x|)$ has negative imaginary part. This can be seen by using the definition of Hankel functions $H_n^{(1)}(z) = J_n(z) + iY_n(z)$, where J_n and Y_n are the Bessel functions of first and second kind of order n , leads to

$$\operatorname{Im} \left(\overline{H_0^{(1)}(k|x|)} H_1^{(1)}(k|x|) \right) = \operatorname{Im} (-Y_0(k|x|)J_1(k|x|) + J_0(k|x|)Y_1(k|x|)) = -\frac{2}{\pi x},$$

where in the last step we used a Wronskian formula [8, Eq. (14.71)]. And finally the three-dimensional fundamental solution:

$$\begin{aligned} S(\Psi_{3D}) &= \operatorname{Re} \left(\frac{1}{ik} \frac{\exp(-ik|x|)}{4\pi|x|} \frac{\exp(ik|x|)}{4\pi|x|^2} \left(ik - \frac{1}{|x|} \right) x \right) \\ &= \operatorname{Re} \left(1 - \frac{1}{ik|x|} \frac{1}{16\pi^2|x|^3} x \right) = \frac{1}{16\pi^2|x|^3} x, \end{aligned}$$

which is again proportional to the propagation direction x .

We note that the Poynting vector is actually proportional to the gradient of the complex argument of the sound pressure function p , as a simple computation (we assume

²The Poynting vector often appears in the framework of Maxwell equations [82]. However, it can also be translated to the time-harmonic acoustic setting, as defined in (6.1.4).

6.2 Numerical comparison of contour and standard circular truncation

that $p(x, y)$ is distant from the incontinuity jump from the complex argument function) shows (assuming $\text{Re}(p(x, y)) > 0$, other cases follow similarly)

$$\begin{aligned}
\nabla \arg p(x, y) &= \nabla \text{atan2}(\text{Im}(p(x, y)), \text{Re}(p(x, y))) \\
&= \nabla \text{atan} \frac{\text{Im}(p(x, y))}{\text{Re}(p(x, y))} \\
&= \frac{1}{1 + \left(\frac{\text{Im}(p(x, y))}{\text{Re}(p(x, y))}\right)^2} \frac{\text{Im}(\nabla p(x, y))\text{Re}(p(x, y)) - \text{Im}(p(x, y))\text{Re}(\nabla p(x, y))}{\text{Re}(p(x, y))^2} \\
&= \frac{\text{Im}\left(\overline{p(x, y)} \nabla p(x, y)\right)}{|p(x, y)|^2} \\
&= \frac{\text{Re}\left(\frac{1}{i} p(x, y) \nabla p(x, y)\right)}{|p(x, y)|^2}
\end{aligned} \tag{6.19}$$

These connection leads us to propose truncating the domain at a contour line of the complex argument of the solution p of the exterior Helmholtz problem to achieve a possibly more accurate solution than for simply truncating with a circular domain.

6.2 Numerical comparison of contour and standard circular truncation

In this section the proposed method of shaping the domain's boundary to the contour of the argument of the solution is demonstrated and evaluated for several model problems. For this we consider the truncated problem of (6.3):

$$\begin{aligned}
-\Delta p - k^2 p &= 0 \text{ in } \Omega, \\
p &= p_0 \text{ on } \Gamma_{\text{sca}}, \\
\mathcal{B}(p) &= 0, \text{ on } \Gamma,
\end{aligned} \tag{6.20}$$

where p_0 is some Dirichlet condition like an incoming scattering wave, Γ_{sca} is the boundary of the scattering object and $\mathcal{B}(p)$ is either the impedance or the curvature boundary condition. The weak formulation then reads: Find $p \in H_{\Gamma_{\text{sca}}}^1(\Omega)$ such that

$$\int_{\Omega} \nabla p \cdot \nabla q \, dx - k^2 \int_{\Omega} p q \, dx - ik \int_{\Gamma} p q \, ds = 0 \quad \forall q \in H_{\Gamma_{\text{sca}}}^1(\Omega)$$

for the impedance boundary condition and

$$\int_{\Omega} \nabla p \cdot \nabla q \, dx - k^2 \int_{\Omega} p q \, dx - \int_{\Gamma} \left(ik - \frac{\kappa}{2} \right) p q \, ds = 0 \quad \forall q \in H_{\Gamma_{\text{sca}}}^1(\Omega)$$

for the curvature boundary condition.

We consider problem (6.20) for different Γ_{sca} , i.e., different scattering objects, and

different p_0 . For each of the problems we first construct the contour domain by solving the problem on a large circular domain, computing the argument of the solution and choosing a level set of that. This defines the contour truncation. As comparison we also construct an area-equivalent circular domain with the same area, such that the computational cost of solving on these domains is comparable due to a similar number of degrees of freedom.

6.2.1 Scattering problems

We will now consider the problem discussed in the beginning of this chapter: A circular scatterer with an incoming plane wave. Hence, Γ_{sca} is a circle with radius $a = 0.5$ m and $p_0 = -p_{\text{inc}}$ defined as in (6.4) with angle $\theta_{\text{inc}} = \frac{3}{2}\pi$, i.e., a wave coming from the right. We solve problem (6.20), or rather its weak formulation, on a domain with outer boundary Γ being a circle with radius 2 m. The solution for $f = 1478$ Hz is visualized on the left-hand side in Figure 6.6 for the complex argument and the absolute value. From the complex argument we construct the contour domain and an area-equivalent circular domain. These are considered on the right-hand side of the figure. Due to the contour lines the boundary in the contour plot is much closer to the scatterer at the right side, while the distance on the left side is rather large. For the area-equivalent domain the distance to the scatterer is obviously constant for each direction.

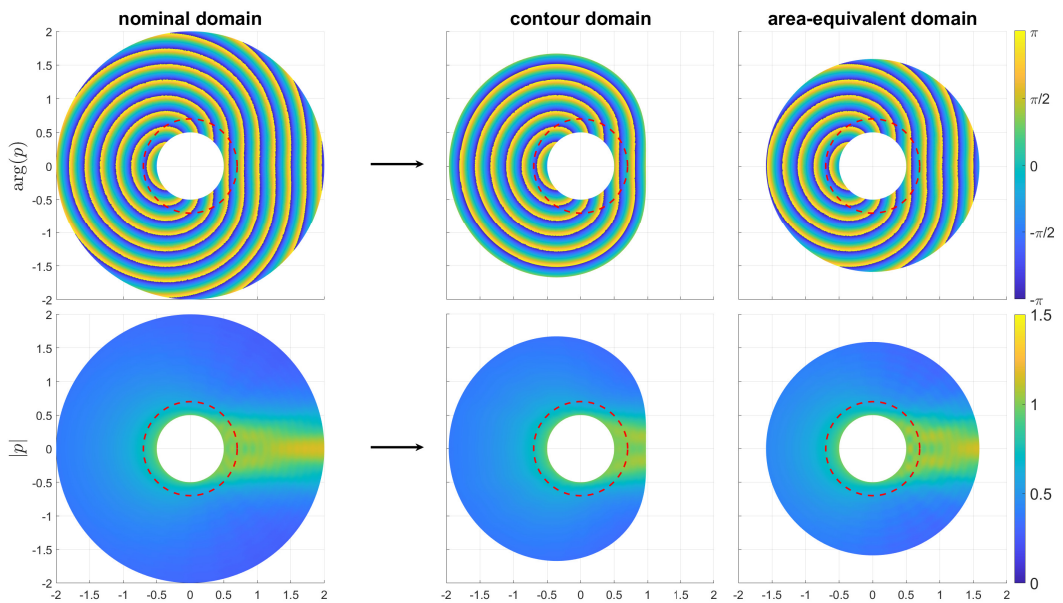


Figure 6.6: Circular scatterer: Complex argument (top) and absolute value (bottom) of the solution p on original domain, contour domain and area-equivalent domain for $f = 1478$ Hz. The red circle indicates the domain Ω_s .

Using quadratic finite elements we solve problem (6.20) on each domain twice: once

6.2 Numerical comparison of contour and standard circular truncation

with the simple boundary condition and once with the curvature absorbing boundary condition. We compute the relative L^2 -errors for each case for different frequencies f . We can observe significant lower errors for the contour domain for the larger frequency range. We can also observe that the curvature absorbing boundary condition performs superior in the low frequency range, while this difference becomes smaller for high frequency. For the impedance boundary condition in the area-equivalent domain and both boundary conditions in the contour domain we can observe shrinking error with respect to the frequency. This is presumably partially because in two dimensions the frequency has a similar effect as the distance (see the argument of the fundamental solution Ψ_{2D}): Since decaying waves decay as $\mathcal{O}(r^{-\frac{1}{2}})$, for $d = 2$, in free space the boundary conditions imposed here lead to better approximations if the boundary is farther away from the source, i.e., for the scattering wave, the scatterer. Since for the fundamental solution $\Psi_{2D} = H_0^{(1)}(kr)$, the wave number k is part of the argument in the same way as the distance r , the fundamental solution also decays in k , hence high frequency has a similar effect on the approximation at the truncation boundary as if the boundary would be farther away. This means the reflectance at the boundary is smaller absolutely and thus better models a fully absorbing boundary.

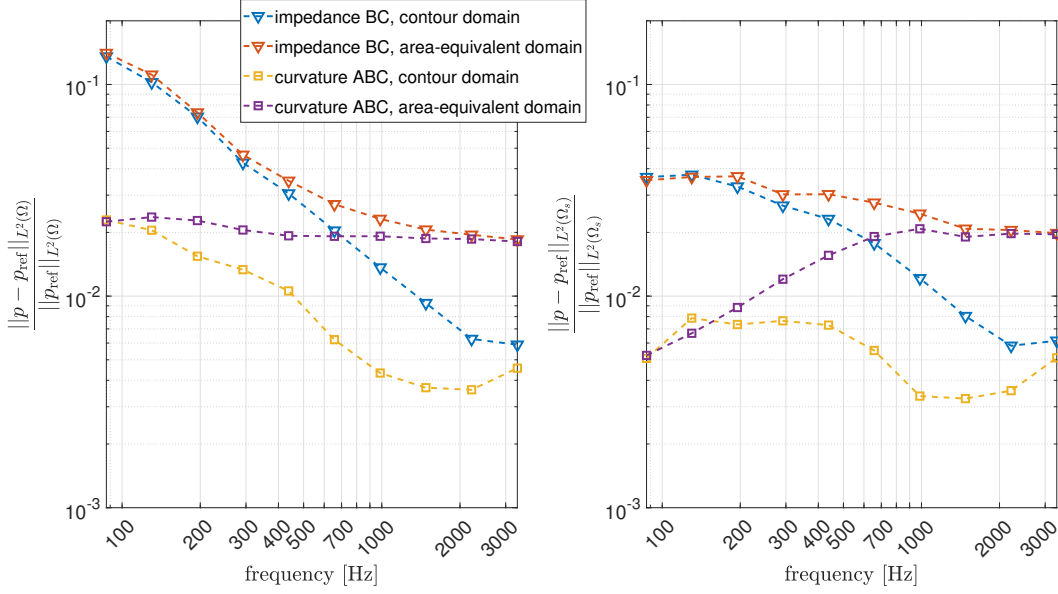


Figure 6.7: Relative L^2 -error $\frac{\|p - p_{\text{ref}}\|_{L^2(\Omega)}}{\|p_{\text{ref}}\|_{L^2(\Omega)}}$ and $\frac{\|p - p_{\text{ref}}\|_{L^2(\Omega_s)}}{\|p_{\text{ref}}\|_{L^2(\Omega_s)}}$ on the whole domain and a small circular domain around the circular scatterer, respectively, with respect to frequency for impedance and C-ABC on the contour and area-equivalent domains.

Since the contour and area-equivalent domain reflect different parts of the solution the comparison of the L^2 -error over the whole domain might not be quite fair. For this reason we also consider the error just in a *small* neighborhood $\Omega_s = B_{0.7}(0) \setminus \Omega_{\text{sca}}$ of

the scatterer. The results are shown on the right-hand side of Figure 6.7. Overall we observe a similar behavior compared to the errors on the whole domain Ω . The error on the contour domain is in general smaller and the difference between curvature absorbing boundary condition and impedance boundary conditions vanishes for higher frequency.

Contour domains for different scattering obstacles

In this part problem (6.20) is considered with other obstacles: A rectangular and a kite-shaped scatterer. The analytic solutions to these problems is not available and a reference solution is computed using perfectly matched layers. Figures 6.8 and 6.9 consider the case of a quadratic and a kite shaped scatterer respectively. Note that for the kite-shaped scatterer we used a larger nominal domain with radius 2.5 m, since otherwise we could not find a continuous contour line inside the domain. Also $\Omega_s = B_{0.8}(0) \setminus \Omega_{\text{sca}}$ in this case, such that the scatterer is actually fully included in the domain. As in the case with the circular scatterer, the relative L^2 -error is computed with respect to the whole domain Ω and also a smaller circular domain Ω_s around the scatterer. The results are illustrated in Figures 6.10 and 6.11. We can observe rather similar results as in the case of a circular scatterer qualitatively. The contour domain again leads to significant lower errors.

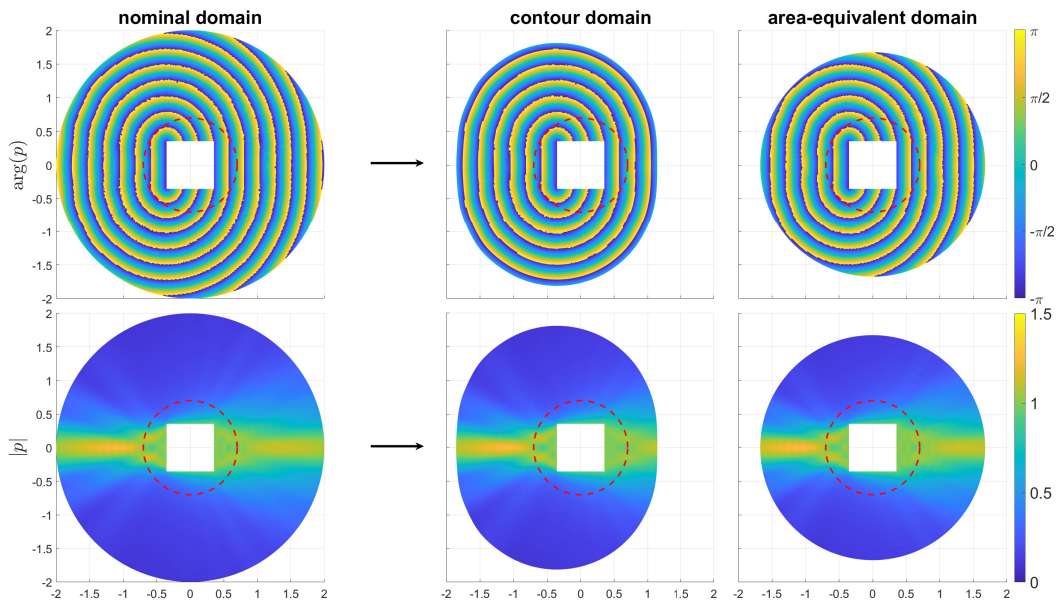


Figure 6.8: Rectangular scatterer: Complex argument (top) and absolute value (bottom) of the solution p on original domain, contour domain and area-equivalent domain for $f = 1478$ Hz. The red circle indicates the domain Ω_s .

6.2 Numerical comparison of contour and standard circular truncation

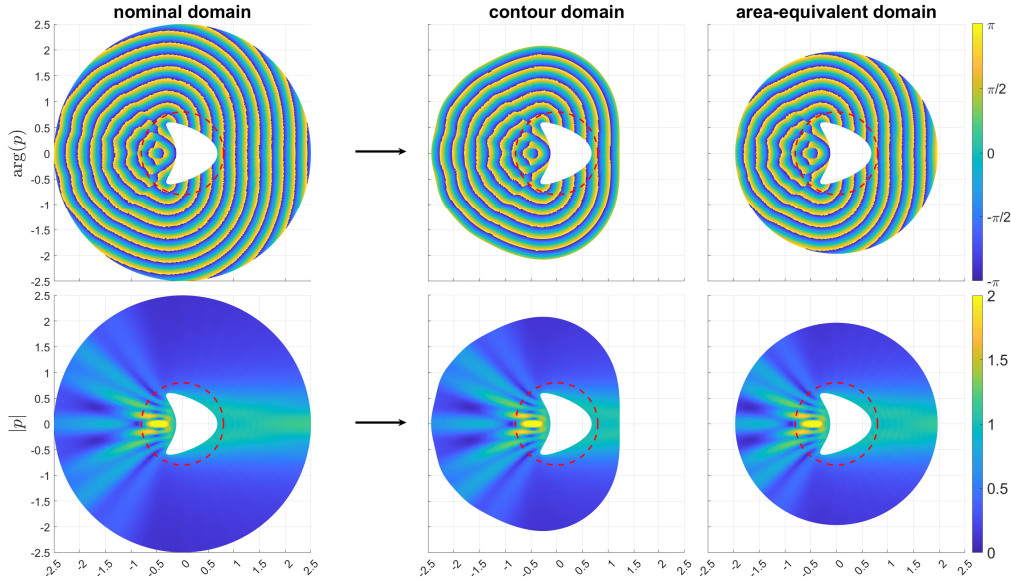


Figure 6.9: Kite-shaped scatterer: Complex argument (top) and absolute value (bottom) of the solution p on original domain, contour domain and area-equivalent domain for $f = 1478$ Hz. The red circle indicates the domain Ω_s . Note that the original domain is chosen larger ($r = 2.5$ m) since otherwise it was not possible to find a continuous contour line inside the domain. The small comparison domain Ω_s is also slightly larger with radius 0.8 m to fully enclose the scatterer.

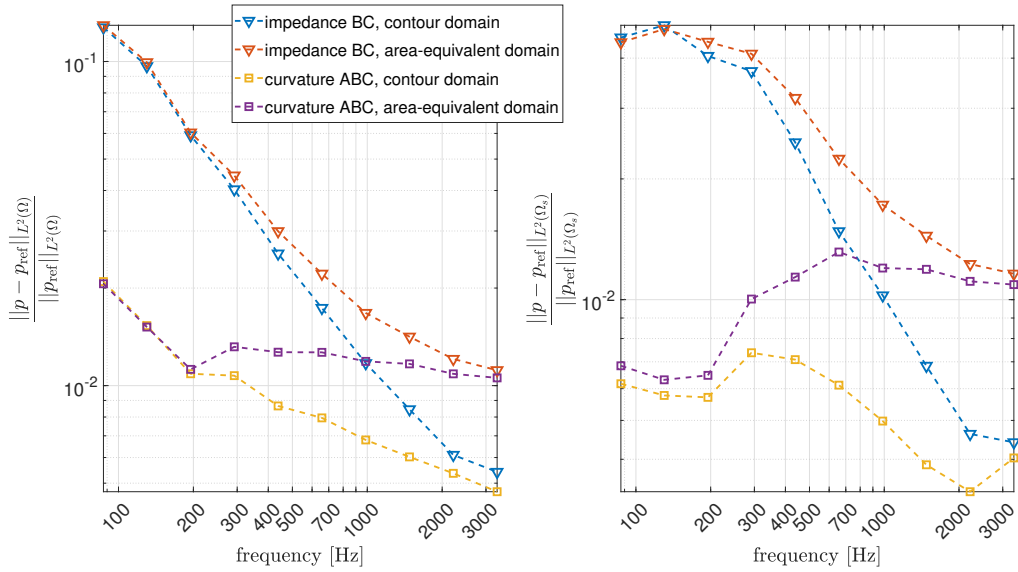


Figure 6.10: Relative L^2 -error $\frac{\|p - p_{\text{ref}}\|_{L^2(\Omega)}}{\|p_{\text{ref}}\|_{L^2(\Omega)}}$ and $\frac{\|p - p_{\text{ref}}\|_{L^2(\Omega_s)}}{\|p_{\text{ref}}\|_{L^2(\Omega_s)}}$ on the whole domain and a small circular domain around the rectangular scatterer with respect to frequency for impedance and C-ABC on the contour and area-equivalent domains.

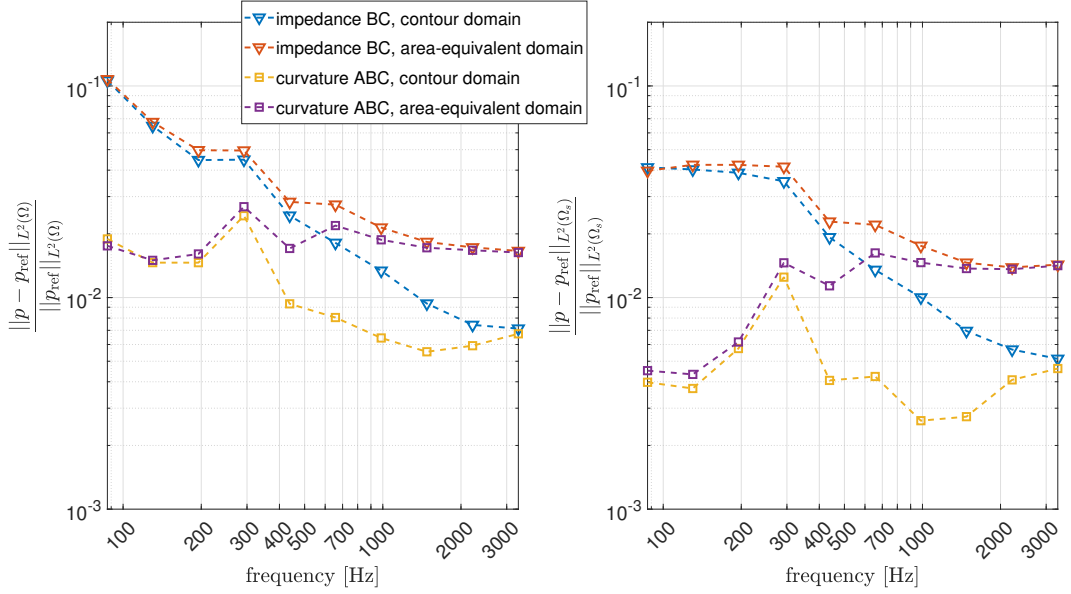


Figure 6.11: Relative L^2 -error $\frac{\|p - p_{\text{ref}}\|_{L^2(\Omega)}}{\|p_{\text{ref}}\|_{L^2(\Omega)}}$ and $\frac{\|p - p_{\text{ref}}\|_{L^2(\Omega_s)}}{\|p_{\text{ref}}\|_{L^2(\Omega_s)}}$ on the whole domain and a small circular domain around the kite-shaped scatterer, respectively, with respect to frequency for impedance and C-ABC on the contour and area-equivalent domains.

6.2.2 Problem with point sources as Dirichlet data

As final experiment again consider an exterior Dirichlet Helmholtz problem. In principle this is the same as the scattering problem, only the Dirichlet data at the interior boundary is different. Here it is composed of a sum of point sources in the following form

$$p = \sum_{n=1}^{50} H_1^{(0)} \left(k \sqrt{(x - c_1^{(n)})^2 + (y - c_2^{(n)})^2} \right), \quad (6.21)$$

where the $c^{(n)}$ are the centers of the point sources distributed by $c^{(n)} = (0, 0.4 - \frac{0.8}{49}(n-1))$, $n = 1, \dots, 50$. The solution to this linear array of sources is plotted in nominal, contour and area-equivalent domain in Figure 6.12. Comparing the relative L^2 -error one observes again, that for the the impedance boundary condition again performs worse than the absorbing boundary condition. For high frequencies however there is no significant difference. Here we also observe slightly better results using the nominal domain. This is presumably because the circular domain has already rather small angle of incidences over the whole boundary. Hence for low frequencies the contour truncation does not lead to improved results and might be worse because of the smaller distance to the obstacle for some parts of the boundary. For high frequencies we can again see that the contour domain leads to better results for the small ring around the scatterer.

6.2 Numerical comparison of contour and standard circular truncation

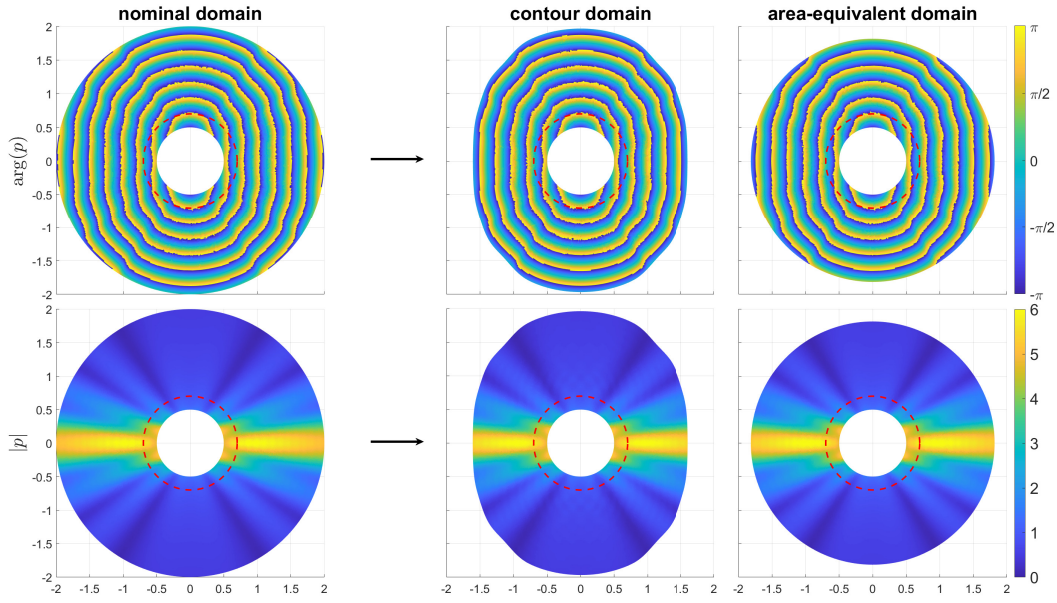


Figure 6.12: Point sources. Complex argument (top) and absolute value (bottom) of solution on original domain, contour domain and area-equivalent domain for $f = 1478$ Hz. The red circle indicates the domain Ω_s .

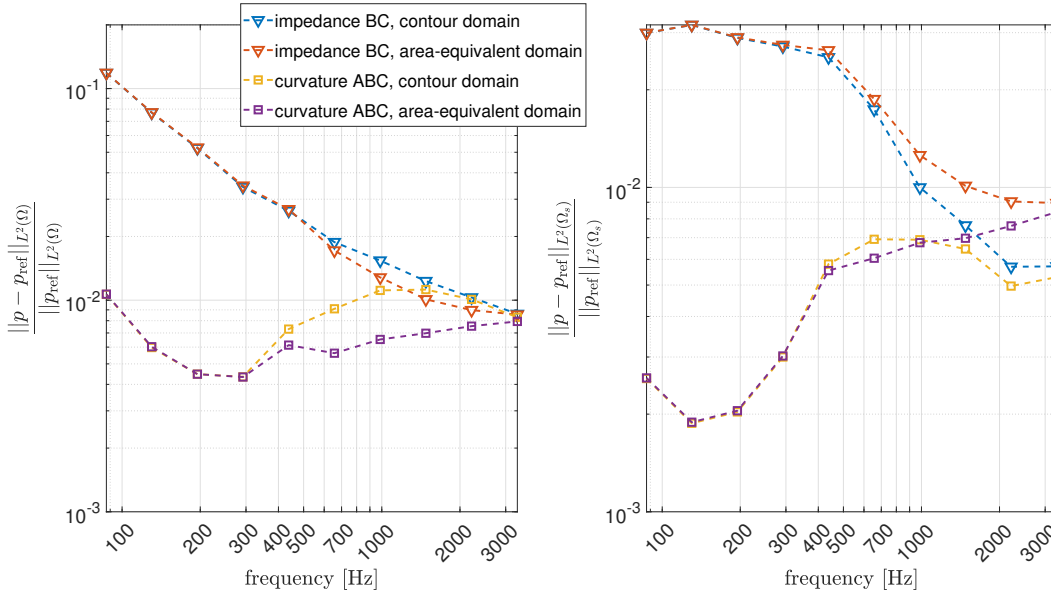


Figure 6.13: Relative L^2 -error $\frac{\|p - p_{\text{ref}}\|_{L^2(\Omega)}}{\|p_{\text{ref}}\|_{L^2(\Omega)}}$ and $\frac{\|p - p_{\text{ref}}\|_{L^2(\Omega_s)}}{\|p_{\text{ref}}\|_{L^2(\Omega_s)}}$ on the whole domain and a small circular domain around the circle that surrounds the point sources, respectively, with respect to frequency for impedance and C-ABC on the contour and area-equivalent domains.

6.3 Conclusions

This chapter, we introduced a domain truncation method for exterior Helmholtz problems, focusing on optimizing the geometry of the computational boundary. The results show that contour-based domain shapes significantly improve accuracy when using simple boundary conditions like the impedance or curvature absorbing boundary conditions. Numerical experiments confirm that this approach effectively reduces residuals and reflections.

While this method has advantages, it also has certain limitations, such as handling disconnected contour lines or jumps caused by interference. Nevertheless, it provides a valuable alternative when memory constraints preclude the use of larger domains or when higher-order boundary conditions are difficult to implement or not available. To effectively use this method in practice one also needs to compute the truncation domain without solving the problem on a large domain first. Potentially this could be done iteratively starting with the nominal domain and shifting the domain slightly in each iteration to fit the boundary to a contour line of the complex argument of the solution. For this, shape optimization techniques discussed in Chapter 5 could be used.

Chapter 7

Conclusions and Outlook

In this thesis we have developed and analyzed several approaches to enhance accuracy of time-harmonic wave propagation simulations using numerical methods. We focused on different applications and worked on closing the gap between measurements and computational models and using these models to improve existing geometries. For this we used and further developed concepts of finite elements, parameter estimation, shape optimization and domain truncation.

In particular, we developed a framework for estimating geometric and physical parameters of the ear canal from input impedances. This enabled us to construct a one-dimensional surrogate model that is similar in accuracy than a full three-dimensional finite element model. This surrogate reduces the computational cost without significant fidelity decrease. It further can be build with only input impedance measurements whereas the three-dimensional model needs additional scans of the ear canal itself which in general is more elaborate to get.

Further we demonstrated the ability to estimate surface impedances from noisy measurement data, provided the underlying physical model was correctly specified. In cases of model discrepancy, we identified the model misfit. This work also included rigorous convergence proofs for computing moments using ratio estimators.

Through shape optimization, we improved the performance of systems constrained by the Helmholtz equation, particularly in scenarios involving uncertain source locations. These optimizations not only led to localized improvements but also, for the low-frequency range, exhibited robustness across neighboring wave numbers.

Finally, we proposed a novel domain truncation technique to improve accuracy in exterior wave propagation problems. By optimizing the geometry of the artificial computational boundary, we successfully minimized reflections, leading to improved accuracy in finite element simulations. Numerical experiments demonstrated reductions in L^2 -error across the entire domain, as well as near scattering objects, showing the effectiveness of the proposed method in mitigating artificial boundary artifacts.

Outlook and future directions

While the methods used and developed in this thesis have yielded good results, they also open further possible research areas for improving the methods. The author of this thesis is particularly interested in building on the methods in Chapters 3 and 4 in the following:

Improving efficiency by using fast methods

While the methods used in this thesis lead to improvements in their respective areas, the focus did not lie on fast methods. Specifically room acoustics or exterior problems will improve in efficiency by using the boundary element method, particularly fast variations of it.

Coupling of the ear canal with the exterior sound field

In Chapter 3 we developed a framework to estimate a model for the sound propagation in the ear canal only from input impedances. These are relatively easy to obtain. The overall head and torso geometry of a human can also be scanned without invasive methods, see for example IHA database [93]. A coupling of both leads to direct sound propagation from the exterior field to the ear drum (or vice versa in a reciprocal point of view). This introduces new difficulties since the relevant geometries have different scales and hence these aspects need to be carefully considered.

Bayesian parameter estimation using BEM


Building upon the last point, the framework from chapter 4 can be used to estimate the impedance of skin, hair and clothes of a human, based on (noisy) measurements. This is particularly interesting in simulating more accurate Head-related transfer functions (HRTFs) or for more realistic sound propagation in the world of virtual reality.

Bibliography

- [1] M. Abramowitz and I. A. Stegun. *Handbook of mathematical functions with formulas, graphs, and mathematical tables*, volume No. 55 of *National Bureau of Standards Applied Mathematics Series*. Washington, DC, 1964.
- [2] R. A. Adams and J. J. F. Fournier. *Sobolev spaces*, volume 140 of *Pure and Applied Mathematics (Amsterdam)*. Elsevier/Academic Press, Amsterdam, second edition, 2003.
- [3] G. Allaire and C. Dapogny. A deterministic approximation method in shape optimization under random uncertainties. *SMAI J. Comput. Math.*, 1:83–143, 2015.
- [4] G. Allaire, C. Dapogny, and F. Jouve. Shape and topology optimization. In *Geometric partial differential equations. Part II*, volume 22 of *Handb. Numer. Anal.*, pages 1–132. Elsevier/North-Holland, Amsterdam, 2021.
- [5] H. W. Alt. *Lineare Funktionalanalysis*. Springer Berlin Heidelberg, Berlin, Heidelberg, 2012.
- [6] R. Anderssohn and S. Marburg. Nonlinear Approach to Approximate Acoustic Boundary Admittance in Cavities. *Journal of Computational Acoustics*, 15(01):63–79, 2007.
- [7] L. Antiga. Patient-specific modeling of geometry and blood flow in large arteries. *PhD Thesis*, 2002.
- [8] G. B. Arfken, H.-J. Weber, and F. E. Harris. *Mathematical methods for physicists : A comprehensive guide*. Academic Press/Elsevier, Waltham, MA, Seventh edition, 2013.
- [9] L. Armijo. Minimization of functions having Lipschitz continuous first partial derivatives. *Pacific J. Math.*, 16:1–3, 1966.
- [10] H. Azegami. *Shape Optimization Problems*, volume 164. Springer Singapore, Singapore, 2020.
- [11] I. M. Babuška and S. A. Sauter. Is the pollution effect of the fem avoidable for the helmholtz equation considering high wave numbers? *SIAM Journal on Numerical Analysis*, 34(6):2392–2423, 1997.
- [12] Babuška, I. Survey lectures on the mathematical foundations of the finite element method. *The Mathematical Foundations of the Finite Element Method with Applications to Partial Differential Equations*, pages 3–359, 1972.

Bibliography

- [13] A. Barth, C. Schwab, and N. Zollinger. Multi-level Monte Carlo Finite Element method for elliptic PDEs with stochastic coefficients. *Numerische Mathematik*, 119:123–161, 2011.
- [14] H. Barucq, M. Bergot, J. Chabassier, and E. Estecahandy. Derivation of high order absorbing boundary conditions for the Helmholtz equation in 2D. *Research Report RR-8632, INRIA, Bourdeaux*, 2014.
- [15] A. Bermúdez, P. Gamallo, and R. Rodríguez. Finite element methods in local active control of sound. *SIAM J. Control Optim.*, 43(2):437–465, 2004.
- [16] A. Bermúdez, L. Hervella-Nieto, A. Prieto, and R. Rodríguez. An optimal perfectly matched layer with unbounded absorbing function for time-harmonic acoustic scattering problems. *J. Comput. Phys.*, 223(2):469–488, 2007.
- [17] T. Betcke, S. N. Chandler-Wilde, I. G. Graham, S. Langdon, and M. Lindner. Condition number estimates for combined potential integral operators in acoustics and their boundary element discretisation. *Numerical Methods for Partial Differential Equations*, 27(1):31–69, 2011.
- [18] G. Birkhoff, M. H. Schultz, and R. S. Varga. Piecewise Hermite interpolation in one and two variables with applications to partial differential equations. *Numerische Mathematik*, 11(3):232–256, 1968.
- [19] M. Blau, T. Sankowsky, P. Roeske, H. Mojallal, M. Teschner, and C. Thiele. Prediction of the Sound Pressure at the Ear Drum in Occluded Human Cadaver Ears. *Acta Acustica united with Acustica*, 96(3):554–566, 2010.
- [20] C. Bourlier, N. Pinel, and G. Kubické. *Method of moments for 2D scattering problems: Basic concepts and applications*. FOCUS series. Wiley and ISTE, Hoboken and London, 2013.
- [21] D. Braess. *Finite Elemente: Theorie, schnelle Löser und Anwendungen in der Elastizitätstheorie*. Masterclass. Springer Spektrum, Berlin and Heidelberg, 5. überarbeitete Auflage edition, 2013.
- [22] S. C. Brenner and L. R. Scott. *The mathematical theory of finite element methods*, volume 15 of *Texts in Applied Mathematics*. Springer, New York, third edition, 2008.
- [23] S. N. Chandler-Wilde, I. G. Graham, S. Langdon, and E. A. Spence. Numerical-asymptotic boundary integral methods in high-frequency acoustic scattering. *Acta Numer.*, 21:89–305, 2012.
- [24] S. N. Chandler-Wilde and S. Langdon. A Galerkin Boundary Element Method for High Frequency Scattering by Convex Polygons. *SIAM Journal on Numerical Analysis*, 45(2):610–640, 2007.

- [25] S. N. Chandler-Wilde and P. Monk. Wave-number-explicit bounds in time-harmonic scattering. *SIAM Journal on Mathematical Analysis*, 39(5):1428–1455, 2008.
- [26] P. G. Ciarlet. *The finite element method for elliptic problems*, volume 40 of *Classics in Applied Mathematics*. Society for Industrial and Applied Mathematics (SIAM), Philadelphia, PA, 2002. Reprint of the 1978 original [North-Holland, Amsterdam; MR0520174 (58 #25001)].
- [27] D. Claxton. Frenet [MATLAB Code]. <https://www.mathworks.com/matlabcentral/fileexchange/11169-frenet>, 2022.
- [28] COMSOL. Comsol multiphysics . *Stockholm, Sweden, www.comsol.com*.
- [29] S. Conti, H. Held, M. Pach, M. Rumpf, and R. Schultz. Shape Optimization Under Uncertainty—A Stochastic Programming Perspective. *SIAM Journal on Optimization*, 19(4):1610–1632, 2009.
- [30] J. C ea. Approximation variationnelle des probl emes aux limites. *Annales de l’institut Fourier*, 14(2):345–444, 1964.
- [31] M. Dashti and A. M. Stuart. The Bayesian approach to inverse problems. In *Handbook of uncertainty quantification. Vol. 1, 2, 3*, pages 311–428. Springer, Cham, 2017.
- [32] M. Dauge. *Elliptic Boundary Value Problems on Corner Domains*, volume 1341. Springer Berlin Heidelberg, Berlin, Heidelberg, 1988.
- [33] R. Dautray and J.-L. Lions. *Mathematical Analysis and Numerical Methods for Science and Technology: Volume 1 Physical Origins and Classical Methods*. Springer Science & Business Media, 2012.
- [34] T. A. Davis. Algorithm 832: UMFPACK V4.3—an unsymmetric-pattern multifrontal method. *ACM Trans. Math. Softw.*, 30(2):196–199, June 2004.
- [35] M. C. Delfour and J. P. Zol esio. *Shapes and geometries: Analysis, differential calculus, and optimization*, volume 4 of *Advances in design and control*. Society for Industrial and Applied Mathematics, Philadelphia, Penn., 2001.
- [36] J. D’Errico. `fminsearchbnd`, `fminsearchcon` [MATLAB Code]. <https://www.mathworks.com/matlabcentral/fileexchange/82777-fminsearchbnd-fminsearchcon>, 2022.
- [37] T. J. Dodwell, C. Ketelsen, R. Scheichl, and A. L. Teckentrup. A hierarchical multilevel markov chain monte carlo algorithm with applications to uncertainty quantification in subsurface flow. *SIAM/ASA Journal on Uncertainty Quantification*, 3(1):1075–1108, 2015.

Bibliography

- [38] T. J. Dodwell, C. Ketelsen, R. Scheichl, and A. L. Teckentrup. Multilevel Markov Chain Monte Carlo. *SIAM Review*, 61(3):509–545, 2019.
- [39] G. Dutilleul, F. C. Sgard, and U. R. Kristiansen. Low-frequency assessment of the in situ acoustic absorption of materials in rooms: an inverse problem approach using evolutionary optimization. *International Journal for Numerical Methods in Engineering*, 53(9):2143–2161, 2002.
- [40] S. Engel, D. Hafemeyer, C. Münch, and D. Schaden. An application of sparse measure valued Bayesian inversion to acoustic sound source identification. *Inverse Problems*, 35(7):075005, 2019.
- [41] B. Engquist and A. Majda. Absorbing Boundary Conditions for the Numerical Simulation of Waves. *Mathematics of Computation*, 31(139):629, 1977.
- [42] O. G. Ernst and M. J. Gander. Why it is Difficult to Solve Helmholtz Problems with Classical Iterative Methods. In I. G. Graham, T. Y. Hou, O. Lakkis, and R. Scheichl, editors, *Numerical Analysis of Multiscale Problems*, volume 83 of *Lecture Notes in Computational Science and Engineering*, pages 325–363. Springer Berlin Heidelberg, Berlin, Heidelberg, 2012.
- [43] L. C. Evans. *Partial differential equations*, volume 19 of *Graduate studies in mathematics*. American Mathematical Society, Providence, Rhode Island, second edition edition, 2010.
- [44] S. J. Fletcher and M. Zupanski. A hybrid multivariate Normal and lognormal distribution for data assimilation. *Atmospheric Science Letters*, 7:43–46, 2006.
- [45] G. N. Gatica, L. F. Gatica, and E. P. Stephan. A FEM-DtN formulation for a non-linear exterior problem in incompressible elasticity. *Math. Methods Appl. Sci.*, 26(2):151–170, 2003.
- [46] C. Geiersbach, E. Loayza-Romero, and K. Welker. Stochastic Approximation for Optimization in Shape Spaces. *SIAM Journal on Optimization*, 31(1):348–376, 2021.
- [47] C. Geiger and C. Kanzow. *Numerische Verfahren zur Lösung unrestringierter Optimierungsaufgaben*. Springer-Lehrbuch. Springer, Berlin and Heidelberg, 1999.
- [48] A. Gelman, G. O. Roberts, and W. R. Gilks. Efficient Metropolis Jumping Rules. In J. M. Bernardo, J. O. Berger, A. P. Dawid, and A. F. M. Smith, editors, *Bayesian Statistics 5*, pages 599–608. Oxford University Press Oxford, 1996.
- [49] M. B. Giles. Multilevel Monte Carlo Path Simulation. *Operations Research*, 56(3):607–617, 2008.
- [50] I. G. Graham and S. A. Sauter. Stability and finite element error analysis for the Helmholtz equation with variable coefficients. *Mathematics of Computation*, 89(321):105–138, 2019.

- [51] P. Grisvard. *Problèmes aux limites dans les polygones: Mode d'emploi*. Bulletin Direction Etudes Recherches, Mathematiques, Serie C(1):21–59, 1984.
- [52] P. Grisvard. *Elliptic problems in nonsmooth domains*, volume 69 of *Classics in Applied Mathematics*. Society for Industrial and Applied Mathematics (SIAM), Philadelphia, PA, 2011. Reprint of the 1985 original [MR0775683], With a foreword by Susanne C. Brenner.
- [53] H. Haario, E. Saksman, and J. Tamminen. Adaptive proposal distribution for random walk Metropolis algorithm. *Computational Statistics*, 14(3):375–395, 1999.
- [54] W. Hackbusch. *Elliptic differential equations*, volume 18 of *Springer Series in Computational Mathematics*. Springer-Verlag, Berlin, second edition, 2017. Theory and numerical treatment.
- [55] W. K. Hastings. Monte Carlo sampling methods using Markov chains and their applications. *Biometrika*, 57(1):97–109, 1970.
- [56] S. Heinrich. Multilevel Monte Carlo methods. In S. Margenov, J. Waśniewski, and P. Yalamov, editors, *Large-Scale Scientific Computing: Third International Conference, LSSC 2001 Sozopol, Bulgaria, June 6-10, 2001 Revised Papers*, volume 2179 of *SpringerLink Bücher*. Springer Berlin Heidelberg, Berlin, Heidelberg, 2001.
- [57] U. Hetmaniuk. Stability estimates for a class of Helmholtz problems. *Communications in Mathematical Sciences*, 5(3):665 – 678, 2007.
- [58] H. Holm, M. Maischak, and E. P. Stephan. The *hp*-version of the boundary element method for Helmholtz screen problems. *Computing*, 57(2):105–134, 1996.
- [59] H. Hudde and A. Engel. Measuring and Modeling Basic Properties of the Human Middle Ear and Ear Canal. Part I: Model Structure and Measuring Techniques. *Acta Acustica*, (84):720–738, 1998.
- [60] H. Hudde and A. Engel. Measuring and Modeling Basic Properties of the Human Middle Ear and Ear Canal. Part III: Transfer Functions and Model Calculations. (84):1091–1109, 1998.
- [61] H. Hudde, A. Engel, and A. Ludwig. Methods for estimating the sound pressure at the eardrum. *The Journal of the Acoustical Society of America*, 106(4 Pt 1):1977–1992, 1999.
- [62] F. Ihlenburg. *Finite element analysis of acoustic scattering*, volume 132 of *Applied Mathematical Sciences*. Springer-Verlag, New York, 1998.
- [63] ISO 10534-1:1996. *Acoustics — Determination of sound absorption coefficient and impedance in impedance tubes — Part 1: Method using standing wave ratio*. ISO, Geneva, Switzerland, 1996.

Bibliography

- [64] ISO 10534-2:1998. *Acoustics — Determination of sound absorption coefficient and impedance in impedance tubes — Part 2: Transfer-function method*. ISO, Geneva, Switzerland, 1998.
- [65] ISO 354:2003. *Acoustics — Measurement of sound absorption in a reverberation room*. ISO, Geneva, Switzerland, 2003.
- [66] J. Jost. *Partial differential equations*, volume 214 of *Graduate texts in mathematics*. Springer, New York and London, 2nd ed. edition, 2011.
- [67] P. Knabner and L. Angermann. *Numerik partieller Differentialgleichungen: Eine anwendungsorientierte Einführung*. Springer-Lehrbuch. Springer, Berlin and Heidelberg, 2000.
- [68] W. Kondrachov. Sur certaines propriétés des fonctions dans l'espace. *C. R. (Doklady) Acad. Sci. URSS (N.S.)*, 48:535–538, 1945.
- [69] F. Y. Kuo and D. Nuyens. Application of Quasi-Monte Carlo Methods to Elliptic PDEs with Random Diffusion Coefficients: A Survey of Analysis and Implementation. *Foundations of Computational Mathematics*, 16(6):1631–1696, 2016.
- [70] H. Kuttruff. *Akustik: Eine Einführung*. S. Hirzel Verlag, Stuttgart and Leipzig, 2004.
- [71] R. Leis. *Initial Boundary Value Problems in Mathematical Physics*. Vieweg+Teubner Verlag, Wiesbaden, 1986.
- [72] J. P. Madrigal-Cianci, F. Nobile, and R. Tempone. Analysis of a Class of Multilevel Markov Chain Monte Carlo Algorithms Based on Independent Metropolis–Hastings. *SIAM/ASA Journal on Uncertainty Quantification*, 11(1):91–138, 2023.
- [73] J. R. Magnus. *Matrix Differential Calculus with Applications in Statistics and Econometrics*. Wiley series in probability and statistics. Wiley, Hoboken, NJ, third edition edition, 2019.
- [74] J. M. Melenk. *On generalized finite-element methods*. University of Maryland, College Park, 1995.
- [75] J. M. Melenk and S. Sauter. Convergence analysis for finite element discretizations of the Helmholtz equation with Dirichlet-to-Neumann boundary conditions. *Math. Comp.*, 79(272):1871–1914, 2010.
- [76] J. M. Melenk and S. Sauter. Wavenumber explicit convergence analysis for galerkin discretizations of the helmholtz equation. *SIAM Journal on Numerical Analysis*, 49(3):1210–1243, 2011.

- [77] N. Metropolis, A. W. Rosenbluth, M. N. Rosenbluth, A. H. Teller, and E. Teller. Equation of State Calculations by Fast Computing Machines. *The Journal of Chemical Physics*, 21(6):1087–1092, 1953.
- [78] A. Mjaavatten. Curvature of a 1D curve in a 2D or 3D space [MATLAB Code]. <https://www.mathworks.com/matlabcentral/fileexchange/69452-curvature-of-a-1d-curve-in-a-2d-or-3d-space>, 2022.
- [79] A. Moiola and E. A. Spence. Is the Helmholtz Equation Really Sign-Indefinite? *SIAM Review*, 56(2):274–312, 2014.
- [80] I. S. Molčanov. *Theory of random sets*, volume 87 of *Probability theory and stochastic modelling*. Springer Nature, London, Second edition, 2017.
- [81] M. Möser. *Technische Akustik*. Springer Berlin Heidelberg, Berlin, Heidelberg, 2012.
- [82] J.-C. Nédélec. *Acoustic and Electromagnetic Equations: Integral Representations for Harmonic Problems*, volume 144 of *Springer eBook Collection Mathematics and Statistics*. Springer, New York, NY, 2001.
- [83] J. A. Nelder and R. Mead. A Simplex Method for Function Minimization. *The Computer Journal*, 7(4):308–313, 1965.
- [84] H. Niederreiter. *Random number generation and quasi-Monte Carlo methods*, volume 63 of *Regional conference series in applied mathematics*. Society for Industrial and Applied Mathematics, Philadelphia, Pa., 1992.
- [85] J. Nocedal and S. J. Wright. *Numerical optimization*. Springer series in operation research and financial engineering. Springer, New York, NY, second edition edition, 2006.
- [86] A. Paganini. *Numerical Shape Optimization with Finite Elements*. PhD thesis, ETH Zurich, 2016.
- [87] J. Piechowicz and I. Czajka. Determination of Acoustic Impedance of Walls Based on Acoustic Field Parameter Values Measured in the Room. *Acta Physica Polonica A*, 123(6):1068–1071, 2013.
- [88] H. Rappel, L. A. A. Beex, J. S. Hale, L. Noels, and S. P. A. Bordas. A Tutorial on Bayesian Inference to Identify Material Parameters in Solid Mechanics. *Archives of Computational Methods in Engineering*, 27(2):361–385, 2020.
- [89] D. M. Rasetshwane and S. T. Neely. Inverse solution of ear-canal area function from reflectance. *The Journal of the Acoustical Society of America*, 130(6):3873–3881, 2011.

Bibliography

- [90] D. M. Rasetshwane, S. T. Neely, J. B. Allen, and C. A. SHERA. Reflectance of acoustic horns and solution of the inverse problem. *The Journal of the Acoustical Society of America*, 131(3):1863–1873, 2012.
- [91] F. Rellich. Ein Satz über mittlere Konvergenz. *Nachrichten von der Gesellschaft der Wissenschaften zu Göttingen, Mathematisch-Physikalische Klasse*, 1930:30–35, 1930.
- [92] M. Renardy and R. C. Rogers. *An introduction to partial differential equations*, volume 13 of *Texts in applied mathematics*. Springer, New York and Berlin and Heidelberg, second edition, 2004.
- [93] R. Roden and M. Blau. The IHA database of human geometries including torso, head and complete outer ears for acoustic research. In *Proc. Internoise, Seoul, Korea, Aug. 2020*, pages 4226–4237, 08 2020.
- [94] J. J. Rosowski, P. J. Davis, S. N. Merchant, K. M. Donahue, and M. D. Coltrera. Cadaver middle ears as models for living ears: comparisons of middle ear input immittance. *The Annals of otology, rhinology, and laryngology*, 99(5 Pt 1):403–412, 1990.
- [95] T. Sankowsky-Rothe, M. Blau, S. Köhler, and A. Stirnemann. Individual Equalization of Hearing Aids with Integrated Ear Canal Microphones. *Acta Acustica united with Acustica*, 101(3):552–566, 2015.
- [96] T. Sankowsky-Rothe, M. Blau, E. Rasumow, H. Mojallal, M. Teschner, and C. Thiele. Prediction of the Sound Pressure at the Ear Drum in Occluded Human Ears. *Acta Acustica united with Acustica*, 97(4):656–668, 2011.
- [97] A. H. Schatz. An observation concerning Ritz-Galerkin methods with indefinite bilinear forms. *Mathematics of Computation*, 28(128):959–962, 1974.
- [98] R. Scheichl, A. M. Stuart, and A. L. Teckentrup. Quasi-Monte Carlo and Multilevel Monte Carlo Methods for Computing Posterior Expectations in Elliptic Inverse Problems. *SIAM/ASA Journal on Uncertainty Quantification*, 5(1):493–518, 2017.
- [99] J. Schmid, M. Eser, and S. Marburg. Bayes’scher Ansatz zur Bestimmung der akustischen Wandadmittanz, 2023.
- [100] L. R. Scott and S. Zhang. Finite element interpolation of nonsmooth functions satisfying boundary conditions. *Mathematics of Computation*, 54(190):483–493, 1990.
- [101] I. H. Sloan and S. Joe. *Lattice methods for multiple integration*. Oxford science publications. Clarendon Press, Oxford, repr edition, 1994.
- [102] J. Sokolowski and J.-P. Zolesio. *Introduction to Shape Optimization*, volume 16. Springer Berlin Heidelberg, Berlin, Heidelberg, 1992.

- [103] N. N. Souza, S. Dhar, S. T. Neely, and J. H. Siegel. Comparison of nine methods to estimate ear-canal stimulus levels. *The Journal of the Acoustical Society of America*, 136(4):1768–1787, 2014.
- [104] O. Steinbach. *Numerical Approximation Methods for Elliptic Boundary Problems: Finite and Boundary Elements*, volume 99 of *Texts in applied mathematics*. Springer New York, Berlin, 1. ed. edition, 2008.
- [105] M. R. Stinson and B. W. Lawton. Specification of the geometry of the human ear canal for the prediction of sound-pressure level distribution. *The Journal of the Acoustical Society of America*, 85(6):2492–2503, 1989.
- [106] A. Stirnemann. Ein Mittelohrmodell basierend auf der Aussenohr-Transferimpedanz. *Fortschritte der Akustik - DAGA 2011, Düsseldorf*, 2011.
- [107] A. M. Stuart. Inverse problems: A Bayesian perspective. *Acta Numerica*, 19:451–559, 2010.
- [108] M. Vorländer and S. Feistel. Raumakustische Simulation und Auralisation. In S. Weinzierl, editor, *Handbuch der Audiotechnik*, pages 1–21. Springer Berlin Heidelberg, Berlin, Heidelberg, 2023.
- [109] A. G. Webster. Acoustical Impedance and the Theory of Horns and of the Phonograph. *Proceedings of the National Academy of Sciences of the United States of America*, 5(7):275–282, 1919.
- [110] N. Wulbusch. Ear canal parameter fitting 1D [MATLAB Code]. <https://github.com/nickwulbusch/ear-canal-parameter-fitting-1d>, 2023.
- [111] N. Wulbusch, R. Roden, M. Blau, and A. Chernov. Bayesian Parameter Identification in Impedance Boundary Conditions for Helmholtz Problems. *SIAM Journal on Scientific Computing*, 46(4):B422–B447, 2024.
- [112] N. Wulbusch, R. Roden, A. Chernov, and M. Blau. Using a one-dimensional finite-element approximation of Webster’s horn equation to estimate individual ear canal acoustic transfer from input impedances. *The Journal of the Acoustical Society of America*, 153(5):2826, 2023.